

The
University
Of
Sheffield.

***In situ* surface functionalisation of scaffolds using
block copolymer self-assembly**

Priyalakshmi Viswanathan

Department of Biomedical Sciences
2013

Submitted in partial fulfillment of the PhD degree for the Department of
Biomedical Sciences, The University of Sheffield

Acknowledgements

First and foremost I would like to thank my supervisors Beppe Battaglia and Gwen Reilly for the opportunities and resources presented to me during this PhD. I only hope that I have made the most of it.

I would also like the following people without whom this work would not be possible:

Dr. Adam Engler and Somyot Chirasatitsin, our collaborators in UCSD, as part of the HFSP grant.

In particular, I thank them for all their help in obtaining results for matrix adhesive heterogeneity, chemical force spectroscopy mapping and qPCR microarrays (Chapter 6)

Prof. Steve Armes and Dr. Efrosyni Themistou (Department of Chemistry) for the synthesis and characterisation of the all the PLA- diblock copolymers used in the electrospinning sections of this thesis.

Nok, who has helped me endlessly with cell culture and qPCR experiments during her Masters project and her PhD.

Prof. Neil Cameron and Dr. David Johnson for mercury intrusion porosimetry data.

Dr. Emily Smith and Dr. Adrian Boatwright at the University of Nottingham for the use of their XPS services.

The BMS electron microscopy unit, The University of Sheffield for use of the gold coating and SEM facilities

The BMS Light Microscopy Facility, The University of Sheffield for the use of their confocal microscopes.

I would also like to thank my friends who have been supportive throughout my PhD; Robin, Irene, Russell, Milica, Becca, Shirin and Laura. Thank you to all the lab members of the Battaglia and Reilly groups (past and present) for all their help.

Lastly, I want to whole-heartedly thank my family and my parents for all the opportunities they have given me in my life and supporting me through an education in the UK.

Publications

P. Viswanathan, S. Chirasatitsin, K. Nghamkham, A.J. Engler and G. Battaglia
Cell instructive microporous scaffolds through interface engineering
Journal of the American Chemical Society, 2012 **134**: 20103-20109

P. Viswanathan, D.W. Johnson, N.R. Cameron and G. Battaglia
3D surface functionalization of emulsion-templated polymeric foams
ACS Applied Materials & Interfaces, in review

P. Viswanathan, K. Nghamkham, S. Chirasatitsin, G.R. Reilly, A.J. Engler and G. Battaglia
Topological control of stem cell differentiation using functionalised polyHIPE foams
In preparation for Advanced Healthcare Materials

P. Viswanathan, R.T. Pearson, L. Ruiz-Perez and G. Battaglia,
Topological control of cell-material interface (invited review)
In preparation for Biomaterials Science

P. Viswanathan, E. Themistou, S.P. Armes and G. Battaglia
Directing surface topology and functionality in biodegradable electrospun fibres
In preparation

Other Publications

P. Viswanathan and G. Battaglia
Exploiting interfacial instability to control nanoscale topography in 3D polymer foams
In preparation for Soft Matter

Abbreviations	8
List of Figures	11
List of Tables	14
Summary	15
Chapter 1: Introduction to Tissue Engineering and Regenerative Medicine	16
<i>1.1 The clinical drive</i>	<i>16</i>
<i>1.2 Tissue Engineering and Regenerative Medicine</i>	<i>17</i>
<i>1.2 References</i>	<i>20</i>
Chapter 2: Stem cells and the microenvironment	21
<i>2.1 Mimicking in vivo extracellular matrix</i>	<i>21</i>
<i>2.2 Cell adhesion to the extracellular matrix</i>	<i>22</i>
<i>2.3 Stem cells</i>	<i>24</i>
<i>2.3 Stem cells and topography</i>	<i>27</i>
<i>2.5 Stem cells and surface chemistry</i>	<i>30</i>
<i>2.8 References</i>	<i>34</i>
Chapter 3: Polymeric Scaffolds for Tissue Engineering	37
<i>3.1.1 Natural versus synthetic polymers</i>	<i>39</i>
<i>3.1.2 Current technologies for materials fabrication</i>	<i>42</i>
<i>3.2 Emulsion templating as a method for fabricating 3D porous matrices</i>	<i>46</i>
<i>3.2.1 Controlling HIPE morphology and stability</i>	<i>47</i>
<i>Role of the surfactant</i>	<i>47</i>
<i>Effects of monomer and crosslinker concentration</i>	<i>48</i>
<i>Water and oil soluble porogens</i>	<i>48</i>
<i>Electrolytes</i>	<i>49</i>
<i>3.2.2 Applications in tissue engineering and stem cell differentiation</i>	<i>49</i>
<i>3.3 Electrospinning as a method for the preparation of 3D matrices</i>	<i>50</i>
<i>3.3.1 Controlling Electrospun fibre morphologies</i>	<i>50</i>
<i>Solution viscosity/concentration</i>	<i>50</i>
<i>Surface tension</i>	<i>51</i>

3.3.2 Applications in Tissue Engineering and Stem Cell Differentiation	52
3.4 Amphiphilic block copolymers	54
3.5 Aims and objectives	57
3.5.1 Functionalisation of porous polyHIPEs	57
3.5.2. Functionalisation of electrospun fibres	59
References	61
Chapter 4: Materials and Methods	65
4.1 HIPE templating	65
4.1.1 Foam preparation	65
4.1.2 Foam morphology and interconnectivity	66
4.1.3 Mercury Intrusion porosimetry	67
4.1.4 X-ray photoelectron spectroscopy (XPS)	67
4.1.5 Water contact angle measurements	67
4.1.6 Preparation of 2D films for atomic force microscopy (AFM) analysis	67
4.1.7 Chemical Force Spectroscopy Mapping (CFSM)	68
4.1.8 Protein adsorption and detection	70
4.1.9 Fibronectin Matrix Preparation and Imaging	71
4.1.10 3D cell culture	71
4.1.11 Determination of scaffold toxicity	72
4.1.10 Cell Viability	73
4.1.12 Nuclear and actin cytoskeleton staining	73
4.1.13 Sample preparation for biological SEM	74
4.1.14 Calcium staining by Alizarin Red S	74
4.1.15 RNA isolation and cDNA synthesis for RT qPCR microarray	75
4.1.16 Statistical analysis	75
4.2 Electrospinning	77
4.2.1 Preparation and characterisation of electrospun fibres	77
4.2.1.1 Optimisation of fibre morphology and wettability	78
4.2.2 Effect of PLA block length	81
4.2.3 Fibre Degradation	82
4.2.4 Imaging of protein adsorption	83

4.2.5	<i>Water contact angles</i>	83
4.2.6	<i>Actin cytoskeleton and nuclear staining of hES-MP cell morphology</i>	83
4.2.7	<i>Preparation of ‘patchy’ electrospun fibres</i>	84
4.2.8	<i>Synthesis of cross-linked PLA-Diblock Copolymer PLA30-b-P(OEGMA30-stat-DSDMA1) using a one step ROP-RAFT simultaneous polymerisation.</i>	84
4.2.9	<i>Disulphide Cleavage and Functionalization of the PLA-b-POEGMA Block Copolymer with Divinyl Sulfone</i>	85
4.2.10	<i>Polymer Characterisation</i>	86
4.2.11	<i>Conjugation of linear RGDC to the POEGMA block</i>	87
4.3	<i>References</i>	88
Chapter 5: Preparation and Characterisation of Porous polyHIPEs		89
5.1	<i>Introduction</i>	89
5.2	<i>Methods</i>	92
5.3	<i>Results and discussion</i>	92
5.3.1	<i>Oil-soluble versus water-soluble initiator effects</i>	92
5.3.2	<i>Concentration Effects</i>	98
5.3.3	<i>Surface structure of polyHIPE foams</i>	101
5.3.4	<i>Shear and aqueous phase effects</i>	102
5.3.5	<i>HIPEs with triblock copolymer surfactants</i>	104
5.3.6	<i>Wettability studies</i>	106
5.3.7	<i>Determination of surface functional groups</i>	107
5.4	<i>Summary and further work</i>	109
5.6	<i>References</i>	111
Chapter 6: Characterisation of ‘patchy’ foams and its effects on hES-MP adhesion and differentiation		113
6.1	<i>Introduction</i>	113
6.2	<i>Methods</i>	115
6.2.1	<i>Cell assays and time points</i>	115
6.3	<i>Results</i>	115
6.3.1	<i>Adhesive heterogeneity in extracellular matrix</i>	115
6.3.2	<i>Morphology of porous and non-porous patchy foams</i>	116
6.3.3	<i>Surface topology characterisation</i>	119

6.3.4 <i>Surface chemistry and topology effects on stem cells: Open-porous vs closed-porous foams</i>	123
6.4.5 <i>Foam topological effects on hES-MP differentiation</i>	128
6.5 Discussion	134
6.5.1 <i>polyHIPEs as a 3D scaffold template for stem cell culture</i>	134
6.5.2 <i>Differential stem cell differentiation in response to block copolymer nano-domains</i>	137
6.5.3 <i>Mechanotransduction pathways</i>	138
6.5.4 <i>Clinical relevance for bone tissue engineering</i>	138
6.6 Summary and further work	139
6.7 References	141
Chapter 7: Functionalisation of electrospun fibres using PLA-amphiphilic block copolymers	144
7.1 Introduction	144
7.2 Methods	146
7.3 Results and Discussion	146
7.3.1 <i>Electrospinning and fibre morphologies</i>	146
7.3.2 <i>Block length dependency on surface segregation</i>	148
7.3.3 <i>Degradation profile of functionalised PDLLA fibres</i>	150
7.3.5 <i>Surface topological effects on hES-MP adhesion and spreading</i>	157
7.4 Summary and further work	159
7.5 References	161
Chapter 8: Conclusions and Future Directions	163
8.1 Development of 3D matrices- What's been achieved	163
8.2 Stem cell response- What's been achieved	165
8.3 The life and times of tissue engineering and regenerative medicine: where are we headed next?	167
8.4 References	169
Appendix	170

Abbreviations

2D	two dimensional
3D	three dimensional
AA	ascorbic acid
AFM	atomic force microscopy
AIBN	azobisisobutyronitril
ALP	alkaline phosphatase
ANOVA	analysis of variance
b-FGF	basic fibroblast growth factor
BGP	betaglycerol phosphate
BSA	bovine serum albumin
CD	cluster of differentiation
CFSM	chemical force spectroscopy mapping
CLSM	confocal laser scanning microscopy
DEX	dexamethasone
DI	de-ionised
DMF	dimethylformamide
DVB	divinylbenzene
ECM	extracellular matrix
ERK1/2	extracellular regulating kinase 1/2
ESC	embryonic stem cell
EtOH	ethanol
FAK	focal adhesion kinase
FBS	foetal bovine serum
FN	fibronectin
GAG	glycosaminoglycan
HA	hyaluronic acid
hES-MP	human embryonic derived mesoderm progenitors
HIPE	high internal phase emulsion
HLB	hydrophile-lipophile balance
hMSC	human mesenchymal stem cell
iPSC	induced pluripotent stem cell

MAPK	mitogen activated protein kinase
MC3T3	mouse calvarial pre osteoblasts
MG63	human osteosarcoma cell line
MeOH	methanol
μCP	microcontact printing
OCN	osteocalcin
OPN	osteopontin
o/w	oil-in-water emulsion
PBD-PAA	poly(1,4-butadiene)-poly(acrylic acid)
PBD-PEO	poly(1,4-butadiene)-b-poly(ethylene oxide)
PCL	poly(caprolactone)
PDLLA	poly(D,L-lactic acid)
PDMS	poly(dimethyl siloxane)
PEG/PEO	poly(ethylene glycol)/poly(ethylene oxide)
PHSRN	proline-histidine-serine-arginine-asparagine
PLL	poly(L-lysine)
PLLA	poly(L-lactic acid)
PLA-PDMA	poly(lactic acid)-b-poly(dimethyl aminoethyl methacrylate)
PLA-PEG	poly(lactic acid)-b-poly(ethylene glycol)
PLA-PMPC	poly(lactic acid)-b-poly((2-methacryloyloxy) ethyl phosphorylcholine)
PLA-POEGMA	poly(lactic acid)-b-poly(oligo ethylene glycol methacrylate)
polyHIPE	polymerised high internal phase emulsion
PS-PAA	polystyrene-b-poly(acrylic acid)
PS-PAA-PS	polystyrene-b-poly(acrylic acid)-b-polystyrene
PS-PEO	polystyrene-b-poly(ethylene oxide)
qPCR	quantitative polymerase chain reaction
RGD	arginine-glycine-aspartic acid
SEM	scanning electron microscopy
Span 80	sorbitan monooleate
Sty	styrene
TE	tissue engineered
THF	tetrahydrofuran

w/o	water-in-oil emulsion
XPS	x-ray photoelectron spectroscopy

Symbols

Φ_w	volume fraction water
g/mol^{-1}	grams per mole
kDa	kiloDalton
kPa	kiloPascal
mg	milligram
mm	millimetre
mol%	mole %
μg	microgram
μL	microlitre
μm	micrometre
$\mu\text{m/s}$	micrometer/second
nN	nanoNewton
kV	kilovolt
wt/wt%	weight by weight percent
wt/v%	weight by volume percent

List of Figures

Figure 1.1: Central dogma of tissue engineering	18
Figure 2.1: Cell membrane attachment to a matrix mediated by integrins	24
Figure 2.2: Human mesenchymal stem cell differentiation pathways	26
Figure 2.3: Surface topographies of materials	29
Figure 2.4: Surface stiffness direct human mesenchymal stem cell differentiation	30
Figure 2.5: Adhesion mediated mechanotransduction	33
Figure 3.1: Cell attachment to scaffolds of various porosities	39
Figure 3.2: Microcontact printing and photolithography substrates to control cell morphology	43
Figure 3.3: Self-assembled peptide amphiphiles	45
Figure 3.4: Morphology of a polyHIPE	47
Figure 3.5: Typical electrospinning set-up	52
Figure 3.6: Self-assembly of amphiphilic block copolymers	56
Figure 3.7: Microphase separation between two different block copolymers	56
Figure 3.8: Surface functionalisation of polyHIPE matrices	59
Figure 3.9: Surface functionalisation of electropun matrices	61
Figure 4.1.1: Preparation of 2D cross-linked film for CFSM analysis	69
Figure 4.1.2: Functionalisation of AFM probe	70
Figure 4.1.3: Force histograms to determine adhesive threshold	71
Figure 4.2.1: Electrospun fibre morphologies using CHCl ₃ :DMF	80
Figure 4.2.2: Effect of flow rates on electrospun fibre diameters	81
Figure 4.2.3: Optimisation of fibre diameters for each block copolymer	82
Figure 4.2.4: Synthesis of Branched PLA-Diblock Copolymer PLA ₃₀ -b-P(OEGMA ₃₀ -stat-DSDMA ₁)	86
Figure 4.2.5: Disulphide Cleavage and Functionalization of the PLA-b-POEGMA Block Copolymer with Divinyl Sulfone for RGD conjugation	87
Figure 4.2.6: hES-MP cultured on RGD functionalised surface	

Figure 5.1: Hierarchical structure of bone	91
Figure 5.2: Morphologies of polyHIPEs using block copolymer surfactants by aqueous phase initiation	95
Figure 5.3: Morphologies of polyHIPEs using block copolymer surfactants by oil phase initiation	96
Figure 5.4: polyHIPE foams prepared at high shear	97
Figure 5.5: Mercury intrusion plots of block copolymer functionalised foams	98
Figure 5.6: Effect of surfactant concentration on polyHIPE morphology using AIBN as the initiator	100
Figure 5.7: Effect of surfactant concentration on void diameters	101
Figure 5.8: Effect of surfactant concentration on polyHIPE morphology using $K_2S_2O_8$ as the initiator	102
Figure 5.9: Surface structure of a pore	103
Figure 5.10: Effect of shear rate and aqueous phase volume using AIBN as the initiator	104
Figure 5.11: Effect of shear rate and aqueous phase volume using $K_2S_2O_8$ as the initiator	105
Figure 5.12: polyHIPE morphologies using triblock surfactants	106
Figure 5.13: Contact angles of open and closed porous foams	108
Figure 5.14: Wide scan XPS spectra of polyHIPE foams	109
Figure 5.15: High resolution C1s XPS spectra of polyHIPE foams	109
Figure 6.1: Schematic of HIPE templating process using amphiphilic block copolymers	115
Figure 6.2: Adhesive heterogeneity in native extracellular matrix	117
Figure 6.3: Scanning electron micrographs of closed-porous foams	119
Figure 6.4: Scanning electron micrographs of open-porous foams	119
Figure 6.5: Porosity of open-porous foams	120
Figure 6.6: AFM topographs and surface roughness of 2D films	121
Figure 6.7: Chemical force spectroscopy mapping of block copolymer domains	122
Figure 6.8: Block copolymer domain surface area of 2D films	123
Figure 6.9: Inter-Domain spacing of 2D films	124
Figure 6.10: Total cell number and scaffold toxicity	125

Figure 6.11: hES-MP cell adhesion on open and closed porous HIPE scaffolds	126
Figure 6.12: hES-MP cell morphologies after 14, 21 and 28 days	127
Figure 6.13: Protein adsorption and detection on HIPE scaffolds	128
Figure 6.14: qPCR micro-array heat maps of hES-MPs grown on scaffolds after 7 days	130
Figure 6.15: Volcano plots of gene expression data	131
Figure 6.16: Scanning electron micrographs of mineral deposition on Span 80 scaffolds	132
Figure 6.17: Scanning electron micrographs of mineral deposition on block copolymer scaffolds	133
Figure 6.18: Alizarin Red quantification after 28 days	134
Figure 7.1: Scanning electron micrographs of electrospun fibre morphologies	148
Figure 7.2: Block length dependence on fibre morphologies	150
Figure 7.3: Degradation morphologies of PMPC-PLA, POEGMA-PLA and PEG-PLA functionalised fibres	152
Figure 7.4: Degradation morphologies of PDMA-PLA functionalised fibres	152
Figure 7.5: Mass loss determination of PMPC-PLA, POEGMA-PLA and PEG-PLA functionalised fibres	153
Figure 7.6: Mass loss determination of PDMA-PLA functionalised fibres	154
Figure 7.7: Schematic of electrospun fibre degradation	155
Figure 7.8: BSA protein adsorption on electrospun fibres	156
Figure 7.9: hES-MP cell morphology on functionalised fibres after 48 hours	157
Figure 7.10: Determining toxicity of electrospun scaffolds	158
Figure 7.11: Total cell number of hES-MPs cultured on 'patchy' fibres	159

List of Tables

Table 3.1: FDA approved synthetic polymers	41
Table 4.1-1: HLB values of amphiphilic block copolymer surfactants	66
Table 4.2-1: Amphiphilic block copolymers used for electrospinning	78
Table 4.2-2: Average fibre diameter and contact angle measurements of electrospun fibres	80
Table 4.2-3: PDMA-PLA block copolymers with varied PLA block lengths	83
Table 5.1: Mercury intrusion porosimetry for AIBN initiated foams	99
Table 5.2: Mercury intrusion porosimetry for $K_2S_2O_8$ initiated foams	99
Table 5.3: XPS spectral assignments	109
Table 6.1: Block copolymer foam compositions by molar ratios	118
Table 7.1: PDMA-PLA block copolymers used to study effect of block length	150
Table 7.2: Block copolymer fibre compositions by molar ratios	158

Summary

Understanding human mesenchymal stem cell (hMSC) adhesion and differentiation in three-dimensional matrices in vitro is important for potential regenerative medicine and stem cell therapies. One of the key requirements for the use of scaffolds is that they correctly display the physicochemical properties mimicking those of the native extracellular matrix (ECM), in particular adhesive heterogeneity. Previous studies in 2D provide evidence for the effects of matrix properties such as stiffness, topography and surface chemistry. Yet, there are very few examples to date where ECM heterogeneity has been recapitulated and its effects on hMSCs investigated.

The main aim of this research was to design topologically defined three-dimensional porous scaffolds. This was achieved by exploiting the self-assembly of amphiphilic diblock copolymers confined at an interface. Two methods of scaffold fabrication were used in these studies; high internal phase emulsion (HIPE) templating and electrospinning. In both studies, mixtures of two amphiphilic block copolymers were used to induce phase separation between the dissimilar hydrophilic blocks thereby creating distinct copolymer domains in the nanometer length scales on the scaffold surface. In both scaffold fabrication methods the amphiphilic block copolymers used were a combination of cell inert and cell adhesive chemistries, thereby generating matrices with distinct cell binding sites. The functionality and adhesive heterogeneity of these materials were characterised using varying techniques including x-ray photoelectron spectroscopy, chemical force spectroscopy mapping and contact angle measurements. The effect of adhesive heterogeneity of such matrices on human mesenchymal progenitor adhesion and differentiation based on block copolymer domains were investigated. It was found that hMSCs adhered in a block copolymer dependent manner to scaffolds that most closely mimicked the adhesive heterogeneity in native extracellular matrix.

Chapter 1: Introduction to Tissue Engineering and Regenerative Medicine

1.1 The clinical drive

Organ failure or major loss of tissue can lead to serious health risks or reduce the quality of a person's life. Surgical intervention is often necessary to restore the function of damaged tissue when spontaneous healing is not possible. A common practise is to implant a graft from a donor site; though this is accompanied by complications depending on the tissue donor. Tissue can be taken from the patient (also known as autologous) from another part of the body, but availability is often low and patients requiring multiple surgeries often run the risk of donor site morbidity. Other methods include using donor tissue from a different individual (allogenic) or an animal (xenogenic) but these often carry the risk of infection and immunological rejection.

Artificial transplants are also possible, for example, bone implants made from metals (such as titanium) or polymers may be used. These however, cannot undergo wound healing or tissue remodelling. Often the mechanical properties of the materials do not match that of the injured tissue and can cause wearing of the native tissue, thus requiring multiple surgeries. In fact, current statistics show that musculoskeletal disorders have one of the greatest requirements for transplantation in the developed world. Data from the National Health Service (NHS) in the UK reveals that today 3 million people are affected by musculoskeletal disorders such as osteoporosis with 230,000 of them per year suffering a fracture because of osteoporosis. Furthermore, over 70,000 patients require hip replacements due to osteoarthritis, hip fractures or rheumatoid arthritis each year in addition to 70,000 patients (mostly above the age of 60) requiring artificial knee transplants. The estimated cost to the NHS for such surgeries is estimated to be in excess of £5 billion a year (NHS, Choices, 2012). Mainly the cost of these illnesses to the NHS is caused by the lengthy recovery process with 1/10 transplantations requiring a revision surgery with intense patient care associated to these type of malignancies.

1.2 Tissue Engineering and Regenerative Medicine

The aim of tissue engineering and regenerative medicine is to replace or repair the physiological functions of damaged tissues or organs that cannot heal themselves without the limitations of organ transplant (availability of donors, rejection, infectious diseases). This is ideally achieved by using cells from the same patient (autologous) or from donors (allogenic) often requiring the aid of a scaffolding material that supports the growth of the new tissue. One appropriate source of cells are stem cells.

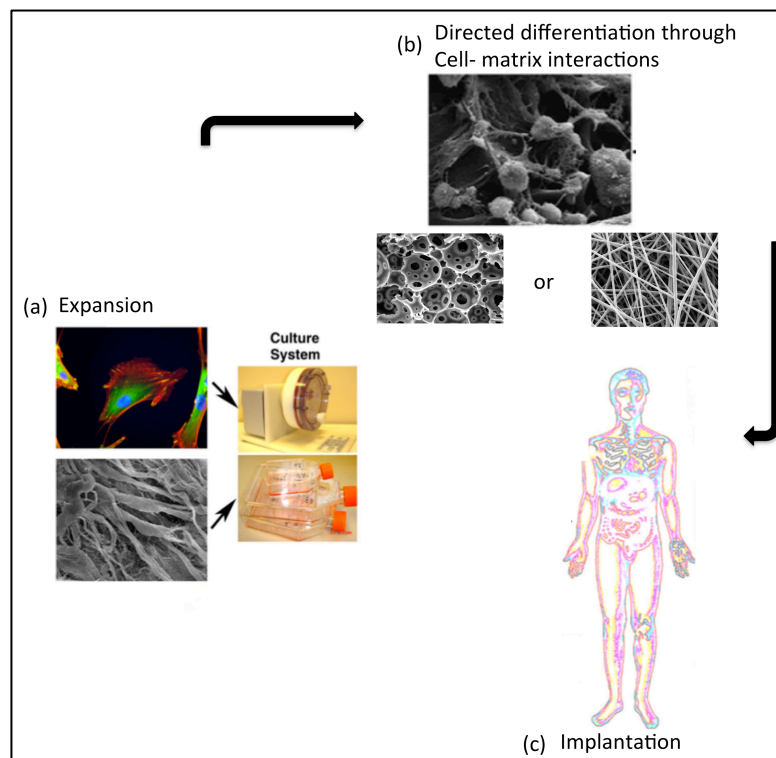


Figure 1.1 The central dogma of tissue engineering. a) Stem cells or progenitor cells are ideally isolated from the patient and expanded in culture in an *in vitro* culture system. b) These cells are then grown on 3D scaffolds that guide the cells differentiation or proliferation through cell-matrix and cell-cell interactions before being c) implanted back into the patient at the site of injury or repair. (Image modified from Biggs; 2008).

Stem cells are naïve cells that are capable of differentiating into several adult cell types. Embryonic stem cells (ESCs) are pluripotent, meaning that, they have the potential to turn into almost any type of tissue found in the body. Other stem cells, derived from adult bone marrow, known as mesenchymal stem cells (MSCs) are multipotent cells. These are capable of differentiating into several cell types in the body including bone, cartilage, fat and muscle¹.

Implantation of these stem cells often requires a scaffold that acts as a support to the developing tissue in the regeneration of its physiological functions. The aim of a scaffold is to provide appropriate structure and mechanical support that allows cells to attach and proliferate within the material. These scaffolds may be naturally derived, however these may elicit an immune response resulting in patient rejection upon transplantation. The Food and Drug Administration (FDA) has approved the use of many synthetic polymers that provide an alternate choice of biocompatible and/or biodegradable materials. The more popular of these include poly(ethylene glycol) (PEG), poly(vinyl alcohol) (PVA), poly(acrylic acid) (PAA), poly(lactic acid) (PLA), and poly(caprolactone) (PCL).

The success of these bench to bedside treatments relies on the collaborative efforts of researchers from backgrounds ranging from basic sciences of chemistry and biology to materials and engineering and clinicians. The field of tissue engineering and regenerative medicine has evolved over the years and current focus relies on the complex designing and engineering of biomaterials. Thus, many biomaterials scientists believe that a key design aspect of the new generation of materials requires that they influence cell behaviour in a defined and controlled manner at the molecular level². Furthermore, for potential clinical applications, the scaffold or matrix alone should ideally be sufficient to control stem cell differentiation as traditional *in vitro* soluble induction factors such as dexamethasone for osteogenesis, insulin for adipogenesis or hydrocortisone for smooth muscle differentiation are not clinically viable solutions. Importantly, the design and fabrication of such materials must preferably be achieved using manufacturing methods that are readily available. There is growing evidence of the importance of physicochemical properties such as substrate topography both in the micro- and nano- length scales, elasticity as well as surface chemistry and ligand presentation on cell behaviour, in particular the differentiation of MSCs³. Inspiration of such design features arises from mimicking the physicochemical properties of the extracellular matrix (ECM) *in vivo*. The ECM is a heterogeneous fibrillar network of proteins including collagen, laminin, fibronectin and elastin among others as well as non-fibrous components such as glycosaminoglycans. Apart from providing a structural support for cells, the ECM provides physical as well as chemical cues intricately organised on multiple length scales in a spatio- temporal manner⁴ to regulate cellular functions such as

proliferation, migration, differentiation and apoptosis. ECM structure and organisation can vary between tissue types (for example bone, lung, skin), within specific tissue or even from one physiological state to another for example cancerous versus normal.

Much of the investigation on substrate effects on stem cell differentiation has been demonstrated using adult stem cells such as MSCs. These cells exhibit reduced differentiation capabilities and heterogeneous populations compared to embryonic or haematopoietic stem cells⁵. Nonetheless, their restricted multi lineage potential and relative ease of availability has made them an appealing choice as a cell source for tissue engineering applications. The work presented in this thesis aims to understand some of these challenges through basic research in both the design of novel biomaterials as well as understanding stem cell differentiation and their potential to provide therapies with hope of improving patient health care in the near future. As such, our discussion begins with an understanding of the effects of substrate physical and chemical properties (topography, elasticity and surface chemistry) in regulating MSC lineage commitment and possible mechanotransduction pathways. Current strategies in biomaterials design, particularly for three-dimensional cell and tissue culture as well as challenges in designing these biomaterials will be discussed. Finally, the approach used in this thesis for the design of hierarchical 3D matrices using macromolecular self-assembly in two well-established scaffold fabrication methods will be examined. Their potential to direct human mesenchymal stem cell behaviour will be demonstrated herein.

1.2 References

1. Pittenger, M. F. Multilineage Potential of Adult Human Mesenchymal Stem Cells. *Science* **284**, 143–147 (1999).
2. Langer, R. & Vacanti, J. P. Tissue engineering. *Science* **260**, 920–926 (1993).
3. Reilly, G. C. & Engler, A. J. Intrinsic extracellular matrix properties regulate stem cell differentiation. *J. Biomech* **43**, 55–62 (2010)
4. Vogel, V. & Sheetz, M. Local force and geometry sensing regulate cell functions. *Nat Rev Mol Cell Biol* **7**, 265–275 (2006).
5. Saha, K., Pollock, J. F., Schaffer, D. V. & Healy, K. E. Designing synthetic materials to control stem cell phenotype. *Curr. Opin. Chem. Biol.* **11**, 381–387 (2007).

Chapter 2: Stem cells and the microenvironment

2.1 Mimicking in vivo extracellular matrix

The extracellular matrix (ECM) plays an essential role in providing structural support for the cells that reside within it. The ECM facilitates cell-matrix interactions through cell surface receptors and thereby transduces environmental cues to the cell interior to maintain tissue specific functions such as proliferation, migration and differentiation. Thus, in order to truly mimic the heterogeneity of the native ECM for the synthesis of novel 3D biomaterials, an understanding of how its structure and composition relate to its function is important. The ECM consists of a fibrillar network of proteins which includes collagens, laminins, and fibronectins. The ECM also consists of proteoglycans, which are composed of glycosaminoglycan (GAG) chains covalently bound to a specific protein core (except for hyaluronic acid). Below is a description of key ECM proteins and their main functions.

Collagen is the most abundant ECM protein, constituting 30% of total protein mass in multicellular organisms¹ and 90% of bone matrix proteins². To date, 28 different types of collagens have been identified¹ most of which form a triple stranded helical structure ~300nm long consisting of a distinct pattern with 67nm periodicity³. These helices can thereafter form fibrillar or non-fibrillar networks and other supramolecular structures depending on the type of collagen. Collagen is the primary structural protein of the ECM involved in tissue tensile strength, regulation of cell adhesion, migration and development⁴. Collagen is also associated with elastin, a secondary structural protein that provides recoil to tissues that require repeated stretching⁴. The structural importance of collagen was first noted in embryos lacking the collagen I gene, that reached late stages of development but experienced sudden death due to aortic rupture⁵.

Fibronectin (FN) is secreted as a dimer joined by C-terminal disulphide bonds. It is also a fibrous protein functioning primarily in regulating cell attachment. FN, which possesses RGD binding motifs, can influence integrin binding affinity and clustering⁶. Furthermore, this force-dependent stretching of FN (through actin-myosin contractility of the cell) exposes cryptic binding sites for cell attachment and has been widely implicated in MSC differentiation⁷.

Glycosaminoglycans (GAGs) are made of linear unbranched disaccharides with remarkable physical properties such as force resistance owing to their carboxyl, sulphate, and hydroxyl functional groups¹. The charged nature of the GAGs makes them highly susceptible to swelling and thus they form the hydrated network that occupies the extracellular interstitial space. The presence of these groups determines the type of GAG formed; heparan sulphates, chondroitin and so on. GAGs are covalently linked to core proteins except for hyaluronan and are known to regulate cell migration and diffusion of secreted growth factors through this hydrated network⁸.

2.2 Cell adhesion to the extracellular matrix

Cell adhesion to the ECM is regulated by cell surface receptors known as integrins. These are heterodimeric transmembrane proteins consisting of an α and β subunit. 24 different combinations of α and β subunits may be formed that determine ligand binding specificity for specific ECM motifs such as the RGD tri-peptide found on fibronectin, vitronectin and laminin⁹. It must be noted that not all ECM proteins contain a functional RGD sequence and not all integrin types bind RGD. These heterodimeric complexes are linked to the actin cytoskeleton through transmembrane anchor proteins such as talin, vinculin and paxillin¹⁰ (Figure 2.1). Ligand binding can consequently affect integrin binding affinity, and in the case of multi-ligand binding cause clustering of integrins. Thus this early cell-substrate anchoring leads to the formation of focal adhesions. The regulation of focal adhesions in combination with the release of specific soluble growth factors initiates signalling pathways and the regulation of nuclear transcription factors which ultimately facilitates cellular processes such as migration, adhesion, proliferation and differentiation^{11,12}.

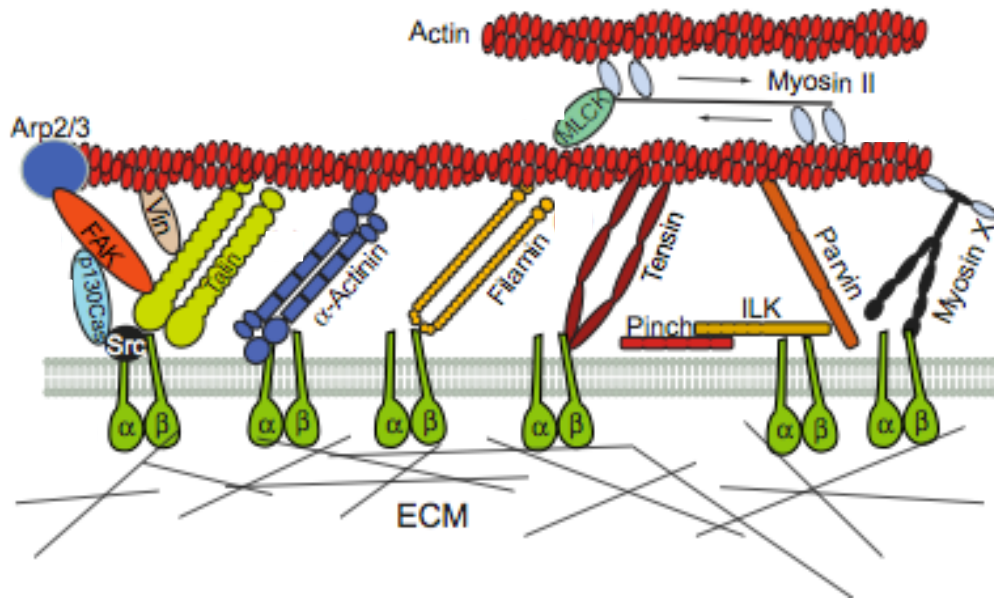


Figure 2.1 Cell attachment to the matrix is mediated by transmembrane proteins called integrins. Integrins are associated with various anchor proteins such as vinculin (Vin) that link the actin cytoskeleton of the cell to the substrate. (Image from Roca-Cusachs, 2011)

Spatz and co-workers have published several studies investigating the effects of cellular adhesion and spreading on RGD ligand spacing and density on integrin clustering and therefore cell adhesion. One study explored Au-patterned (< 8 nm in diameter) surfaces conjugated to cyclic RGDfK ligands which have a high affinity for the $\alpha_v\beta_3$ integrin¹³. They found that ligand spacings of 28 nm and 58 nm supported MC3T3- osteoblast adhesion and spreading while ligand spacings of 73 nm and 85 nm lead to poor cell adhesion and eventual apoptosis. Another study confirmed the requirement of ligand spacing to be < 70 nm for the formation of stable focal adhesions¹⁴. Furthermore, ligand ordering (order versus disorder) for each ligand spacing was found to affect osteoblast adhesion; ligands spaced > 70 nm on disordered surfaces lead to greater integrin clustering and stronger adhesions. This was attributed to less global ligand density compared to the ordered counterpart. Moreover, targeting specific integrin mediated adhesion has also been implicated in hMSC differentiation. For example, Martino *et al.* showed that recombinant fibronectin fragments (FN III9-10 domains) increased hMSC specificity for the integrins $\alpha_5\beta_1$ and $\alpha_v\beta_3$ that facilitated cell adhesion to the matrix¹⁵. This distinct adhesion was shown to direct hMSC differentiation towards the osteogenic lineage suggesting that hMSC adhesion to the ECM via integrins may provide the earliest cues in determining adhesion mediated hMSC fate decisions. These studies demonstrate that cell adhesion is dependent on the local order of RGD adhesions induced by integrin clustering which is controlled by the spatial pattern of the surfaces.

Additionally, how these ligands are presented and their density, affects integrin binding and clustering, eventually regulating cellular adhesion and differentiation. The implication of surface chemistry presentation on MSC differentiation is of importance to scientists developing novel synthetic materials as understanding how cell-substrate interactions mediated by integrin binding provides an insight into developing new synthetic materials with spatially controlled surface patterns. By controlling materials surface properties in a way that integrin specific interactions may be controlled precisely, it is possible to then initiate the right signalling cascades involved in MSC differentiation.

2.3 Stem cells

Stem cells are naive cells capable of self-renewal and differentiation into several tissue types. For example, embryonic stem (ES) cells are pluripotent and have the capability to differentiate into cells of all the three germ layers; ectoderm, endoderm and mesoderm. However, ethical issues that surround ES cells as well as the formation of teratomas due to their ability to rapidly proliferate has led to concerns over their potential use as a stem cell source for tissue engineering applications¹⁶. Furthermore, ES cells *in vitro* often need a feeder layer (mouse embryonic fibroblasts) to maintain their self-renewal and proliferative capacity which limits their use in clinical applications.

Adult stem cells are multipotent in that they are capable of self-renewal but can only differentiate towards a specific subset of tissues (Figure 2.2). Unlike ES cells, adult stem cells do not possess the ethical problems or form teratomas and their relative ease of isolation makes them a more viable cell source for TE applications despite their reduced plasticity. The bone marrow consists to two stem cell populations; 1) haematopoietic stem cells that give rise to the cells of the blood lineage and 2) mesenchymal stem cells that provide the structural and functional support for haemopoiesis. Human mesenchymal stem cells or hMSCs are derived from the stroma of the bone marrow, often referred to as stromal cells and are known to differentiate into cells of the mesoderm lineage i.e. bone, cartilage, muscle and fat¹⁷. In humans, MSCs are isolated from the bone marrow through biopsies of the iliac crest. Alternatively, hMSCs can also be harvested from the femoral marrow compartments, thoracic and lumbar spine^{18,19}. Cultures of hMSCs are isolated by their surface antigen markers,

Stro-1⁺, CD13⁺ CD29⁺, CD44⁺, CD73⁺, CD105⁺, CD106⁺, CD11b⁻, CD31⁻, CD34⁻, CD117⁻ and CD45⁻ 18,20.

As bone marrow biopsies can be highly invasive, other sources for the extraction of MSCs are being extensively investigated. This includes isolation from adipose tissue, blood from the umbilical cord and amniotic fluid¹⁹. Additionally, cell lines such as human embryonic derived- mesenchymal progenitors (hES-MPs), derived from human embryonic stem cell lines are being used as an alternative source to reduce the *in vitro* effects of patient variability often observed with primary human MSCs.

In vivo, MSCs are also known to migrate to sites of inflammation, engraft into a variety of tissues and thus play an active role in wound healing and tissue repair. This is done by the secretion of chemokines and their differentiation towards mature cell types which is regulated by the MSC niche. The *in vivo* niche refers to the microenvironment which MSCs reside within, which consists of other support cells, growth factors and the ECM. MSC interact within this niche through cell-cell and cell-matrix contacts and are important for maintaining the undifferentiated state of the stem cells as well as providing the right cues for differentiation.

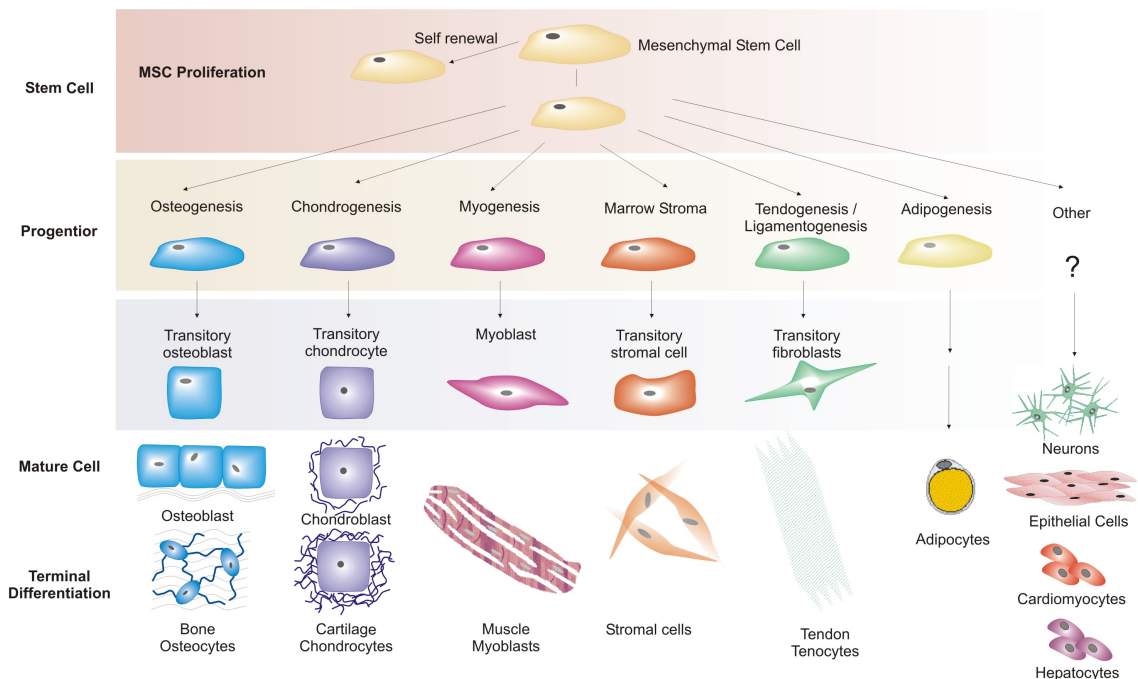


Figure 2.2 Self-renewal and differentiation pathways of human mesenchymal stem cells into mature cell types. (Image modified from Caplan and Bruder, 2001).

In culture, MSC differentiation towards the mesoderm lineage are characterised by several key markers depending on the lineage fate. The mesoderm lineage refers to differentiation towards bone(osteogenesis), fat(adipogenesis), cartilage(chondrogenesis) and muscle(myogenesis); see Figure 2.2. For example, in culture, osteogenesis is often induced through the soluble factors ascorbic acid (AA), β -glycerolphosphate (BGP) and dexamethasone (DEX). AA is required for the formation of stable collagen which is the most abundant bone matrix protein. BGP is a phosphate source for mineral deposition in osteoblasts while DEX is a synthetic corticosteroid that is present in induction media for osteogenesis, chondrogenesis and adipogenesis. In the absence of DEX however, osteogenesis does not proceed to completion in hMSCs and mineral associated with the bone matrix is not deposited. Common characteristics of osteogenic differentiation at the early stages include the increase in alkaline phosphatase (ALP) activity which is an early marker of osteogenesis. Increased mRNA expression of Runt-related transcription factor-2 / Core binding factor alpha-1 (RUNX2/CBF α 1), bone morphogenic protein (BMP) and transforming growth factor beta (TGF β) are also observed. Later stages of differentiation are characterised by a decrease in ALP activity and increase in expression of proteins such as osteopontin (OPN) and osteocalcin (OCN), associated with mineral formation as well as secretion of specific ECM proteins such as collagen I.

In 2006, Takahashi and Yamanaka published the induction of pluripotent cells, termed induced pluripotent stem cells or iPSCs²¹. Adult fibroblasts were reprogrammed by introducing four transcription factors: Oct3/4, Sox2, c-Myc and Klf4 which, when cultured in embryonic stem (ES) culture conditions, exhibited morphology and growth properties of ES cells in addition to expressing ES cell genes. Despite the many comparisons made between ES and iPS cells, there are subtle differences in the teratoma-forming and differentiation abilities *in vitro*. For example, it has been shown that some mouse iPSCs have lower teratoma forming efficiency than mouse ES cells²² while human iPSCs have less differentiation capabilities towards the haematopoietic, neuroepithelial and neural lineages compared to human ES cells²³. Despite the rapid progression in iPSC technology, questions remain over their use in stem cell and regenerative medicine therapies. Reprogramming of somatic cells to a pluripotent state requires global epigenetic changes, either through the reprogramming itself or as a result of the reprogramming process²⁴. It is therefore crucial to fully

understand differences in gene expression between iPS and ES cells to unearth the full potential of iPS cells in regenerative medicine therapies.

2.3 Stem cells and topography

Surface topography is known to be a physical cue to guide cell attachment, proliferation and migration as cells *in vivo* rarely encounter a smooth surface. Nano-scale topographical features (5-200 nm) have been reported in the basement membrane of many tissues in the form of protrusions, pits, striations and fibres²⁵ leading to the idea that topography may provide a biomimetic cue to control cell behaviour *in vitro*.

Fabrication techniques such electron beam- colloidal or dip pen lithography have been often used to design micro and nanometer scale topographies with remarkable reproducibility. These topographical features include islands, pits, ridges and grooves. *In vitro* synthetic substrates have proved to enable cells to sense and respond to its topographical surrounding. For example, human corneal epithelial (HCE) cells elongate and align in the direction of ridged features²⁶. Substrates with grooves and ridges offer predictability in cell morphologies in that such substrates are often used to align cells through contact guidance (Figure 2.3). Subsequent studies showed that lateral spacing of these features were shown to dictate the alignment response of HCE cells demonstrating that as the feature size decreases from the micro- to the nano scale, cell alignment preference shifted from parallel to perpendicular relative to feature size²⁷. This observation was attributed to the effects of both the topography and the culture medium the cells were grown in.

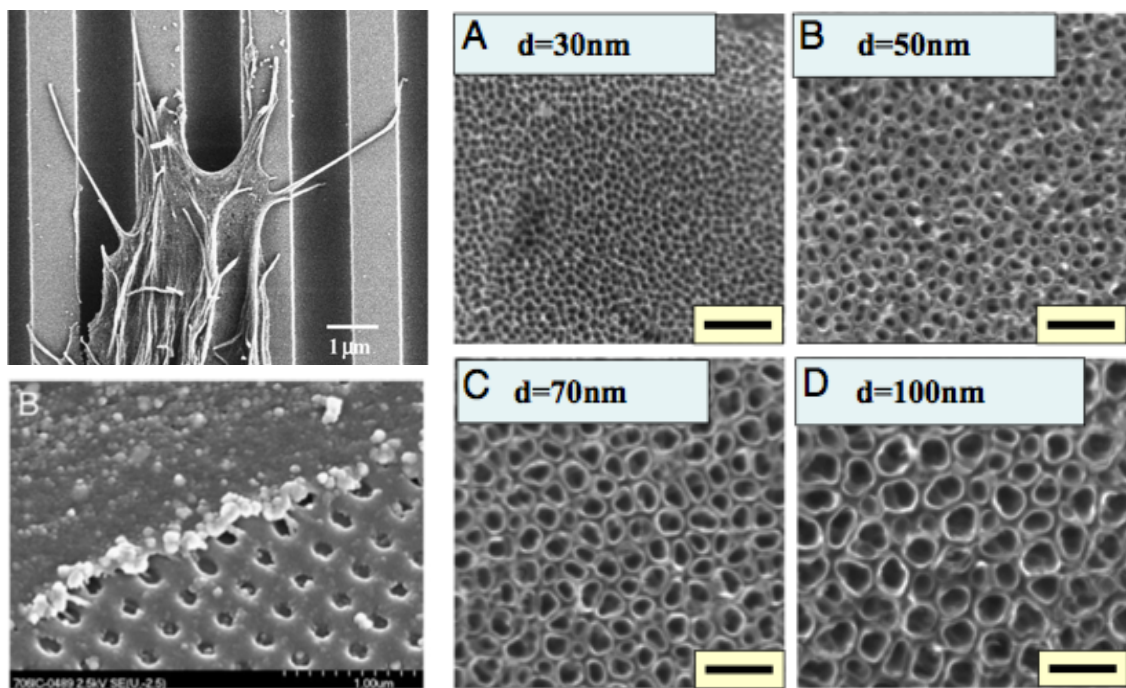


Figure 2.3. Surface topographies ranging from grooves, ridges, pits and tubes in the nano- and micrometre length scales can influence cell behaviour such as alignment, adhesion and differentiation. (Images modified from Teixeira; 2006, Biggs; 2008 and Oh; 2007).

Although there is no universal agreement on the length scale of substrates consisting of grooved and ridged topographies, response and behaviour may be a result of specific cell type. Size dependent behaviour results from the shape and size of focal adhesions formed on such substrates. Focal adhesions not only provide adhesion sites but also mediate adhesion-dependent signalling and varying topographical features can therefore control focal adhesion dynamics and thus cell shape and morphology. Moreover, how specific components in culture media interact with cell-matrix or cell-cell adhesions may also play an important role in topographical guidance²⁷.

As cell shape and morphology have shown to predict cell fate, the use of progenitor cells such as mesenchymal stem cells allow us to elucidate the differentiation inducing capabilities of nano-topographies. Studies have shown that the spacing and density of nanoscale pits are influential in cell adhesion and the order of these features can fundamentally alter cell adhesion and function. In a series of studies, Dalby and co-workers showed that slightly disordered 120 nm wide nanopit topographies with an inter-feature spacing of 300 nm induced ostespecific differentiation of hMSCs by regulating cell attachment²⁸. Ordered arrays on the other hand, disrupted focal adhesion formation resulting in reduced cell adhesion. Similarly, the effect of nano sized titania pillars²⁹ show that tubes with diameters of 30 nm or less promote adhesion but not

differentiation while tubes of diameters of 70 nm - 100 nm result in hMSC elongation into osteoblast like cells and thus promoting osteogenesis.

2.4 Stem cells and stiffness

Most *in vitro* biology studies have commonly been investigated on rigid polystyrene or glass which may be coated with ECM proteins. Such coated surface often do not mimic the properties of the ECM or the mechanical properties of the specific tissue. Variation in tissue elasticity are present during development and its spatial and temporal organisation may guide organogenesis for example, ESCs, endoderm or smooth muscle³⁰. In adult stem cells such as hMSCs, matrix rigidity alone has shown to direct lineage commitment³¹. When cultured on soft polyacrylamide gels (0.1-1 kPa) mimicking the environment of the brain, hMSCs expressed early neuronal differentiation markers. On stiffer gels (11 kPa), cells expressed myogenic markers and rigid gels (>34 kPa) mimicking collagenous bone, promoted osteogenesis (Figure 2.4).

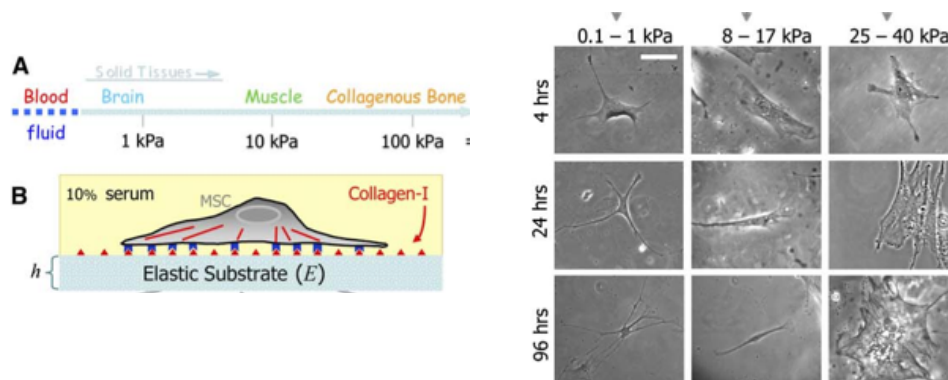


Figure 2.4 Human mesenchymal stem cell differentiation can be controlled by matrix rigidity alone. Gels of specific stiffness induced differentiation of cells mimicking tissue specific rigidities. (Image modified from Engler;2006).

Even within a specific range of substrate elasticity, progenitor differentiation and maturation may be guided by further fine tuning of the substrate elastic modulus. Adult neural stem cells cultured in serum free conditions, on soft substrates with stiffness ranging from 10 - 10,000 Pa differentiated towards neurons (on 100-500 Pa substrates) or glial cells (on 1,000-10,000 Pa substrates)³². Thus even within a tissue type, rigidity gradients can specify progenitor fate.

2.5 Stem cells and surface chemistry

Biochemical regulation of stem cell lineage commitment is not limited to soluble growth factors. ECM composition is important in determining integrin specificity and binding. An example of this is decellularised heart constructs exhibiting matrix composition that interacts with specific MSC surface integrin to direct differentiation towards functional cardiomyocytes in the absence of soluble growth factors. *In vitro*, functionalisation of matrices plays an important role in hydrophilicity and adhesion of cells to the substrate. Tethering of chemistries naturally found on the ECM to PEG based hydrogels have shown to play a direct role in determining MSC differentiation³³. For example, hydrogels bearing hydrophobic t-butyl methacrylate groups chosen because of their abundance in adipose cells, promoted adipogenesis. On the other hand hydrogels with ethylene glycol methacrylate phosphate directed osteogenesis probably because phosphates are key components of mineralised bone. Many other functional groups such as -COOH, -NH₂, or -OH present in ECM components such as GAGs, modified onto glass substrates have shown to guide hMSC differentiation depending on specific chemistries^{34,35}. Altering hydrophobic/hydrophilic interactions between the cell and the substrate can directly or indirectly alter cell adhesion, morphology and eventual function through integrin binding specificity³⁶.

2.6 Mechanotransduction and gene regulation

Cellular mechanotransduction can be defined as the process in which a physical stimulus is converted to a biochemical signal to activate downstream signaling pathways^{10,11}. For the cell to sense its physical micro-environment relies on its ability to pull against the matrix and subsequently requires its mechanotransducers to generate signals based on their ability to deform its underlying matrix. *In vivo*, there are many examples of mechanotransduction pathways that regulate transcriptional activity and gene expression important in organ development and tissue maintenance. Force sensing occurs through several ways; the conformational changes in proteins of transmembrane receptors, the cell cytoskeleton, and the nucleus, all of which mediate the conversion of force into a chemical signal and thereby influence gene expression.

Transmembrane receptors such as stretch-activated ion channels, G-protein coupled receptors, tyrosine kinase receptors and integrins are known to transfer physical forces

from the cell-surface interface to adhesion complexes such as focal adhesions or cell-cell adhesions^{37,38}. This can lead to the activation of signaling molecules such as the mitogen activated protein kinases (MAPKs) and Rho-family small GTPases which are involved in a myriad of cell functions including proliferation, migration and differentiation. Activation of MAPKs such as extracellular regulating kinase 1/2 (ERK1/2) which are also known as MAPK3 and MAPK1 have shown to be activated by focal adhesion kinase (FAK) stimulation, resulting in the up-regulation in the expression of genes such as collagen 1 and osteopontin, important for osteogenic differentiation³⁹.

Focal adhesion proteins that couple integrins to the actin filaments mediate force transmission through various adhesion anchoring proteins such as vinculin, paxillin, talin and thus regulate cytoskeletal tension. These focal adhesion proteins translate force to chemical signals through the Rho-ROCK signaling pathway which controls myosin II generated cytoskeletal tension. Rho A is a small GTPase protein and along with its effector ROCK (RhoA kinase) is known to regulate the actin cytoskeleton through the formation of stress fibres. This has important consequences in hMSC fate decisions, where it has recently been shown that hMSCs alter fate specific gene regulation based on matrix rigidity, a direct consequence of cytoskeletal tension. Furthermore, cell shape and contractility regulated by the Rho-ROCK pathway on fibronectin patterned islands was shown to determine osteogenesis or adipogenesis⁴⁰.

Cellular tensegrity (short for tensional integrity) termed by Ingber in the 1990's^{41,42} relates to the shape stability of a living cell that results from a balance of tensional and compressive forces acting on the cell and inside the cell. Tensional pulling forces generated by the cells contractile filaments are counterbalanced by the traction forces of the cell exerted on the ECM and the internal microtubules that resist compression within the cell. This balance of forces is said to generate a state of isometric tension or 'prestress' that regulates cell shape and is important for determining cell fate decisions. As cells sense their environment and its mechanical properties, it has been proposed that cytoskeletal stresses and strains on the ECM can propagate into the nucleus and therefore alter gene expression. In most cells, the nucleus is enveloped by the cytoskeleton near the centre of the cell. When deformed (by micropipette aspiration experiments), the nucleus has been shown to 'flow' resulting in chromatin

reorganisation⁴³, highlighting the possibility that nuclear plasticity associated with decreased levels of lamin a/c expression may ultimately influence gene expression.

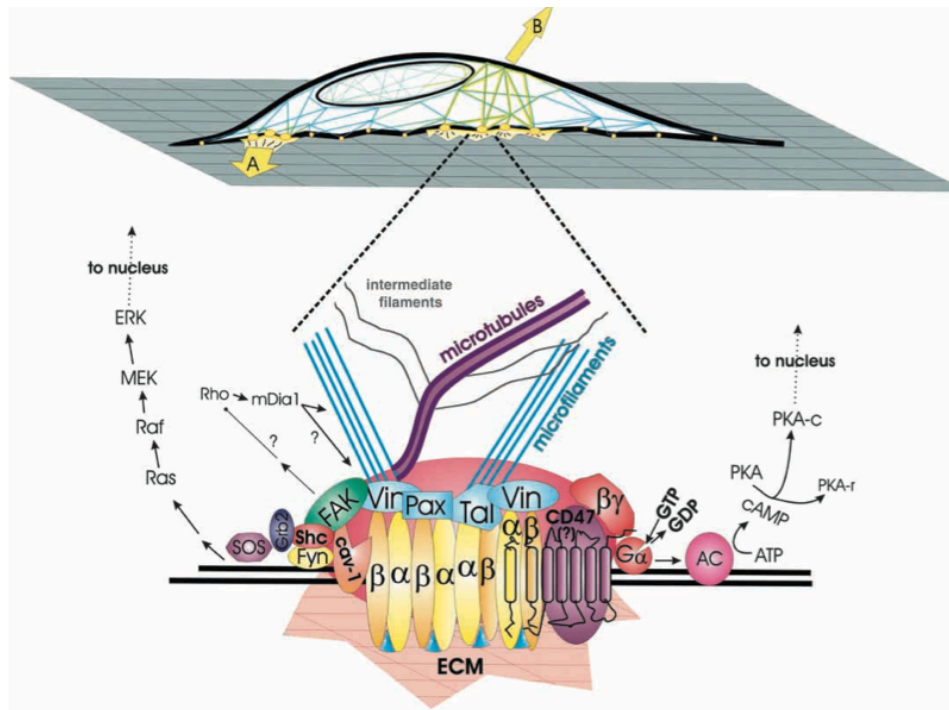


Figure 2.5 Schematic of adhesion mediated mechanotransduction. Forces applied are applied to the ECM (A) or directly to the cell surface (B). Forces applied within focal adhesions initiates integrin clustering and recruitment of focal adhesion proteins that connect directly to microfilaments and indirectly to microtubules. Force generation can trigger specific signalling pathways associated with FAK and ERK1/2 and thereby controlling gene regulation. (Image from Ingber; 2003)

Furthermore, in adherent cells, the area of cell surface and the nucleus are directly coupled to integrins through cytoskeletal tension. This physical deformation leads to the nucleus being prestressed to balance the contractile forces of the cytoskeleton and the condensation forces of chromatin. Thus nuclear mechanotransduction leading to reorganisation of the cytoskeleton and the nuclear membrane may be crucial to cell fate decisions.

2.7 Spatial regulation of mechanotransduction

Taken together, these observations indicate that the overall cell shape and morphology is a result of its response to the local environment; the rigidity and geometry (i.e topography and topology). This in turn can regulate cell function and fate at the genetic level. Furthermore, the spatial organisation of ECM ligands such as fibronectin, laminin and vitronectin, along with the nanotopographies of the ECM control the organisation and clustering of integrins, adhesion dynamics and eventual signal transduction are

responsible for cell function (Figure 2.5)³⁷. Thus when designing synthetic matrices, the regulation of cellular responses ultimately relies on the materials surface chemistry and its ability to induce integrin-mediated signaling pathways either directly through the adhesion of specific motifs or indirectly, through selective protein adsorption.

Much of our understanding of mechanosensing has been undertaken in 2D environments. Focal adhesion formation and dynamics have been shown to be different in 3D matrices compared to those in 2D substrates. For example, integrin mediated adhesion followed by cytoskeletal tension and focal adhesion formation in 2D occur within a short period of time⁴⁴. In a 3D environment, however, cells must compensate or proteolytically degrade the environment resulting in adhesions that take hours to days to form rather than minutes⁴⁵.

Advances in micro-engineered environments that mimic the spatial distribution of adhesions have enabled us to understand integrin mediated adhesion and its implication in cellular function, particularly MSC differentiation. Such spatial organisation in 3D remains a challenge, however the understanding of adhesions in 3D has been aided by the use of cell-derived ECM, which provides the necessary physicochemical cues⁴⁶. Such studies indicate that cells incorporate different integrins in 3D environments to that in 2D suggesting that the design of novel 3D synthetic matrices require the careful consideration and balance of physical and chemical properties.

2.8 References

1. Frantz, C., Stewart, K. M. & Weaver, V. M. The extracellular matrix at a glance. *J Cell Sci.* **123**, 4195–4200 (2010).
2. Stevens, M., Biomaterials for bone tissue engineering. *Materials Today* **11**, 18-25 (2008).
3. Hulmes, D. J. S., Jesior, J.-C., Miller, A., Berthet-Colominas, C. & Wolff, C. Electron microscopy shows periodic structure in collagen fibril cross sections. *PNAS* **78**, 3567–3571 (1981).
4. Rozario, T. & DeSimone, D. W. The extracellular matrix in development and morphogenesis: A dynamic view. *Dev Biol* **341**, 126–140 (2010).
5. Lohler, J., Timpl, R. & Jaenisch, R., Embryonic Lethal Mutation in Mouse Collagen I Gene Causes Rupture of Blood Vessels and Is Associated with Erythropoietic and Mesenchymal Cell Death. *Cell*, **38** 597-607 (1984).
6. Mao, Y. & Schwarzbauer, J. E. Fibronectin fibrillogenesis, a cell-mediated matrix assembly process. *Matrix Biol* **24**, 389–399 (2005).
7. Singh, P. & Schwarzbauer, J. E. Fibronectin and stem cell differentiation - lessons from chondrogenesis. *J Cell Sci.* **125**, 3703–3712 (2012).
8. Burdick, J. A. & Prestwich, G. D. Hyaluronic Acid Hydrogels for Biomedical Applications. *Adv. Mater.* **23**, 41–56 (2011).
9. Barczyk, M., Carracedo, S. & Gullberg, D. Integrins. *Cell Tissue Res* **339**, 269–280 (2009).
10. Geiger, B., Spatz, J. P. & Bershadsky, A. D. Environmental sensing through focal adhesions. *Nat Rev Mol Cell Biol* **10**, 21–33 (2009).
11. Vogel, V. & Sheetz, M. Local force and geometry sensing regulate cell functions. *Nat Rev Mol Cell Biol* **7**, 265–275 (2006).
12. Harburger, D. S. & Calderwood, D. A. Integrin signalling at a glance. *J Cell Sci.* **122**, 1472–1472 (2009).
13. Arnold, M. *et al.* Activation of Integrin Function by Nanopatterned Adhesive Interfaces. *ChemPhysChem* **5**, 383–388 (2004).
14. Huang, J. *et al.* Impact of Order and Disorder in RGD Nanopatterns on Cell Adhesion. *Nano Lett.* **9**, 1111–1116 (2009).
15. Martino, M. M. *et al.* Controlling integrin specificity and stem cell differentiation in 2D and 3D environments through regulation of fibronectin domain stability. *Biomaterials* **30**, 1089–1097 (2009).
16. Griffith, L. G. & Naughton, G. Tissue Engineering--Current Challenges and Expanding Opportunities. *Science* **295**, 1009–1014 (2002).
17. Pittenger, M. F. Multilineage Potential of Adult Human Mesenchymal Stem Cells. *Science* **284**, 143–147 (1999).
18. Croft, A. P. & Przyborski, S. A. Mesenchymal stem cells from the bone marrow stroma: basic biology and potential for cell therapy. *Current Anaesthesia & Critical Care* **15**, 410–417 (2004).
19. Delaine-Smith, R. M. & Reilly, G. C. The Effects of Mechanical Loading on Mesenchymal Stem Cell Differentiation and Matrix Production. *Vitamins & Hormones.* **87**, 417–480 (2011).
20. Kolf, C. M., Cho, E. & Tuan, R. S. Biology of adult mesenchymal stem cells: regulation of niche, self-renewal and differentiation. *Arthritis Res Ther* **9**, 204 (2007).
21. Takahashi, K. & Yamanaka, S. Induction of Pluripotent Stem Cells from Mouse Embryonic and Adult Fibroblast Cultures by Defined Factors. *Cell* **126**, 663–676 (2006).

22. Miura, K. *et al.* Variation in the safety of induced pluripotent stem cell lines. *Nat Biotechnol* **27**, 743–745 (2009).
23. Hu, B. Y. *et al.* Neural differentiation of human induced pluripotent stem cells follows developmental principles but with variable potency. *PNAS* **107**, 4335–4340 (2010).
24. Robinton, D. A. & Daley, G. Q. The promise of induced pluripotent stem cells in research and therapy. *Nature* **481**, 295–305 (2012).
25. Curtis, A. S. G. & Wilkinson, C. D. W. Topographical control of cells. *Biomaterials* **18**, 1573–1583 (1997).
26. Teixeira, A. I., Abrams, J., Bertics, P. J., Murphy, C. J. & Nealy, P. F., Epithelial contact guidance on well-defined micro- and nanostructured substrates. *J Cell Sci* **116**, 1881–1892 (2003).
27. Teixeira, A. I. *et al.* The effect of environmental factors on the response of human corneal epithelial cells to nanoscale substrate topography. *Biomaterials* **27**, 3945–3954 (2006).
28. Dalby, M. J. *et al.* The control of human mesenchymal cell differentiation using nanoscale symmetry and disorder. *Nat Mater* **6**, 997–1003 (2007).
29. Oh, S. *et al.* Stem cell fate dictated solely by altered nanotube dimension. *PNAS* **106**, 2130–2135 (2007).
30. Krieg, M. *et al.* Tensile forces govern germ-layer organization in zebrafish. *Nat Cell Biol* **10**, 429–436 (2008).
31. Engler, A. J., Sen, S., Sweeney, H. L. & Discher, D. E. Matrix Elasticity Directs Stem Cell Lineage Specification. *Cell* **126**, 677–689 (2006).
32. Saha, K. *et al.* Substrate Modulus Directs Neural Stem Cell Behavior. *Biophys J* **95**, 4426–4438 (2008).
33. Benoit, D. S. W., Schwartz, M. P., Durney, A. R. & Anseth, K. S. Small functional groups for controlled differentiation of hydrogel-encapsulated human mesenchymal stem cells. *Nat Mater* **7**, 816–823 (2008).
34. Curran, J. M., Chen, R. & Hunt, J. A. The guidance of human mesenchymal stem cell differentiation in vitro by controlled modifications to the cell substrate. *Biomaterials* **27**, 4783–4793 (2006).
35. Curran, J. M., Chen, R. & Hunt, J. A. Controlling the phenotype and function of mesenchymal stem cells in vitro by adhesion to silane-modified clean glass surfaces. *Biomaterials* **26**, 7057–7067 (2005).
36. Llopis-Hernández, V., Rico, P., Ballester-Beltrán, J., Moratal, D. & Salmerón-Sánchez, M. Role of Surface Chemistry in Protein Remodeling at the Cell-Material Interface. *PLoS ONE* **6**, e19610 (2011).
37. DuFort, C. C., Paszek, M. J. & Weaver, V. M. Balancing forces: architectural control of mechanotransduction. *Nat Rev Mol Cell Biol* **12**, 308–319 (2011).
38. Roca-Cusachs, P., Iskratsch, T. & Sheetz, M. P. Finding the weakest link - exploring integrin-mediated mechanical molecular pathways. *J Cell Sci.* **125**, 3025–3038 (2012).
39. Salasznyk, R. M., Klees, R. F., Boskey, A. & Plopper, G. E. Activation of FAK is necessary for the osteogenic differentiation of human mesenchymal stem cells on laminin-5. *J. Cell. Biochem.* **100**, 499–514 (2007).
40. McBeath, R., Pirone, D. M., Nelson, C. M., Bhadriraju, K. & Chen, C. S. Cell Shape, Cytoskeletal Tension, and RhoA Regulate Stem Cell Lineage Commitment. *Dev Cell* **6**, 483–495 (2012).
41. Ingber, D. E. Tensegrity I. Cell structure and hierarchical systems biology. *J Cell Sci.* **116**, 1157–1173 (2003).
42. Ingber, D. E. Tensegrity II. How structural networks influence cellular information processing networks. *J Cell Sci.* **116**, 1397–1408 (2003).

43. Pajerowski, J. D., Dahl, K. N., Zhong, F. L., Sammak, P. J. & Discher, D. E. Physical plasticity of the nucleus in stem cell differentiation. *PNAS* **104**, 15619–15624 (2007).
44. Baker, B. M. & Chen, C. S. Deconstructing the third dimension- how 3D culture microenvironments alter cellular cues. *J Cell Sci.* **125**, 3015–3024 (2012).
45. Khetan, S. & Burdick, J. A. Patterning network structure to spatially control cellular remodeling and stem cell fate within 3-dimensional hydrogels. *Biomaterials* **31**, 8228–8234 (2010).
46. Cukierman, E., Pankov, R., Stevens, D. R. & Yamada, K. M. Taking Cell-Matrix Adhesions to the Third Dimension. *Science* **294**, 1708–1712 (2001).

Chapter 3: Polymeric Scaffolds for Tissue Engineering

3.1 Introduction

Recapitulating tissue complexity *in vitro* is a current challenge faced by tissue engineers. For example, bone is a highly ordered tissue that experiences cues from the nano- to the micrometer length scales. Molecular interplay within tissues is governed heavily by weak molecular interactions, including hydrogen bonding, hydrophobic interactions, Van der Waals forces and electrostatic interactions. These weak forces allow cell-cell and cell-matrix interactions to be a highly dynamic. An example of this at the molecular level involves protein folding and unfolding resulting from membrane tension. This may ultimately lead to signal transduction from outside the cell to inside the cell and thereby regulating expression of specific nuclear transcription factors by triggering the appropriate signalling pathways. Indeed, one of the current challenges in designing tissue engineered (TE) constructs is controlling surface properties at multiple length scales to promote cell responses at the cell-matrix interface. These responses must consequently illicit desired cell functions, *in vitro* and/or promote tissue repair and regeneration *in vivo*.

The design of 3D scaffolds or matrices for applications in tissue engineering and regenerative medicine must fulfil certain criteria as suitable constructs. These include an interconnected porous or fibrous structural network capable of maintaining cellular proliferation and survival through sufficient cell-matrix and cell-cell contacts¹. Additionally the scaffold must facilitate the diffusion of nutrients and metabolic wastes by means of porosity and permeability. For *in vivo* applications, scaffolds must be biocompatible i.e. non-toxic and non immunogenic and biodegradable preferably at the rate of tissue repair².

As porosity and permeability are key features of a 3D porous matrix, their effects on cell attachment and proliferation have been widely explored in an attempt to achieve the ideal architectural properties. Oh *et al.* showed that fibroblast proliferation was found to be the greatest on PCL scaffolds with pore sizes ranging from 180 - 260 μm ,

while bone mineralisation was best supported on scaffolds with pore sizes between 290 - 310 μm^3 . In contrast, Murphy *et al.* determined that collagen-GAG scaffolds with an average pore size of 325 μm was required for osteogenic differentiation⁴, while human dermal fibroblasts were indifferent to pore sizes of 38 - 150 μm in terms of ECM deposition on porous PLLA scaffolds⁵. The apparent disparities in determining ideal porosity points to the fact that there is no ‘one size fits all’ approach to fabricating 3D matrices. Rather, the choice of porosity will depend on

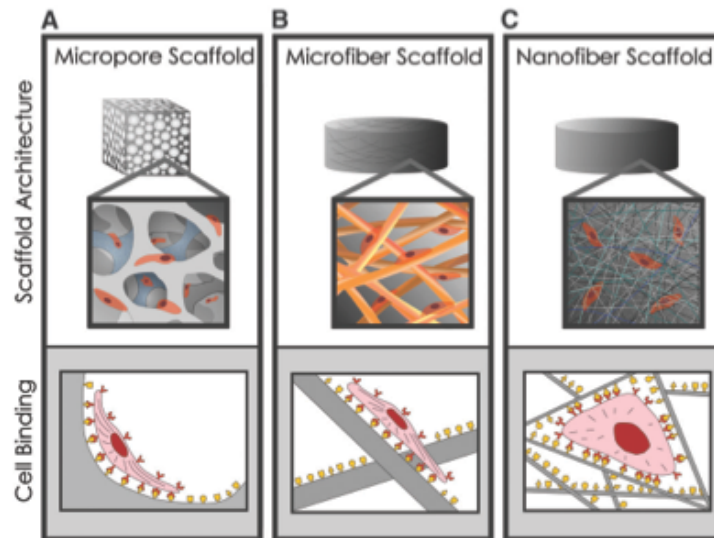


Figure 3.1 Cells attach to microporous/microfibrous scaffolds differently to scaffolds exhibiting nano-scale features. Local curvature experienced by cells affect integrin clustering and eventual adhesion. (Image from Stevens;2005).

the end application. Cells cultured macro-porous and micro-fibrous scaffolds spread in a similar manner to flat surfaces as the local curvature that cells experience resemble most closely a 2D environment. On the other hand, scaffolds of nano-fibres provide large surface areas for cell binding, attachment and protein adsorption (Figure 3.1). Differences in local curvature and therefore forces, felt by cells cultured on such scaffolds may trigger different signalling pathways than those on macro-porous scaffolds^{6,7}. However, these matrices intrinsically consist of much lower porosity, limiting cell proliferation and nutrient exchange within the material, a prerequisite for long periods of culture.

Biomaterials design over the past 10 years have predominantly focused on ‘cell instructive’ 3D scaffolds or matrices. In an article by Hench *et al.*, the development of the third generation of biomaterials required that they control the desired cellular behaviour at the molecular level⁸. Such materials are designed to provide the

necessary cues (physical, chemical and mechanical) to illicit the desired response. Scaffolds designed for the controlled differentiation of hMSCs must ideally incorporate a range of physicochemical properties such as stiffness, surface chemistry and topography which includes ligand spacing. Here, current strategies in designing novel scaffolds tailored for stem cell differentiation are briefly reviewed followed by a description of the strategies that will be employed in this PhD thesis.

3.1.1 Natural versus synthetic polymers

There are currently a variety of natural and synthetic polymers used *in vitro* as 3D cell culture supports. Natural polymers often consist of ECM constituents some of which are commercially available such as Matrigel™ (composed of ECM components extracted from mouse tumours). One major advantage using natural polymers is because of their inherent physical and chemical properties such as biological recognition. This includes spatial control and presentation of ligand binding sites and their susceptibility to cell-triggered degradability and remodeling of the matrix⁹.

As collagen is one of the most abundant ECM proteins, it is extensively used as a natural scaffold. Collagen is readily obtained from skin and tendon and can be easily tuned into fibrillar networks by controlling the pH or the temperature of the solution. Although collagen has restricted applications due to risks of immunogenicity, recombinant collagen I and II are currently clinically available¹⁰.

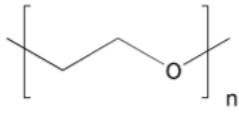
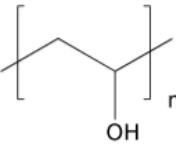
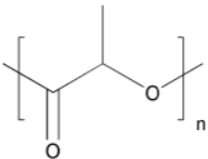
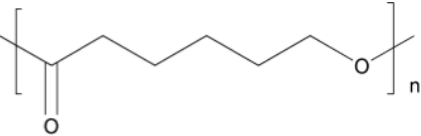
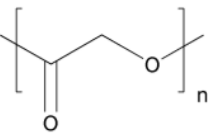
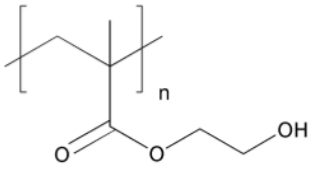
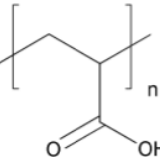
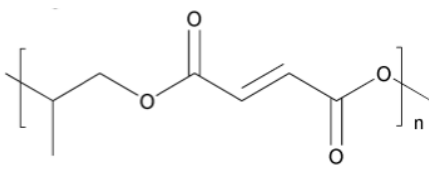
Although fibrin is not an ECM protein secreted by cells, it is still a highly specialised fibrillar protein network formed during the spontaneous repair of tissue and therefore is widely used as a 3D matrix. *In vitro*, a fibrin matrix is formed by the polymerisation of fibrinogen, in the presence of thrombin protease¹⁰. Fibrinogen is specifically cleaved by thrombin into fibrinopeptides which is catalysed by the blood transglutaminase factor XII to form the fibrin network *in vivo*¹¹. Varying the porosity, stiffness and mechanical properties of the fibrin hydrogel by controlling the gelation time have been investigated and used widely for cell transplantation.

Hyaluronan or hyaluronic acid (HA), is the only GAG that is not associated with a core protein but rather is entangled within the ECM. Its ability to swell in aqueous

media, makes it a useful hydrogel substrates with compressive properties for 3D tissue culture¹². HA can be isolated from various animal tissues and can also be produced by Streptococcus bacterium. Hydrogels formed by HA can be further synthetically modified to bear pendant thiol-, amine- or hydrazide- groups which modifies their cross-linking, swelling and therefore mechanical properties¹³. HA may also be known to interact directly with cells through CD44 and other cell surface receptors. As these hydrogels are not fibrillar, they are often used in applications for encapsulation of small molecules or cells.

Despite the advantages that ECM polymers may have, certain limitations still prevail. This includes batch-to-batch variability which makes it difficult to obtain reproducible results while the physical and chemical nature of ECM based scaffolds make it difficult to decouple the effects of individual ECM properties to cell function and behaviour. Furthermore, immunogenicity *in vivo* still remains a concern for clinical translation regardless of the progress made in recombinant protein technologies¹⁰. Synthetic polymers on the other hand offer greater control over materials properties (in particular mechanical properties) mimicking specific tissue. Synthetic matrices can also be used to tailor degradation rates and scaffolds can be made using a wide variety of chemistries. Polymers can often be synthesised under mild conditions allowing for the incorporation of bioactive molecules without much loss of function⁹. While synthetic polymers require careful design strategies to present the same level of biological complexity as natural ones, understanding the hierarchical structure of ECM polymers provides the perfect platform for biomimicry. Several synthetic polymers are currently approved by the Food and Drug Administration (FDA) for *in vivo* applications; examples of which are shown in Table 3.1 and many of these are used the the synthesis of new biomaterials.

Table 3.1 FDA approved and commonly used synthetic polymers used in tissue engineering and regenerative medicine.

Polymer	Chemical structure
poly(ethylene glycol) (PEG)	
poly(vinyl alcohol) (PVA)	
poly(lactic acid) (PLA)	
poly(caprolactone) (PCL)	
poly(glycolic acid) (PGA)	
poly(hydroxyethyl methacrylate) (PHEMA)	
poly(acrylic acid) (PAA)	
poly(propylene fumarate) (PPF)	

3.1.2 Current technologies for materials fabrication

The design and fabrication of novel biomaterials or scaffolds for biomedical applications fall broadly under two categories; bottom-up or top-down strategies. A ‘top down’ approach, uses bulk materials with which hierarchy (micro or nano scales) is created externally. Topographical features can be created through electron beam-, photo- and dip-pen lithographic and micro-contact printing techniques. Such techniques offer the advantage that features can be organised spatially and temporally in a precise and highly reproducible manner. Many of these techniques have been widely used to produce 2D substrates to in surface chemistry, protein biology, biosensing and even cell biomechanics.

Microcontact printing (μ CP), first described by George Whitesides¹⁴ is a simple method for generating patterned substrates. In this method, an elastomeric polymer, poly(dimethyl siloxane) (PDMS), is most commonly used as a stamp. The stamp, with bas relief features is then used to transfer an ‘inked’ material onto a substrate. In this way, many chemicals can be stamped onto the substrate including proteins, and DNA and features as small as 50 nm have been easily reproduced. μ CP has been extensively used by Chen and co-workers¹⁵ who used μ CP to stamp ECM proteins such as fibronectin onto substrates with specific geometries. Such substrates have been used to study the effects of cell morphologies, their associated cytoskeletal tension, and how this influences hMSC differentiation (Figure 3.2).

Photolithographic techniques such as electron beam lithography involve the use of high energy electrons to expose an electron sensitive resist to manufacture topographical features. Resolutions of around 3-5 nm may be achieved using this technique however, studying cell behaviour requires a high density array of single features which limits the resolution to 30-40 nm. Indeed substrates with patterns such as square and hexagonal arrays with precise spacing between features have been widely used by Dalby *et al.* and Spatz *et al.* to study adhesion dynamics and hMSC differentiation in response to surface topography^{16,17}.

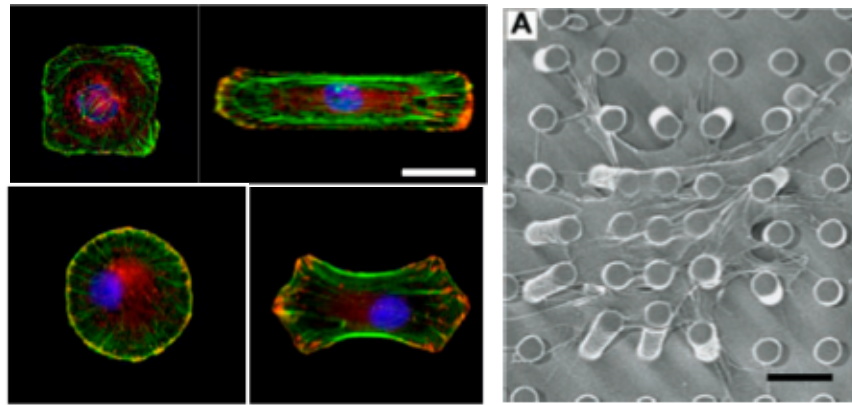


Figure 3.2. Cell shape and morphology can be controlled by ECM protein stamping fabricated by microcontact printing. Elastomeric PDMS micron pillars on the other hand fabricated by photolithography are used to understand cell generated forces resulting from micropillar displacement (i.e. rigidity sensing). Both techniques enable control over surface chemistry and topography to direct stem cell differentiation. (Images modified from Kilian; 2010 and Tan; 2002)

A ‘bottom-up’ approach for scaffold synthesis on the other hand, exploits self-assembly using non-covalent intermolecular forces to generate hierarchically structured scaffolds and much of the inspiration is derived from understanding protein self-assembly. Synthetically, peptide self-assembly requires non-aqueous and non-physiological conditions. However, there have been many advances in this area of research including work done by Zhang *et al.* who developed nano-fibrillar peptide hydrogels with high water content (99%)¹⁸. The peptides used in their study were ionic self-complementary peptides that consist of alternating hydrophobic and hydrophilic amino acid sequences that form β -sheets. The ionic nature of the β -sheets means that they spontaneously form 3D matrices in an aqueous solution consisting of monovalent cations. One specific ionic peptide is EAK16 (AEAEAKAKAEAEAKAK), found in a yeast protein, which was subsequently redesigned to produce RAD16 (RARADADARARADADA). This specific peptide has since been widely studied and used in many tissue engineering applications such as wound-healing and myocardial repair^{19,20}. One disadvantage of self-assembling peptides is that they do not possess any cell-specific interactions. To overcome this, many researchers have engineered RAD peptide alternatives bearing biofunctional ligands to significantly enhance cell-material interactions¹⁹.

Peptide amphiphiles (PA), such as those developed by Stupp and co-workers (Figure 3.3) have received considerable attention due to their fibrillar gel forming capabilities²¹. PA's consist of an N-terminal alkyl tail, a central segment that forms a

β -sheet and a C-terminal functional segment. The modular nature of the C-terminal and the ease of synthesis provide a flexible platform for many tissue engineering applications. For example, attachment of the peptide IKVAV, present in the ECM protein laminin which is the main component of neural ECM has been investigated in neural tissue engineering applications^{22,23}.

Another family of peptides includes the elastin-like polypeptides (ELPs). These consist of a repeat sequence of Val-Pro-Gly-X-Gly, where X is any amino acid apart from proline. They are found in human tropoelastin and exhibit thermo-responsive properties in aqueous solutions. Given their mechanical properties, their uses have been primarily in cartilage tissue engineering²⁴. Moreover, like the RAD16 and polypeptide and PA's, ELPs have also required ligand conjugations to enhance cell activity.

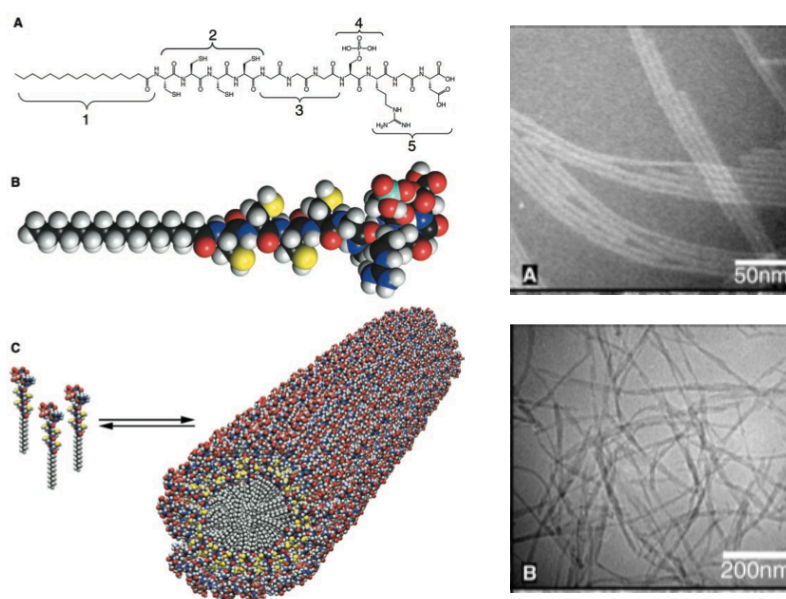


Figure 3.3. Self assembled nanostructures from peptide amphiphilics. (Image modified from Hartgerink; 2001).

Although research in self-assembled polypeptides have received much popularity, there are limitations that must be taken into consideration which relate to structural and temporal heterogeneities. Conjugation of biofunctional components have been shown to affect the topology of the central β -sheet segment which in turn affect bulk fibril formation and bulk peptide properties such as gelation. Moreover, within a biological context, the macromolecular organisation of self-assembling peptides can undergo transformations in physiological conditions e.g. fibrillar to globular

morphologies²⁵. This introduces challenges in detecting or measuring the effects of spatial distributions of cell-receptor binding, resulting from the biofunctional component as well as reproducing spatial and temporal ligand presentation difficult using peptide gels.

We have so far discussed the the importance of key scaffold properties which provides not only structural support for cells seeded within them but must also have intrinsic physical and chemical properties. These include topography, stiffness and chemistry organised spatially and temporally in the nano-scale very much mimicking the ECM. Many of these studies have been investigated in 2D systems which is physiologically different from 3D *in vivo*. Although 2D studies have enabled us to understand many aspects of cell-matrix interactions and how specific substrate properties affect cell behaviour, controlling cell behaviour in 3D is particularly important if such materials are to be used as artificial implants. Current strategies in 3D porous matrices discussed here present uniform surface chemistry via surface immobilization or direct crosslinking of a binding motif to the scaffold, yielding either homogeneous or protein polymer hydrogels²⁶. However, these materials often have very little control over their surface topology; their topology and the surface motifs they present can also be substantially different from native ECM⁷. In order to better mimic the heterogeneities of the native ECM, this thesis investigates, producing highly porous 3D scaffolds using two well-established techniques; high internal phase emulsion templating and electrospinning. While emulsion templating is a bottom up self-assembly approach, functionalisation of electrospun fibres adopts a top-down approach.

3.2 Emulsion templating as a method for fabricating 3D porous matrices

High internal phase emulsions (HIPEs) are defined by an internal or droplet phase volume fraction (Φ) of 0.74²⁷. This volume fraction represents the theoretical volume fraction where the droplet phase is closely packed spheres. Above this volume, droplets adopt a polyhedral geometry. In real emulsion systems however, droplets become polydisperse. HIPEs maybe prepared as oil-in-water or water-in-oil emulsions stabilised either by surfactants or colloidal particles. The latter is referred to as Pickering HIPEs²⁸. Either one or both phases of the emulsion may consist of polymerisable monomers leading to polyHIPEs²⁹. Composites result when both phases are polymerised³⁰. When the continuous phase of the emulsion is polymerised (often by radical initiation), this results in a porous polymer. Finally, when the internal phase of the emulsion is polymerised, this yields in polymerised particles³¹.

For the purpose of tissue engineered (TE) constructs, this discussion is limited to water-in-oil HIPEs leading to porous polymers. To date, the most widely studied HIPEs of this kind are water-in-oil emulsions, where the oil consists of styrene crosslinked with divinylbenzene. These emulsions traditionally use Span 80 as the surfactant and $K_2S_2O_8$ as the water-soluble radical initiator^{29,30,32}. Such polyHIPEs display a hierarchy of porosity where large pores, termed as voids, result from the evaporation of the water droplets. Each 3D pore consists of smaller pores referred to as interconnects or windows, responsible for the interconnectivity between adjacent droplets leading to ‘open porous’ foams (Figure 3.4).

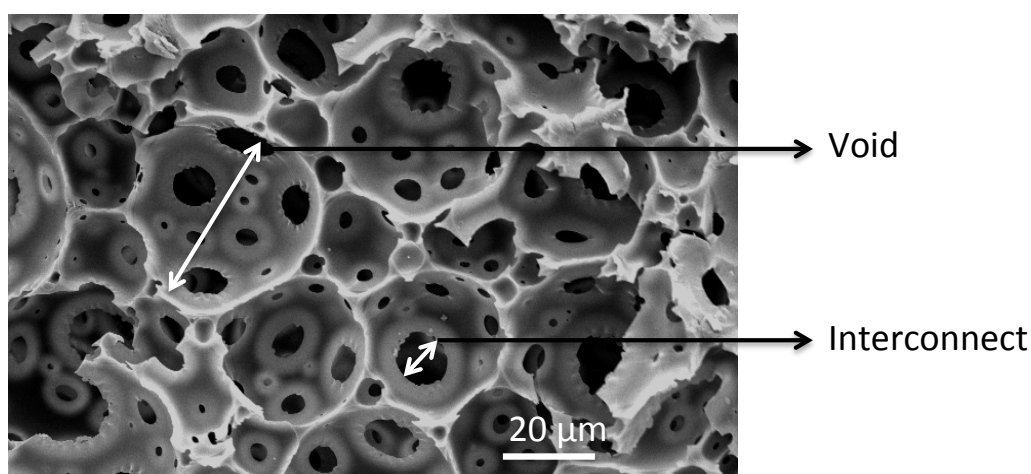


Figure 3.4 Scanning electron micrograph of a typical polyHIPE foam showing a hierarchical porous structure consisting of voids and interconnects.

3.2.1 Controlling HIPE morphology and stability

As the emulsion serves as a template for the final porous polymer structure, controlling the architecture of the parent emulsion is crucial in obtaining the desired polyHIPE morphology. The stability of high internal phase emulsions in general is governed by droplet coalescence (a kinetic effect) and Ostwald ripening (a thermodynamic effect). Thus one way of controlling the final structure of the porous polymer is through optimising the composition and concentration of each of the HIPE components to control (kinetically or thermodynamically) emulsion stability. Here traditional methods of tuning polyHIPE architectures are briefly discussed.

Role of the surfactant

The most important component of a HIPE is the surfactant. For non-ionic surfactants the hydrophilic-lipophilic balance (HLB) is an important indicator of emulsion efficiency. Surfactants with a low HLB (between 2-6) are more oil soluble hence suitable for water-oil-emulsions. While the most widely used surfactant for water-in-oil emulsions are fatty acid esters such as sorbitan monooleate (or Span 80), ionic surfactants such as cetyltrimethylammonium bromide³³, dodecylbenzosulphonic acid³⁴ or a combination of surfactants³⁴ have also been used. As the majority of literature incorporates Span 80 as the surfactant, the discussion on surfactant effects is limited to the non-ionic surfactant, Span 80. It has been shown that the incorporation of 3-5 wt% (of the oil phase) of surfactant is needed for the formation of a stable emulsion while interconnectivity arises at 7 wt%, although exact values may be dependent on the processing conditions. In general, as the concentration of the surfactant is increased, void diameter decreases, a result of lowering the interfacial tension. Furthermore, the interconnect diameter increases with increasing surfactant concentration having an overall effect of increased porosity (as the ratio between voids : interconnects decreases). It has been postulated that an increase in Span 80 concentration is responsible for the thinning of the oil film separating the water droplets which is responsible for increasing interconnectivity in such foams. At a critical Span 80 concentration, (80 wt% as reported by Williams and Wroblecky)³⁵, the resulting polystyrene foam is no longer considered interconnected but rather just a porous material.

Effects of monomer and crosslinker concentration

One effective way of controlling HIPE morphology is through crosslinker concentration. Divinylbenzene (DVB) is the most commonly used crosslinker for styrene based foams and as its concentration is increased, two notable effects have been reported. Firstly, a decrease in void diameter is observed, as DVB is more hydrophobic than styrene. This results in more stable foams and therefore smaller void diameters. Secondly, a decrease in interconnecting pores are seen as the concentration of the crosslinker is increased. This is because the presence of the crosslinker reduces the motility of the monomers and hence trapping the configuration of the foam at early stages of the polymerisation³⁶.

Water and oil soluble porogens

The use of solvents such as chlorobenzene (CB), chloroethylbenzene (CEB), toluene (T), tetrahydrofuran (THF) and methanol (MeOH) have been incorporated both in the oil and aqueous phases of a HIPE and their effects on emulsion stability and subsequent polyHIPE morphology have been studied^{37,38}. In general, porogens cause an increase in void diameters. The solvent packing at the oil-water interface chlorobenzene, chloroethylbenzene and toluene have been determined by Langmuir-Blodgett films³⁸ when employed as oil soluble porogens. It was found that the larger the solubility (CEB>CB>T), the smaller the void diameter. Further investigations using MeOH and THF as water soluble solvents explained the dramatic increase in void and interconnect diameters in terms of Ostwald ripening and droplet coalescence³⁹, the two driving forces of emulsion stability. The partition coefficients ($\log P_{ow}$) of MeOH and THF are -0.77 and 0.45 respectively, correlating with larger void diameters observed with THF than MeOH. This is because THF is more oil soluble, allowing it to diffuse through the interface into the oil phase. This results in emulsion instability and increases the propensity to induce Ostwald ripening and larger droplets to be formed³⁹. While MeOH remained largely in the aqueous phase, void diameters were still found to be larger than without the use of a porogen, although smaller than with the use of THF.

Electrolytes

The addition of salts (electrolytes) in the aqueous phase however has the opposite effect of suppressing Ostwald ripening and enhancing emulsion stability. Williams *et al.* showed that when AIBN was used as the initiator, and the concentration of K_2SO_4 was increased from 10^{-6} - 0.1g/ml, a 10 fold increase in void diameter was seen³⁰. Other electrolytes such as $CaCl_2$ and $NaCl$ have also been utilised with similar results. Thus, the use of porogens and electrolytes offers a controlled way of preparing deliberately destabilised emulsions and polyHIPEs with optimal porosities and interconnectivity to produce desired final foam structures.

3.2.2 Applications in tissue engineering and stem cell differentiation

Since the patenting of polyHIPEs in the 1980's by Unilever, they have been used for various applications including their use as 3D scaffolds for cell culture. A variety of cell types have been grown on polyHIPEs and show preferential growth in 3D compared to 2D environments. For example, Akay *et al.* cultured primary rat osteoblasts grown on styrene/DVB polyHIPEs with porosities ranging from 40 μm to 100 μm and showed that cells were able to maintain not only their osteoblast phenotype but mature over the course of cell culture expressing greater levels of osteopontin and osteocalcin in 3D compared to cells grown in 2D tissue culture plastic^{40,41}. Similarly MG63 human osteosarcoma cells cultured for a maximum of 35 days survived, proliferated and expressed greater levels of alkaline phosphatase (ALP) activity and osteocalcin expression, cultured on polyHIPEs compared to cells cultured in 2D⁴².

3.3 Electrospinning as a method for the preparation of 3D matrices

Electrospinning is a versatile and facile method technique for generating fibrous mats from a variety of synthetic and natural polymers. The structure and morphology of such fibres can be controlled from the nano- to the micro- scale and randomly oriented or highly aligned fibrous matrices can be fabricated. Although electrospinning was first demonstrated in the early 1900's⁴³, it has received much attention since the early 1990's for potential applications particularly in the biomedical field including drug delivery, carriers for controlled release as well as three dimensional scaffolds for tissue engineering⁴⁴.

Typically, the electrospinning set-up (Figure 3.5) requires three main components; a high voltage power source, a spinneret (generally a flat ended needle) and an electrically conductive collector. The process of electrospinning involves the polymer solubilised in the appropriate solvent. When an electric field is applied, this leads to the formation of a charged pendent droplet at the apex of the needle referred to as the Taylor cone. A polymer jet is then formed when the polymer solution overcomes the surface tension at the Taylor cone. As the jet travels, whipping or splaying occurs as a result of instabilities originating from the surface charge of the jet and the electric field. As the solvent evaporates from the polymer solution, the polymer solidifies to form fibres, which are deposited on the electrically grounded collector. Thus, processing conditions play a critical role in determining the morphologies of electrospun fibres. These include the molecular weight of the polymer, solution viscosity and concentration, solution conductivity, temperature and humidity; some of these will be discussed below.

3.3.1 Controlling Electrospun fibre morphologies

Solution viscosity/concentration

Solution concentration and viscosity are two of the most important parameters in determining the morphology of electrospun fibres. The effect on several synthetic polymers have been studied including poly(L-lactic acid) (PLLA), poly(D,L-lactic acid)(PDLLA), polystyrene (PS), poly(lactic-co-glycolic acid)(PLGA), poly(ethylene oxide) (PEO) and poly(methyl methacrylate)(PMMA). Polymer solutions of low

concentrations form beaded fibres or electrospray to form an aerosol. This often occurs if the solution

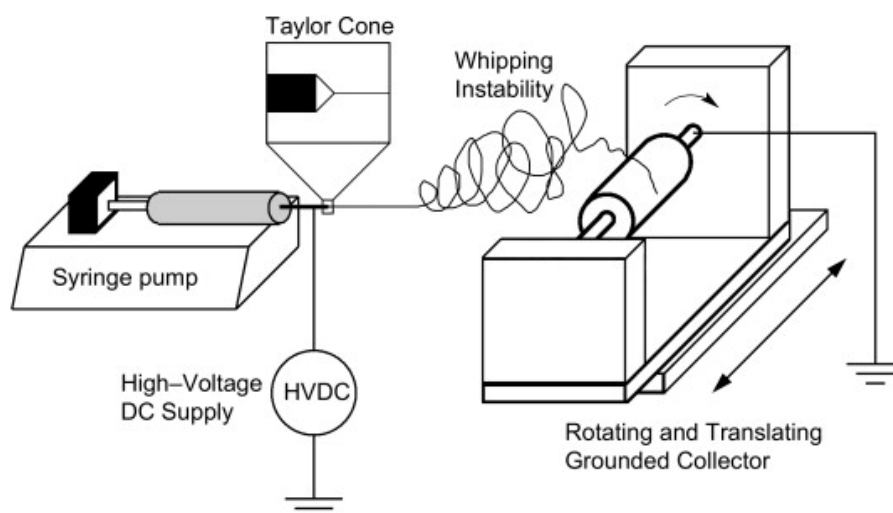


Figure 3.5 Schematic of a typical electrospinning set-up. (Image from von Reecum; 2008)

concentration is less than the critical chain overlap concentration (c^*) where insufficient polymer chain overlap leads to bead formation i.e. dilute solutions. As shown for PMMA linear and branched polymers⁴⁵, at solution concentration in the semi dilute region between c^* and c_e ; where c_e is the chain entanglement concentration, beaded fibres were occasionally observed. At high solution concentrations however (where $c^* > 2c_e$), uniform bead free fibres were formed. In general, electrospun fibre diameters have been shown to increase as solution concentration (and subsequently viscosity) is increased which also results in decreased fibre surface areas⁴⁶.

Surface tension

The surface tension of the solution can affect the diameter of fibres produced. Additives in the polymer solution can increase or decrease the surface tension and affect the stability of the polymer jet. For example, the addition of EtOH to solutions of poly(ethylene oxide) (PEO) and poly(vinyl alcohol) (PVA) resulted in beaded fibre morphologies for PVA fibres compared to non-beaded morphologies for PEO fibres⁴⁷. This was because EtOH is a selective solvent for PEO thereby decreasing the surface tension of the polymer solution and decreasing jet instability, while the opposite was found true of PVA as EtOH is a non-solvent.

Ambient parameters- temperature and humidity

Ambient parameters such as temperature and humidity can have profound effects on the morphology of electrospun fibres as they directly affect the solution viscosity. When polyamide fibres were electrospun at a range of temperatures from 25°- 60° C, the authors found that the fibre diameters were larger at higher temperatures⁴⁸. This was attributed to solution viscosity which decreases as temperature of the solution is increased. Studies involving humidity effects on the other hand show fibres forming topographical features (i.e. pores) on the surface of the fibres as humidity of the atmosphere was found to increase.

A variety of parameters affect electrospinning, including those not discussed here such as tip-needle distance and set up, voltage, solution flow rates, which have been reviewed extensively elsewhere^{43,49}. The effects of each parameter ultimately may be difficult to decouple as they are often inter-related. What this points to is that careful tuning of parameters is required for each polymer system to obtain consistent results despite the vast literature available. However, the ease of the manufacture has allowed electrospinning to become a popular technique for producing fibres for many applications including tissue engineering.

3.3.2 Applications in Tissue Engineering and Stem Cell Differentiation

Due to their ease of manufacturing and processing, electrospun scaffolds have been widely used as 3D cell culture matrices. In particular, the physical properties of such scaffolds which can be easily controlled to produce aligned and randomly oriented, nano- and micro- sized fibrous matrices as well as introducing surface topography and functionality have made them ideal for understanding cell proliferation, migration and differentiation. The vast majority of the literature concerning electrospun fibres deals with biodegradable and biocompatible polymers (mostly polyesters) such as poly(L-lactic acid) (PLLA) poly(glycolic acid) and their copolymers, poly(hydroxy butyrate) (PHB), poly(hydroxy valerate) (PHV) and their copolymers and poly(caprolactone) (PCL) which are particularly useful for clinical

applications⁵⁰. Furthermore, the fibrous nature of electrospun constructs possess similarities to the fibrous nature of the ECM, making them a convenient tool for exploring matrix induced hMSC differentiation.

Processing conditions during electrospinning allow the user to control the random and aligned morphologies of the fibrous mats. Aligned fibre orientation allows for the alignment of cells through contact guidance and is exploited extensively in neural tissue engineering, particularly as nerve guidance conduits. For example, the culture of dorsal root ganglia (DRG) or Schwann cells on aligned fibres resulted in neurite outgrowth⁵¹. The effectiveness of neural stem cell culture on such fibres is also enhanced when coated with proteins such as laminin⁵², the main protein of the neural ECM. Electrospun scaffolds have also been extensively utilised in the field of bone tissue engineering. The ability to fine tune fibre properties and morphologies allows for *in vitro* investigations on matrix directed osteogenesis. For example, the incorporation of hydroxyapatite⁵³ and tricalcium phosphate⁵⁴ in the polymer (PCL) solution prior to electrospinning has shown to induce osteogenesis of hMSCs. By producing a bone-like matrix, the fibrous scaffolds are rendered osteoinductive and therefore did not require soluble induction factors.

Despite the progress in both synthesis, materials processing and understanding of biological processes, challenges still remain in successfully translating these technologies into viable therapies for regenerative medicine. One of these challenges *in vitro* is mimicking the level of complexity present in the ECM for the design of TE constructs. Physical and chemical design features must be presented in a physiological relevant 3D environment and must display spatial and temporal control of these features. Importantly, such materials properties must be controlled independently to decouple the effects of each parameter separately. This thesis aims to address some of these demands.

3.4 Amphiphilic block copolymers

Block copolymers have been exploited extensively in many areas of research because of the possibilities of a variety of architectures, chemistry, and molecular weights. Advances in polymerisation techniques furthermore, allow for precise control of their architecture which in the case of amphiphilic block copolymers can control their size, shape, self-assembly in aqueous solutions and their hence their properties. As, such amphiphilic block copolymers are used in applications varying from the electronics industry to drug delivery and medical devices^{55,56}. For tissue engineering applications in particular, block copolymers consisting of a stimuli responsive block such as poly(N-isopropylacrylamide) (PNIPAM), which has an LCST of 32°C and poly(ethylene oxide) (PEO) which exhibits temperature sensitivity have been widely exploited in controlled release and tissue engineering scaffold applications, respectively⁵⁷. More recently, thermoresponsive block copolymers of poly(glycerol monomethacrylate)-b-poly(2-hydroxypropyl methacrylate) (PGMA-PHPMA)⁵⁸, that form wormlike micelle gel at 21°C and spherical micelles at 4°C have been developed, which could potentially be used as injectable scaffolds. Triblock copolymers such as PEO-PPO-PEO and PEO-PLGA-PEO undergo a sol-gel transition dependent on temperature⁵⁹. Similarly, PLGA-PEO-PLGA triblock copolymers gel at physiological temperatures via aggregation of percolated micelles⁶⁰. Self-assembled block copolymer hydrogels have been used in cell and drug encapsulation and as tissue engineered scaffolds⁶¹.

In bulk, amphiphilic block copolymers undergo entropically and enthalpically driven microphase separation, constrained by a chemical bond, into well ordered domains^{62,63}. On the other hand, it is well known that amphiphilic block copolymers self-assemble in aqueous solutions in order to minimise hydrophobe-water interactions known as the hydrophobic effect⁶⁴. The precise nature of the self-assembled structure depends on molecular curvature and how this dictates the packing of the polymer chains is described by the dimensionless packing factor, (commonly used for small amphiphiles) p :

$$p = v_0 / al_c$$

where v_0 is the volume of the hydrophobic chains, a , is the optimal area of the head group and l_c is the length of the hydrophobic chain. In most cases, the packing factor determines the self-assembled structure (Figure 3.6); micelles are favoured when $p \leq \frac{1}{3}$, cylindrical micelles when $\frac{1}{3} \leq p \leq \frac{1}{2}$ and enclosed membranes when $\frac{1}{2} \leq p \leq 1$.

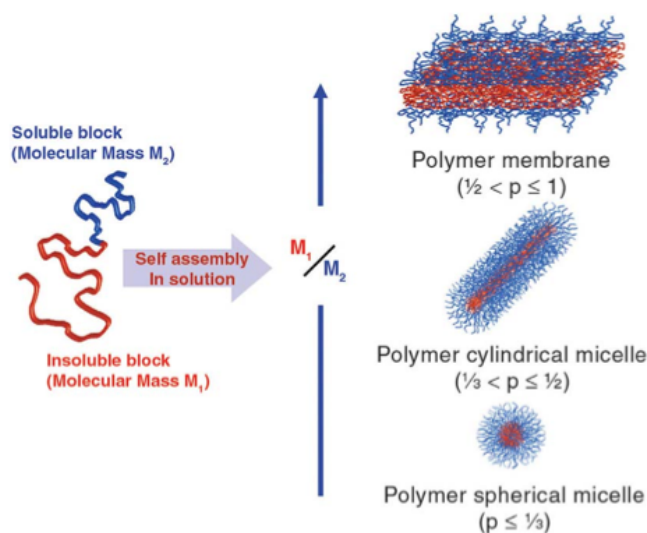


Figure 3.6. Self assembly of amphiphilic block copolymers in solution based on the hydrophilic and hydrophobic ratio. (Image from Smart; 2008)

The addition of a second block copolymer to the solution increases the complexity of the self-assembly of structures formed. Work done by Massignani and LoPresti^{64,65} showed that when binary mixtures of different membrane forming amphiphilic block copolymers (PMPC-PDPA and PEG-PDPA) were formed in solution, the chemically immiscible hydrophilic blocks PMPC and PEG underwent thermodynamically driven micro-phase separation (Figure 3.7) to form ‘patchy’ vesicles. These features were reported to be in the nanometre length scale. The size, shape and morphologies of such phase separated structures were also found to be strongly dependent on the molar ratios of the two copolymers.

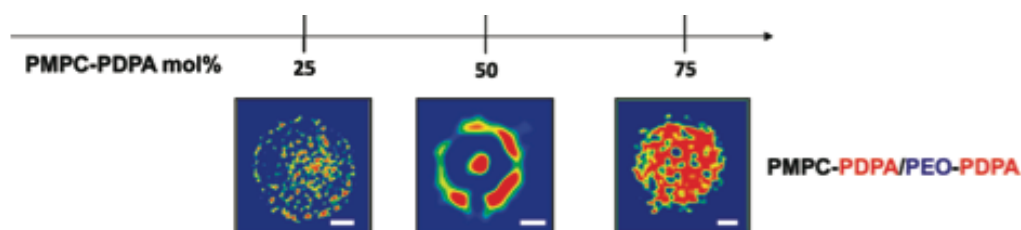


Figure 3.7 Phase separation between two amphiphilic block copolymers (PMPC-PDPA and PEG-PDPA) self-assembled in aqueous solution. Surface topology is dependent on copolymer molar ratio. (Figure modified from LoPresti; 2011)

The ability of two amphiphilic block copolymers in a bilayer system (i.e. vesicle membrane), to micro-phase separate allows for a unique way to control surface topology in 3D. Therefore, we can expect that amphiphilic block copolymers will also undergo such phase separation in a monolayer system at i) an oil-water interface in an emulsion and ii) a solid-air interface in a polymer fibre. Such an observation has not been reported to date. Moreover, copolymer phase separation could provide a distinct way to control surface topology in 3D scaffolds to mimic the physicochemical properties of the ECM, in particular, adhesive heterogeneity to effectively control cell behaviour.

3.5 Aims and objectives

The main aims of this thesis were to functionalise and characterise 3D scaffolds using amphiphilic block copolymers for the purpose of understanding how the physical and chemical properties of a 3D matrix alone could influence human mesenchymal stem cell behaviour. To do this, two different 3D scaffold fabrication techniques were used to demonstrate the universality of surface functionalisation using amphiphilic block copolymers.

3.5.1 Functionalisation of porous polyHIPEs

This project proposes the use of amphiphilic block copolymers as macromolecular surfactants in the HIPE process to control surface chemistry and topology in 3D in a one step process. Traditional polyHIPE fabrication is inherently limited by the hydrophobicity of the monomers commonly used and thus requires multi-step processes to introduce surface functionality. On the other hand, block copolymers can form nanostructured materials in bulk and in solution by exploiting controlled micro-phase separation⁶⁶. These nanomaterials have now been translated successfully to control cell adhesion in 2D⁶⁷, but they cannot form structured 3D microenvironments. Thus we combine the HIPE process with macromolecular block copolymer surfactants at the oil-water interface to control surface topology in 3D.

All foams in this study are based on polystyrene cross-linked with divinylbenzene. Poly(butadiene)-b-poly(ethylene oxide) (PBD-PEO), polystyrene-b-poly(acrylic acid) (PS-PAA), polystyrene-b-poly(ethylene oxide) (PS-PEO) and poly(butadiene)-b-poly(acrylic acid) (PBD-PAA) will be employed as the macromolecular surfactants and are compared to foams prepared with a traditional low molecular weight surfactant, sorbitan monooleate (Span 80).

We will investigate:

- 1) Parameters required for obtaining porous foams by varying emulsion conditions.
- 2) What determines open porosity of these foams as previous studies indicated closed porosity with block copolymer surfactants⁶⁸.

- 3) The surface functionality of the foams in 3D using various characterisation techniques (Figure 3.8).
- 4) To what extent can we mix two dissimilar copolymers (in this case PS-PAA and PBD-PEO) to form interface confined phase separation within a 3D foam to effectively control foam topology.
- 5) How this block copolymer phase separation ('patches') of PEO (cell inert) and PAA (cell adhesive) affect hES-MP (mesenchymal progenitor) adhesion
- 6) If the heterogeneity of PEO and PAA on a 3D scaffold can direct hES-MP differentiation towards specific lineages
- 7) If the rigidity of the underlying polystyrene/divinylbenzene matrix in conjunction specific scaffold chemistries can support osteogenesis.

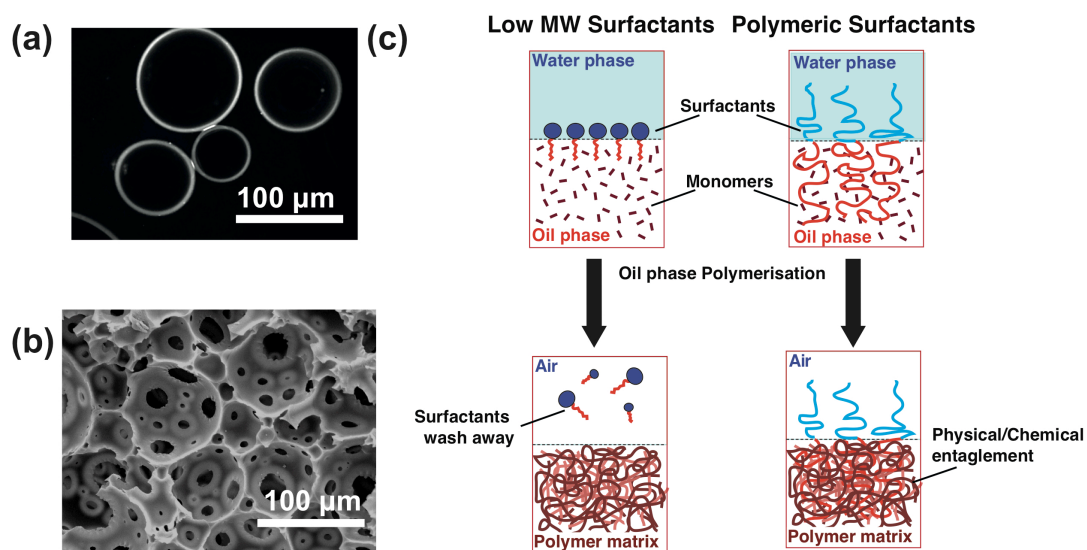


Figure 3.8 Mechanism of polyHIPE surface functionalisation. a) Optical micrograph of a HIPE, when polymerized forms b) a highly porous polystyrene /divinylbenzene foam as shown in the scanning electron micrograph. c) HIPEs stabilized by amphiphilic A-B type block copolymers as surfactants can be surface functionalised through physical or chemical entanglement compared to low molecular weight surfactants.

3.5.2. Functionalisation of electrospun fibres

The second polymer processing method used was electrospinning where we propose the functionalisation of electrospun poly(D,L-lactic acid) (PDLLA) fibres using amphiphilic block copolymers of PLLA and PDLLA homopolymer blends. The block copolymers that were used are poly(ethylene oxide)-b-poly(L-lactic acid) (PEO-PLA), poly((2-methacryloyloxy) ethyl phosphorylcholine)-b-poly(L-lactic acid)(PMPC-PLA), poly(dimethylaminoethyl methacrylate)-b-poly(L-lactic acid) (PDMA-PLA) and poly(oligo ethylene glycol methacrylate)-b-(poly(L-lactic acid) (POEGMA-PLA)

For this project we will investigate:

- 1) If the addition of small amounts of a PLA- amphiphilic diblock copolymer segregate on the surface of fibre thereby creating a hydrophilic surface in 3D (Figure 3.9).
- 2) What electrospinning parameters are required to obtain hydrophilic fibres.
- 3) If the addition of the block copolymer affects the degradation rates of the PDLLA fibres.
- 4) What architecture of the block copolymer is required for surface segregation i.e. hydrophobic:hydrophilic block ratio.
- 5) As with interface confined phase separation with 3D foams, to what extent can two block copolymers be mixed to form 'patches' and if the topology of the fibres can be controlled this way. The block copolymers PMPC-PLA and POEGMA-PLA will be used for this study.
- 6) How hES-MP adhesion is affected by the presentation of patchy surfaces particularly if one of the hydrophilic blocks is conjugated to a recognisable peptide such as RGD.

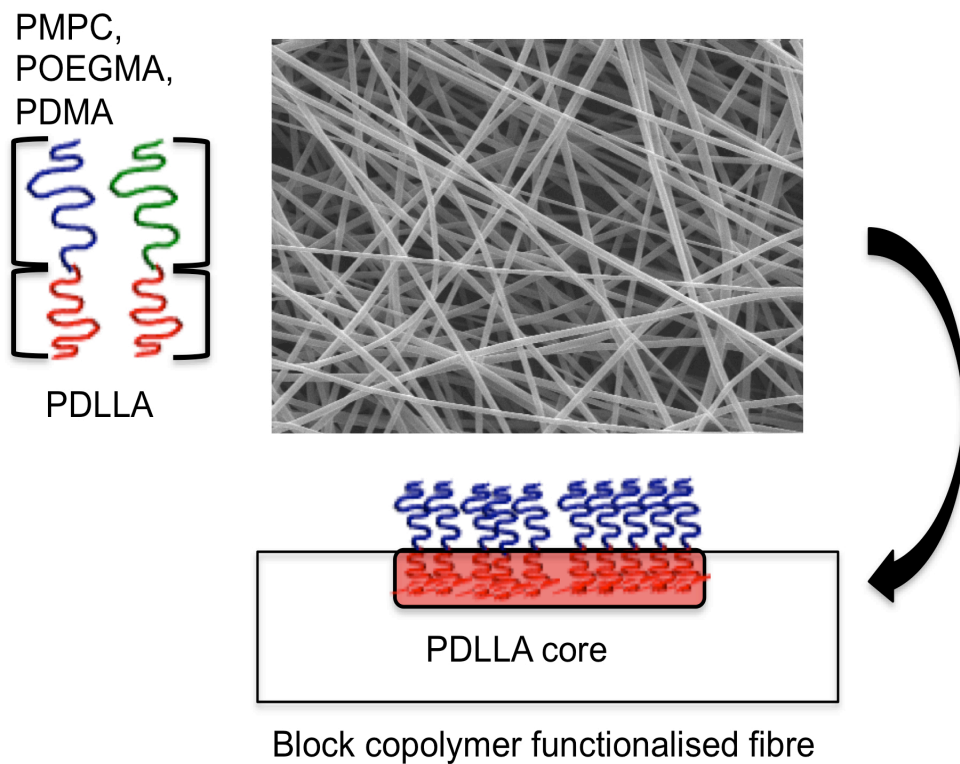


Figure 3.9 Schematic of PDLLA fibre functionalisation by using amphiphilic block copolymer as additives in the electrospinning process resulting in hydrophilic surfaces.

References

1. Engel, E., Michiardi, A., Navarro, M., Lacroix, D. & Planell, J. A. Nanotechnology in regenerative medicine: the materials side. *Trends Biotechnol* **26**, 39–47 (2008).
2. Karageorgiuo, V. & Kaplan, D. Porosity of 3D biomaterial scaffolds and osteogenesis. *Biomaterials* **26**, 5474–5491 (2005).
3. Oh, S. H., Park, I. K., Kim, J. M. & Lee, J. H. In vitro and in vivo characteristics of PCL scaffolds with pore size gradient fabricated by a centrifugation method. *Biomaterials* **28**, 1664–1671 (2007).
4. Murphy, C. M., Haugh, M. G. & O'Brien, F. J. The effect of mean pore size on cell attachment, proliferation and migration in collagen–glycosaminoglycan scaffolds for bone tissue engineering. *Biomaterials* **31**, 461–466 (2010).
5. Zeltinger, J., Sherwood, J. K., Graham, D. A., Muller, R. & Griffith, L. Effect of Pore Size and Void Fraction on Cellular Adhesion, Proliferation and Matrix Deposition. *Tissue Eng* **7** 557–572 (2001).
6. Stevens, M. M. Exploring and Engineering the Cell Surface Interface. *Science* **310**, 1135–1138 (2005).
7. Reilly, G. C. & Engler, A. J. Intrinsic extracellular matrix properties regulate stem cell differentiation. *J. Biomech.* **43**, 55–62 (2010).
8. Hench, L. L. & Polak, J. M. Third-Generation Biomedical Materials. *Science* **295**, 1014–1017 (2002).
9. Shoichet, M. S. Polymeric Scaffolds for Biomedical Applications, *Macromolecules*, **43**, 581–591 (2010)
10. Patterson, J., Martino, M. M. & Hubell, J. A. Biomimetic materials in tissue engineering. 1–9 (2012).
11. Stevens, M. M. Biomaterials for bone tissue engineering. *Materials Today* **11**, 18–25 (2008).
12. Frantz, C., Stewart, K. M. & Weaver, V. M. The extracellular matrix at a glance. *Journal of Cell Science* **123**, 4195–4200 (2010).
13. Burdick, J. A. & Prestwich, G. D. Hyaluronic Acid Hydrogels for Biomedical Applications. *Adv. Mater.* **23**, 41–56 (2011).
14. Mrksich, M. & Whitesides, G. M. Patterning self-assembled monolayers using microcontact printing: a new technology for biosensors? *Trends Biotechnol* **13**, 228–235 (1995).
15. McBeath, R., Pirone, D. M., Nelson, C. M., Bhadriraju, K. & Chen, C. S. Cell Shape, Cytoskeletal Tension, and RhoA Regulate Stem Cell Lineage Commitment. *Dev Cell* **6**, 483–495 (2012).
16. Arnold, M. *et al.* Activation of Integrin Function by Nanopatterned Adhesive Interfaces. *ChemPhysChem* **5**, 383–388 (2004).
17. Dalby, M. J. *et al.* The control of human mesenchymal cell differentiation using nanoscale symmetry and disorder. *Nat Mater* **6**, 997–1003 (2007).
18. Zhang, S. *et al.* Self-complementary oligopeptide matrices support mammalian cell attachment. *Biomaterials* **16**, 1385–1393 (1995).
19. Horii, A., Wang, X., Gelain, F. & Zhang, S. Biological Designer Self-Assembling Peptide Nanofiber Scaffolds Significantly Enhance Osteoblast Proliferation, Differentiation and 3-D Migration. *PLoS ONE* **2**, e190 (2007).
20. Jung, J. P., Gasiorowski, J. Z. & Collier, J. H. Fibrillar peptide gels in biotechnology and biomedicine. *Biopolymers* **94**, 49–59 (2010).

21. Ryadnov, M. G. & Woolfson, D. N. Engineering the morphology of a self-assembling protein fibre. *Nat Mater* **2**, 329–332 (2003).
22. Silva, G. A. Selective Differentiation of Neural Progenitor Cells by High-Epitope Density Nanofibers. *Science* **303**, 1352–1355 (2004).
23. Tysseling-Mattiace, V. M. *et al.* Self-Assembling Nanofibers Inhibit Glial Scar Formation and Promote Axon Elongation after Spinal Cord Injury. *J. Neurosci.* **28**, 3814–3823 (2008).
24. Lim, D. W., Nettles, D. L., Setton, L. A. & Chilkoti, A. In Situ Cross-Linking of Elastin-like Polypeptide Block Copolymers for Tissue Repair. *Biomacromolecules* **9**, 222–230 (2008).
25. Gazit, E. Self-assembled peptide nanostructures: the design of molecular building blocks and their technological utilization. *Chem. Soc. Rev.* **36**, 1263 (2007).
26. Lutolf, M. P., Gilbert, P. M. & Blau, H. M. Designing materials to direct stem-cell fate. *Nature* **462**, 433–441 (2009).
27. Lissant, K. J. Geometry of Emulsions. *J. Soc. Cosmetic Chemists* **21**, 141–154 (1970).
28. Chen, Y., Ballard, N., Gayet, F. & Bon, S. A. F. High internal phase emulsion gels (HIPE-gels) from polymer dispersions reinforced with quadruple hydrogen bond functionality. *Chem. Commun.* **48**, 1117 (2012).
29. Zhang, H. & Cooper, A. I. Synthesis and applications of emulsion-templated porous materials. *Soft Matter* **1**, 107 (2005).
30. Cameron, N. R. High internal phase emulsion templating as a route to well-defined porous polymers. *Polymer* **46**, 1439–1449 (2005).
31. Zhang, S. Fabrication of novel biomaterials through molecular self-assembly. *Nat Biotechnol* **21**, 1171–1178 (2003).
32. Kimmins, S. D. & Cameron, N. R. Functional Porous Polymers by Emulsion Templating: Recent Advances. *Adv. Funct. Mater.* **21**, 211–225 (2010).
33. Zhang, S., Chen, J. & Perchyonok, V. T. Stability of high internal phase emulsions with sole cationic surfactant and its tailoring morphology of porous polymers based on the emulsions. *Polymer* **50**, 1723–1731 (2009).
34. Barbetta, A. & Cameron, N. R. Morphology and Surface Area of Emulsion-Derived (PolyHIPE) Solid Foams Prepared with Oil-Phase Soluble Porogenic Solvents: Three-Component Surfactant System. *Macromolecules* **37**, 3202–3213 (2004).
35. Williams, J. M. High Internal Phase Water-in-Oil Emulsions: Influence of Surfactants and Cosurfactants on Emulsion Stability and Foam Quality. *Langmuir* **7** 1370–1377 (1991).
36. Livshin, S. & Silverstein, M. S. Cross-linker flexibility in porous crystalline polymers synthesized from long side-chain monomers through emulsion templating. *Soft Matter* **4**, 1630 (2008).
37. Cameron, N. R. & Barbetta, A. The influence of porogen type on the porosity, surface area and morphology of poly(divinylbenzene) PolyHIPE foams. *J. Mater. Chem.* **10**, 2466–2471 (2000).
38. Barbetta, A. & Cameron, N. R. Morphology and Surface Area of Emulsion-Derived (PolyHIPE) Solid Foams Prepared with Oil-Phase Soluble Porogenic Solvents: Span 80 as Surfactant. *Macromolecules* **37**, 3188–3201 (2004).
39. Carnachan, R. J., Bokhari, M., Przyborski, S. A. & Cameron, N. R. Tailoring the morphology of emulsion-templated porous polymers. *Soft Matter* **2**, 608 (2006).
40. Akay, G., Birch, M. A. & Bokhari, M. A. Microcellular polyHIPE polymer supports osteoblast growth and bone formation in vitro. *Biomaterials* **25**, 3991–4000 (2004).
41. Bokhari, M. A., Akay, G., Zhang, S. & Birch, M. A. The enhancement of osteoblast growth and differentiation in vitro on a peptide hydrogel—polyHIPE polymer hybrid material. *Biomaterials* **26**, 5198–5208 (2005).

42. Bokhari, M., Carnachan, R. J., Przyborski, S. A. & Cameron, N. R. Emulsion-templated porous polymers as scaffolds for three dimensional cell culture: effect of synthesis parameters on scaffold formation and homogeneity. *J. Mater. Chem.* **17**, 4088 (2007).
43. Greiner, A. & Wendorff, J. H. Electrospinning: A Fascinating Method for the Preparation of Ultrathin Fibers. *Angew. Chem. Int. Ed.* **46**, 5670–5703 (2007).
44. Xie, J., Li, X. & Xia, Y. Putting Electrospun Nanofibers to Work for Biomedical Research. *Macromol. Rapid Commun.* **29**, 1775–1792 (2008).
45. Gupta, P., Elkins, C., Long, T. E. & Wilkes, G. L. Electrospinning of linear homopolymers of poly(methyl methacrylate): exploring relationships between fiber formation, viscosity, molecular weight and concentration in a good solvent. *Polymer*, **46** 4799–4810 (2005)
46. Pham, Q. P., Sharma, U. & Mikos, A. Electrospinning of Polymeric Nanofibers for Tissue Engineering Applications: A Review. *Tissue Eng* **12**, 1197–1211 (2006).
47. Zhang, C., Yuan, X., Wu, L., Han, Y. & Sheng, J. Study on morphology of electrospun poly(vinyl alcohol) mats. *Eur. Polym. J.* **41**, 423–432 (2005).
48. Mit-uppatham, C., Nithitanakul, M. & Supaphol, P. Ultrafine Electrospun Polyamide-6 Fibers: Effect of Solution Conditions on Morphology and Average Fiber Diameter. *Macromol. Chem. Phys.* **205**, 2327–2338 (2004).
49. Li, D. & Xia, Y. Electrospinning of Nanofibers: Reinventing the Wheel? *Adv. Mater.* **16**, 1151–1170 (2004).
50. Liang, D., Hsiao, B. S. & Chu, B. Functional electrospun nanofibrous scaffolds for biomedical applications. *Adv. Drug Deliver. Rev.* **59**, 1392–1412 (2007).
51. He, L. *et al.* Surface modification of electrospun nanofibrous scaffolds via polysaccharide–protein assembly multilayer for neurite outgrowth. *J. Mater. Chem.* **22**, 13187 (2012).
52. Koh, H. S., Yong, T., Chan, C. K. & Ramakrishna, S. Enhancement of neurite outgrowth using nano-structured scaffolds coupled with laminin. *Biomaterials* **29**, 3574–3582 (2008).
53. Phipps, M. C. *et al.* Mesenchymal Stem Cell Responses to Bone-Mimetic Electrospun Matrices Composed of Polycaprolactone, Collagen I and Nanoparticulate Hydroxyapatite. *PLoS ONE* **6**, e16813 (2011).
54. Polini, A., Pisignano, D., Parodi, M., Quarto, R. & Scaglione, S. Osteoinduction of Human Mesenchymal Stem Cells by Bioactive Composite Scaffolds without Supplemental Osteogenic Growth Factors. *PLoS ONE* **6**, e26211 (2011).
55. Smart, T. *et al.* Block copolymer nanostructures. *Nano Today* **3**, 38–46 (2008).
56. Blanazs, A., Armes, S. P. & Ryan, A. J. Self-Assembled Block Copolymer Aggregates: From Micelles to Vesicles and their Biological Applications. *Macromol. Rapid Commun.* **30**, 267–277 (2009).
57. Liu, S. Q. *et al.* Synthetic hydrogels for controlled stem cell differentiation. *Soft Matter* **6**, 67 (2009).
58. Blanazs, A. *et al.* Sterilizable Gels from Thermoresponsive Block Copolymer Worms. *J. Am. Chem. Soc.* **134**, 9741–9748 (2012).
59. Qiu, Y. & Park, K. Environment-sensitive hydrogels for drug delivery. *Adv. Drug Deliver. Rev.* **64**, 49–60 (2012).
60. Yu, L., Chang, G., Zhang, H. & Ding, J. Temperature induced sol-gel transitions of poly(lactic-co-glycolic acid)-poly(ethylene oxide)-poly(lactic-co-glycolic acid) triblock copolymers and their end-cap derivatives in water. *J. Polym. Sci. A. Polym. Chem.* **65**, 1122–1133 (2007).
61. Lee, K. & Mooney, D. *Chem. Rev.* **101**, 1869–1880 (2001).
62. Ruzette, A.-V. & Leibler, L. Block copolymers in tomorrow's plastics. *Nat Mater* **4**, 19–31 (2005).

63. Hamley, I. W. Nanostructure fabrication using block copolymers. *Nanotechnology* **14**, 39–54 (2003).
64. Meyer, E. E., Rosenberg, K. J. & Israelachvili, J. Recent progress in understanding hydrophobic interactions. *PNAS* **103**, 15739–15746 (2006).
65. Massignani, M. *et al.* Controlling Cellular Uptake by Surface Chemistry, Size, and Surface Topology at the Nanoscale. *Small* **5**, 2424–2432 (2009).
66. LoPresti, C. *et al.* Controlling Polymersome Surface Topology at the Nanoscale by Membrane Confined Polymer/Polymer Phase Separation. *ACS Nano* **5**, 1775–1784 (2011).
67. George, P. A., Quinn, K. & Cooper-White, J. J. Hierarchical scaffolds via combined macro- and micro-phase separation. *Biomaterials* **31**, 641–647 (2010).
68. Viswanathan, P. Emulsion Templated Porous Scaffolds for Bone Tissue Engineering. *MPhil Thesis, The University of Sheffield* 1–46 (2010).

Chapter 4: Materials and Methods

4.1 HIPE templating

4.1.1 Foam preparation

All chemicals were purchased from Sigma Aldrich UK unless otherwise stated. The monomers styrene and divinylbenzene (80% technical grade) were passed through a column of activated basic alumina (Brockmann Activity I) to remove the inhibitor *p*-tert butylcatechol prior to use. The initiators $K_2S_2O_8$ and AIBN (Fisher Scientific), tetrahydrofuran (THF), block copolymers poly(1,4-butadiene)-*b*-poly(ethylene oxide) (PBD-PEO) and polystyrene-*b*-poly(acrylic acid) (PS-PAA) (PolymerSource Inc., Montreal) and the surfactant Span 80 were all used as received and all have a reported polydispersity index (PDI) of 1.1-1.3. Poly(1,4-butadiene)-*b*-poly(acrylic acid) (PBD-PAA, PDI= 1.2) was synthesized as previously reported¹.

Table 4.1-1. Hydrophile-lipophile balance (HLB) values calculated for block copolymer surfactants according to Griffin's formula. * Denotes estimation for ionic surfactants as the formula is based on non-ionic surfactants.

Surfactant	$M_w / g\ mol^{-1}$	HLB
Span 80	483	4.8
PS-PAA	18700	3.95*
PBD-PAA	3000	7.3*
PS-PEO	25000	0.8
PBD-PEO	14300	3.87
PS-PAA-PA	20100	13.4*

The high internal phase emulsions were prepared as follows; the surfactant was first solubilised in the oil phase. Due to the poor solubility of PS-PAA and PS-PAA-PS in styrene/divinylbenzene (Sty/DVB), THF (10 μ l/mg) was used to make a solution of PS-PAA or PS-PAA-PS before its addition to the oil phase. The surfactant concentration was maintained at 0.01 mole% (relative to the monomer) for all copolymer. For concentration dependent studies, copolymer concentration was increased from 8×10^{-4} mole% - 0.02 mole%. The aqueous phase consisting of 0.1w/v% of $K_2S_2O_8$ was added

using a peristaltic pump at a rate of 10 ml/min. The oil phase was continuously stirred either using an overhead mechanical stirrer with a stainless steel paddle at 750 rpm or an UltraTurrax homogeniser at 11500 rpm. Once the aqueous phase was added, the resulting viscous white emulsions were stirred for a further 5 minutes to homogenise. When AIBN (1 wt/wt% of the oil phase), was used as the initiator, the appropriate amount was added to the oil phase and stirred immediately before the addition of DI water. The emulsions were then polymerised in a convection oven at 50 °C for 24 hours resulting in porous monolithic foams. The foams were subsequently Soxhlet extracted in isopropyl alcohol for 24 hours to remove all unreacted monomers. Emulsions prepared with Span 80 as the surfactants were done using previously established protocols^{2,3}. All emulsions, with the exception of those stabilised by PS-PEO consisted of an aqueous phase of either 80% or 90% by volume. The remaining oil phase consisted of 90 wt/wt% styrene and 10 wt/wt% divinylbenzene. Emulsions using PS-PEO as the surfactant on the other hand were prepared with an aqueous phase volume of 80%, with the oil phase consisting of only DVB. Formulations with higher aqueous phase volumes or the addition of styrene to the oil phase resulted in unstable emulsions at the polymerisation temperature.

Foams with block copolymer mixtures were prepared by maintaining the surfactant concentration at 0.01 mole%. Copolymers (PS-PEO:PS-PAA) were mixed in molar ratios of 3:1, 1:1 and 1:3. Oil phase monomers were maintained at 90 wt/wt% Sty and 10 wt/wt% DVB.

4.1.2 Foam morphology and interconnectivity

Sectioned foams were prepared for scanning electron microscopy by placing them on an aluminium stub with an adhesive carbon pad. Samples were coated with gold (approximately 15 nm) using an Edwards S150B Sputter Coater. Foams were imaged using a Philips XL20 scanning electron microscope at an accelerating voltage of 10 kV and spot size of 3.0 nm. Void diameters were estimated by image analysis using Image J. Roughly 100 voids and 100 interconnects were measured from each emulsions composition from various micrographs to obtain an average porosity of the foams. A statistical correction, previously described⁴ was used to gain a more accurate measurement of void diameters.

4.1.3 Mercury Intrusion porosimetry

(This work was carried out by Dr. David Ward Johnson at Durham University)

Mercury intrusion porosimetry analysis was performed using a Micromeritics AutoPore IV. Intrusion and extrusion mercury contact angles of 130° were used. Penetrometers with a stem volume of 1.836 ml and a bulb volume of 4.25 ml were used. The intrusion volumes were between 25 and 90% of the stem volume. Intrusion pressures for the polyHIPE did not exceed 1600 psia.

4.1.4 X-ray photoelectron spectroscopy (XPS)

Surface analysis was carried out using a Kratos AXIS ULTRA spectrophotometer with a mono-chromated Al $\kappa\alpha$ X-ray source operated at 10mA emission current and 12kV anode potential. The spot size used was 700 μm x 300 μm . The pressure in the main ultra-high vacuum chamber was maintained below 1×10^{-8} mbar for all analyses. Samples were mounted onto the sample bar with double-sided tape and data was collected at an angle of 90° (from the surface). Wide scans of low resolution (pass energy 80eV) and high resolution scans for the core level electrons were set at a pass energy of 20 eV. The timing for each wide scan was 10 minutes and between 5-10 minutes for the high resolutions scans (C 1s, O 1s, N 1s). A total of 3 scans with a step size of 1 mm were made for each foam composition. All data collected was then analysed using CasaXPS software Peaks were again fitted by removing unwanted background using CasaXPS software. Asymmetry of the peaks was fixed at zero and the position of each peak was fixed relative to the C 1s peak centred at 285 eV.

4.1.5 Water contact angle measurements

Static water contact angle measurements were made using a Rame-Hart contact angle goniometer using MilliQ water at pH 7 and pH 2 adjusted with 0.1M HCl. 4 μL volume of water was placed on each foam and was allowed to settle for 30 minutes. A total of 3 measurements were made for each sample.

4.1.6 Preparation of 2D films for atomic force microscopy (AFM) analysis

2D films were characterised for all AFM analysis. 2D film preparation employs the same compositions and oil:aqueous phase volume fractions as the 3D foams (Table

1). Briefly, the aqueous phase was added to a glass vial using a syringe. The oil phase (monomer + block copolymer surfactant) was then carefully layered on top of the aqueous phase to maintain phase separation. The copolymer mixtures were then allowed to adsorb at the oil-water interface for 24 hours without agitation and then polymerised at 60 °C for 24 hours. The resulting films were washed extensively with deionised water (DI H₂O), left in ethanol for 1 week to remove unreacted monomers, and dried before analysis.

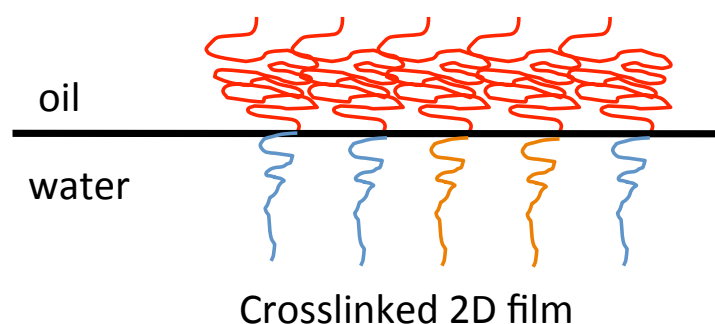


Figure 4.1.1 Preparation of 2D films for CFSM. Copolymer surfactants and their mixtures were allowed to adsorb at the oil water interface prior to film crosslinking.

4.1.7 Chemical Force Spectroscopy Mapping (CFSM)

(this work was carried out during a collaborative visit to UCSD)

CFSM provides adhesive force maps generated by measuring the rupture force between bonds that form between a functionalised tip and the surface. As shown in Fig 4.1.2 a tips were functionalised by poly-L-lysine (PLL, M_w 1000-5000) based on a technique described developed by Chirasatitsin and Engler⁵. Briefly, AFM tips were cleaned by chloroform and immersed in 5 M ethanolamine-hydrochloride in dimethyl sulfoxide overnight. After washing with phosphate buffered saline (PBS), cantilevers were immersed in 25 mM BS3 (bis[sulfosuccinimidyl] suberate; Pierce) for 30 min. After washing again with PBS, cantilevers were then immersed in 1 mg/ml poly-L-lysine for 30 min. All steps were done at room temperature. Functionalised cantilevers were air-dried and kept in 4°C until use. CFSM was performed on the MFP3D-BIO atomic force microscope (AFM, Asylum Research) to measure the adhesive interactions with films maintained at pH 9 overnight and immersed in pH 7 immediately before tested.

Functionalised cantilevers were calibrated before indenting samples to account for batch-to-batch variability in tip functionalisation. Using PEO100 (large adhesion forces) and PAA100 (minimal adhesion forces), force maps of 16×16 pixel resolution over $20 \mu\text{m} \times 20 \mu\text{m}$ were performed so that adhesive forces could be internally calibrated to each cantilever. Maximum adhesion forces for PEO100 and PAA100 were 10 and 2 nN, respectively. From the force histograms (Figure 4.1.3), adhesion between the tip and PEO100 film was determined to be from one standard deviation below the average force measured ($\mu - \sigma$, figure 4.1.3). The adhesion measured between the functionalised tip and PAA100 films were below this value ($\mu - \sigma$), and was therefore used as the adhesion threshold. Thus, films with the two block copolymers were mapped based on the differential tip-surface adhesive profiles.

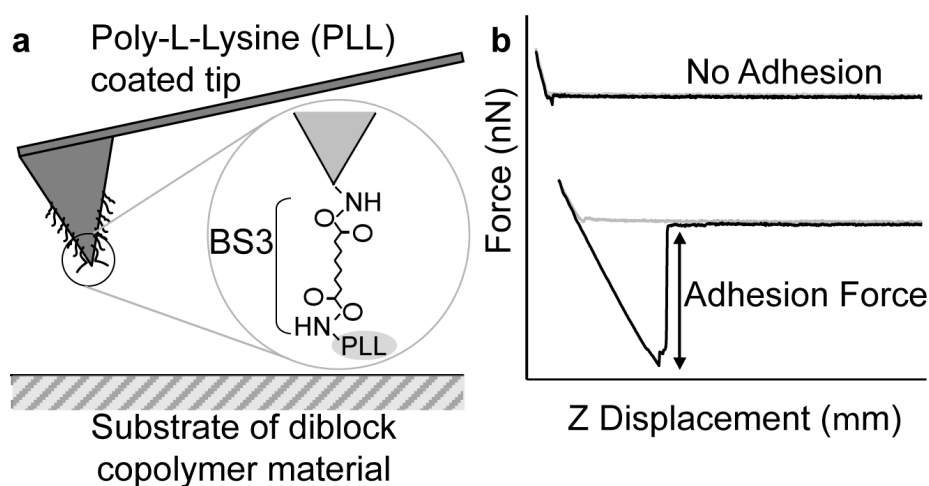


Figure 4.1.2 a) Probe for CFMS which is covalently bonded to bis[sulfosuccinimidyl] substrate (BS3) and poly-L-lysine (PLL). b) Force curves with (bottom) and without (top) interaction between probe and surface. Note the adhesion force indicated during retraction (black line) versus indentation (grey line).

Using this definition, a distribution of the normalised adhesion forces was generated from all images and the ratio of adhesive to total area was determined for each image, i.e. the PEO area fraction. A nano-domain, calculated by ImageJ software, was defined as at least 4 adjacent data points higher or lower than the threshold in the case of PEO or PAA domains, respectively.

Force curves were generated with a $2 \mu\text{m/s}$ approach velocity, 1 nN surface trigger force, 3 second dwell time between tip indentation and retraction, and a 32×32 pixel

scan resolution over $2\ \mu\text{m} \times 2\ \mu\text{m}$ and $20\ \mu\text{m} \times 20\ \mu\text{m}$ scan areas (resolutions of 62.5 and 625 nm, respectively). Typical force curves for interactions without (top) and with adhesion (bottom) are shown in Figure. 4.1.2 b. Area fraction and domain surface areas were determined using ImageJ software from a thresholding scheme.

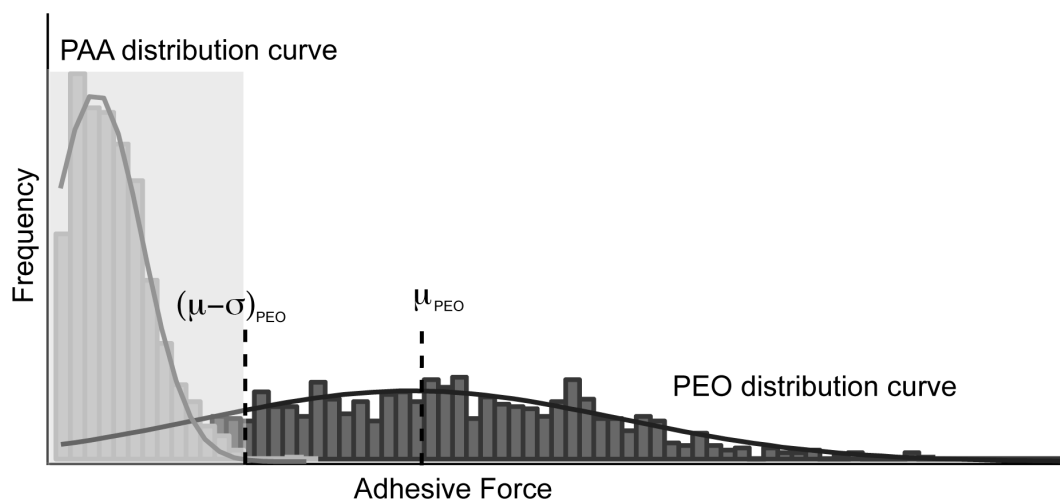


Figure 4.1.3. Force Histograms. An adhesive force threshold was estimated using the difference between PAA and PEO films by normalising the distribution curves for PAA100 (light grey bars) and PEO100 (dark grey bars). Virtually all events observed from PAA100 were below one standard deviation below the PEO100 film average; the grey box illustrates this threshold.

4.1.8 Protein adsorption and detection

Cylindrical foams of ~ 12 mm in diameter and ~ 4 mm thick were placed in a 24-well tissue culture plate and submerged in the culture media. After 2 hrs in culture media, foams were rinsed with PBS 3 times. Absorbed protein was dissociated with mRIPA buffer (Pierce, UK) plus the protease inhibitor phenylmethanesulfonylfluoride overnight. Protein concentration within the lysates was measured by the bicinchoninic acid (BCA) assay (Pierce, UK).

(The following work related to fibronectin detection by AFM was carried out by Dr. Somyot Chirasatitsin at UCSD)

Micro- and nano-scale protein clustering was visualised by immunofluorescence and CFM. $100\ \mu\text{g/ml}$ rat plasma fibronectin in PBS was incubated with film samples for 2 hours at 37°C and washed with PBS. For those samples observed by confocal microscopy, films were incubated with the R457 fibronectin antibody in 2% bovine serum albumin (BSA) in PBS (1:500) for an hour at 37°C . After rinsing with PBS, samples were incubated with an Alexa Fluor® 647-conjugated secondary antibody in

2% BSA in PBS (1:1000) for an hour at 37°C. A spinning disc confocal fluorescent microscope (BD CARV II, BD Bioscience) and 60X water-immersion objective was used for image acquisition. For those samples observed by CFSM, the R457 fibronectin antibody was bound to an AFM tip using the same chemistry as PLL. The scan area was set to $2 \times 2 \mu\text{m}$ with 62.5 nm resolution and CFSM parameters used were the same as for copolymer domain detection described above. The specific interaction between the antibody and fibronectin was identified from the rupture force-loading rate graph, providing the threshold as 300 pN, which we have previously established for fibronectin⁵. Again, area fraction and domain surface areas were determined using ImageJ software.

4.1.9 Fibronectin Matrix Preparation and Imaging (this work was carried out by Dr. Somyot Chirasatitsin at UCSD)

NIH3T3 fibroblasts were cultured at 100% confluence on 25 mm coverslips for 7 days in growth media (89% Dulbecco's Minimum Eagle's Media, 1% Penicillin-Streptomycin, and 10% fetal bovine serum). The serum used to culture the fibroblasts was fibronectin-depleted by passing the serum first over a gelatin column prior to use in the media. All serum was confirmed to be fibronectin free by silver staining and western blotting methods. Growth media was then spiked with human fibronectin to a concentration equal to what was depleted from the serum originally.

Once the fibroblasts had been grown for 7 days, the cells were lysed and removed by a previously described method that maintains the fibronectin network intact⁶. The rabbit polyclonal R457 antibody was then used to stain all fibronectin fibrils⁷ while cell adhesion sites were detected specifically on the human fibronectin that had been incorporated into the network during fibroblast-mediated assembly by the hFN7.1 antibody (Developmental Studies Hybridoma Bank; Iowa City, IA). Images were acquired on a BD CARV II spinning disc confocal fluorescent microscope using 20x objective. Image analysis was performed with NIH ImageJ software.

4.1.10 3D cell culture

Human Embryonic Stem cell derived Mesenchymal Progenitors (hES-MPTM, Cellartis, UK) was the chosen cell source for all studies herein. These cells have been shown to differentiate towards osteogenic, chondrogenic and adipogenic

lineages^{8,9}. According to the manufacturer, hES-MP are positive for CD105, CD166, CD13 and CD10 and are negative for CD133 and CD117 surface antigens.

hES-MPs were cultured in Alpha modified Minimum Essential Medium (Alpha-MEM, Gibco, UK) supplemented with 10% foetal bovine serum (FBS), 1% Penicillin/Streptomycin (Invitrogen, UK) and 10 ng/ml basic fibroblast growth factor (b-FGF, Invitrogen, UK) also referred to as FGF 2 to maintain proliferation. Cells were maintained in a humidified 37 °C incubator at 5% CO₂. Cultures were passaged at 70-80% confluence using Trypsin EDTA and split at a 1:8 ratio and media was replenished ever 2-3 days. Passages from 5-15 were used for all experiments.

Scaffolds of dimensions 1.2 cm in diameter and 3-5 mm in height were sterilised for cell culture using 70% EtOH overnight and then washed three times with PBS (1 hour between washes) to remove all traces of EtOH. To prevent buoyancy of the scaffolds in the well plate, they were weighed down with custom made stainless steel, dental grade rings for the first week in culture. Scaffolds were then briefly washed once with basal media before being seeded with the hES-MPs at a density of 100,000 cells/scaffold in a 50 µL volume. Cells were incubated at 37 °C for 90 minutes before adding 1ml of basal media / well (i.e. without b-FGF) unless otherwise stated. After 24 hours of seeding, the medium was changed and scaffolds were transferred to a new well plate. Subsequent media changes were every 2-3 days until the assay point. For experiments investigating mineral deposition, hES-MPs seeded on scaffolds were treated with 10nM dexamethasone (DEX) 24 hours after seeding. in conjunction with experiments in the absence of any soluble growth factors.

4.1.11 Determination of scaffold toxicity

Scaffold toxicity was determined by a non-contact experiment. Sterilised scaffolds for each block copolymer composition was incubated in serum containing media for 5 days. hES-MPs cultured in a 24 well plate at a density of 10,000 cells/well for 24 hours to allow for cell attachment. The media was then exchanged with scaffold conditioned media for a further 48 hours. Any soluble cytotoxic components from the scaffolds would therefore affect cell proliferation and viability. Cell viability by

assessed by the MTT assay and was compared to Span 80 as well as tissue culture plastic control where cell were replenished with growth media.

4.1.10 Cell Viability

MTT assay

MTT (A3-(4,5-dimethylthiazol-2-yl)-2,5-diphenyltetrazolium bromide) assay is a frequently used methods for measuring cell growth and viability. Cell viability was determined by the MTT assay for non-contact toxicity experiments as follows. Scaffolds were washed with PBS once then incubated with 1 ml of MTT solution (0.5 mg/ml) in PBS / well at 37 °C for 1 hour. The formazan salt is converted to an insoluble purple product by the mitochondria of living cells. The product was destained using acidified isopropyl alcohol (500 µl/ well). 200 µl of the de-stained solution was transferred to a flat-bottomed 96 well plate in duplicate and the optical density was measured at 570 nm and referenced at 630 nm using a microplate reader.

MTS assay

The MTS (3-(4,5-dimethylthiazol-2-yl)-5-(3-carboxymethoxyphenyl)-2-(4-sulfophenyl)-2H-tetrazolium) assay is similar to the MTT assay but produces a soluble metabolic product. The MTS assay was used to assess cell viability and cell number for hES-MPS cultured on scaffolds after 7 days. Growth media was removed and treated with 600 µl of MTS/PMT solution (Promega, UK) in culture medium at a final concentration of 333 µg/ml and 25 µM respectively were added to each well. Cells were then incubated for 3 hours at 37°C to let the substrate react with the dehydrogenase enzyme present in mitochondria of living cells. 200 µl of the resulting solution was transferred to a flat-bottomed 96-well plate in duplicate and the absorbance was measured at 490 nm. Number of viable cells on scaffolds were calculated from a calibration curve using cell densities ranging from 0 to 10⁶ cells.

4.1.12 Nuclear and actin cytoskeleton staining

Cells were fixed and stained for nuclear and actin staining for days 7, 14, 21 and 28 as follows. Scaffolds were washed once with PBS and fixed with 3.7% formaldehyde for 40 minutes then permeabilised with 0.1% Triton X for 20 minutes. Cell were then

incubated with Phalloidin-Texas Red (Invitrogen, 1:100 in PBS) and imaging mounting media with DAPI (approx. 25 μ l, Invitrogen) for 1 hour on a plate rocker at room temperature. Unbound stain was washed with PBS three times and scaffolds were stored in PBS at 4 °C until imaged. Imaging was performed using an inverted Zeiss LSM 510 confocal laser scanning microscope with a 10x objective.

4.1.13 Sample preparation for biological SEM

All procedures were carried out on 24 well plates. Cells cultured on foams for 28 days were fixed in 2.5% gluteraldehyde (1 ml/ well) overnight. Scaffolds were then rinsed in PBS twice for 15 minutes each followed by DI H₂O once for 15 minutes. Samples were then dehydrated using an ethanol gradient of 35%, 60%, 80%, 90% and finally absolute EtOH for 15 minutes each. Scaffolds were then critically dried using a 1:1 v:v of absolute EtOH:HMDS (hexamethyldisilazane) for 1 hour. This was followed by HMDS wash twice, each for 10 mins before samples were left to dry completely under vacuum. Samples were then sputter coated and viewed under SEM as before.

4.1.14 Calcium staining by Alizarin Red S

hES-MPs were fixed in 3.7% formaldehyde at days 21 and 28 for 30 minutes and washed with PBS once and in DI H₂O twice. Alizarin Red S powder made up to a concentration of 5 mg/ml of DI H₂O (0.5 w/v%) was adjusted to a pH of 4.1 using 0.1M NaOH. 1 ml of the Alizarin Red solution was added to each scaffold and place on a rocker for 30 minutes. Scaffolds were then washed carefully three times in DI H₂O to remove all unbound stain and left to air dry before quantification. A blank scaffold (no cells) also treated with Alizarin Red was used as a background as the red solution lightly stains the scaffold itself.

To quantify the amount of mineral, a 5 v/v% of perchloric acid in dH₂O was prepared. 0.5 ml of this solution was added to each scaffold to de-stain. 200 μ L of the de-stain was pipetted to a 96 well plate and the absorbance was read at 405 nm. Solutions ranged from clear (no calcium deposited) to dark yellow depending on the amount of calcium deposited.

4.1.15 RNA isolation and cDNA synthesis for RT qPCR microarray

Scaffolds were washed once with PBS and total RNA was extracted using the Qiagen RNase Mini Kit (Qiagen, UK) following the manufacturers protocols. Briefly, cells were lysed using the lysis buffer containing an RNase inhibitor. Then 70% EtOH was added to the lysate and the mixture was added to a column with selective RNA binding. The RNA was purified using two buffers (RW1 and RPE) and RNA was eluted in 20 μ L of RNase free water. Concentrations were then determined using a NanoDrop spectrophotometer (ThermoScientific, UK).

Reverse transcription was applied using 5 μ g total RNA to obtain cDNA using the QuantiTect Reverse Transcription Kit (Qiagen, UK) according to manufacturers instructions for real time-quantitative PCR arrays. Genomic DNA (gDNA) was eliminated from RNA samples by incubating in gDNA Wipeout buffer for 2 minutes at 42 °C. Samples were then placed in ice and the reverse-transcription master mix which consists of Quatiscript Reverse Transcriptase, Quantiscript RT Buffer and RT Primer Mix (mixture of oligo-dT and random primers) was added to each sample. The reactions were incubated for 15 minutes at 42 °C and 3 minutes at 95 °C for cDNA synthesis and inactivation of enzyme respectively.

(qPCR microarray was carried out by Dr. Engler and Somyot Chirasatitsin at UCSD)

A customised Low density Taqman array (Applied Biosystems; for genes, see Appendix) was used to detect gene expression analysed by the relative quantification $2^{-\Delta\Delta CT}$ method. Gene expression was expressed as a fold change of the cells cultured in each foam composition versus those undifferentiated cells maintained on tissue culture plastic plates.

4.1.16 Statistical analysis

All experiments were performed three times with three samples per condition (n=9). Analysis of variance (ANOVA) followed by a Tukey's post-hoc test was performed as indicated to determine significant differences between more than two sample means (e.g. the 5 combinations of PS-PAA/PS-PEO foams). An unpaired Students t-test was performed to test for significance between two sample means.

Wilcoxon rank-sum tests were performed to assess significant differences between sample means for gene expression data. The significant difference in fold change plotted in volcano graphs was evaluated by the student t-test comparing the group with the control treatment.

All values are shown as mean \pm standard deviation. Significance was defined as p-value of less than 0.05 except for volcano plots where the significant differences were determined to be at p-values of less than 0.1.

All micrographs are representative of at least 3 replications for each sample condition.

4.2 Electrospinning

4.2.1 Preparation and characterisation of electrospun fibres

All block copolymers used in this study (listed in table 4.2) were synthesised by Dr. Efrosyni Themistou, The University of Sheffield by RAFT and ROP according to recently published methodologies¹⁰ (Further work has been submitted to Macromolecular Rapid Communications). Poly(D,L-Lactic acid) (PDLLA) with a molecular weight of 300 kDa was purchased from Polysciences Inc. and used without further purification. Chloroform (CHCl₃), Methanol (MeOH) and N,N-dimethylformamide (DMF) were purchased from Sigma Aldrich and used as received.

Table 4.2-1. Amphiphilic block copolymers utilised for electrospinning

Block copolymer	Molecular weight /g mol ⁻¹	PDI	Chemical structure
PLA ₂₅ -PMPC ₂₅	11360	1.43	
PLA ₂₆ -PDMA ₂₅	8060	1.34	
PLA ₂₉ -POEGMA ₂₉	17700	1.32	
PLA ₁₁₄ -PEG ₁₁₃	26500	1.1-1.3	

4.2.1.1 Optimisation of fibre morphology and wettability

The objectives of this optimisation was to standardise electrospinning parameters to obtain consistent results with respect to fibre morphology and functionality. Fibres were prepared as follows; 1.9 μ moles of copolymer (3-6 wt/wt % of the solution depending on the molecular weight) was added to 100 mg of PDLLA (10 wt/v%) homopolymer in 1 ml solutions of 3:1 CHCl_3 :DMF. Solutions with PMPC-PLA were prepared in 3:1 CHCl_3 :MeOH given that the PMPC block is most soluble in alcohols or alcohol mixtures. PDLLA homopolymer controls were electrospun in 3:1 CHCl_3 :DMF at a concentration of 10 wt/v% . Viscous solutions of 1ml were electrospun using a homemade rig with a rotating collector covered with an aluminium foil. The tip to needle distance was maintained at 15 cm while the voltage used was 20 kV. The solution was ejected at a rate of 1ml/hr and in all cases random non-woven mats were collected. Fibre morphologies were characterised by electron microscopy using previously described sample preparation methods. A random selection of 100 fibres was measured for diameters using Image J software. Initial data shown in figure 4.2-1 indicated a significantly smaller fibre diameters when block copolymers were employed. This maybe a result of a lower surface tension resulting from the segregation of the copolymer at the solid (fibre) air interface. This was confirmed by the water contact angle measurements (detailed below) showing an increase in wettability with all copolymer-based fibres although measurements for PMPC-PLA and PEG-PLA indicate possible insufficiency of functionalisation. While the addition of a small amount of amphiphilic block copolymer functionalising the surface of the fibres is proof of concept, the fibre diameter must be kept constant across the formulations in order to carry out further investigations such as degradation rates, which are affected by surface area (directly related to fibre diameters) and MSC response to matrix properties.

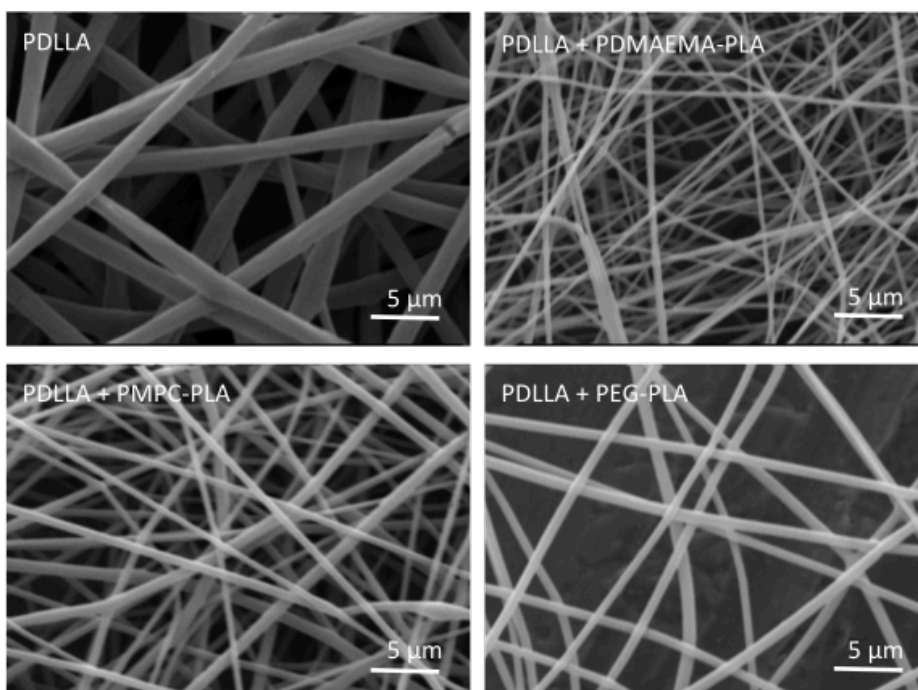


Figure 4.2.1 Electrospun fibre morphologies with block copolymer formulations in a 3:1 CHCl₃:DMF solvent mixture. Data is mean \pm SD.

Table 4.2.2 Average fibre diameter and contact angle measurements of electrospun fibres using 3:1 CHCl₃:DMF mixtures

Composition	Diameter/ μm	Contact angle / $^{\circ}$
PDLLA	1.62 ± 0.24	136 ± 2
PDLLA + PDMA-PLA	0.34 ± 0.04	0
PDLLA + PMPC-PLA	0.53 ± 0.14	70 ± 2
PDLLA +PEG-PLA	0.64 ± 0.28	78 ± 3.5

Electrospinning processing parameters have been shown to tune fibre morphologies as previously discussed. Here, the effects of solution flow rates and solvent mixtures on final fibre morphologies was examined. In all cases, the tip to needle distance was maintained at 15 cm and voltage at 20 kV as before.

Solution flow rates were varied from 1ml/hr, 0.5 ml/hr, 0.25ml/hr and 0.1ml/hr for all formulations. This resulted in a decrease in fibre diameter of PDLLA as the flow rate was decreased but no change was observed for block copolymer formulations (Figure 4.2-2). At 0.1ml/hr flow rates, it was possible to achieve fibre diameters of PDLLA to that of all the copolymer fibres.

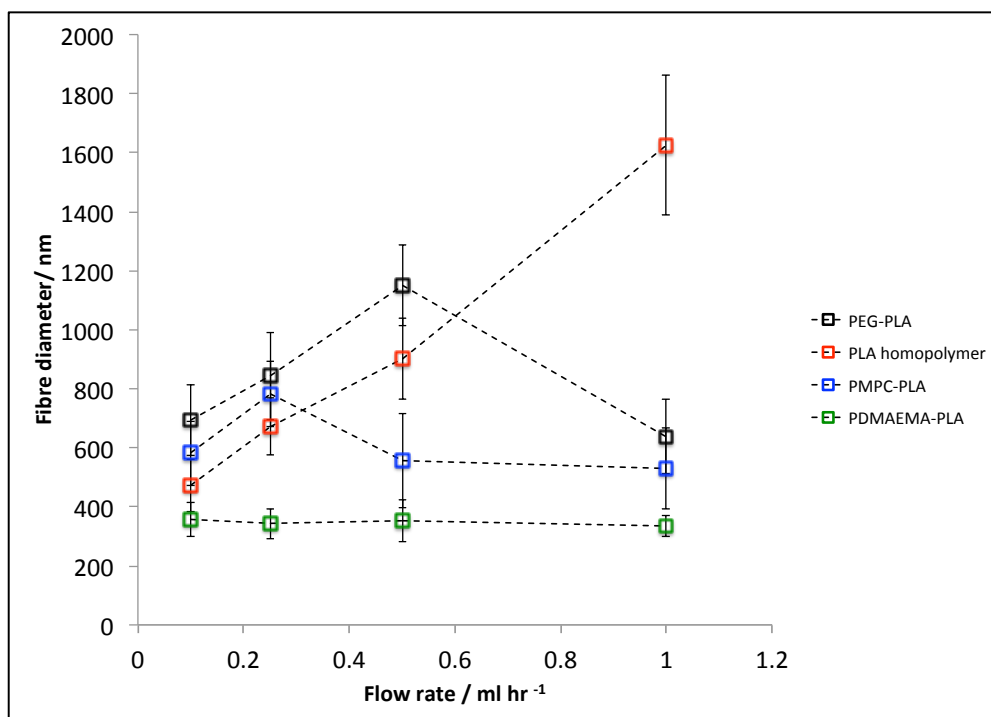


Figure 4.2.2 Effect of flow rates on electrospun fibres using PDLLA and mixtures with block copolymers. Data is mean \pm SD.

Solvent mixtures were also varied to optimise fibre diameters. 2:1 CHCl₃:MeOH solvent mixtures were employed to modify both solution viscosity as well as conductivity (not measured). Additionally, this solvent mixture was used to primarily aid the dissolution of PMPC-PLA as PMPC is soluble only in water, alcohols (ethanol, methanol) and mixtures of CHCl₃:MeOH. Each formulation was repeated three times independently to account for variations in temperature and humidity. These results show that while some variation is present within each fibre mat, fibre diameters remain consistent (ranging from 0.8 - 1.2 μ m) across the various copolymer formulations (Figure 4.2-3). Wettability of electrospun fibres with 2:1 CHCl₃:MeOH were tested (Chapter 7). While wettability was greatly enhanced for fibres containing PMPC-PLA and POEGMA-PLA, wettability was greatly reduced for fibres with PDMA-PLA with a water contact angle of $115^\circ \pm 4^\circ$.

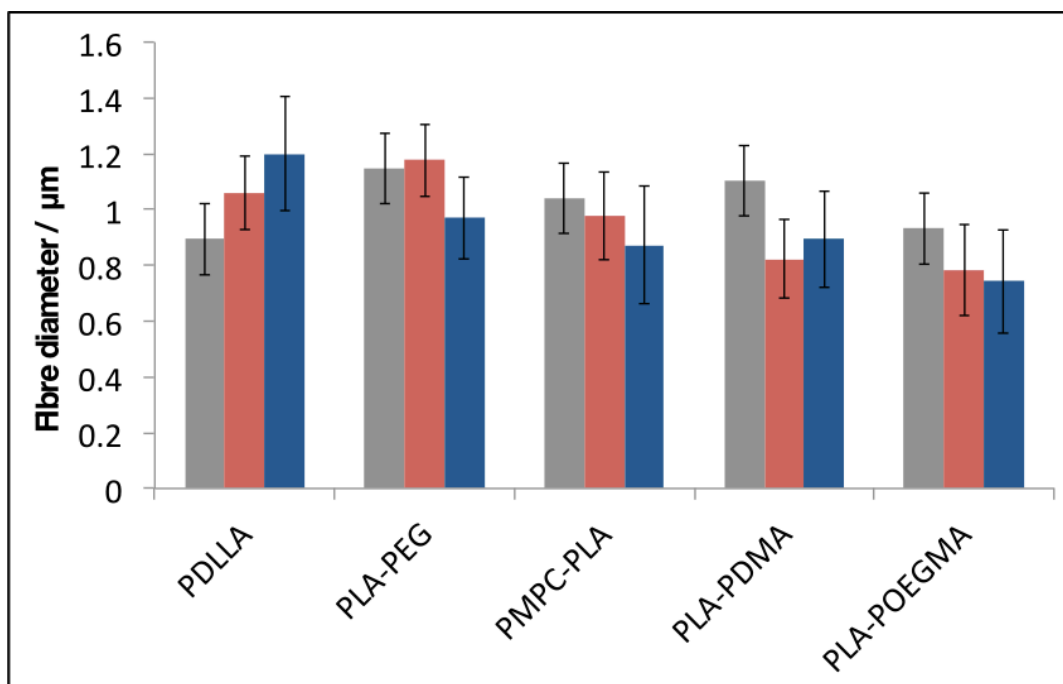


Figure 4.2.3 Optimisation of fibre diameter for each block copolymer formulation using a solvent mixture of 2:1 CHCl_3 :MeOH . Experiments were conducted three independent times to check for consistency. Data is mean \pm SD. n=100 fibres

As a result a solvent mixture of 3:1 CHCl_3 :DMF was herein used for all PDMA-PLA formulations producing fibres with diameters in the range of 0.3-0.5 μm while 2:1 CHCl_3 :MeOH mixtures were employed for all other block copolymer formulations producing functionalised fibres with diameters ranging from 0.8-1.2 μm .

4.2.2 Effect of PLA block length

To study the effect of the hydrophobic block length on the efficiency of surface functionalisation, PDMA-PLA was chosen as an example. PDMA-PLA block lengths and molecular weights are listed in the table below. Processing conditions were maintained as before with tip-needle distance at 15 cm at 20 kV. Resulting fibre diameters were measured using SEM micrographs and water contact angles were measured using milliQ water at pH 7 as well as pH 10 adjusted with 0.1M NaOH to study pH dependent surface wettability.

Table 4.2.2 PDMA-PLA block copolymers with varied PLA block lengths

Block copolymer	Molecular Weight / g mol⁻¹	PDI
PDMA ₂₅ -PLA ₂₆	8,060	1.34
PDMA ₃₀ -PLA ₄₁	11,000	1.37
PDMA ₂₈ -PLA ₄₈	11,700	1.34
PDMA ₂₇ -PLA ₅₈	12,980	1.32
PDMA ₂₅ -PLA ₁₁₅	21,200	1.30
PDMA ₂₄ -PLA ₁₉₅	32,260	1.30

4.2.3 Fibre Degradation

Degradation rates for all copolymer functionalised fibres were investigated and compared to PDLLA fibres with similar morphology. Given that PDLLA/PDMA-PLA fibres could not be effectively optimized for fibre diameter with fibres ranging from 300-500 nm compared to 0.8-1.2 μm for all other fibres under the same electrospinning processing conditions, these fibres were not used to assess their degradation profiles. This is because the effective surface area of PDMA-PLA fibres will be much higher compared to all other formulations leading to a possible higher rate of degradation and hence making results incomparable. Thus to assess PDMA-PLA fibre degradation, PDLLA homopolymer was electrospun at a flow rate of 0.1 ml/hr producing fibre diameters of 410 nm \pm 190 nm. All fibres were first sterilised in 70% cold EtOH and rinsed in cold PBS prior to the degradation study. 10-20 mg of randomly aligned fibre meshes for each formulation was weighed out prior to degradation. Samples were placed in a centrifuge tube under physiological conditions, i.e. in phosphate buffered saline (PBS) and kept in a 37 °C water bath. The PBS was replenished twice a week to maintain physiological pH as PLLA/PDLLA is known to degrade faster in acidic and basic conditions¹¹. At specific time points (day 1, 7, 14, 21 and 28), fibres were washed in deionised water three times and vortexed to ensure removal of all soluble degradation products. Fibres were then dried in vacuum at room temperature for 72 hours and re-weighed to determine mass loss. A total of three measurements for each time point were made to determine an

average mass loss. An extra sample that was washed but not vortexed was imaged for degradation morphologies.

4.2.4 Imaging of protein adsorption

Sterilised fibres of dimensions 1.5 cm x 1.5 cm were treated with 200 μ L of BSA conjugated Alexa Fluor 594 (Molecular Probes, Invitrogen) at a concentration of 100 μ g/ml (in PBS) for 30 minutes and 2 hours. Fibres were then washed thoroughly in PBS three times. Protein adsorption was qualitatively assessed using a Zeiss LSM510 Meta inverted confocal laser scanning microscope using a x25 objective with untreated fibres as the control.

4.2.5 Water contact angles

Contact angles were measured using a Rame-Hart goniometer. 4-5 μ L of MilliQ water at pH 7 or pH 10 adjusted using 0.1M NaOH was placed on 1cm x 1cm mats of electrospun fibres placed on a glass coverslip. A total of 3-4 measurements were made for each fibre composition.

4.2.6 Actin cytoskeleton and nuclear staining of hES-MP cell morphology

Fibres of dimensions 2 cm x 2 cm were first sterilised in cold 70% EtOH and rinsed immediately with 1ml PBS. hES-MPs were cultured and maintained as previously described.

hES-MPs were trypsinised and seeded on to fibres at a density of 2500/cm² of a non-woven fibrous mat (Note: not fibre surface area) Cells were examined for adhesion and morphology 48 hours and 72 hours by fixing them in 3.7% formaldehyde for 20 minutes followed by permeabilisation with 0.1% Triton X for 10 minutes. The actin cytoskeleton was stained with Phalloidin Texas-Red (1:1000, Molecular Probes, UK) and the nucleus was stained with 25 μ l of mounting medium with DAPI (VectorLabs, UK). Cell morphology was visualised using a Zeiss LSM510 Meta inverted confocal laser scanning microscope using a x10 objective.

4.2.7 Preparation of 'patchy' electrospun fibres

Electrospun PDLLA fibres surface-functionalised with mixtures of PLA-POEGMA and PLA-PMPC were prepared as follows. As before 1.9 μ moles of total copolymer in molar ratios (POEGMA:PMPC) of 3:1, 1:1, 1:3 was used. All electrospinning parameters and solvents used were as previously mentioned (section 4.2.1.1)

4.2.8 Synthesis of cross-linked PLA-Diblock Copolymer PLA_{30} - b - $P(OEGMA_{30}$ - $stat$ - $DSDMA_1)$ using a one step ROP-RAFT simultaneous polymerisation. (The synthesis and characterisation of PLA_{30} - b - $P(OEGMA_{30}$ - $stat$ - $DSDMA_1)$ was performed by Dr. Efrosyni Themistou)

The disulfide-based dimethacrylate (DSDMA) branching monomer was synthesised following a previously reported method¹². The protocol used for the simultaneous ROP and RAFT synthetic process yielding the $[LA]_0:[OEGMA]_0:[DSDMA]_0:[ROP$ -RAFT reagent]₀ 30:30:1:1 branched copolymer at 45 wt.% of solvent 1,2-dichloroethane, is described below:

LA (0.20 g, 1.37 mmol), OEGMA (0.62 g, 1.37 mmol), ROP-RAFT reagent (0.02 g, 0.05 mmol), AIBN (1.5 mg, 0.01 mmol), DMAP (0.02 g, 0.18 mmol) and 0.57 mL of 1,2-dichloroethane were added in a 5 mL round bottom flask equipped with a magnetic stirring bar and sealed with a rubber septum. The reaction mixture was purged with nitrogen for 20 min and placed in an oil bath at 74°C for 24 h, resulting in the formation of a very viscous (gel-like) polymer solution. The solution was characterised by gel permeation chromatography (GPC) (DMF).

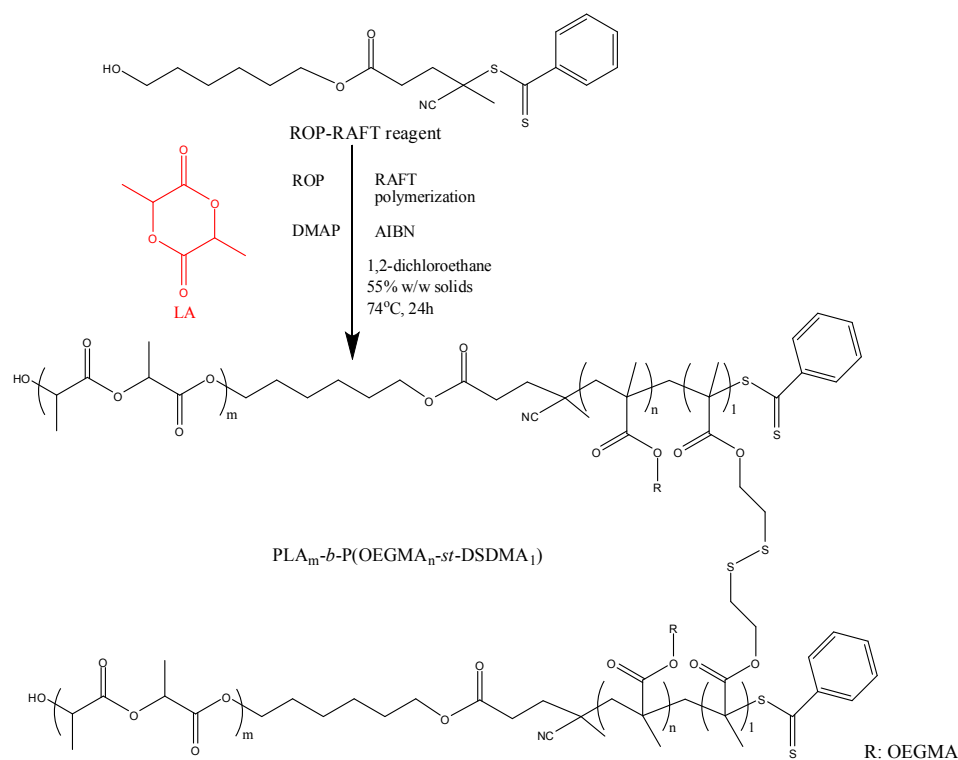


Figure 4.2.4 Schematic of synthesis of cross-linked PLA-Diblock Copolymer PLA₃₀-b-P(OEGMA₃₀-stat-DSDMA₁)

4.2.9 Disulphide Cleavage and Functionalization of the PLA-b-POEGMA Block Copolymer with Divinyl Sulfone

500 mg (275 mg solids content) of the PLA₃₀-b-P(OEGMA₃₀-stat-DSDMA₁) polymer network were placed in a 50 mL round bottom flask equipped with a magnetic stirring bar and sealed with a rubber septum containing 20 mL DMF (0.55% w/v). The mixture was purged with nitrogen for 20 min and placed in an oil bath at 30°C. In order for the disulfide cleavage to occur, allowing the conversion of 1 unit of DSDMA to 2 units of 2-thioethylmethacrylate (TEMA), a solution of Bu₃P (91.9 μmol, 18.6 mg, 3.0 eq. relative to the DSDMA disulfide bond) and Et₃N (64.3 μmol, 6.5 mg, 2.1 eq. relative to the DSDMA disulfide bond) in 5mL DMF was added under a nitrogen atmosphere via a syringe to the round bottom flask. The reaction was allowed to proceed for 2 h at 30°C to afford a thiol-functionalised linear PLA₃₀-b-P(OEGMA₃₀-stat-TEMA₂) block copolymer solution. A sample was extracted from the reaction flask for GPC analysis before a degassed solution of divinyl sulfone (0.92 mmol, 108.6 mg, 15 eq. relative to the thiol -SH group) in 5mL DMF was added. The resulting mixture was stirred at 30°C for 15 h. The final

solution was dialysed (MWCO 1000 Da), against acetone (5 times / 3 days). The solvent was removed (rotary evaporator followed by vacuum oven) and the dried polymer was characterised by GPC.

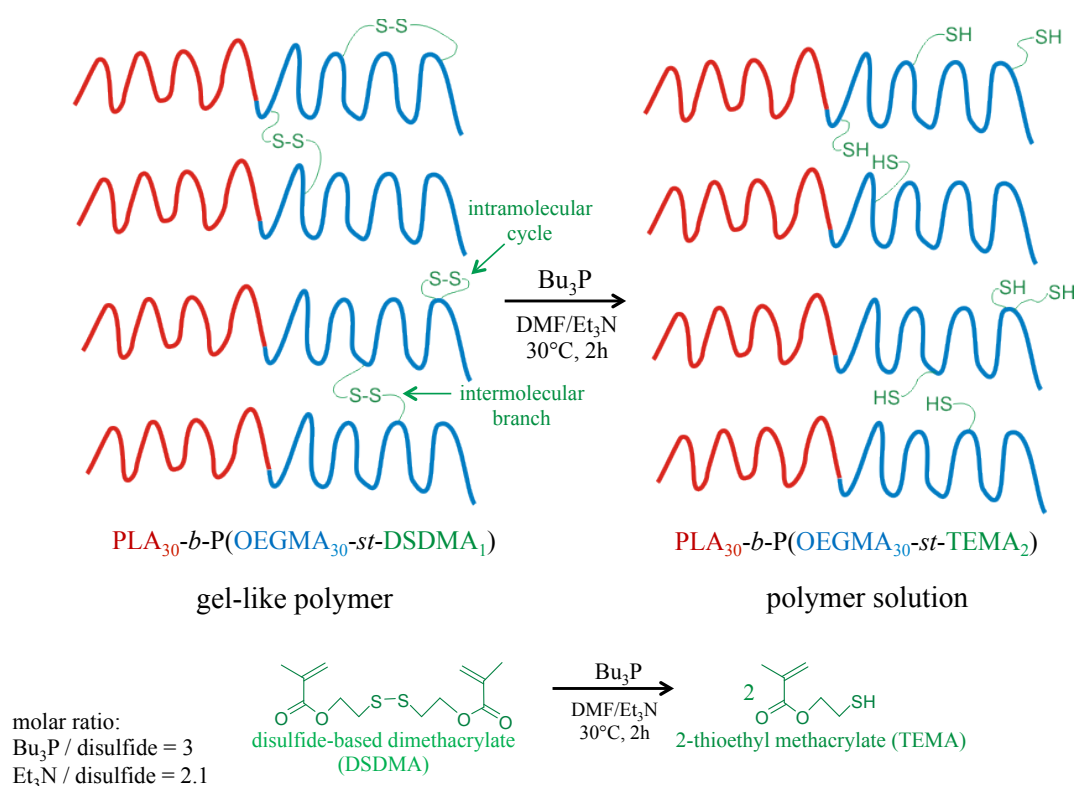


Figure 4.2.5 Disulphide Cleavage and Functionalisation of the PLA-*b*-POEGMA Block Copolymer with Divinyl Sulfone for RGD conjugation.

4.2.10 Polymer Characterisation

The molecular weight distributions of the cross-linked PLA₃₀-*b*-P(OEGMA₃₀-*stat*-DSDMA₁) block copolymer, its cleavage product and the resulting functionalized polymer were assessed by DMF gel permeation chromatography (GPC). The system contained two Polymer Laboratories PL gel 5 μm mixed C columns and one PL polar gel 5 μm guard column arranged in series and maintained at 60 °C, followed by a Varian 390 LC refractive index (RI) detector. The eluent (DMF) containing 10 mM LiBr was kept at a flow rate of 1.0 mL min⁻¹. Ten near monodisperse poly(methyl methacrylate) standards with MWs ranging from 625 g mol⁻¹ to 618 000 g mol⁻¹ were used for calibration. ¹HNMR spectra were acquired using either a 250 or 400 MHz Bruker spectrometer using the appropriate NMR solvent for each block copolymer.

4.2.11 Conjugation of linear RGDC to the POEGMA block

Linear RGDC and scrambled DRGC peptides with a terminal cysteine residue (Pepceuticals, UK) were conjugated to the thiol-functionalised PLA-POEGMA block post electrospinning. Fibrous mats of dimensions 2 cm x 2 cm were cut and placed in 6-well plates. A solution of the RGD (or scrambled) peptide (0.36 mg/ 8mL PBS) was added to a solution of tris (2-carboxyethyl) phosphine (TCEP) (0.2 mg/ 80 mL) in equi-volume ratios. This solution was purged with N₂ gas for 30 minutes and 2 mL was added to each well. The well plates were covered with parafilm and the solution covering each fibrous mat was purged with N₂ gas for a further 10 minutes and left covered at room temperature on a plate rocker for 4 hours for conjugation. The fibres were washed extensively in cold PBS three times. Fibres were sterilised with cold 70% EtOH and air dried prior to cell seeding. This procedure was repeated for all copolymer mixtures with PLA-PMPC and PLA-POEGMA, rendering the POEGMA block cell adhesive and the PMPC block cell inert. To confirm RGD conjugation, hES-MPs were cultured on POEGMA100 functionalised fibres that were conjugated with both RGDC and a scrambled sequence DRGC for a period of 24 hours and cell attachment was assessed by confocal microscopy (Figure 4.2.6).

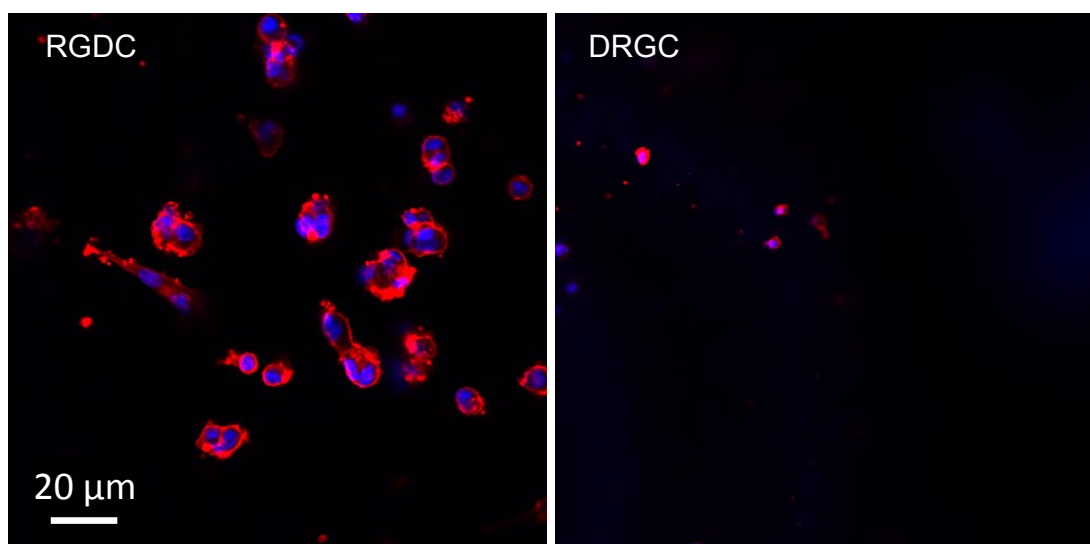


Figure 4.2.6 hES-MPs cultured on POEGMA100 functionalised fibres conjugated with RGDC and GRDC after 24 hours. Nucleus is stained in Blue (DAPI). Cytoskeleton is stained in red (Phalloidin Texas-Red).

4.3 References

1. Fernyhough, C., Ryan, A. J. & Battaglia, G. pH controlled assembly of a polybutadiene–poly(methacrylic acid) copolymer in water: packing considerations and kinetic limitations. *Soft Matter* **5**, 1674 (2009).
2. Zhao, C., Danish, E., Cameron, N. R. & Kataky, R. Emulsion-templated porous materials (PolyHIPEs) for selective ion and molecular recognition and transport: applications in electrochemical sensing. *J. Mater. Chem.* **17**, 2446 (2007).
3. Chen, Y., Ballard, N., Gayet, F. & Bon, S. A. F. High internal phase emulsion gels (HIPE-gels) from polymer dispersions reinforced with quadruple hydrogen bond functionality. *Chem. Commun.* **48**, 1117 (2012).
4. Christenson, E. M., Soofi, W., Holm, J. L., Cameron, N. R. & Mikos, A. G. Biodegradable Fumarate-Based PolyHIPEs as Tissue Engineering Scaffolds. *Biomacromolecules* **8**, 3806–3814 (2007).
5. Chirasatitsin, S. & Engler, A. J. Detecting cell-adhesive sites in extracellular matrix using force spectroscopy mapping. *J. Phys.: Condens. Matter* **22**, 194102 (2010).
6. Mao, Y. & Schwarzbauer, J. E. Stimulatory effects of a three-dimensional microenvironment on cell-mediated fibronectin fibrillogenesis. *J. Cell Sci.* **118**, 4427–4436 (2005).
7. Engler, A. J., Chan, M., Boettiger, D. & Schwarzbauer, J. E. A novel mode of cell detachment from fibrillar fibronectin matrix under shear. *J. Cell Sci.* **122**, 1647–1653 (2009).
8. Karlsson, C. *et al.* Human embryonic stem cell-derived mesenchymal progenitors—Potential in regenerative medicine. *Stem Cell Res.* **3**, 39–50 (2009).
9. de Peppo, G. M. *et al.* Osteogenic Potential of Human Mesenchymal Stem Cells and Human Embryonic Stem Cell-Derived Mesodermal Progenitors: A Tissue Engineering Perspective. *Tissue Eng. Part A* **16**, 3413–3426 (2010).
10. Oh, J. K. Polylactide (PLA)-based amphiphilic block copolymers: synthesis, self-assembly, and biomedical applications. *Soft Matter* **7**, 5096 (2011).
11. Burkersroda, von, F., Schedl, L. & Gopferich, A. Why degradable polymers undergo surface erosion or bulk erosion. *Biomaterials* **23**, 4221–4231 (2002).
12. Rosselgong, J. & Armes, S. P. Quantification of Intramolecular Cyclization in Branched Copolymers by ¹H NMR Spectroscopy. *Macromolecules* **45**, 2731–2737 (2012).

Chapter 5: Preparation and Characterisation of Porous polyHIPEs

This chapter is under review for publication as:

3D Surface Functionalization of Emulsion-Templated Polymeric Foams
ACS Applied Materials & Interfaces, in review

5.1 Introduction

Controlling the architecture of polyHIPE foams is important for applications in 3D cell culture where highly porous matrices are required for cell infiltration, proliferation, vascularisation and nutrient exchange¹. For example, tissue engineered (TE) constructs or scaffolds for bone tissue engineering often require the right mechanical properties to withstand the physiological load² and restore tissue function. Moreover, tissues such as bone have a hierarchical structure ranging from the micro to the nanometer length scales³ (Figure 5.1a). They also consist irregular geometries, such as trabecular bone as shown in Figure 5.1b,c^{4,5}. PolyHIPE foams are already used in 3D cell culture applications^{6,7} as inert substrates as well as potential injectable bone grafts⁸. They have been previously tailored to display void diameters ranging from 1 μ m - 100 μ m with compressive moduli ranging from 2 - 60 MPa^{9,10}. For *in vitro* studies however, the use of ECM proteins such as fibronectin or laminin¹¹ to coat the surface of the 3D foam is often necessary to mimic the cells natural environment to obtain optimum cellular viability and proliferation. Moreover given the importance of physicochemical properties of the underlying matrix in influencing cellular behaviour, the surface functionalisation of such foams is important. Yet, there are only few studies that explore control over surface chemistry which remains a challenge as the most often studied polyHIPE matrices of polystyrene/divinylbenzene are hydrophobic.

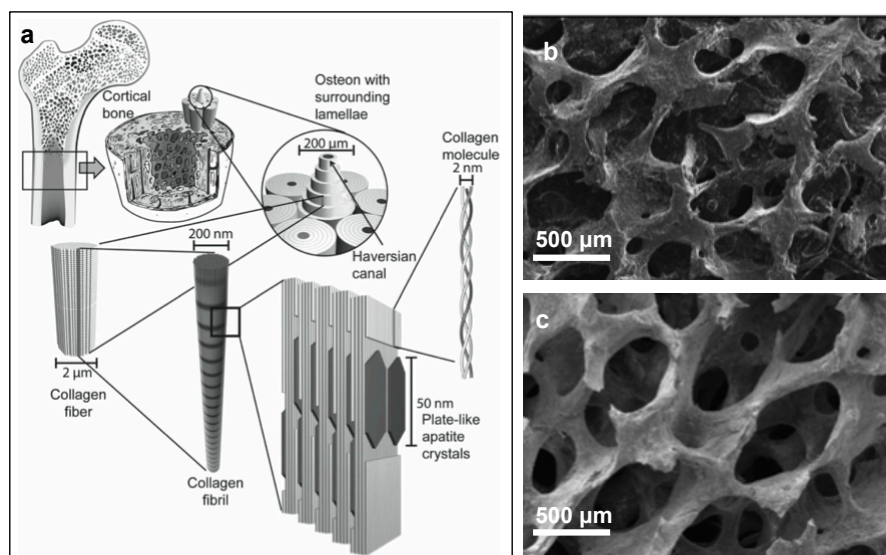


Figure 5.1. Hierarchical organisation of bone a). Scanning electron micrographs showing the highly porous nature of human trabecular bone. Images reproduced from refs 3-5.

Surface chemistry has shown to be modulated post polymerisation, using techniques such as plasma polymerisation¹². However, this approach is limited by depth penetration, with only the top layers of the foam effectively functionalised. Other methods involve polymer grafting using Huigsen type ‘click’ chemistry¹³ or photo-polymerised polyHIPEs incorporating thiolene- or acrylate- functional groups in the organic phase¹⁴. However, in many of these cases, a multi-step process is required which often lacks control and efficiency of surface functionalisation in 3D. More recent advances have shown that ‘inverse’ oil-in-water HIPEs using acrylic acid¹⁵ as the aqueous phase monomer can be used to prepare hydrophilic foams. Alternatively the introduction of hydrophilic monomers such as poly(ethylene glycol) methacrylate in water-in-oil emulsions¹⁶ have been investigated although such foams are often unstable due to the presence of a hydrophilic monomer in the oil phase. Silverstein and co-workers have shown that w/o HIPEs using t-butyl acrylate as the monomer, resulted in hydrophobic matrices that were subsequently hydrolysed to produce hydrophilic foams¹⁷. Surfactant free HIPEs, also known as Pickering HIPEs that utilises colloidal nanoparticles to stabilise the oil-water interface have also been synthesised. For example, PMMA nanoparticles trapped at the oil-water interface upon polymerisation may offer a new method to establish surface topography and functionality in 3D¹⁸.

Advances in controlled living polymerisation techniques as well as the wide range of chemistries available allows for the precise design of polymeric surfactants at the synthesis level¹⁹. Due to their intrinsic macromolecular nature, amphiphilic block copolymers have the potential to allow higher interfacial rigidity, resulting in more stable emulsions with a higher efficiency than that of traditional low molecular weight surfactants. Amphiphilic block copolymers have been used widely as emulsion stabilisers with few examples in high internal phase emulsions. For example, poly(ethylene oxide)-polybutadiene (PEO-PBO) copolymers have been previously employed in water-in-oil HIPEs by Jakob *et al.* who demonstrated that the macromolecular nature of block copolymer surfactants allows for enhanced emulsion stability²⁰. The long copolymer chains can extend further into adjacent sub-phases than their low molecular weight counterparts²¹. Additionally anionic block copolymer surfactants possess charged head groups that repel each other²⁰ thereby preventing droplet coalescence and catastrophic emulsion failure. More recently, the use of the commercially available triblock copolymer Pluronic F127 (PEO₁₀₁-PPO₅₆-PEO₁₀₁) was used to produce poly(glycidyl methacrylate) polyHIPEs with high surface areas for protein separation applications²². However, to date, the effect of the block copolymer surfactants in 3D surface functionalisation has never been reported.

In chapters 5 and 6 the parameters of emulsion preparation required to produce porous foams are investigated. Porous polyHIPEs (styrene/divinylbenzene) from water-in-oil emulsions are surface functionalised using amphiphilic block copolymer surfactants. This method introduces surface functionality in a one-step process with the desired physical and chemical properties for *in vitro* 3D cell culture applications. Finally, the phase separation of two block copolymer surfactants confined at the oil-water interface upon polymerisation to generate discrete ‘patches’ of cell adhesion sites is demonstrated herein.

5.2 Methods

All foams were prepared using water-in-oil high internal phase emulsions using four different amphiphilic block copolymer surfactants; PBD-PEO, PS-PEO, PBD-PAA and PS-PAA. polyHIPEs were also prepared using an A-B-A triblock copolymer PS-PAA-PS. The effects of surfactant concentration, shear rate, type of initiator and aqueous phase volume fraction on foam morphology were determined by scanning electron microscopy and image analysis. Finally, foam functionality was assessed by XPS and wettability studies (Detailed materials and methods in Chapter 4).

5.3 Results and discussion

5.3.1 Oil-soluble versus water-soluble initiator effects

The hydrophilic-lipophilic balance (HLB) is often considered when choosing the appropriate surfactant and was used in this work as an indicator of effectiveness of block copolymer surfactants. The empirical formula originally defined by Griffin²³ as $20 \times (M_h / M_w)$; where M_h is the molecular weight of the hydrophilic block and M_w is the molecular weight of the surfactant and is based on non-ionic surfactants. As a general rule of thumb, an HLB value between 2-6 is required for the stabilisation of w/o emulsions. Here, polystyrene-*b*-poly(ethylene oxide) (PS-PEO), poly(1,4-butadiene)-*b*-poly(ethylene oxide) (PBD-PEO) poly(1,4-butadiene)-*b*-poly(acrylic acid) (PBD-PAA) and polystyrene-*b*-poly(acrylic acid)(PS-PAA) with various HLB values (see materials and methods) was employed as surfactants for water-in-oil emulsions and result in highly porous and interconnected 3D polystyrene/divinylbenzene foams. The synthesis of polyHIPEs using the A-B-A triblock copolymer surfactant PS-PAA-PS was also studied. This chapter further discusses the relevance of HLB values when using macromolecular surfactants and how emulsion parameters such as the aqueous phase volume fraction and shear rates can be employed to fine-tune the final architecture of polyHIPE foams.

HIPEs synthesised in this work is limited to one specific copolymer concentration (0.01 mole%; see materials and methods for further details), unless otherwise stated. Traditionally, water-soluble initiators such as $K_2S_2O_8$ have been used in conjunction with low molecular weight surfactants such as Span 80 to produce porous polyHIPEs (as discussed in Chapter 3). However, in the present studies, it was observed that the

choice of initiator strongly affected the open porosity and interconnectivity of the foams. Moreover, the choice of initiator was found to be the dominant parameter in controlling the final desired morphology of the foams. In contrast to previous work, the oil-soluble initiator, AIBN was the more appropriate choice because it resulted in the formation of interconnecting pores within foams for all block copolymer surfactants utilised (Figures 5.2a-d and 5.3a-d). High magnification scanning electron micrographs shown in Figure 5.2 e-h and 5.3e-h clearly show the closed- and open-porous nature of the foams respectively.

The exception was PS-PAA where interconnecting holes appeared at 90% aqueous phase volume and at high shear (Figure 5.4). In this case, droplet coalescence and an increase in average void diameter was seen suggesting the formation of an unstable emulsion but polymerisation of the matrix, prevented macroscopic phase separation. In contrast, formation of interconnecting pores was seen with all block copolymers used, when the oil-soluble initiator AIBN was employed and was independent of surfactant concentration, shear rate, aqueous phase volume or even the HLB of the copolymer. Furthermore, initiator dependent open porosity is not observed, with low molecular weight amphiphiles such as Span 80 for styrene/divinylbenzene based foams according to published literature.

Seminal work by Williams *et al.*^{24,25} explored the effects of water and oil soluble initiators and found that the water soluble initiator $K_2S_2O_8$ resulted in mechanically stiffer foams with void sizes an order of magnitude lower than foams prepared with AIBN owing to electrolyte stability of the oil-water interface (which holds true for the case of non-ionic surfactants). As such, $K_2S_2O_8$ has been the primary choice of initiator for water-in-oil emulsions over oil soluble ones, though open porous foams may be formed with both initiator types.

The formation of interconnecting pores using styrene/divinylbenzene/Span80/ $K_2S_2O_8$ formulations has been studied and show that interconnectivity arises at the gel point of the emulsion²⁶. It was shown that interconnectivity was due to the thinning of the

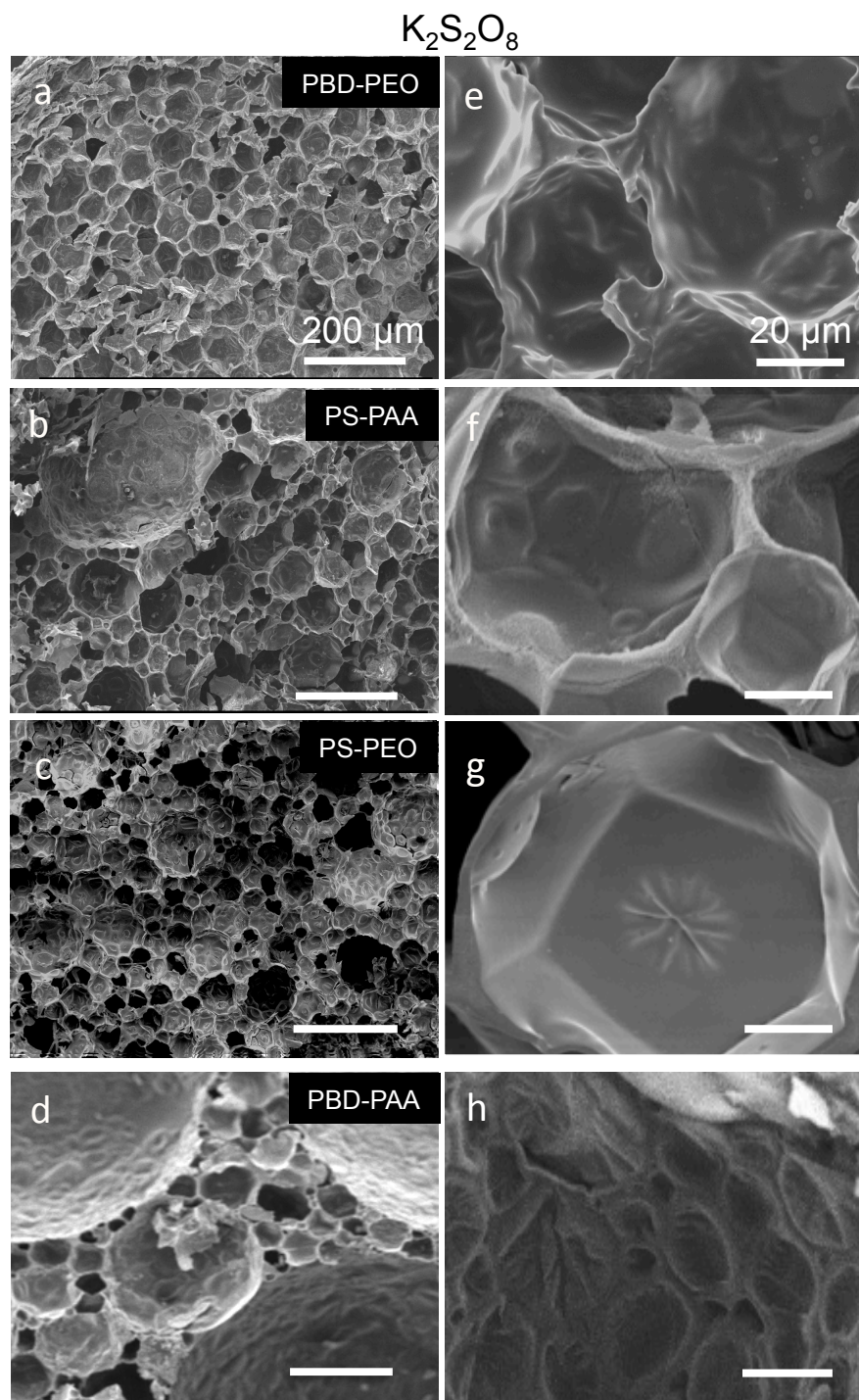


Figure 5.2 Morphologies of polyHIPEs using the block copolymer surfactants a) and e) poly(1,4-butadiene)-b-poly(ethylene oxide), b) and f) polystyrene-b-poly(acrylic acid), c) and g) polystyrene-b-poly(ethylene oxide), d) and h) poly(1,4-butadiene)-b-poly(acrylic acid). Scanning electron micrographs of the foams prepared with the initiator $K_2S_2O_8$. Emulsions were produced at low shear and an aqueous phase volume fraction, Φ_w , of 0.9 apart from those functionalised with PS-PEO where $\Phi_w = 0.8$. Scale bars in the left column represent 200 μm . Scale bars in the right column represent 20 μm .

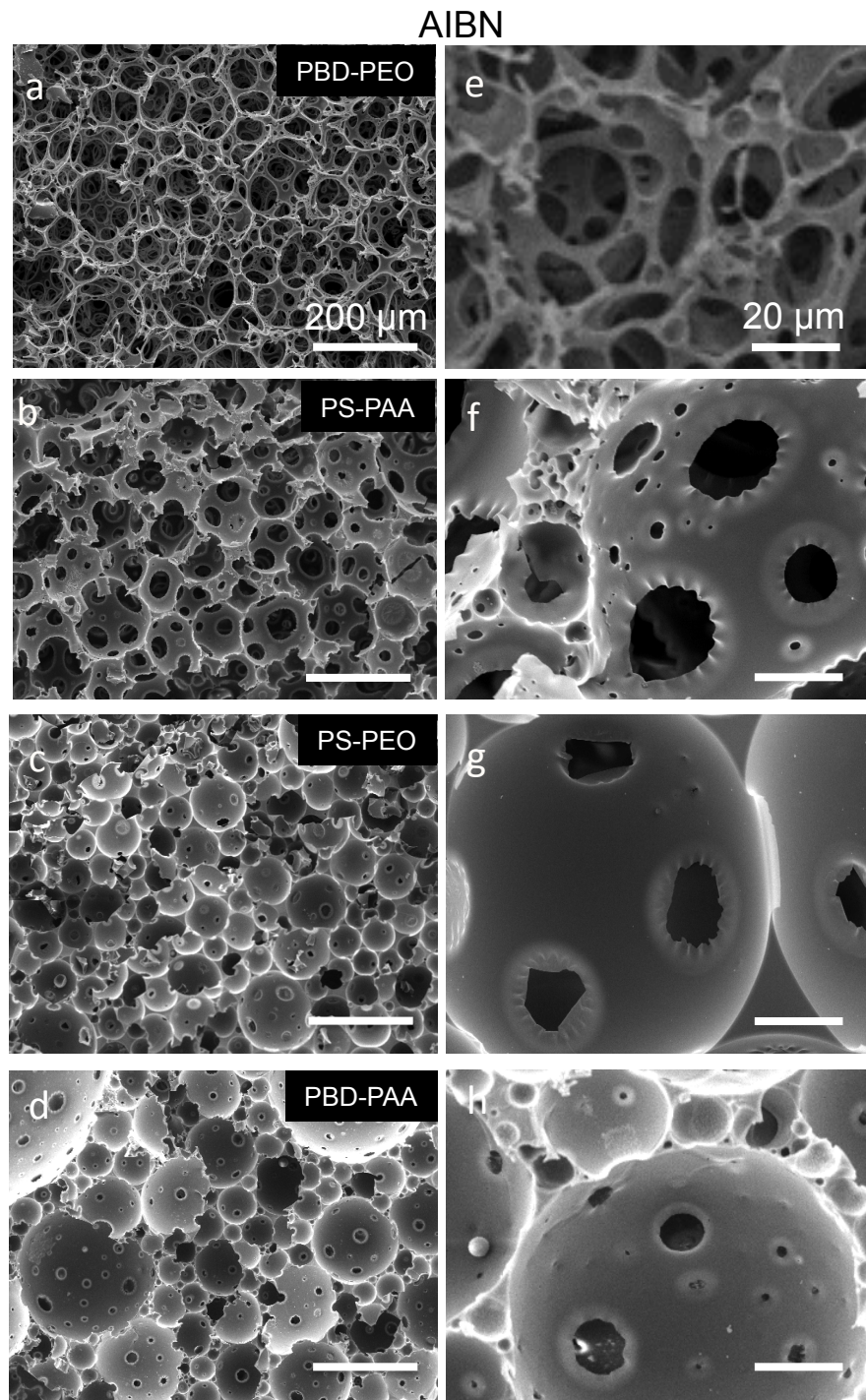


Figure 5.3 Morphologies of polyHIPEs using the block copolymer surfactants a) and e) poly(1,4-butadiene)-b-poly(ethylene oxide), b) and f) polystyrene-b-poly(acrylic acid), c) and g) polystyrene-b-poly(ethylene oxide), d) and h) poly(1,4-butadiene)-b-poly(acrylic acid). Scanning electron micrographs of the foams prepared with the initiator AIBN. Low magnification micrographs and high magnification (e-h) showing open-porous foam structures. Emulsions were produced at low shear with an aqueous phase volume fraction, Φ_w , of 0.9 apart from those functionalised with PS-PEO where $\Phi_w = 0.8$. Scale bars in the left column represent 200 μm . Scale bars in the right column represent 20 μm .

oil film between droplets that rupture upon conversion of monomer to polymer (as a result of increase in density). This phenomenon on the other hand was not observed with block copolymer surfactants in the present study when $K_2S_2O_8$ was used as the initiator, which resulted in foams with closed porosity (Figure 5.2). Recent studies by Silverstein and co-workers have also investigated the effects of oil- and aqueous-phase initiation on the final foam morphology and interconnectivity^{18,27}. They observed that for Pickering polyHIPEs stabilised with either PMMA¹⁸ or silica nanoparticles²⁷, greatly affected the final foam morphology. While aqueous phase initiation (using $K_2S_2O_8$) resulted in closed-porous foams, oil phase initiation using benzoyl peroxide resulted in foams with open, interconnected morphologies.

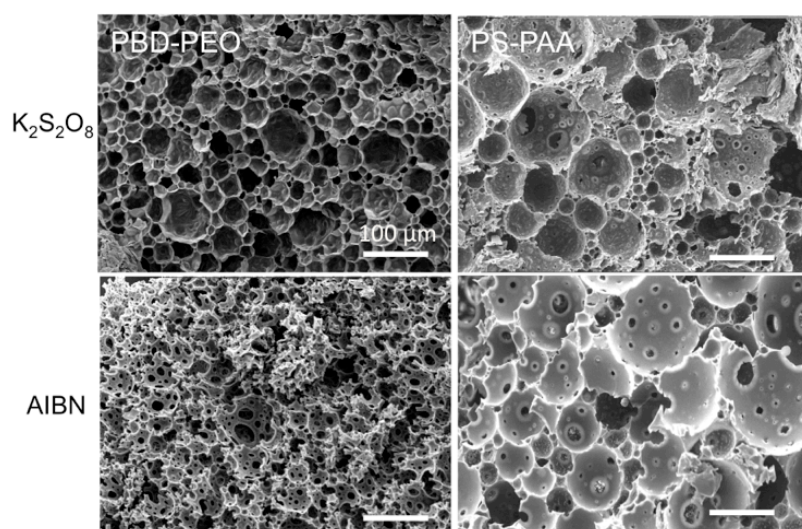


Figure 5.4 polyHIPE foams using PBD-PEO and PS-PAA block copolymers at high shear (11500 rpm). Aqueous phase volume was maintained at 90% and surfactant concentration was 0.01mole% relative to the monomers. Note: Emulsions with PBD-PAA and PS-PEO formed inverse oil-in-water emulsions at high shear. Scale bars represent 100 μm

To further evaluate porosity and interconnectivity, mercury intrusion porosimetry analysis was performed on all foam samples. All foams initiated with AIBN exhibited porosities of 90% apart from PBD-PAA, which exhibited a porosity of 65%. Average interconnect diameters plotted for all foams ranged from 5.8 – 11.9 μm (Figure 5.5 bottom, Table 5.1), indicating a high level of porosity. Closed-porous foams using $K_2S_2O_8$ initiation, on the other hand, showed little interconnectivity of the foams, in particular for PS-PEO and PBD-PEO samples that exhibited porosities of 72 % and 74% respectively with interconnect diameters $< 0.35 \mu\text{m}$ (Figure 5.5 top, Table 5.2). Foams of PBD-PAA and PS-PAA showed higher porosities but low interconnectivity remained with interconnect diameters of 1.19 μm and 1.71 μm for

PBD-PAA and PS-PAA respectively (Figure 5.5 bottom, Table 5.1). What these data demonstrate is the lack of appreciable porosity within foams where aqueous phase initiation was used. On the other hand, for foams made with oil phase initiation, interconnectivity between pores is clearly evident and is supported by the scanning electron micrographs.

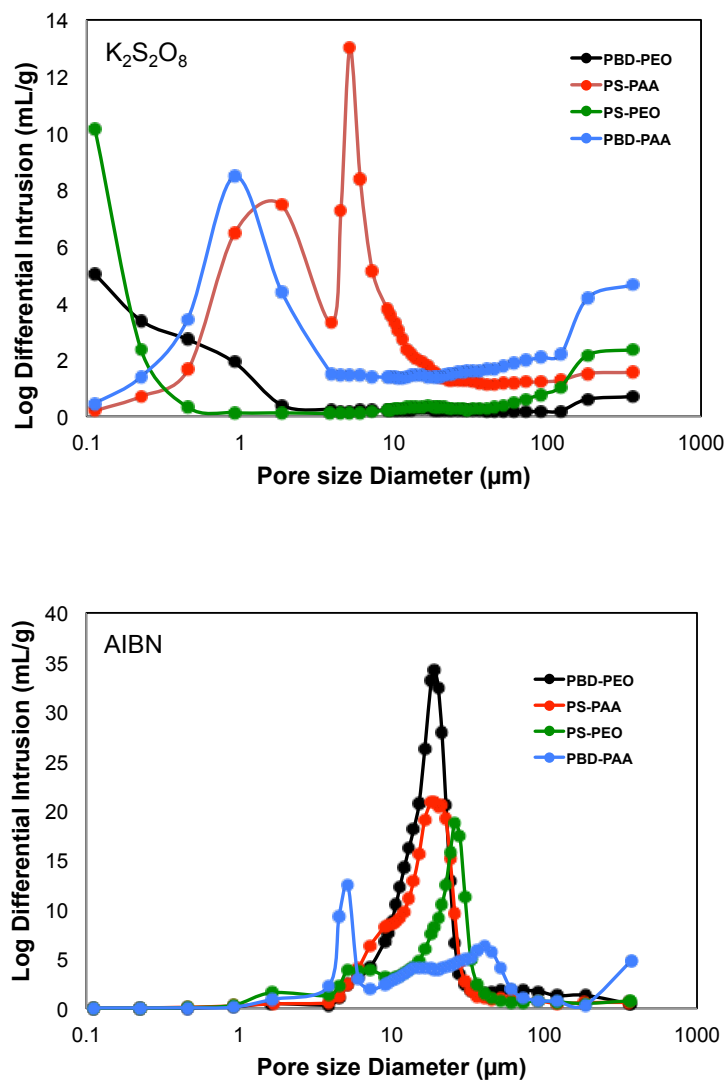


Figure 5.5 Mercury intrusion plots indicating interconnect diameters for all block copolymer foams using both aqueous and oil phase initiation. Data provided by Dr. David Johnson, The University of Durham.

Table 5.1 Porosity measurements for AIBN initiated foams.

AIBN

Sample	Total intrusion volume (mL/g)	Average interconnect diameter (μm) ^c	Porosity %
PBD-PEO	12.2	11.9	92
PS-PAA	9.7	9.3	92
PS-PEO	8.0	6.5	89
PBD-PAA	7.7	5.8	65

Table 5.2 Porosity measurements for $\text{K}_2\text{S}_2\text{O}_8$ foams $\text{K}_2\text{S}_2\text{O}_8$

Sample	Total intrusion volume (mL/g)	Average interconnect diameter (μm) ^c	Porosity %
PBD-PEO	3.91	0.34	74
PS-PAA	11.09	1.71	91
PS-PEO	4.11	0.30	72
PBD-PAA	11.1	1.19	89

5.3.2 Concentration Effects

Surfactant concentration has shown to be one of the most important parameters in tuning porosity and interconnectivity of polyHIPE foams. It has been shown that as surfactant concentration of an emulsion is increased, interfacial tension is decreased, resulting in a smaller void size distribution^{28,29}. As previously described, the ‘thinning’ of the oil phase results in the appearance of interconnecting pores²⁶. This effect is enhanced with increasing surfactant concentration to produce larger interconnecting pores resulting in an overall increase in the ratio between voids:interconnects and leads to greater interconnectivity and ‘open porosity’ of the foams. The effect of concentration was therefore examined in order to determine if varying surfactant concentration would affect open versus closed porosity in block copolymer stabilised emulsions. An ionic (PS-PAA) and a non-ionic (PDB-PEO) surfactant with similar molecular weights were chosen with an aqueous phase volume fraction of 0.9 and a shear rate of 750 rpm. With both surfactants, the concentration were varied from 0.02 mol% until eventual emulsion phase separation occurred. In all cases, regardless of surfactant type or initiator, average void

diameters were slightly lower with increasing surfactant concentration. The highest copolymer concentration yielded the lowest average void diameters ($45.4 \mu\text{m} \pm 18.3 \mu\text{m}$, $41.8 \mu\text{m} \pm 13.2 \mu\text{m}$ for PS-PAA and $18.9 \mu\text{m} \pm 5.3 \mu\text{m}$, $21.3 \pm 6.1 \mu\text{m}$ for PBD-PEO) than all other concentrations (Figure 5.7). At the lowest copolymer concentrations the void diameter distribution also displayed a broad polydispersity, particularly for PS-PAA. This is probable as insufficient surfactant leads to higher surface tensions and increase in the rate of droplet coalescence.

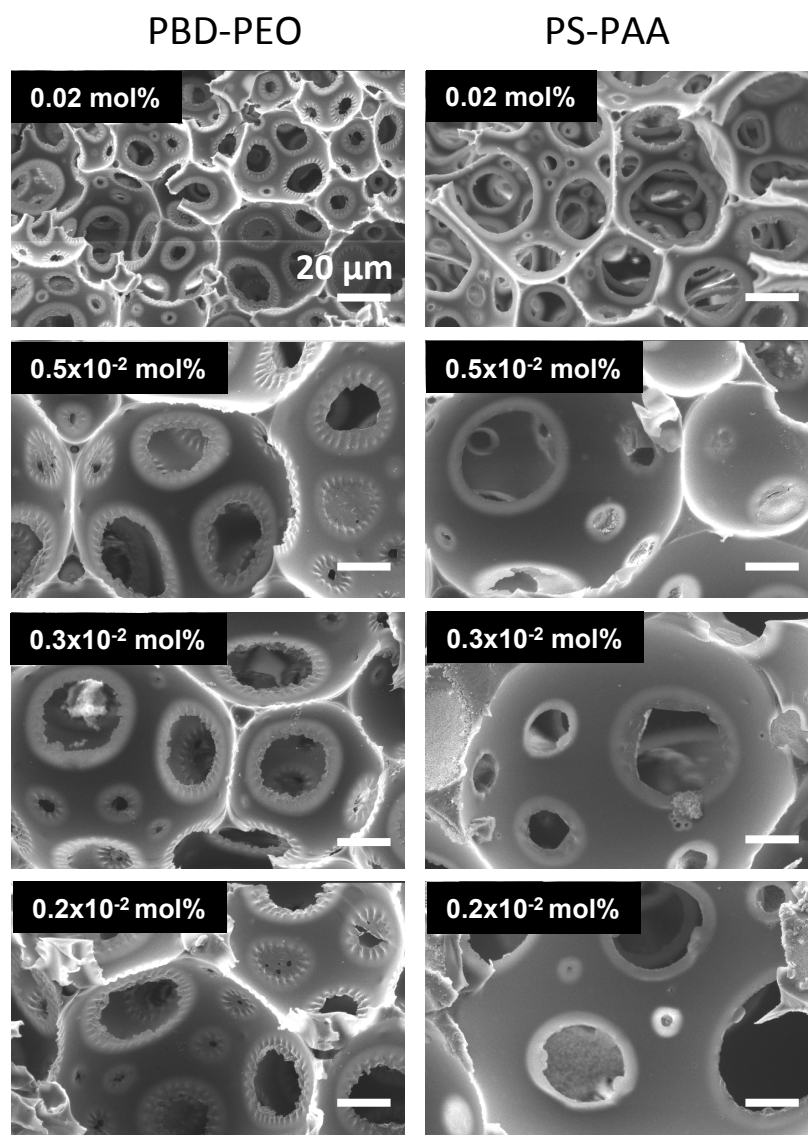


Figure 5.6 Effect of surfactant concentration on foam morphologies prepared with PBD-PEO and PS-PAA with AIBN initiation. An aqueous phase volume of 90% and a shear rate of 750 rpm was maintained. Scale bars represent 20 μm . All concentrations are quoted as mole%

Figure 5.7 shows that the void diameters of the PS-PAA functionalised foams were larger those functionalised with PBD-PEO, for both initiator types, which may relate to surfactant efficiency. However, for both copolymers, interconnected foams were formed with oil phase initiation only (Figures 5.6 and 5.8), increasing evidence for initiator driven porosity. As $K_2S_2O_8$ proceeds from the aqueous phase, locking in the conformation of the droplets, does not provide sufficient thinning of the oil phase to lead to interconnectivity between two adjacent droplets. Eventual phase separation of the oil and aqueous phase upon emulsification was observed at a surfactant concentration of 0.08×10^{-2} mol% for PBD-PEO with both initiators while PS-PAA emulsions failed at a lower concentration of 0.125×10^{-2} mol% for $K_2S_2O_8$ and 0.1×10^{-2} mol% for AIBN.

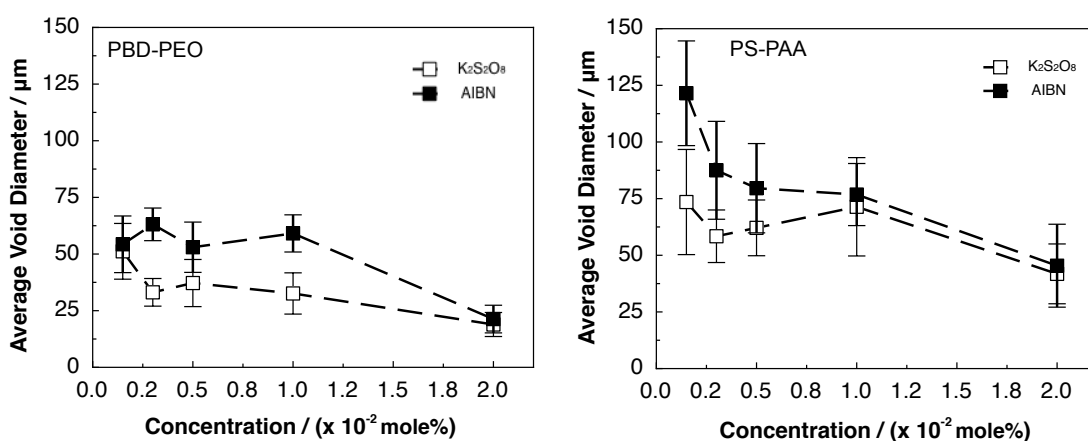


Figure 5.7 Average void diameters of foams prepared with a) PBD-PEO and b) PS-PAA as a function of copolymer concentration in mole%, with oil phase and aqueous phase initiation. Data is mean \pm SD. $n=100$ void diameters from 3 independent experiments.

Higher concentrations of PS-PAA are required for stable emulsions at the polymerisation temperature and is a result of surfactant efficiency. Decreasing PS-PAA concentration may result in insufficient charge repulsion between polymer chains to prevent droplet coalescence, thereby decreasing the stability of the emulsion. We thus propose that the locus of initiation of polymerisation determines open porosity. For $K_2S_2O_8$, initiation occurs at the oil-water interface and proceeds towards the bulk whereas for AIBN the opposite is true. Therefore, with amphiphilic block copolymer surfactants, initiation at the oil-water interface results in a rigid pore wall, thereby reducing mobility of two adjacent water droplets to coalesce and form interconnects. On the contrary, when initiation originates from the bulk oil phase (with AIBN), the oil-water interface remains ‘fluid’ until the gel point allowing

droplets to fuse and form interconnecting pores. For Span 80 based foams however, their low molecular weight nature enables interfacial fluidity at the polymerisation temperature regardless of the initiator employed forming porous foams with both $K_2S_2O_8$, and AIBN.

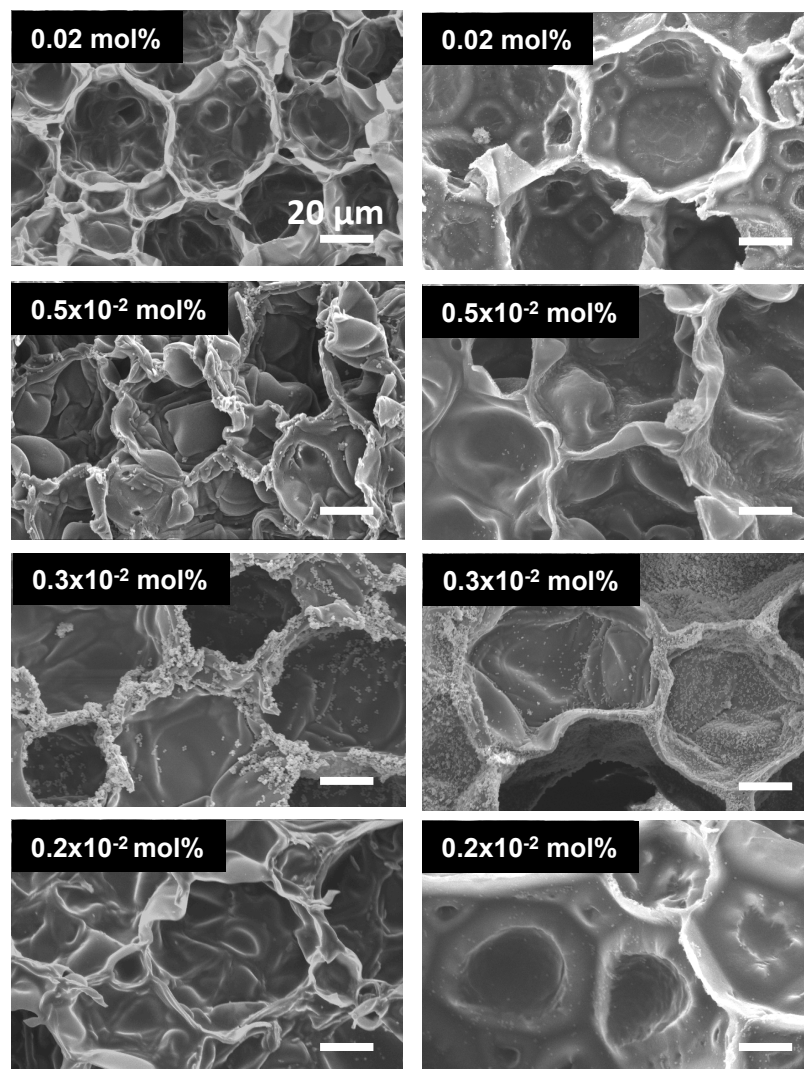


Figure 5.8 Effect of foam morphologies of polyHIPEs prepared using PBD-PEO and PS-PAA as a function of surfactant concentration with $K_2S_2O_8$ initiation. An aqueous phase volume of 90% and a shear rate of 750 rpm was maintained. Scale bars represents 20 μ m. All concentrations are quoted as mole%

5.3.3 Surface structure of polyHIPE foams

Upon closer inspection of the surface within each void, differences in surface roughness was observed, depending on the initiator employed for both ionic (PS-PAA) and non-ionic (PS-PEO) surfactant based foams. For $K_2S_2O_8$ based initiation, foam surfaces reveal topographical features in the nanometer length scale for both PS-PEO and PS-PAA based foams (Figure 5.9 a). This surface roughness perhaps

arises from the ability of the block copolymer surfactants to form both oil-in-water and water-in-oil emulsions when a water-soluble initiator is used. On the other hand for AIBN initiated emulsions, foams resulted in flat surfaces within the voids, with typical drying patterns that result from the evaporation of water droplets and dehydration of the foam (Figure 5.9 b). The origin of this interfacial instability and whether surface patterns and roughness can be controlled through surfactant and initiator concentrations is subject to further investigation for each block copolymer

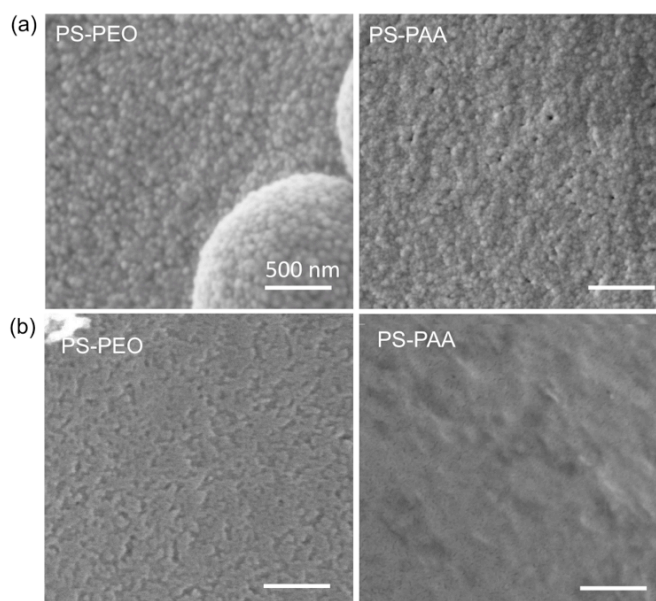


Figure 5.9 Void surface structure of foams using a) $K_2S_2O_8$ and b) AIBN as the initiators. Scale bars represent 500 nm.

employed. This means, that by systematically varying the polymerisation temperature which controls the rate of cross-linking, the size and polydispersity of such topographical features could be further controlled³⁰.

5.3.4 Shear and aqueous phase effects

While the main factors that have shown to control polyHIPE scaffold architecture is the surfactant and crosslinker concentrations, and in our case the choice of initiator, fine-tuning of emulsion process parameters allows for a further degree of control over the final desired physical structure. This includes shear, aqueous phase volume, the addition of inert porogens in both the oil and water phases and polymerisation temperature all of which have shown to be influential. Here, we explore two parameters to modify foam porosity; shear rate and aqueous phase volume fraction.

The effect of shear rate on emulsions formed with all block copolymers was investigated using both oil phase (AIBN, Figure 5.10) and aqueous phase ($K_2S_2O_8$, Figure 5.11) initiation. The main outcome was a decrease in average void diameter and narrow polydispersity of droplet diameter size, as the shear rate was increased from 750 rpm to 11500 rpm. This is not surprising as an increase in shear allows a more efficient dispersal and break up of water droplets in the emulsion. Two main anomalies arose in these studies. Firstly, a complete emulsion inversion occurred for

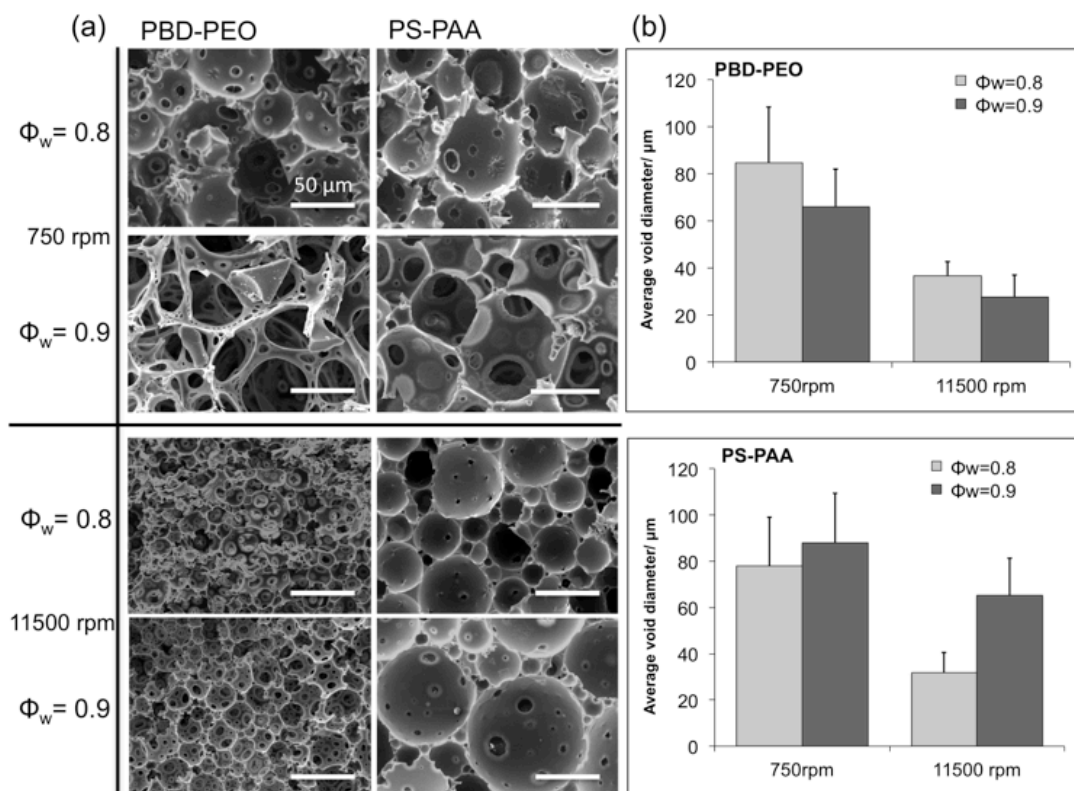


Figure 5.10 The effect of shear rate and aqueous phase volume fraction of polyHIPE foams prepared with PBD-PEO and PS-PAA block copolymers. a) Scanning electron micrographs showing foam morphology and b) average void diameters as a function of shear rate and aqueous phase volume fraction. The initiator AIBN was used and a surfactant concentration of 0.1 mole% relative to the monomers was maintained. Data is mean \pm SD. Scale bars represent 50 μm .

the cases of PS-PEO and PBD-PAA when homogenised at 11500 rpm resulting in inverse oil-in-water emulsions. Here, we predict that the HLB value of PS-PEO (0.8) and PBD-PAA (7.3) becomes applicable, noting that while these copolymers form interconnected foams, it was only possible within a limited window of parameters. Secondly, interconnecting pores were observed on foams functionalised with PS-PAA using the aqueous phase initiator, $K_2S_2O_8$. The effect of aqueous phase volume was found to be surfactant dependent. For PS-PAA, as the aqueous phase volume was increased from 80% to 90%, an increase in average void diameter was observed

using image analysis. This was regardless of the initiator used (Figure 5.10 and 5.11). In contrast, for foams synthesised with PBD-PEO, an increase in aqueous phase volume resulted in a decrease in average void diameter for both open- (AIBN initiated) and closed- ($K_2S_2O_8$ initiated) foams. This difference perhaps relates to the

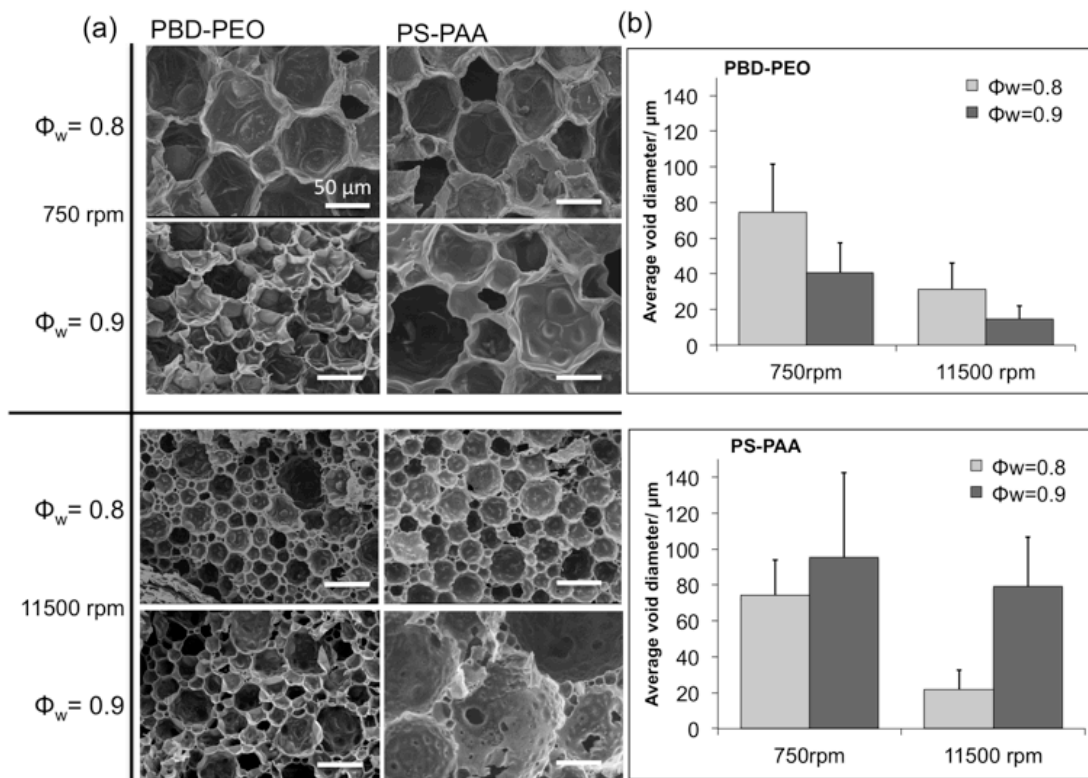


Figure 5.11 Effects of shear and aqueous phase volume fraction of polyHIPE foams using PBD-PEO and PS-PAA block copolymers with $K_2S_2O_8$ as the initiator. a) Scanning electron micrographs showing foam morphology and b) average void diameters as a function of shear rate and aqueous phase volume fraction. Surfactant concentration was 0.01 mole% relative to the monomers. Data is mean \pm SD. Scale bars represent 50 μm .

efficiencies of each block copolymer as a surfactant. For example, PBD-PEO was found to be more efficient at stabilising high aqueous volumes in contrast to PS-PAA functionalised foams, which exhibited a broad polydispersity of void diameters resulting from an unstable emulsion precursor. The parameters studied here suggest that the final structure of the foam is influenced by both shear and aqueous phase volume and therefore fine-tuning of desired foam morphologies maybe be achieved with optimised processing parameters.

5.3.5 HIPEs with triblock copolymer surfactants

To further establish the relevance of the HLB in predicting surfactant feasibility for a specific type of emulsion, an ionic triblock copolymer PS-PAA-PS, with a calculated

HLB value of 13.4, was utilised to preapre HIPEs. In this study, for each emulsion, an aqueous phase volume of 80%, surfactant concentration 0.01 mol% with a shear rate of 750 rpm was kept constant. When AIBN was used as the initiator, the resulting HIPE was partially stable at the polymerisation temperature (at 50 °C) with an emulsion layer forming between expelled oil and aqueous phase layers. The polymerised monolith under SEM analysis revealed a porous polymer with a high level of interconnectivity between pores (Figure 5.12 a,b). On the other hand, when $K_2S_2O_8$ was used as the initiator, the emulsion underwent an inversion at the polymerisation temperature to form a milky white oil-in-water emulsion. The polymerised product analysed by SEM revealed the formation of polystyrene/divinylbenzene latex particles (Figure 5.12 c,d). This was in contrast to all the diblock copolymer foams, prepared under low shear, where void surfaces displayed topographical features. The triblock copolymer, however caused a macroscopic phase inversion before the onset of emulsion cross-linking. The reason for this emulsion inversion may lie with the chemical nature of the surfactant. Since PS-PAA-PS is ionic, the presence of $K_2S_2O_8$, which dissociates in aqueous solutions, will lead to the screening of the negative charges of the PAA block. This is enhanced in the triblock as the PAA block is is much larger (13.5 kDa) than any of the PAA- diblock copolymers. Thus, most likely, emulsion inversion occurs before polymerisation of the PS/DVB matrix is achieved.

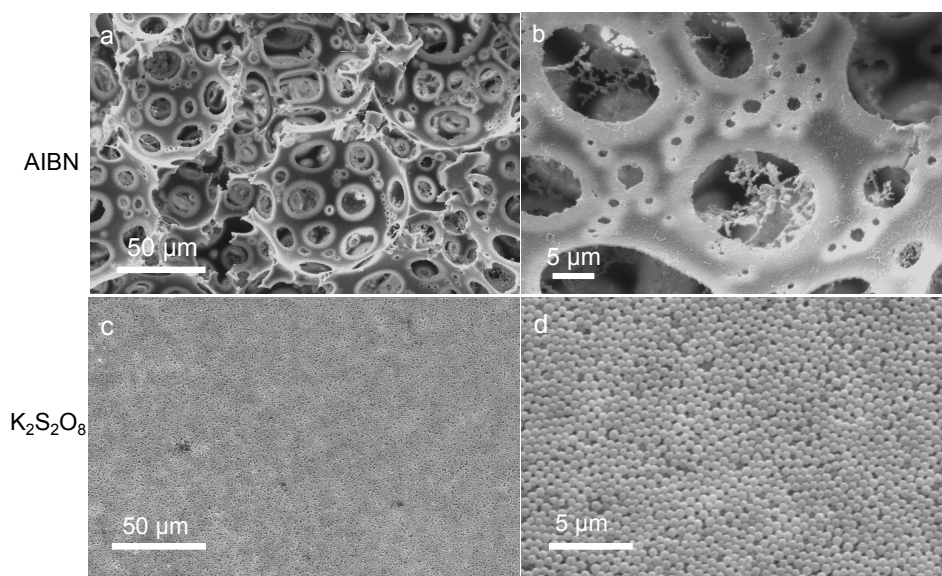


Figure 5.12 Porous foams prepared with PS-PAA-PS at a concentration of 0.01 mole%. a) Low magnification SEM micrograph of a highly porous and interconnected foam and b) high magnification of interconnects within one void with AIBN initiation. Low magnification SEM

micrograph c) when $K_2S_2O_8$ initiation was used and d) high magnification showing the formation of latex particles. An aqueous phase volume fraction of 0.9 and a shear rate of 750 rpm was kept constant.

SynperonicTM (PEO-PPO-PEO) triblock copolymers have been previously used to stabilise oil-in-oil HIPEs³¹ owing to several reasons including the macromolecular nature of the surfactant. Furthermore, low molecular weight surfactants in the study, of similar HLB values failed to stabilise the non-aqueous HIPEs. Although the HLB is a useful tool in determining surfactant suitability, its relevance in choosing block copolymer surfactants may not be as important. Thus we demonstrate that using the same macromolecular surfactant (i.e. with the same HLB), either a water-in-oil or oil-in-water emulsion could be prepared under the same processing conditions, by simply changing the choice of initiator and therefore the interactions with the hydrophilic block of the surfactant.

The work presented here regarding foam morphologies observed with block copolymer surfactants of varying molecular weights, architecture and hydrophilic-lipophile balance indicate that block copolymers offer an alternative route to preparing polyHIPEs while being more efficient at stabilising high internal phase emulsions at low surfactant concentrations compared to their low molecular counterparts such as Span 80. Furthermore, the HLB system in predicting surfactant suitability was found to be ineffective, with polymerisation kinetics playing the predominant role in dictating the porosity of foam morphology.

5.3.6 Wettability studies

Wettability of functionalised foams was determined by water contact angle measurements for both open and closed porous foams. Figure 5.13 shows a two-fold decrease in contact angle measurements for all block copolymer foams (ranging from $51^\circ \pm 15^\circ$ for closed porous PS-PAA to $67^\circ \pm 4^\circ$ for open porous PBD-PEO) compared to those prepared with Span 80 ($128^\circ \pm 5^\circ$) demonstrating an increase in wettability as a result of copolymer functionalisation. It is important to note that functionality is maintained in both closed and open porous foams and suggests that while the choice of initiator determines porosity, it does not determine surface functionalisation.

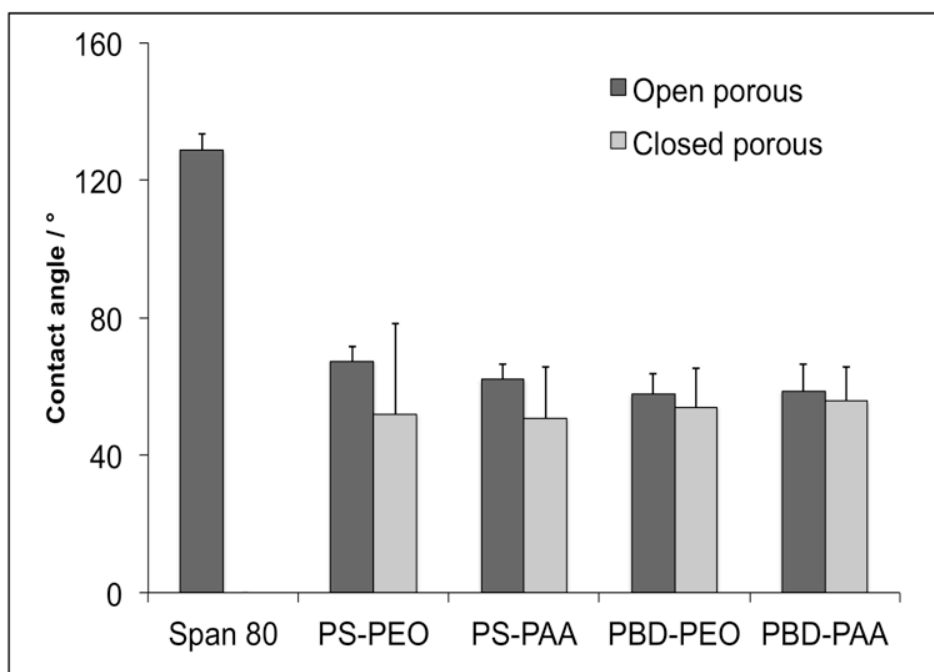


Figure 5.13. Contact angles of open and closed porous foams prepared with block copolymer surfactants. Data is mean \pm SD.

5.3.7 Determination of surface functional groups

To examine surface functional groups, XPS was performed on the porous foams with PS-PAA and PS-PEO (Figure 5.14); spectral assignments are listed in table 5.3. All peaks were compared to an XPS polymer database³². The wide scan of the foams consisting of PBD-PEO and PS-PAA show principally carbon and oxygen environments with Na contamination in the PBD-PEO sample (Figure 5.14). The O/C ratio for PS-PAA foams was 0.185 and for PBD-PEO was 0.195 indicating high oxygen content resulting from the presence of the carboxylic acid and ethylene oxide respectively. High resolution C 1s peak enables us to establish the presence of the hydrophilic block that resulted from polyHIPE surface functionality. For PS-PA, functionalised foams, the high resolution scan for the C1s peak was fit with four components that correspond with the C environment of the carboxylic acid and the underlying polyHIPE matrix. Foams functionalised with PBD-PEO were fit with two components that correspond with the C environment of ethylene oxide and underlying polyHIPE matrix. For foams containing PS-PAA, the primary C 1s peak centred at 285 eV with a secondary higher energy peak at 289eV corresponding to the C=O double bond of the carboxylic acid (Figure 5.15). The primary C 1s peak consists of a hydrocarbon signal (C-C and C-H from the polystyrene matrix)

appearing at 285 eV. The presence of the C-OH single bond of the carboxylic acid appears at 285.5 whose intensity was made to correspond with that of the C=O bond as this signal is from the same carbon atom. Finally, the peak appearing at 286.5 eV corresponds to the α carbon of the acid (\underline{C} -COOH). Similarly for PS-PEO, the C1s signal centred at 285 eV consists of the signal from the hydrocarbon backbone with smaller peak appearing at 286.5 eV representing the C-O-C ether bond. Note that the high oxygen contents from the XPS signal (Table 5.3) signifies that the foam surface is predominantly functionalised by the hydrophilic block of the copolymer surfactants.

The primary motivation for the work described here was to control surface functionalisation of polyHIPEs in 3D. Foams prepared with Span 80 result in inert hydrophobic polystyrene matrices post Soxhlet extraction. It was hypothesised that polymerisation of the HIPE ensures incorporation of the hydrophobic block into the backbone of the oil phase through molecular entanglement only possible with macromolecular surfactants. Similarly, the unsaturated backbone the PBD block may participate in the free radical polymerisation process, thereby ensuring surface functionality. The wettability and XPS thus confirm that the foams bear the chemical functionality of the hydrophilic blocks on the surface of the foams in 3D. Surface wettability is of great importance in biomedical applications such as protein or cell repellent and adhesive surfaces or for tissue engineered constructs. Thus the ability control surface chemistry of porous polyHIPEs with both protein inert (PEO) and protein adhesive (PAA) functionalities could offer greater control over cell adhesion limiting the use coating surfaces with ECM proteins, used often to increase cell attachment and proliferation.

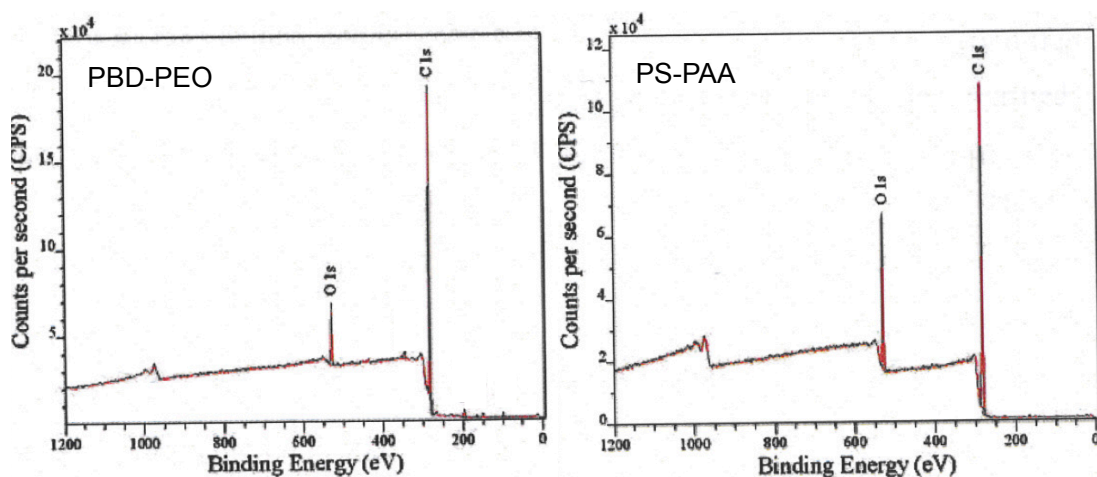


Figure 5.14. Wide XPS scans of foams functionalised with PBD-PEO and PS-PAA

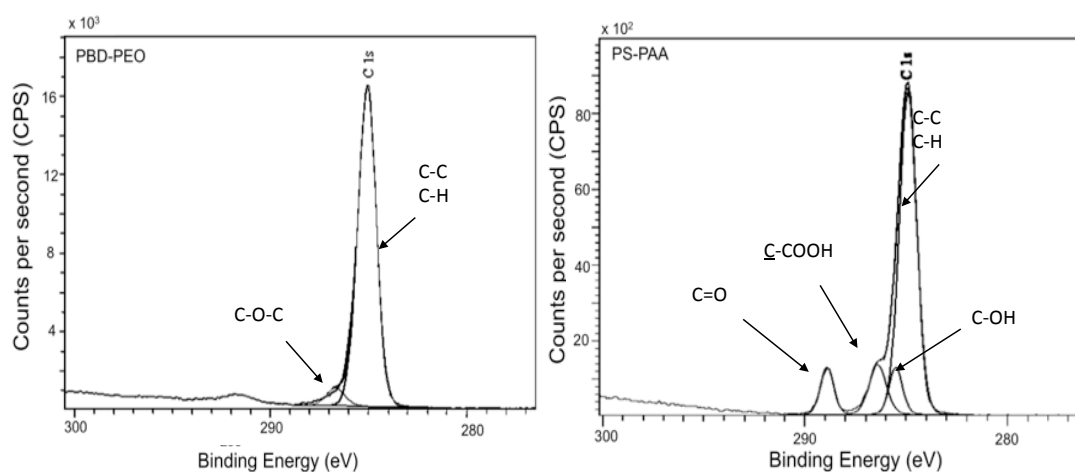


Figure 5.15. High resolution C 1s XPS spectra of foams containing PBD-PEO and PS-PAA

Table 5.3 XPS spectral assignments for foams containing PBD-PEO and PS-PAA

PS-PAA	Binding Energy/ eV	Atomic %	PBD-PEO	Binding Energy/ eV	Atomic %
C 1s	285.0	84.36	C 1s	285.0	83.06
O 1s	529.0	15.64	O 1s	532.6	16.18
			Na 1s	1071.6	0.76

5.4 Summary and further work

The preparation of foams from water-in-oil high internal phase emulsions and their subsequent functionalisation in 3D by employing amphiphilic diblock and triblock copolymer surfactants has been demonstrated. The block copolymer surfactants were incorporated into the HIPE matrix either through physical entanglement or through

radical initiated polymerisation. Moreover, the open porosity of such foams was determined by oil phase initiation while the physical architecture of the foams was demonstrated by varying the different processing parameters of emulsion formation. The fabrication of highly porous and interconnected matrices is important for tissue engineering applications to facilitate cell proliferation and nutrient exchange. Despite previous studies that investigate the mechanisms of open pore morphologies, it is increasingly evident that they are limited to low molecular weight surfactant systems and has encountered short-comings in explaining closed pore morphologies commonly associated with macromolecular surfactant or Pickering based HIPEs¹⁸. The work described here, offers new insights into interconnectivity of polyHIPE foams using a wider range of macromolecular surfactants. Thus, highly porous materials that are surface functionalised make polyHIPEs potentially useful for 3D cell culture applications. Furthermore, such scaffolds possess the ideal architecture and mechanical properties^{9,10} (as a result of the monomers commonly used for the HIPE process) for bone tissue engineering and will be discussed further in the next chapter.

5.6 References

1. Place, E. S., Evans, N. D. & Stevens, M. M. Complexity in biomaterials for tissue engineering. *Nat Mater* **8**, 457–470 (2009).
2. Stevens, M. M. Biomaterials for bone tissue engineering. *Materials Today* **11**, 18-25 (2008).
3. Fong, E. L. S., Watson, B. M., Kasper, F. K. & Mikos, A. G. Building Bridges: Leveraging Interdisciplinary Collaborations in the Development of Biomaterials to Meet Clinical Needs. *Adv. Mater.* **24**, 4995–5013 (2012).
4. Hashimoto, Y. *et al.* The effect of decellularized bone/bone marrow produced by high-hydrostatic pressurization on the osteogenic differentiation of mesenchymal stem cells. *Biomaterials* **32**, 7060–7067 (2011).
5. Fu, H. *et al.* In vitro evaluation of borate-based bioactive glass scaffolds prepared by a polymer foam replication method. *Mat. Sci. Eng: C* **29**, 2275–2281 (2009).
6. Bokhari, M. A., Akay, G., Zhang, S. & Birch, M. A. The enhancement of osteoblast growth and differentiation in vitro on a peptide hydrogel—polyHIPE polymer hybrid material. *Biomaterials* **26**, 5198–5208 (2005).
7. Akay, G., Birch, M. A. & Bokhari, M. A. Microcellular polyHIPE polymer supports osteoblast growth and bone formation in vitro. *Biomaterials* **25**, 3991–4000 (2004).
8. Moglia, R. S. *et al.* Injectable PolyHIPEs as High-Porosity Bone Grafts. *Biomacromolecules* **12**, 3621–3628 (2011).
9. Kimmins, S. D. & Cameron, N. R. Functional Porous Polymers by Emulsion Templating: Recent Advances. *Adv. Funct. Mater.* **21**, 211–225 (2010).
10. Zhang, H. & Cooper, A. I. Synthesis and applications of emulsion-templated porous materials. *Soft Matter* **1**, 107 (2005).
11. Hayman, M. W., Smith, K. H., Cameron, N. R. & Przyborski, S. A. Growth of human stem cell-derived neurons on solid three-dimensional polymers. *J. Biochem. Biophys. Meth.* **62**, 231–240 (2005).
12. Canal, C. *et al.* Topographical and Wettability Effects of Post-Discharge Plasma Treatments on Macroporous Polystyrene-Divinylbenzene Solid Foams. *Plasma Process. Polym.* **6**, 686–692 (2009).
13. Cummins, D. *et al.* Click chemistry as a means to functionalize macroporous PolyHIPE. *Soft Matter* **5**, 804 (2009).
14. Caldwell, S. *et al.* Degradable emulsion-templated scaffolds for tissue engineering from thiol–ene photopolymerisation. *Soft Matter* **8** 10344–10351 (2012).
15. Krajnc, P., Štefanec, D. & Pulko, I. Acrylic Acid ‘Reversed’ PolyHIPEs. *Macromol. Rapid Commun.* **26**, 1289–1293 (2005).
16. Kimmins, S. D., Wyman, P. & Cameron, N. R. Photopolymerised methacrylate-based emulsion-templated porous polymers. *React. Funct. Polym.* **72** 947–954 (2012).
17. Livshin, S. & Silverstein, M. S. Enhancing hydrophilicity in a hydrophobic porous emulsion-templated polyacrylate. *J. Polym. Sci. A Polym. Chem.* **47**, 4840–4845 (2009).
18. Gurevitch, I. & Silverstein, M. S. One-Pot Synthesis of Elastomeric Monoliths Filled with Individually Encapsulated Liquid Droplets. *Macromolecules* **45**, 6450–6456 (2012).
19. Smart, T. *et al.* Block copolymer nanostructures. *Nano Today* **3**, 38–46 (2008).

20. Mork, S. W., Rose, G. D. & Green, D. P. High-Performance Poly(butylene oxide)/ Poly(ethylene oxide) Block Copolymer Surfactants for the Preparation of Water-in-Oil High Internal Phase Emulsions. *J. Surfactants Deterg.* **4**, 127–134 (2001).
21. Jakobs, B., Sottmann, T., Strey, R., Allgaier, J. & Richter, D. Amphiphilic Block Copolymers as Efficiency Boosters for Microemulsions. *Langmuir* **15**, 6707–6711 (1999).
22. Yao, C. *et al.* A novel glycidyl methacrylate-based monolith with sub-micron skeletons and well-defined macropores. *J. Mater. Chem.* **19**, 767-772 (2009).
23. Griffin, W. C. Calculation of HLB Values of Non-ionic Surfactants *J. Soc. Cosmetic Chemists* **5**, 249–256 (1954).
24. Williams, J. M., Gray, A. J. & Wilkerson, M. H. Emulsion Stability and Rigid Foams from Styrene or Divinylbenzene Water-in-Oil Emulsions. *Langmuir* **6**, 437–444 (1990).
25. Williams, J. M. High Internal Phase Water-in-Oil Emulsions: Influence of Surfactants and Cosurfactants on Emulsion Stability and Foam Quality. *Langmuir*, **7**, 1370–1377 (1991).
26. Cameron, N. R. & Sherrington, D. C Study of the formation of the open-cellular morphology of poly(styrene/divinylbenzene) polyHIPE materials by cryo-SEM. *Colloid Polym. Sci.* **274** 592–595 (1996).
27. Gurevitch, I. & Silverstein, M. S. Polymerized pickering HIPEs: Effects of synthesis parameters on porous structure. *J. Polym. Sci. A Polym. Chem.* **48**, 1516–1525 (2010).
28. Cameron, N. R. High internal phase emulsion templating as a route to well-defined porous polymers. *Polymer* **46**, 1439–1449 (2005).
29. Zhang, S., Chen, J. & Perchyonok, V. T. Stability of high internal phase emulsions with sole cationic surfactant and its tailoring morphology of porous polymers based on the emulsions. *Polymer* **50**, 1723–1731 (2009).
30. Viswanathan, P. Emulsion Templated Porous Scaffolds for Bone Tissue Engineering. *MPhil Thesis, The University of Sheffield* 1–46 (2010).
31. Cameron, N. R. & Sherrington, D. C. Non-aqueous high internal phase emulsions. Preparation and stability. *Faraday Trans.* **92**, 1543 (1996).
32. Moulder, J. F., Ed: Chastain, J., King, R.C. & Prairie, E. Handbook of x-ray photoelectron spectroscopy: a reference book of standard spectra for identification and interpretation of XPS data. *Physical Electronics* (1995).

Chapter 6: Characterisation of ‘patchy’ foams and its effects on hES-MP adhesion and differentiation

This chapter has been published or is in preparation for publication as:

Cell instructive microporous scaffolds through interface engineering
Journal of the American Chemical Society, 2012 **134**: 20103-20109

Topological control of stem cell differentiation using functionalised polyHIPE foams
Advanced Healthcare Materials, in preparation

6.1 Introduction

In chapter 5 emulsion parameters that control the open and closed porosity of polyHIPEs were discussed and in each case introduced surface functionality using amphiphilic block copolymer surfactants. One of the current challenges in designing porous 3D matrices however, is spatial control of ligand binding sites and clustering of these binding sites. Although the importance of lateral ligand spacing and clustering have been extensively studied by the Spatz¹⁻³ and Cooper-White^{4,5} groups, much of what is known is through 2D cell culture systems. Given that cell adhesion (extensions of cell filopodia and lamellopodia) in 3D is fundamentally different to that in 2D⁶, extending the same level of complexity to 3D cell culture platforms is therefore required.

Fibronectin is a well studied ECM protein from a mechanical and structural perspective. The well known RGD adhesive binding peptide sequence is located in the 10th type III unit of fibronectin (FN III10)⁷. Upon stretching, through actin-myosin mediated cell contractility, further cryptic binding sites can be exposed. One of these is the PHSRN peptide sequence, a synergistic adhesion site found on the 9th type III unit (FN III9) that enhances cell attachment in the presence of RGD⁸. The presentation of these sites is critical for the clustering of integrins and recruitment of anchor proteins involved in focal adhesion formation and eventually triggering signaling pathways involved in cell adhesion and differentiation. Currently, few 3D scaffolds provide defined matrices with precise ligand presentation in addition to other physicochemical properties. For example, in addition to structural support,

intrinsic properties of the ECM such as topography⁹, stiffness¹⁰, surface chemistry¹¹ and more recently ECM tethering¹² have shown to be important cues in the absence of traditional growth factor cocktails. Furthermore, their spatiotemporal presentation alone can regulate cellular behaviour including hMSC differentiation⁹ or maintaining hMSC phenotype¹³.

In this chapter, the aim was to use a novel way to introduce such spatial control of ligand clustering mimicking the level of organisation as found in native ECM by employing two amphiphilic block copolymer surfactants in the HIPE process. It was hypothesised that the mixing of two dissimilar hydrophilic blocks of the copolymers undergo phase separation at the oil-water interface (Figure 6.1) and when polymerised, the foam displays discrete domains of the two chemistries. Here mixtures of PS-PEO and PS-PAA in various molar ratios were used to induce this phase separation and thereby presenting cell inert (PEO) and cell adhesive (PAA) chemistries. How these block copolymer domains thus influence hMSC behaviour such as adhesion and differentiation were investigated.

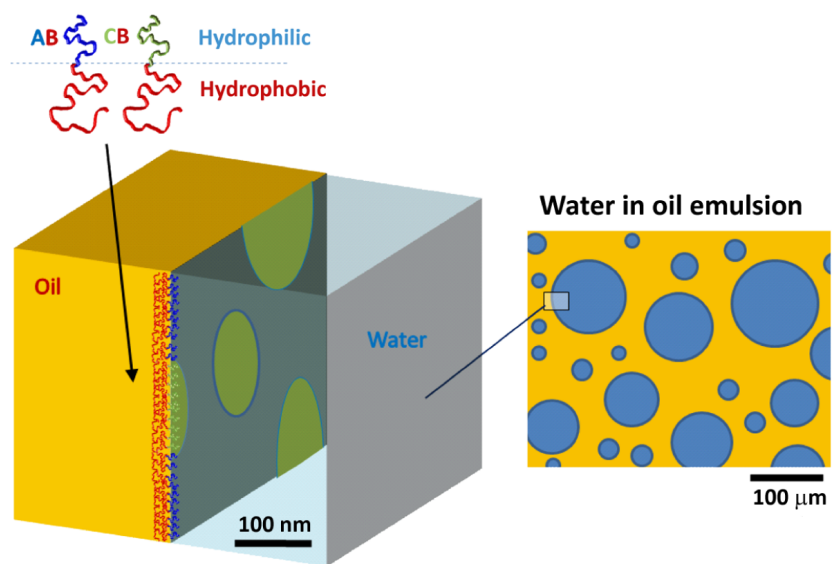


Figure 6.1. Schematic of the HIPE templating process using two different amphiphilic block copolymer surfactants forming domains at the oil-water interface.

6.2 Methods

The adhesive heterogeneity of the native ECM matrix was determined by labeling the adhesive sites of fibroblast derived fibronectin matrix. Mixed formulations of PEO and PAA 2D films were prepared to assess domain formation by chemical force spectroscopy mapping (CFSM). Mixed formulations of foams both closed and open porous were used to assess cell adhesion and differentiation. Furthermore, fibronectin adsorption on 2D matrices were also mapped by CFSM to understand protein and cell binding. Finally, the osteogenic potential of porous 3D foams was investigated. For further details, refer to Chapter 4.

6.2.1 Cell assays and time points

- hES-MP morphology determination by actin and nucleus staining on 3D closed-porous foams on day 7.
- hES-MP morphology determination by actin and nucleus staining on 3D open-porous foams on day 7, 14, 21, 28.
- qPCR microarrays of hES-MP cultured non-porous foams at day 7.
- Alizarin Red assay for calcium deposition determined for hES-MPs cultured on porous scaffolds at day 28.
- Scanning electron microscopy to qualitatively evaluate mineral deposition.

6.3 Results

6.3.1 Adhesive heterogeneity in extracellular matrix

Fibronectin, as well as other ECM proteins, have specific cell binding domains, which when assembled into thick matrix fibrils, may be spaced apart from one another or are otherwise inaccessible from cells^{14,15}. To first demonstrate how heterogeneous cell accessible adhesion sites are in a native matrix, a fibroblast-derived fibronectin matrix was labelled to visualise all matrix fibrils and also regions available for cell adhesion, the latter using 1- μ m diameter beads to simulate a cell

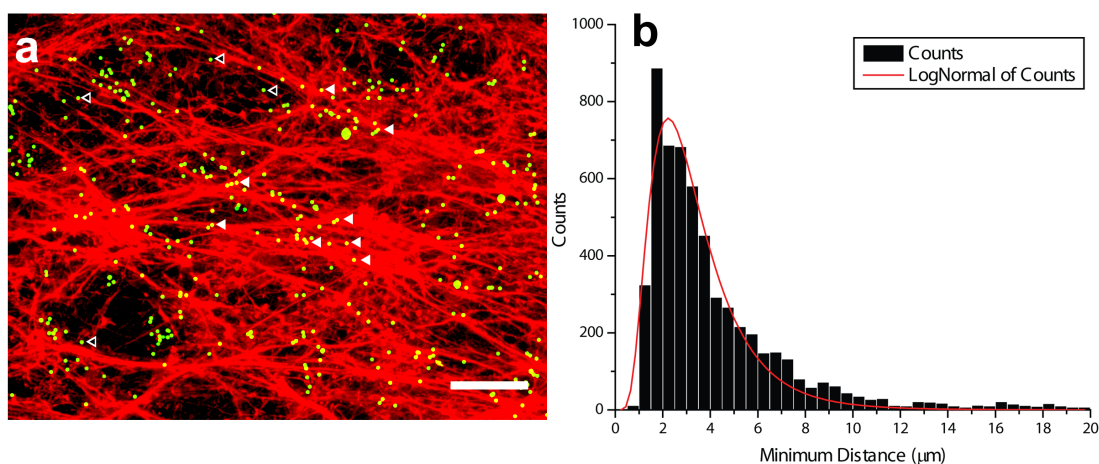


Figure 6.2. Heterogeneous adhesion in a Fibronectin Matrix. (a) A cell-derived fibronectin matrix (red) was dual labelled with 1 μm diameter beads (green) bound to an antibody that recognises the fibronectin region containing the cell binding site. Beads were used to directly probe the region as they may approximate filopodia and identify cell accessible regions. Closed arrowheads indicate beads that were on top of fibrils (yellow coloured) and open arrowheads indicate beads that were adjacent and bound to matrix fibrils (green coloured). The representative image here is a confocal section through the matrix just below its surface. Scale bar is 20 μm . (b) Quantification of the minimum bead-to-bead distance for fibronectin matrix. This work was done by Dr. Chirasatitsin at UCSD as part of a collaboration.

filopodia that could bind to the matrix. While beads always co-localised with fibrils, their distribution was very heterogeneous throughout the matrix (Figure 6.2 a). Minimum bead-to-bead distance, i.e. the length distance adhesive sites for cells, was broadly distributed but averaged $3 \pm 1 \mu\text{m}$ (Figure 6.2 b), reflecting a fairly high degree of adhesive heterogeneity.

6.3.2 Morphology of porous and non-porous patchy foams

In the emulsion process, PS-PEO and PS-PAA were mixed in specific molar ratios as defined in table 6.1. Note that foams will be referred to by their PEO molar content, e.g. 25% PEO will be PEO25 except for pure PS-PAA, which will be referred to as PAA100. PolyHIPE foams prepared with block copolymer surfactants with open and closed pore morphologies were utilised to ascertain differences in cell adhesion and differentiation as a result of the porosity, surface topology and roughness.

Table 6.1 Block copolymer foam compositions by molar mass ratio

Name	PEO-PS molar fraction	PAA-PS molar fraction
PEO100	100	0
PEO75	75	25
PEO50	50	50
PEO25	25	75
PAA100	0	100

Closed porous foams were 80% porous based on aqueous phase volume; emulsions with higher aqueous phase volume (90%) were found to be unstable at the polymerisation temperature. On the other hand, open-porous foams were 90% porous by aqueous phase volume. As previously demonstrated¹⁶, closed-porous foams of PEO, PAA and their mixtures exhibited average void distributions in the micrometer range as shown in figure 6.3 a (top) and 6.3 b (left) and as shown in Chapter 5 such foams display surface topographical features. These features, in the nanometer length scale do not change as a function of chemistry with mixed formulation foams (Figure 6.3 b). Average void diameters and interconnecting diameters shown in figure 6.4 indicate that open-porous foams have comparable porosities and interconnectivity to foams synthesised with the low molecular surfactant Span 80 and have a more narrow polydispersity than average void diameters of closed-porous foams. Interconnect diameters of all copolymer foams containing PAA were higher than that of PEO 100 or Span 80 containing foams (Figure 6.5) and are in agreement with mercury intrusion porosimetry data discussed in Chapter 5. This may relate to stability of parent emulsions at 90% aqueous phase volume as discussed in Chapter 5. Unlike the non-porous foams, open-porous foam surfaces did not display nano-topographical features.

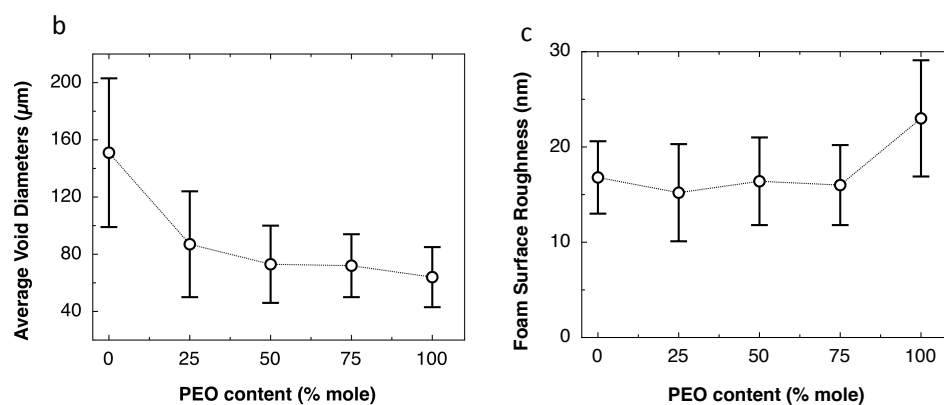
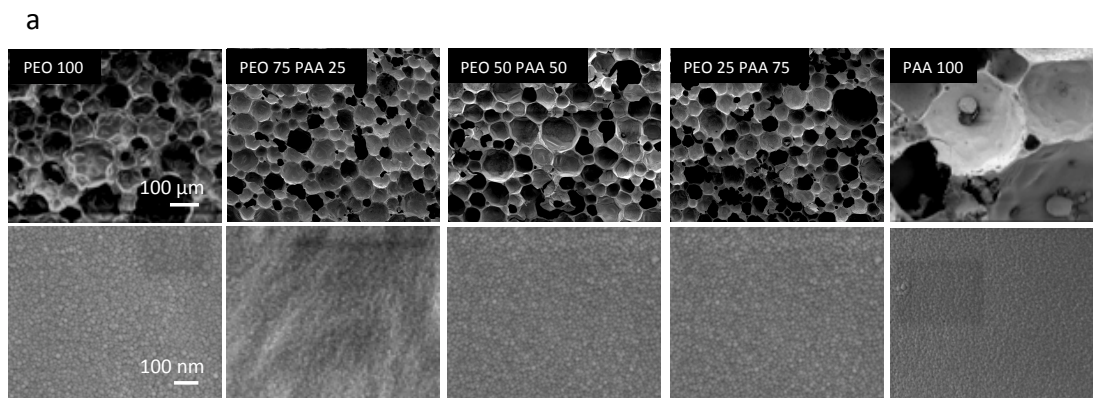


Figure 6.3 a) Morphologies of closed-porous styrene/divinylbenzene foams prepared with PS-PEO, PS-PAA and their mixtures. Average void diameters b) and foam surface roughness c). Data is mean \pm SD. n=100 voids

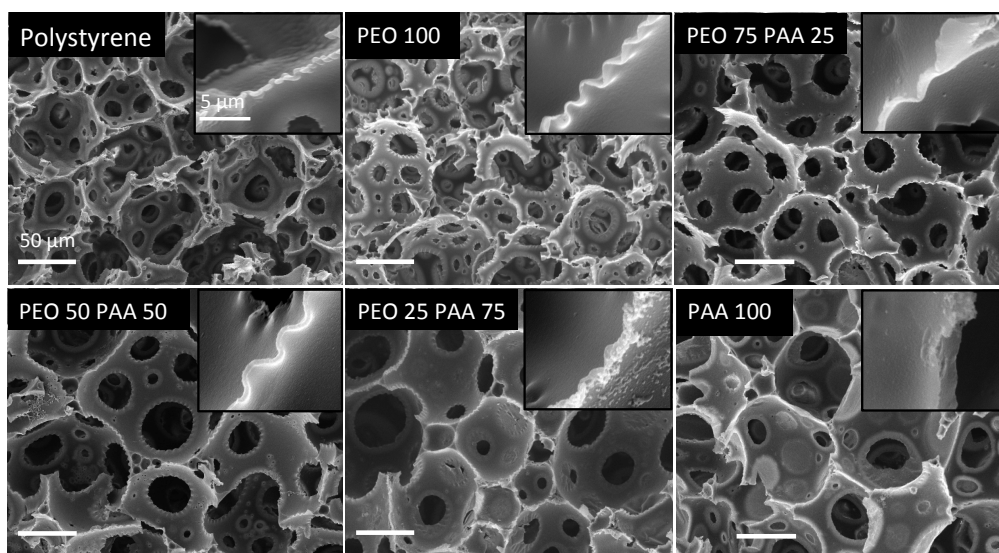


Figure 6.4 Foam morphologies of open-porous styrene/divinylbenzene foams prepared with PBD-PEO and PS-PAA and their mixtures compared to porous foams of Span 80. Inset: structure of the void struts.

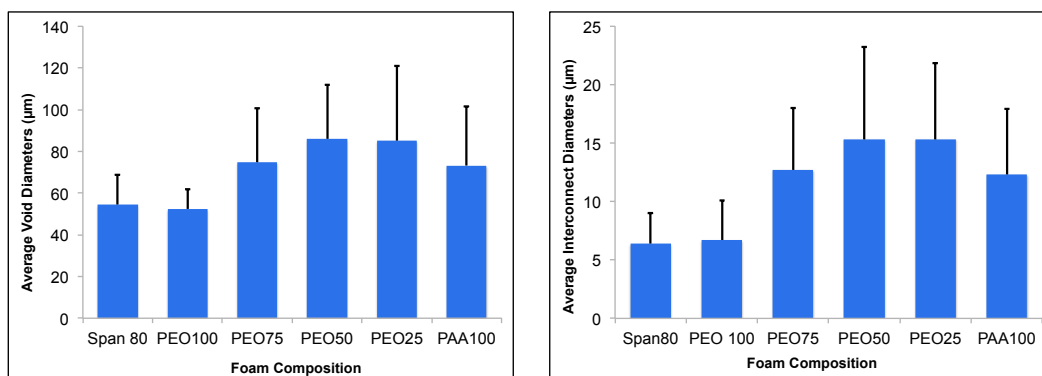


Figure 6.5 Average void diameters a) and average interconnect diameters b) of open porous foams using the block copolymer PEO-PBD and PS-PAA and their mixtures compared to Span 80 based foams. Data is mean \pm SD.

6.3.3 Surface topology characterisation

The surface functionalisation and wettability of block copolymer foams were characterised in Chapter 5. However, homogenous surface chemistry does not mimic the natural adhesive heterogeneity of matrix¹⁴ and might result in less inductive matrix for stem cells. As such, we investigated to what extent mixtures of cell adhesive PAA¹⁷ and cell inert PEO¹⁸ block copolymers could undergo interface-confined phase separation in foam morphologies versus the surface domains have previously observed by the Battaglia lab in amphiphilic polymersomes^{19,20}. While bulk metrics identify composition (as in Chapter 5), they cannot identify copolymer phase segregation, and fluorescent detection is complicated by spatial resolution limitations¹⁹. Chemical force spectroscopy mapping (CFSM)²¹ uses a functionalised AFM probe to monitor adhesion forces between the probe and film. The formation of domains was characterised by CFSM using 2D film analogues of the 3D foams, where the surface morphology was comparable to the surface of non-porous foams (Figure 6.6). Poly-L-lysine (PLL)-functionalized probes mapped adhesive interactions with films of different diblock copolymer composition at 62.5 nm lateral resolution. Though films were maintained at pH 9 to deprotonate PAA (pKa \sim 4.5) and increase its adhesion to the PLL functionalised tip, PEO100 films appeared to be substantially more adhesive than PAA100 (Figure. 4.1.2, Materials and Methods). This is thought to be due to counter ion screening of the PAA-PLL electrostatic interaction and is plausible since negative charges can be screened by free salt present in the solution. Since at pH 9, the PAA chains are negatively charged, the individual chains repel each other and this forces them to stretch in solution²². Thus,

in the presence of free salt, the PAA chains are effectively screened, reducing their electrostatic interaction with the positively charged PLL tip. When charged polymer brushes are largely screened, they are referred to as quasi-neutral brushes²³ and although not experimentally investigated, this indicates that in the present studies, PAA chains may have a dense brush configuration²⁴. Regardless, differential interactions between the PLL functionalised tip and the copolymer functionalised substrates allow us to map the different block copolymer domains (Figure. 6.7 a). By defining adhesion (to the PLL functionalised tip) as any value above one standard deviation below the PEO100 film's average adhesion, more than 84% of PEO sites could be identified. Conversely, this threshold correctly identifies nearly all of the PAA100 film's surface (Figure. 4.1.2 Materials and Methods, shaded box,) and is illustrated again as the grey shaded area in Figure. 6.7 b.

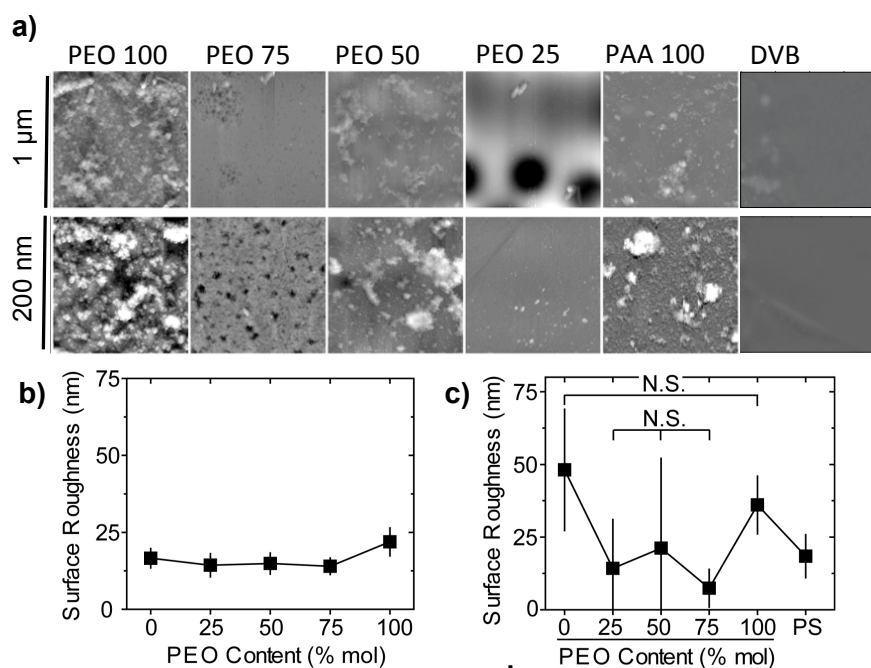


Figure 6.6 a) AFM topographs of films from 20 x 20 (top) and 2 x 2 μm scans (bottom). Image colormap ranges are 0 – 1 μm and 0 – 200 nm. Surface roughness of foams b) determined from high resolution SEM images and films c) from 2 x 2 μm scans from CFMSM

Using this threshold, CFMSM maps and adhesive force histograms were generated for 2 × 2 and 20 × 20 μm scan sizes (Figure. 6.7 a) for the indicated copolymer compositions to show PEO- (white) and PAA-containing (black) regions. For both scan sizes, PEO area fraction reflected the same increasing trend as in bulk, namely higher PEO content yields a higher adhesive area fraction (Figure. 6.8 a). Domain surface area, defined as a cluster of 4 identical and contiguous observations, were

measured from adhesion maps and found to vary from 0.06 to 3.78 μm^2 for PEO (opened squares) and 2.04 to 0.02 μm^2 for PAA (solid circles) as PEO mole fraction increased. ANOVA analysis clearly indicated that low (PAA100 and PEO25) and high (PEO75 and PEO100) PEO mole fraction behaved similarly, reflecting domains of either PEO or PAA, respectively (Figure. 6.8 b).

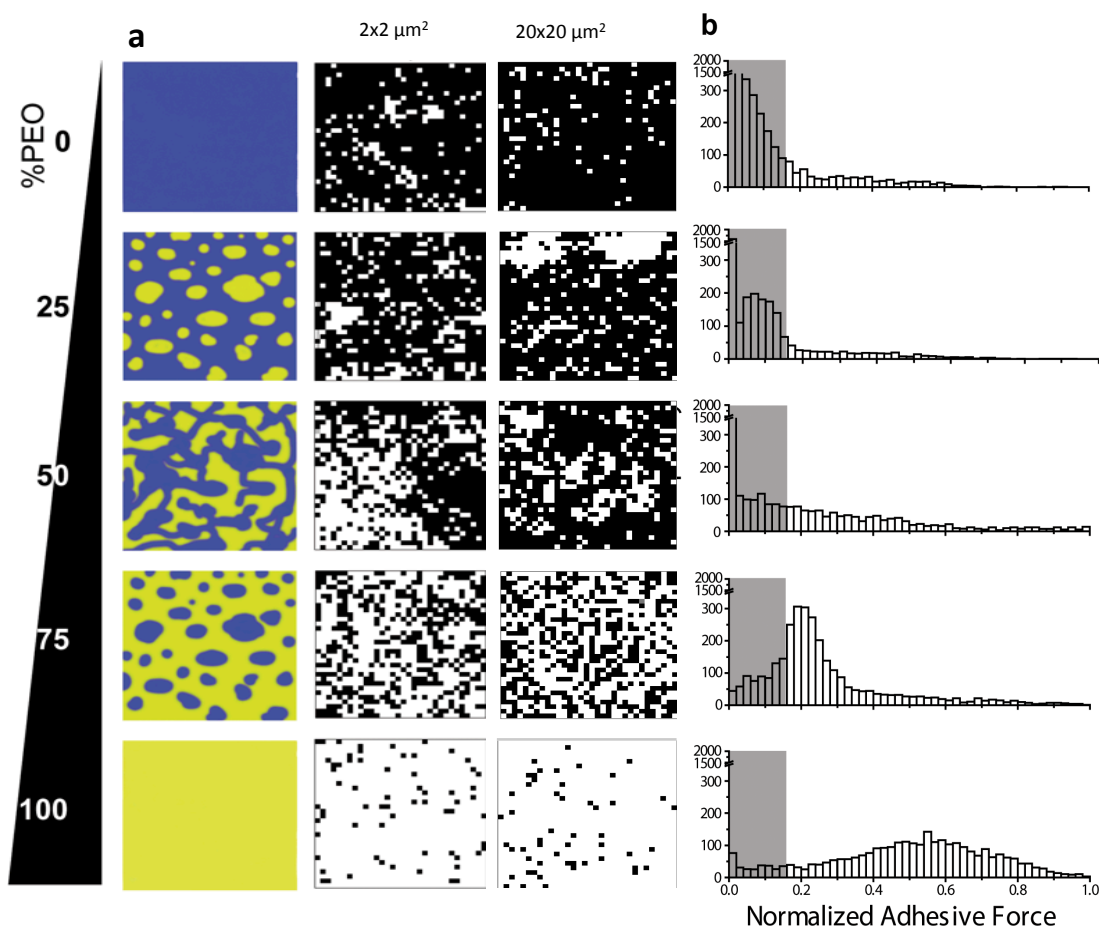


Figure 6.7 Film Characterisation by Chemical Force Spectroscopy Mapping. a) Schematic (left) and experimental (right) adhesion images of the distribution of PS-PAA (blue and black regions, respectively) and PS-PEO (yellow and white regions, respectively) shown for a 2 x 2 μm and 20 x 20 μm scan area with a resolution of 32 x 32 points. b) Normalised adhesive force distribution as a function of the molar ratio of PS-PEO for all samples. The shaded regions correspond to the threshold for PAA determined in the Materials and Methods section.

The force maps suggest typical bimodal (PEO75, PEO25) and spinodal (PEO50) decomposition patterns as represented by the schematic (Figure. 6.7 a, left). In addition to domain surface area, inter-domain spacing was also determined between all domains within a given image, e.g. Figure. 6.9a showing PAA domain spacing in PEO75 films; when examining PEO domains, minimum domain-to-domain spacing was greatest when the PEO mole fraction was lowest and nano-domains were

present; for PEO fraction > 50%, the average spacing was 570 ± 210 nm (Figure 6.9b).

The average minimum domain-to-domain (of adhesive PAA sites) spacing observed in block copolymer films of composition PEO 75 was 520 ± 200 nm and PEO 50 was 570 ± 210 nm. This, compared to the bead-to-bead (cell adhesive sites) spacing in native matrix of 3 ± 1 μm (Figure. 6.2b), exhibited a similar level of adhesive heterogeneity. While these two metrics are dissimilar, occur over different length scales, and probed different matrices, the same amount heterogeneity was observed in both measurements. Thus with increasing PEO composition, domain spacing decreases while size increases (Figure 6.9c).

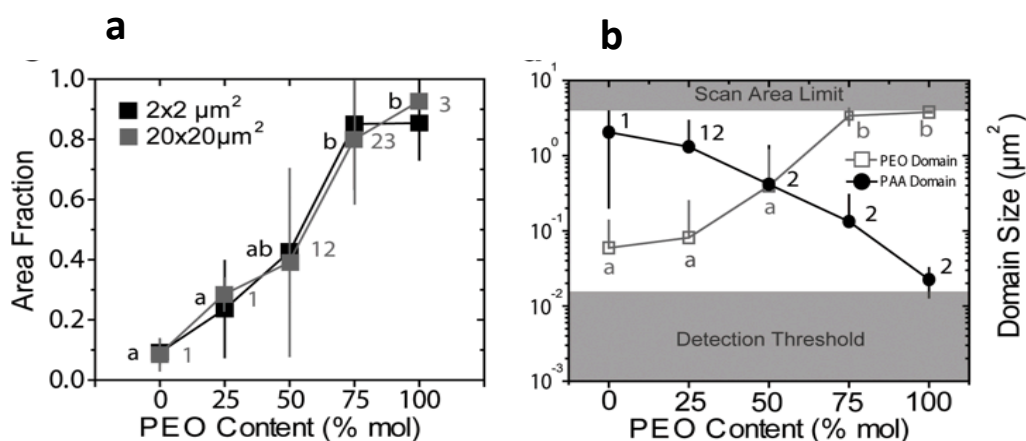


Figure 6.8 a) The average PS-PEO area fraction per image was determined as a function of the PS-PEO mole percent for both scan sizes. b) Average domain surface area of PS-PAA (closed circles) and PS-PEO (open circles). Scan limit indicates the maximum area of the scan and the detection limit is the area of four adjacent measurements. Mean comparisons of one group versus all samples that have the same symbol, e.g. 1, 2, a, and b with $p < 0.05$ versus all data not in the group. By defining adhesion as any value above one standard deviation below the PEO100 film's average adhesion, more than 84% of PEO sites could be identified. Conversely, this threshold correctly identifies nearly all of the PAA100 film's surface (Figure 4.2 Materials and Methods) and is illustrated again as the grey shaded area in Fig. 6.7b.

Surface mechanics are well-known to play a role in stem cell responses¹⁰, especially when coupled with the relatively small pores in the foams which present a 3D environment¹⁴. The stiffness of copolymer films of varying composition was measured by analysing the indentation portions of CFSM data. Irrespective of composition, films were nearly rigid, i.e. stiffness at or exceeding MegaPascals (MPa).

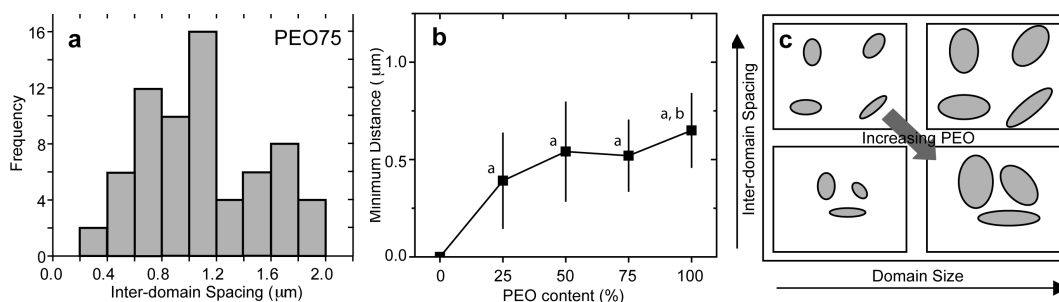


Figure 6.9 Domain Spacing. a) The distribution of inter-domain spacing for PAA domains in a sample PEO75 film. b) Minimum distance between PAA domains as a function of bulk PEO composition. ^a and ^b indicate $p < 0.05$ and 0.01 versus all data not in the group, respectively. c) Schematic relationship between inter-domain spacing and domain size. The dark grey arrow indicates the observed behaviour of PEO: with increasing PEO content, PEO domain size increases while inter-domain spacing of PAA domains decreases.

6.3.4 Surface chemistry and topology effects on stem cells: Open-porous vs closed-porous foams

Having characterised its surface chemistry and topology, how specific surface structures associate with biological function was investigated next. Adhesion and viability was analysed for mesenchymal progenitors (hES-MP) (Figure 6.10a, 6.11), which differentiate towards the adipogenic, myogenic and osteogenic lineages^{25,26} on both closed-porous foams as well as open porous foams. hES-MP viability and cell number was measured after a period of 7 days (Figure 6.10a) by means of an MTS assay. Though this assay does not directly measure proliferation rate of the cultured cells, it is an indication of the number of viable cells present within the scaffolds at the assay time point. It is important to note that hES-MP viability differences were minimal for the non-contact toxicity test, indicating little if any scaffold toxicity (details in Chapter 4, Figure 6.10b). Therefore, observed cell adhesion differences occurred as a response to the surface chemistry. hES-MP adhesion and spreading on both open and closed porous foams were poor on PEO100 foams (Figure 6.11b,c), which is not surprising given PEO's non-fouling and biologically inert properties¹⁸. Interestingly, poor cell spreading was also seen on 'sticky' PAA100 foams, where the highest cell number and well spread morphologies would be expected. Although in all cases, cells remained adherent. Indeed, it has been well documented that surfaces

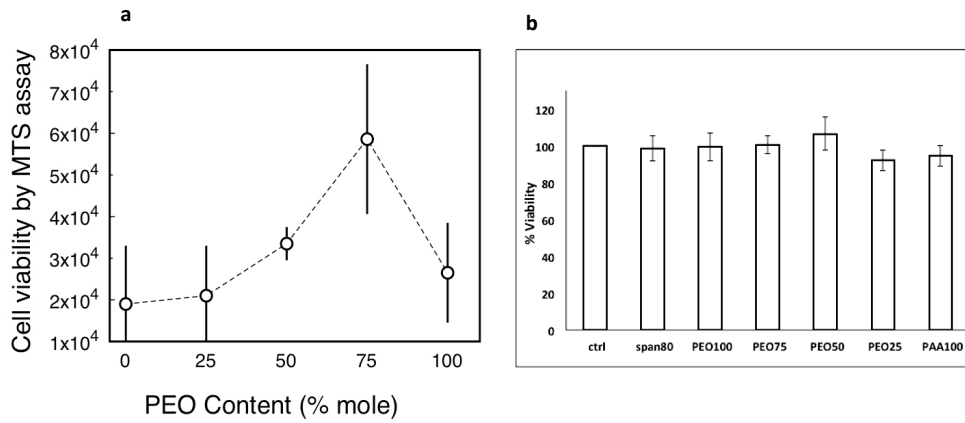


Figure 6.10 a) Total cell number by MTS after 7 days and b) scaffold toxicity showing block copolymer based foams are not toxic. Non-porous foams were used for both experiments. Data is mean \pm SD, n=9.

with a high density of adhesive ligands reduces cell motility inhibiting their ability to migrate and proliferate^{27,28}. Instead, cell spreading was found to be the greatest for hES-MPs on PEO75 and PEO50 foams (Figure 6.11 b,c). High magnification images (Figure 6.11c) of hES-MPs clearly show highly spread morphologies on the PEO75 and PEO50 scaffolds with poor cell spreading on all other copolymer compositions. The adhesion pattern of the hES-MPs reflects the total cell number at day 7 (Figure 6.10a) with the highest number of cells found to be on PEO75 scaffolds. Together these data would indicate that hES-MPs adhere and spread in a composition-dependent matter, in particular to topologies that mimic the heterogeneity of adhesive sites (PAA domains) in native ECM (Figure 6.2a,b). What is important to note is that hES-MP adhesion pattern was observed to be the same regardless of the porous nature, or the differences in nanoscopic surface structure of the foams as shown in figure 6.11b and 6.11c), indicating that the block copolymer domains may in fact be the overriding factor in determining hES-MP adhesion. Whether this affects hES-MP differentiation in the same way will be further investigated.

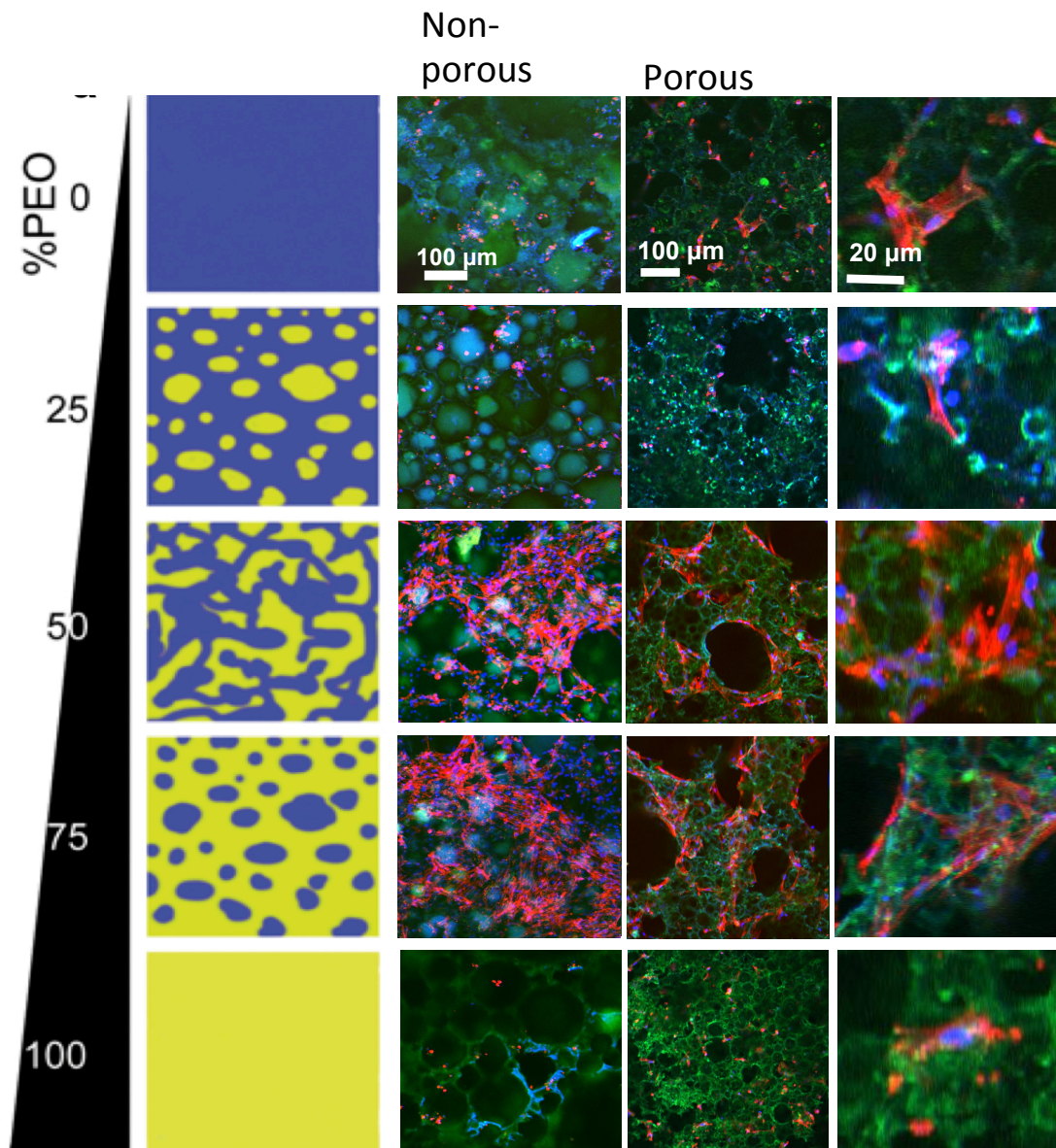


Figure 6.11 Cell viability and protein adsorption on HIPE scaffolds. a) Schematic of phase separation of PS-PAA (blue regions) and PS-PEO (yellow regions) are shown as a function of PS-PEO content. Low magnification images of nuclear (blue) and filamentous actin (red) staining of hES-MPs on b) closed and c) open-porous foams and d) high magnification of cell morphology (right) cultured for 7 days on the foams show varying cell attachment and spreading with changing PS-PEO molar ratio. Note that polystyrene within the scaffolds auto-fluoresces in the green colour channel. Representative images from $n=3$.

Long term cell culture was not possible with foams lacking interconnectivity as they did not support cell growth or proliferation beyond 7 days. On the other hand, hES-MPs were cultured upto 28 days on open-porous foams enabling further investigation on cell morphology. Given the scaffold geometry and stiffness, polyHIPE foams were used to investigate osteogenic differentiation of hES-MPs cultured on them over a period of 28 days. Matrix formation and mineralisation resulting from

osteogenic differentiation in the presence and absence of osteogenic growth factors was studied further. Cells in long-term culture by day 28 (Figure 6.12) display well

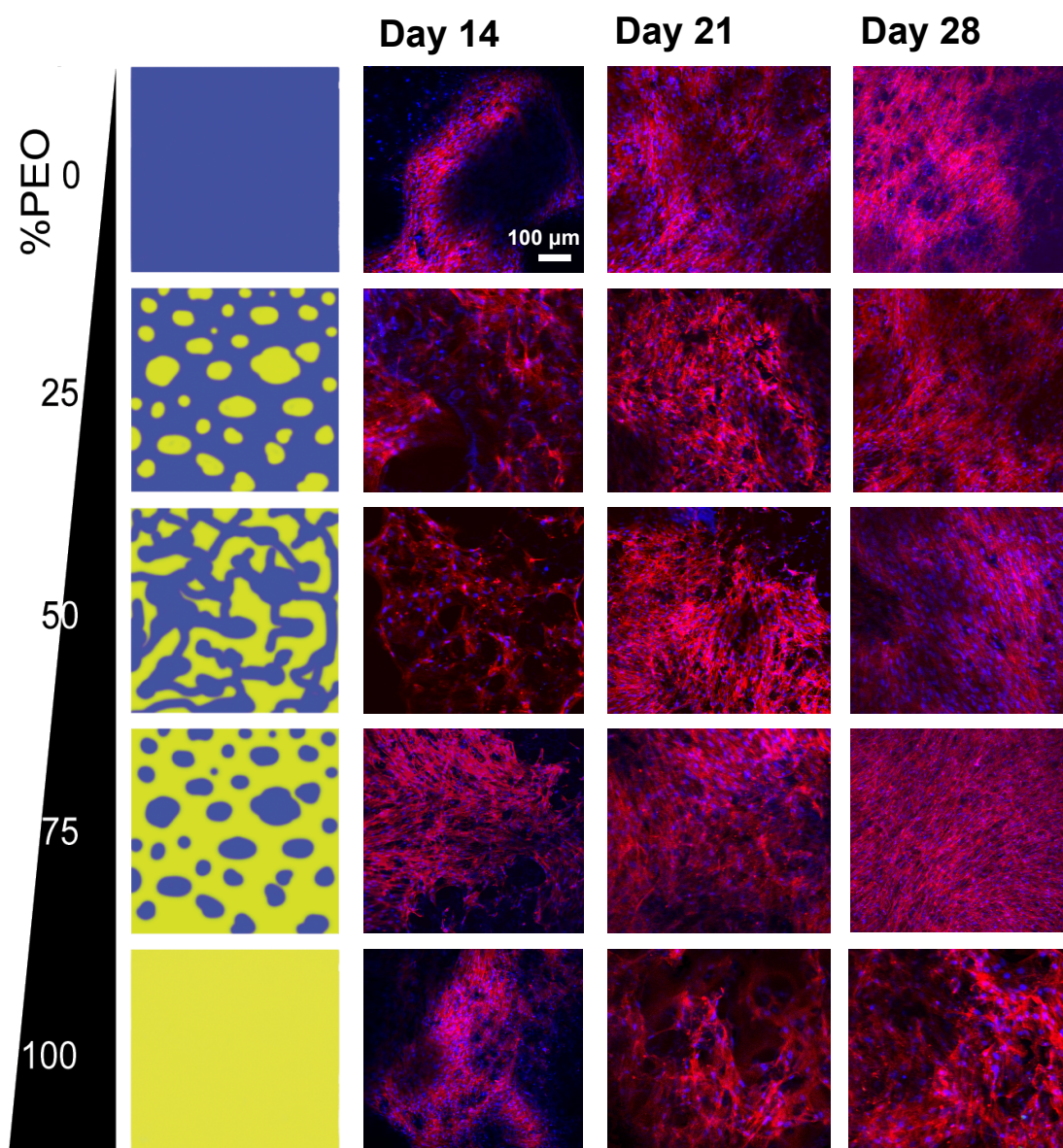


Figure 6.12 hES-MP cell morphologies cultured on block copolymer functionalised foams after 14, 21 and 28 days in the absence of any soluble growth factors. Cells are highly confluent on all copolymer compositions after 28 days. Cells stained with DAPI for nucleus (Blue) and Phalloidin Texas Red for actin cytoskeleton (red). Representative images from n=3.

spread morphologies and indicate proliferation on all scaffold compositions regardless of surface chemistry. Thus, differential cell adhesion was only observed within the first week in culture.

The results show that cells preferentially adhered to certain surface patterns over others. This maybe a result of which PEO/PAA mixtures most closely mimic the natural adhesive heterogeneity of the extracellular matrix, providing the appropriate

spatial distribution of cell binding and cell inert domains¹⁴. To further investigate how cell binding site distribution may play a role in cell adhesion, protein adsorption from serum-containing media was measured by the BCA assay. No statistical difference was found in the quantity of serum proteins adsorbed for any foam composition (Figure 6.13a). While total protein adsorption may not determine how ‘adhesive’ a specific copolymer composition is to cells, how such proteins might cluster due to specific surface chemistry may correlate with cell adhesion and ultimately behaviour. Work done by our collaborators showed that in fact when

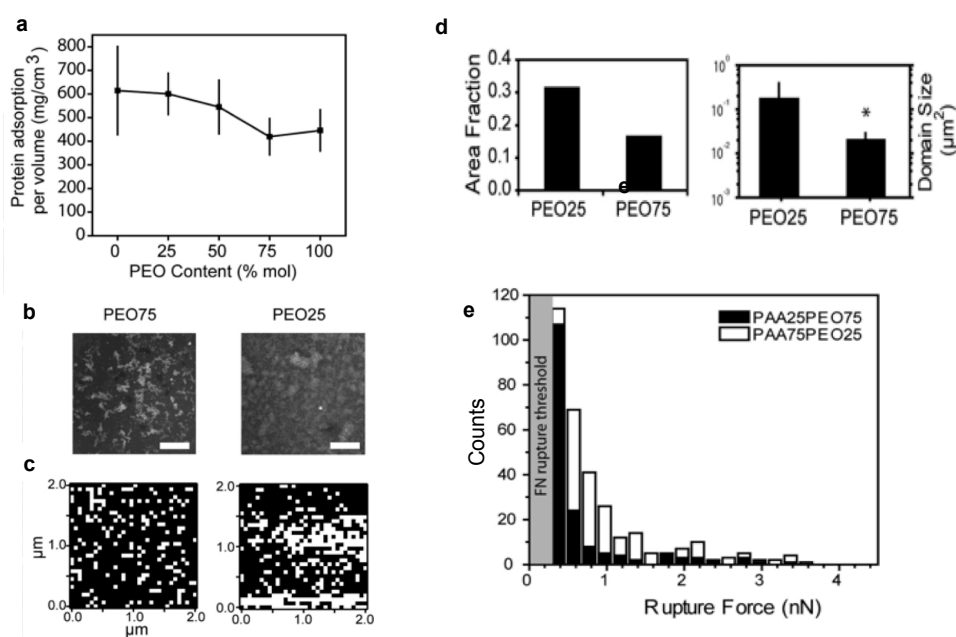


Figure 6.13 a) Average total protein adsorption per foam volume. b) Immunofluorescent staining of fibronectin adsorbed on PEO75 (left) and PEO25 (right) films. Brighter regions represent immobilized fibronectin on the surface. c) Fibronectin adsorption on PEO75 (left) and PEO25 (right) films detected by CFMSM over a $2 \times 2 \mu\text{m}$ scan size. White regions represent immobilized fibronectin on the surface. d) Area fraction of fibronectin adsorption evaluated from CFMSM images for foams of indicated PS-PEO content. e) Average fibronectin domain size determined from CFMSM images corresponding to the indicated PS-PEO content. * $p < 0.01$. f) Rupture force distribution of the fibronectin-antibody interaction ($F_{\text{threshold}} = 300 \text{ pN}$; grey shaded region) from fibronectin immobilized on PEO25 (open bar) and PEO75 (closed bar) films. Parts of the work in this figure were done by Dr. Chirasatitsin in USC as part of a collaboration.

fibronectin binding to films of PEO75 and PEO25 was examined by confocal microscopy (Figure 6.13b) and CFMSM (Figure 6.13c), fibronectin clustering was found to be surface chemistry-dependent (white regions, Figure 13c); the changes in fibronectin distribution on the surface (Figure 6.13d) was found to correspond with area fraction changes previously seen with PAA (see figure 6.8a and 6.8b), where protein adsorption should occur due to its opposing charge.

Fibronectin bound to PEO75 substrates aggregated into $0.13 \mu\text{m}^2$ domains spaced at least $0.52 \mu\text{m}$ apart (Figure 6.13d), reflecting the smaller adhesive domains of PAA on PEO75 substrate's surface. On the other hand, larger adhesive domains spaced much closer together in PEO25 approached the scan size limit (Figure 6.13c) and equated to 50% more rupture events on PEO25 than PEO75 (Figure 6.13e), together implying a more uniform protein coating. Thus it would appear that preferential cell adhesion is likely due to protein surface clustering.

6.4.5 Foam topological effects on hES-MP differentiation

Cell shape and cytoskeletal tension has shown to be a potent regulator of hMSC differentiation²⁹. To better understand how copolymer composition could influence hES-MP fate, cells were seeded onto closed-porous foams for 7 days. mRNA was isolated and converted to cDNA using reverse transcription. The cDNA was then used to investigate the expression of specific lineage markers known for mesenchymal phenotypes in the absence of soluble induction factors using a customised qPCR microarray^{10,29} (performed by my collaborators).

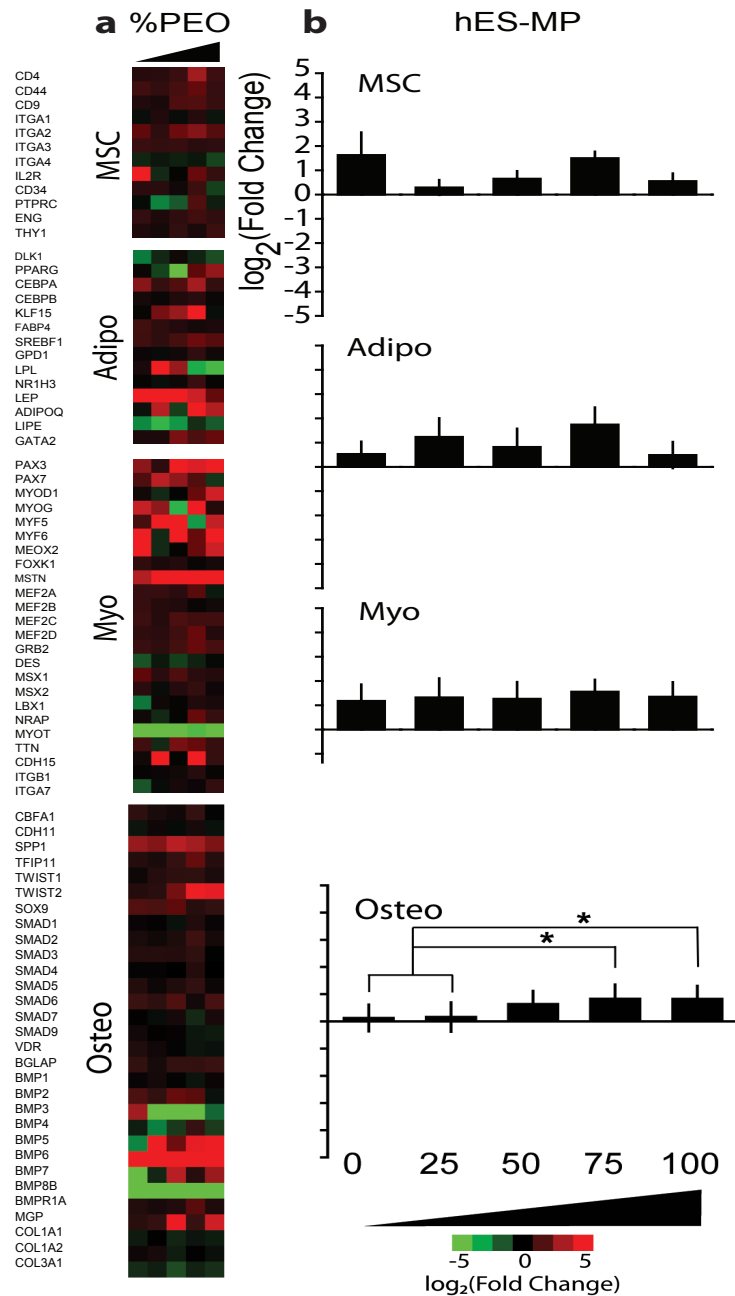


Figure 6.14. Heat maps of hES-MPs (a) were separated by genotypic expression of mesenchymal, adipogenic, myogenic and osteogenic expressions (from top to bottom). Colour bar represents down- (green) and up-regulation (red) relative to undifferentiated cells from the same source. Columns within each heat map represents cell responses on scaffold of 0 - 100 mole% of PEO (left to right). Heat map rows represent individual genes, which are listed at right. The average log base-2 fold change for hES-MPs (b) are also shown as a function of the mole% of PEO for genes of each lineage. * $p < 0.05$, ** $p < 0.01$, and *** $p < 0.001$ based on Wilcoxon rank-sum tests between cells cultured on foams of the indicated compositions.

Little difference and no significant trends with composition was observed in genes specific for the mesenchymal compartment (Figure 6.14a,b, appendix tables). Well spread hES-MP showed their greatest increase from undifferentiated cells with myogenic genes, albeit in a domain-independent manner. Interestingly enough, osteogenic genes were upregulated in a domain-dependent, statistically significant manner (Figure 6.14a,b: Osteo). Volcano plots indicated that genes in hES-MPs that were highly significantly different from undifferentiated cells and also highly upregulated were clustered in the myogenic and osteogenic lineages (Figure 6.15) Few adipogenic genes exhibited the same pattern (Figure 6.14a,b: adipo, Appendix tables), consistent with the lack of global adipogenic differentiation.

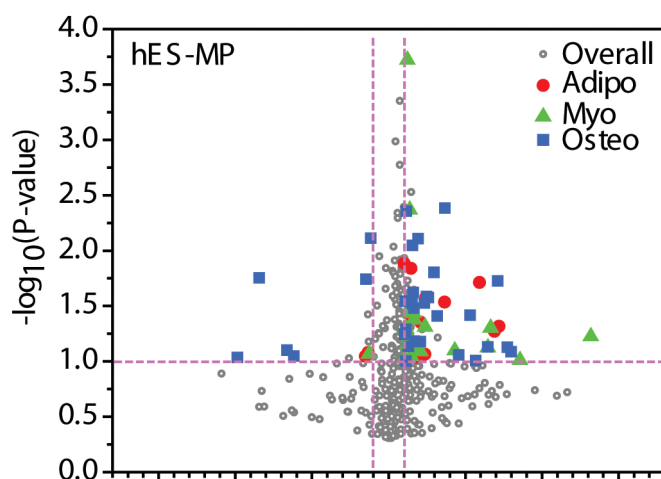


Figure 6.15 Volcano plots compare the log base-2 of the fold change of cells cultured on foams to undifferentiated cells against the negative log base-10 of the p-value for genes from the same composition. The horizontal and vertical red dotted lines indicate significance at $p \leq 0.1$ and fold changes greater than 2, respectively. All genes are indicated in grey except for those genes which met both criteria, in which case they were indicated with red circles, green triangles, and blue rectangles correspond to adipogenic, myogenic and osteogenic expression respectively.

In support with the lineage commitment data, cell interactions with copolymer nano-domains were assessed qualitatively and quantitatively for the lineage that indicated statistical significance; osteogenesis.

Mineral deposition and matrix secretion on ‘patchy’ foams

hES-MPs were cultured on block copolymer foams for a period of 28 days and compared to cells cultured on inert polystyrene scaffolds (prepared with Span 80) in the presence and absence of dexamethasone (DEX). The capacity of the scaffolds to

direct osteogenic differentiation and mineral (calcium phosphate) deposition in the absence of soluble factors was investigated. Qualitative assessment via SEM shows that for cells cultured on inert polystyrene scaffolds in the presence of DEX, hES-MP cells exhibit ECM deposition, most likely to be collagen fibres and mineral deposits, within the pores of the scaffold indicated by the bright spots from calcium phosphate mineralisation, as shown in figure (Figure 6.16, +DEX). In the absence of DEX however, a confluent layer of cells remained on the top of the scaffold, with much less ECM secretion or mineral formation (Figure 6.16, -DEX). We then explored to what extent the combination of matrix stiffness and block copolymer

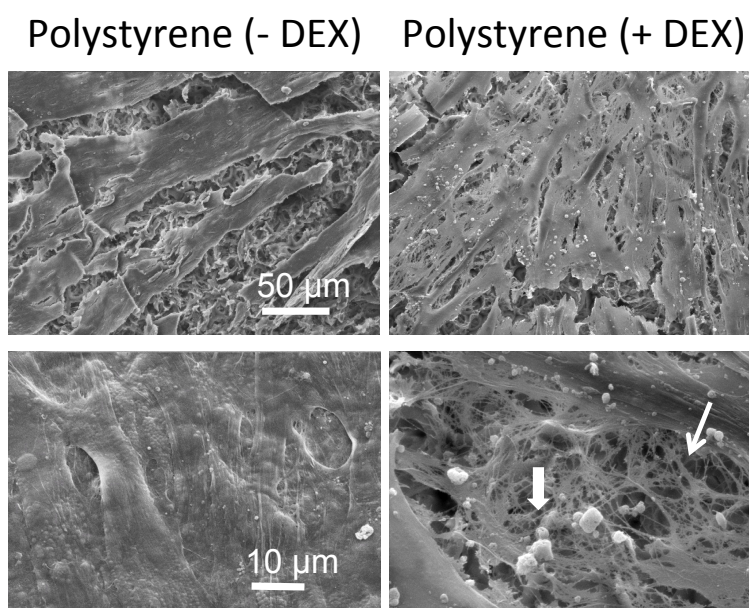


Figure 6.16 Representative SEM micrographs of hES-MP cells cultured on polystyrene scaffolds with and without dexamethasone (DEX). Top: Low magnification images of the cells interacting with the underlying scaffold. Bottom: high magnification images showing no mineral deposition in the absence of DEX in contrast to mineral deposition (block white arrow) and cell secreted ECM (collagen fibres) within the pores of the scaffolds in the presence of DEX (open white arrow). Micrographs are representative n=3.

domains could induce osteogenic differentiation and matrix production in the absence of DEX. Low magnification SEM micrographs in Figure 6.16a show that cells cultured on PEO100, PEO25 and PAA100 exhibited similar behaviour to cells cultured on polystyrene scaffolds without DEX, displaying little interaction with the underlying matrix. A confluent layer of cells remained on the top of the foams and in some cases (PAA100), hES-MPs adopting a fibroblastic morphology was observed in

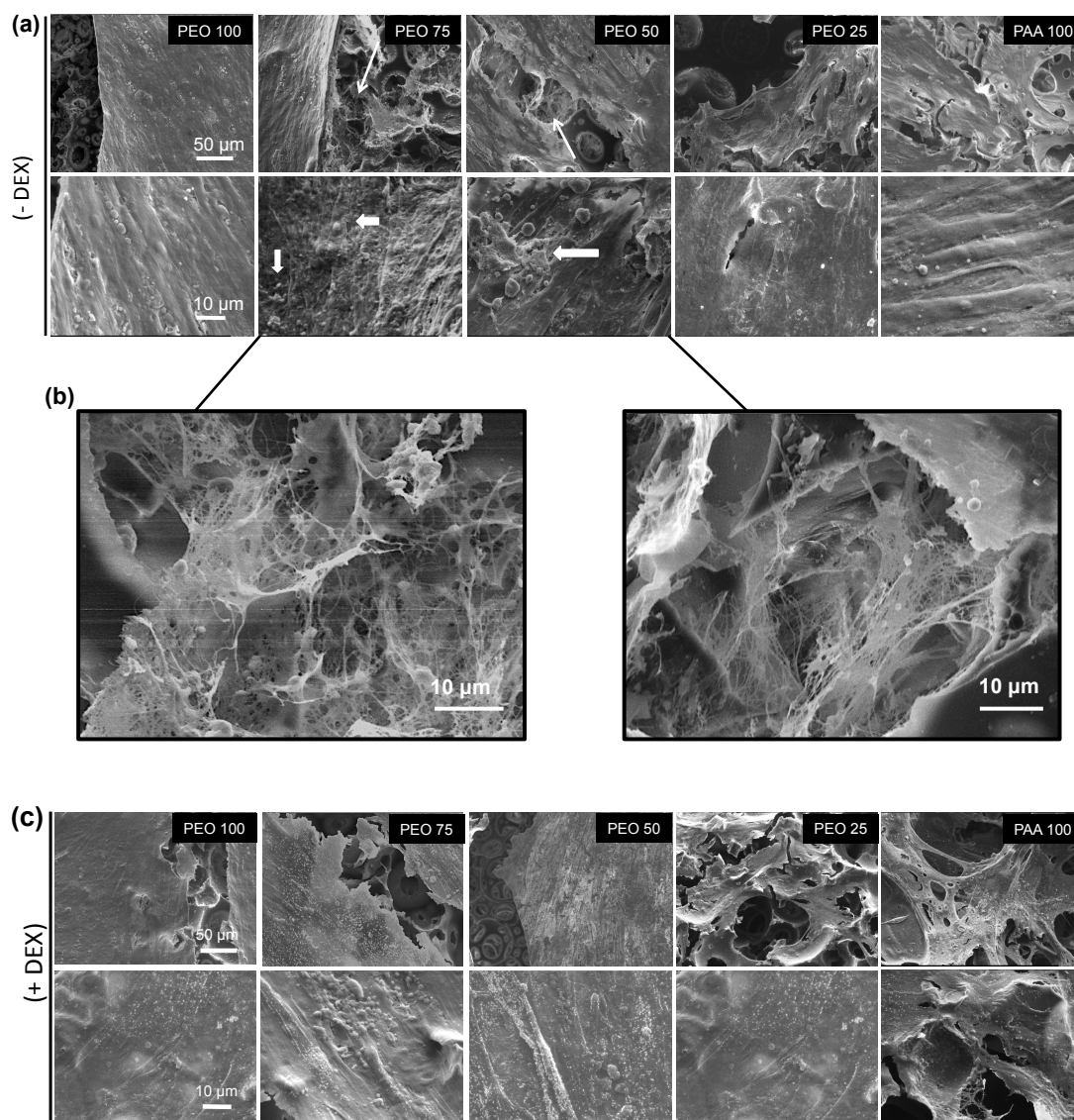


Figure 6.17 Representative SEM micrographs of hES-MPs cultured on block copolymer scaffolds for 28 days. Top: low magnification images of cell matrix interactions showing that hES-MP cells deposited ECM and grew within the pores of the scaffold on PEO75 and PEO50 compositions represented by the open white arrows. Bottom: high magnification images of mineral deposition mostly present on PEO75 and PEO50 foams (block white arrows). Micrographs are representative from $n=3$.

addition to low amounts of mineral formation. In contrast, hES-MPs cultured on PEO75 and PEO50 scaffolds, showed good integration with the scaffolds with cell secreted collagen networks forming within the pores of the scaffold (Figure 6.17b). Furthermore, high magnification images show the most mineral deposits on these two foam compositions suggesting that osteogenic differentiation may be preferential on scaffolds that display a combination of stiffness and topology. However, when treated with DEX, hES-MPs cultured on copolymer scaffolds for 28 days show little morphological differences (Figure 6.17c) where bright spots from the SEM

micrographs are indicative of calcium phosphate present on all copolymer formulations.

To determine quantitatively the amount of mineral deposited, cells cultured on scaffolds for 28 days were fixed and stained for the Alizarin Red S assay which selectively binds to calcium ions. Figure 6.18a shows the even distribution of calcium deposits across the scaffold with and without DEX for the scaffold compositions PEO75 and PEO50. An unpaired two-way t-test was performed to determine difference between the addition of DEX versus the absence of DEX within each scaffold composition (Figure 6.18c). Cells treated with DEX exhibited higher levels of calcium deposition with all scaffold compositions, as expected, and was found to be significantly different ($p < 0.05$) by day 28.

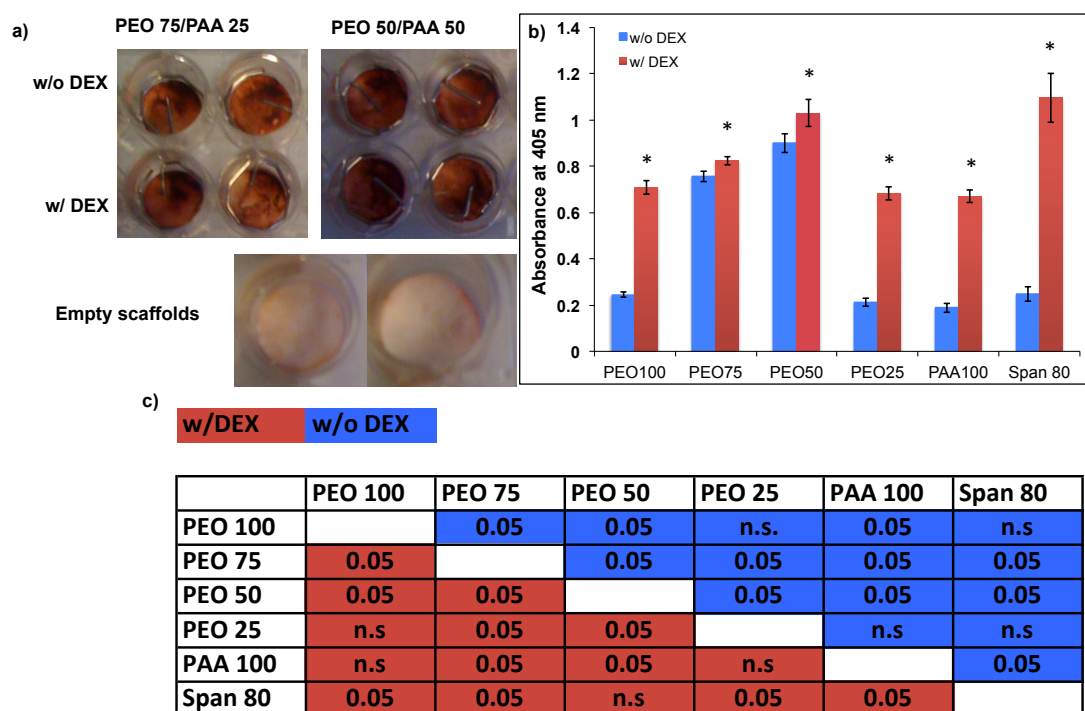


Figure 6.18. Calcium deposition assayed by Alizarin Red S. a) Digital micrographs of cells stained with Alizarin Red on PEO75 and PEO50 foams in the presence and absence of DEX compared to stained empty scaffolds. b) Relative absorbance at 405 for cells treated with and without DEX and c) tabulated significant differences analysed by ANOVA. Data is mean \pm SD, $n=9$. Significant differences indicated by * $p < 0.05$.

However, PEO75 and PEO50 scaffolds exhibited significantly ($p < 0.05$) higher levels of mineral in the absence of DEX compared to other compositions in the same group as shown in Figure 6.18c. Here, (the PEO75 and PEO50 compositions), DEX treatment (although significantly) only slightly increased total absorbance suggesting

that copolymer composition alone has the potential to support hES-MP differentiation.

6.5 Discussion

Together these data generate 3D matrices using a strategy that exploits macromolecular self-assembly and creates chemically and topologically defined surfaces. These data also illustrate how the scaffold patterns can control protein adsorption and thus cell adhesion in a way that better reflects natural heterogeneity in matrix properties. Other systems, which can employ surfaces with discrete, regularly spaced adhesive ligands in 2D^{2,4}, have shown differential cell adhesion, spreading and migration. Cell adhesion and integrin clustering can be reduced or increased by pattern order or disorder, respectively, when inter-ligand spacing exceeds 70 nm³. A similar level of disorder is reflected in the adhesive heterogeneity of native matrix observed here and shown elsewhere¹⁴, and our diblock copolymer foams reflect a similar level of heterogeneity in 3D. We show that our ability to tune the heterogeneity and porosity in foams can directly affect stem cell adhesion and differentiation in a block copolymer domain dependent manner.

6.5.1 polyHIPEs as a 3D scaffold template for stem cell culture

Despite the current advances made in introducing surface functionality to polyHIPEs, many of these techniques do not provide the spatial control of surface chemistry in a 3D matrix. This, achieved by amphiphilic block copolymer phase separation at the oil-water interface provides desirable scaffold properties for 3D cell culture, in particular, for understanding matrix induced stem cell differentiation. A HIPE template provides highly tunable physical and chemical characteristics suitable for cell growth and proliferation e.g. pore size, surface roughness, surface chemistry and interconnectivity. Scaffold pore sizes typically ranging from 100 μm - 600 μm are required to maintain adequate cell infiltration and nutrient exchange^{30,31}; natural biomaterials such as collagen gels sustain excellent cell adhesion and proliferation despite pore sizes of less than 100 μm ³² as they are highly permeable. Depending on emulsion parameters used for cell culture studies, scaffold porosities ranged from 40 μm - 120 μm while maintaining sufficient adhesion and infiltration. With porosity much closer to natural matrices, this suggests that as observed in 2D^{2,33}, adhesive

domains may in fact encourage migration into both closed-porous scaffolds (despite poor interconnectivity) as well as open porous scaffolds that display high permeability. However, interconnectivity of 3D scaffolds or constructs is an important parameter for applications where long *in vitro* cultures or implantation is required²⁷. In these present studies, though closed-porous foams provide a platform to characterise the physicochemical properties of the foams and understand structure-function relationships related to hMSCs, interconnected foams were required for further biological characterisations.

Closed porous polyHIPE templates especially when composed of a mixture of copolymers as they were here, have surfaces with a roughness ranging between 10nm - 50nm. Previous reports using surface topographical features made by electron beam lithography show that substrates with features in excess of 100 nm promote cell adhesion likely via integrin clustering³⁴ and differentiation⁹. Yet there are other studies that describe exceedingly small roughness in the range of ten(s) of nanometers influence adult stem cell differentiation³⁵. In each of these instances, roughness was found to induce osteogenic differentiation. Since scaffold surface roughness was less than 30 nm and composition independent here, roughness may not have influenced stem cell fate to the degree that foam composition did. Given the composition-dependent response for osteogenic genes and global upregulation of myogenic genes in hES-MPs grown on closed-porous foams, it is less certain if hES-MP results are completely roughness- or stiffness- independent. However integrin clustering induced by other HIPE properties, e.g. adhesive domains, may account for the cell and focal adhesion assembly observed and this could ultimately affect differentiation. However, combined with the adhesion trend observed with open-porous foams suggest that adhesive domains may predominate over roughness or stiffness effects.

Most scaffolds with homogeneous surface chemistry do not recapitulate the heterogeneous adhesivity of natural matrix¹⁴. More recently, spatially controlled surface chemistries have been used to better understand how adhesion formation and even differentiation are affected by heterogeneously distributed adhesions in 2D. RGD peptides spaced at small intervals (< 50 nm) favour mature adhesions², spread

cells⁴, and osteogenesis²⁹, whereas larger intervals (> 50 nm) appear to favour an adipogenic fate³⁶ resulting from dynamic adhesions in less spread cells^{2,5}. Given that the link between cell spreading, shape, and fate is due to differences in membrane tension^{29,36} differentiation control by heterogeneous adhesion sites in 2D would appear to have mechanical origins. Scaffold adhesive spots detected by CFMS here were 10-fold larger than the largest domains previously used in these patterned substrates^{2,3} and thus they may support fundamentally different types of adhesions and this size difference may simply be due to detection methods^{21,33}.

Micron-sized pillar arrays also provide discrete adhesion site to cells³⁷, but cell behaviour remains largely unchanged versus continuous surfaces³⁸. Focal adhesion assembly between pillar arrays and continuous substrates are also qualitatively similar; thus differences in hES-MP adhesion observed here with HIPE scaffolds containing well-spaced PS-PAA domains versus conventional substrates are most likely the result of adhesive domains reflecting a length scale more representative of heterogeneously adhesive matrix^{6,14}, i.e. the deviation in adhesion spacing in native fibronectin matrix is similar to that in the foams used here. What is interesting is that despite the differences in foam porosity and surface roughness, the adhesion profiles of hES-MPs follow the same trend with PEO50 and PEO75 supporting well spread cell morphologies.

Protein adsorption at the cell-matrix interface plays an important role in cell adhesion, particularly on synthetic matrices in the absence of recognizable ligand binding sites. Here, we show that upon two hours of fibronectin immobilization on the scaffolds, adsorption occurs through the carboxyl groups of the PAA chains with PEO serving as the non-fouling component of the matrix. Studies have shown the influence of cell-matrix interactions of surface chemistry on the conformation and assembly of proteins at the interface^{39,40}. Hydrophobic surfaces often induce sub-optimal conformations of the adsorption of serum proteins in that hydrophobic groups are often placed towards the substrate surface due to hydrophobic interactions. On the other hand hydrophilic surfaces have been shown to promote adsorption of proteins closer to their native conformations⁴¹. Resulting changes in protein conformation can therefore alter the binding of specific integrins⁴² and

subsequent cell adhesion and differentiation. Taken together, these results combine surface chemistry through non-fouling and adhesive groups as well as their topology, implying that an optimal balance between protein concentration and spatial distribution may be contributing towards the preferential adhesive behavior of the hES-MPs observed here.

6.5.2 Differential stem cell differentiation in response to block copolymer nano-domains

hMSC differentiation depends on Rho-ROCK-induced contractility^{10,29,36} but ultimately relies on sufficient cell adhesion in order to pull against the matrix²⁹. Copolymer composition was not found to influence scaffold stiffness, and such properties could cause composition-independent differentiation. Changing stiffness by altering the monomer to producing softer or elastic foams⁴³ could ultimately modulate stiffness, which would enable one to induce other lineages in a stiffness-dependent fashion⁴⁴. Yet foam stiffness measured by AFM was 2 orders of magnitude higher than what is required to induce a myogenic lineage in 2D culture¹⁰. What this may point to is not the stiffness mismatch with previous work but rather a broader observation that the combination of parameters in 3D is fundamentally different: in 3D, cell fate is not linked to stiffness-induced morphological changes but rather to stiffness regulation of integrin binding and adhesive ligand organization⁴⁵. Thus *in vivo*, a more important coupling of all of these parameters most likely drives fate rather than a reductionist view of any one single matrix property.

What is interesting is that differences in cell adhesion and cytoskeletal spreading were only observed at day 7 but not at days 14, 21 or 28. Thus differential cell responses in the first week indicate that all cells were adherent but not well spread and over time, proliferated independent of copolymer composition. There is increasing evidence suggesting that cell spreading and cytoskeletal tension influence hMSC lineage commitment^{29,36} and thus favour osteogenesis compared to those that are less spread and occupy smaller areas. Well spread cells form a greater number of focal adhesions and more permanent focal adhesions than cells restricted to smaller areas, generating significant cytoskeletal tension. It has been shown that hMSCs must generate a certain threshold of cytoskeletal tension in order to undergo osteogenesis⁴⁶. In contrast, cells that are less spread form less focal adhesions that

tend to be transient and labile in nature. What the current studies suggest is that early changes in cell spreading and cytoskeletal tension is sufficient to induce differentiation (consistent with previous literature) despite that hES-MPs spread and proliferate on all copolymer scaffolds over the period of 28 days.

Although polyHIPEs have shown to be highly tunable matrices for 3D cell culture, certain limitations still prevail. Given the differences observed in scaffold properties depending on the method of HIPE preparation i.e. closed vs open porosity and surface roughness which could not be independently controlled, indicates the difficulty in decoupling the true effects of foam effects on hES-MP adhesion and differentiation. Despite this, several observations remained consistent including copolymer domain dependent adhesion and osteospecific differentiation.

6.5.3 Mechanotransduction pathways

As discussed in Chapter 2, the process of converting a physical stimulus into a biochemical to control cell function is known as mechanotransduction. Of particular importance in recent literature is understanding the molecular basis of matrix physical and chemical properties on hMSC adhesion and fate. Many studies have shown that of focal adhesion proteins such as focal adhesion kinase (FAK) can be activated upon cell attachment to ECM proteins via integrin clustering^{47,48}. This in turn can trigger certain signaling pathways, for example, extracellular regulating kinase (ERK1/2) and thereby induce differentiation of progenitor cells such as hMSCs towards osteogenesis⁴⁹. These studies have wider implications in biomaterials and 3D construct design in which complex differentiation pathways may be triggered by the initial cell attachment to the matrix. Thus, the challenge in designing new scaffolds for controlling cellular functions such as differentiation could rely on mimicking the properties of the ECM; in particular the adhesive heterogeneity. Further experiments to understand how hES-MPs adhere to polyHIPE matrices in a block copolymer dependent manner and how this can control specific differentiation pathways will need to be investigated.

6.5.4 Clinical relevance for bone tissue engineering

The ability to induce osteogenesis on topologically defined foams has potential implications in designing synthetic materials for bone transplants. Bone is the most transplanted tissue (after blood) driving the need for biomaterials based therapies.

The current gold standards for treatment is autografting that usually require further surgery to harvest the patient's own bone often from the iliac crest. In many cases however, this leads to donor site morbidity and complications with secondary surgeries. Alternatively, donor tissue from other patients or species maybe used but these often carry the risk of immune rejection and pathogenic transfer. Thus the use of synthetic materials must not only match the mechanical properties of the tissue and most importantly must be osteoinductive. Biodegradable polymers such as poly(propylene fumerate) (PPF) and PPF composites with β -tricalcium phosphate have shown to have mechanical properties similar to that of trabecular bone⁵⁰. These composites when coated with growth factors such as transforming growth factor β (TGF β) have shown to induce bone growth and development when implanted *in vivo*⁵¹. The effects of bone implants exhibiting surface topography manufactured using numerous commercially available techniques have been extensively reviewed^{52,53}. It has been shown that both micrometre and nanometre length scales enhance osteointegration and bone response, an observation that has been reported *in vitro*⁵⁴ and *in vivo*⁵² and this has shown to be mediated by cell-matrix interactions. The next generation of clinically translatable biomaterials and constructs must eventually consist of both physical, chemical and surface properties in order to enhance cell specific functions for successful therapies.

In the study detailed here, porous polyHIPE foams of compositions exhibited cell adhesion and spreading in a block copolymer domain dependent manner with the foam compositions PEO75 and PEO50 supporting cell spreading. This cell spreading lead to enhanced osteogenesis on the same compositions. Though data relating to the differentiation of hES-MPs is preliminary, polyHIPE foams consisting of appropriate architecture and physicochemical properties may be highly suitable for applications in bone tissue engineering.

6.6 Summary and further work

Together these data show a simple and cost effective method to generate three-dimensional matrices using a strategy that exploits macromolecular self-assembly. This process results in chemically and topologically defined surfaces that control hMSC adhesion and differentiation. The work described here illustrates how topological patterns in a scaffold can control protein adsorption and thus cell

adhesion in a way that better reflects the natural differences in matrix properties. While the work describes adsorbed proteins based on inert (PEO) and adhesive (PAA) copolymers, the results suggest that chemistries with tailored presentation of specific cell recognition peptides, e.g. RGD, could more directly regulate cell-matrix interactions and mimic matrix even better than these PEO/PAA foams. This work also uses a rigid polystyrene backbone, but as shown with hydrogels, controlling mechanical properties is critically important¹⁰; changing the oil phase monomers to viscoelastic ethylhexyl acrylate or methacrylate⁴³ or to biodegradable polycaprolactone⁵⁵ and poly(lactic acid)⁵⁶, all of which have been previously used in the HIPE process, could further soften these foams and make them more clinically translatable. Although hES-MP adhesion was possible on closed-porous scaffolds, long term cultures required open-porous foams recapitulating the need for designing TE constructs that satisfy both architectural needs for cell maintenance as well as physicochemical aspects to control cell behaviour. Regardless of potential modifications, these data show that with careful choice of block copolymer mixtures, HIPE scaffolds can provide a three-dimensional matrix that presents a cue, adhesive heterogeneity, which has the potential to direct stem cell differentiation in the absence of specific growth factors.

6.7 References

1. Arnold, M. *et al.* Activation of Integrin Function by Nanopatterned Adhesive Interfaces. *ChemPhysChem* **5**, 383–388 (2004).
2. Cavalcanti-Adam, E. A. *et al.* Cell Spreading and Focal Adhesion Dynamics Are Regulated by Spacing of Integrin Ligands. *Biophys. J.* **92**, 2964–2974 (2007).
3. Huang, J. *et al.* Impact of Order and Disorder in RGD Nanopatterns on Cell Adhesion. *Nano Lett.* **9**, 1111–1116 (2009).
4. George, P. A., Quinn, K. & Cooper-White, J. J. Hierarchical scaffolds via combined macro- and micro-phase separation. *Biomaterials* **31**, 641–647 (2010).
5. Frith, J. E., Mills, R. J. & Cooper-White, J. J. Lateral spacing of adhesion peptides influences human mesenchymal stem cell behaviour. *J Cell Sci.* **125**, 317–327 (2012).
6. Cukierman, E. Taking Cell-Matrix Adhesions to the Third Dimension. *Science* **294**, 1708–1712 (2001).
7. Singh, P. & Schwarzbauer, J. E. Fibronectin and stem cell differentiation - lessons from chondrogenesis. *J Cell Sci.* **125**, 3703–3712 (2012).
8. Benoit, D. S. W. & Anseth, K. S. The effect on osteoblast function of colocalized RGD and PHSRN epitopes on PEG surfaces. *Biomaterials* **26**, 5209–5220 (2005).
9. Dalby, M. J. *et al.* The control of human mesenchymal cell differentiation using nanoscale symmetry and disorder. *Nat Mater* **6**, 997–1003 (2007).
10. Engler, A. J., Sen, S., Sweeney, H. L. & Discher, D. E. Matrix Elasticity Directs Stem Cell Lineage Specification. *Cell* **126**, 677–689 (2006).
11. Curran, J. M., Chen, R. & Hunt, J. A. The guidance of human mesenchymal stem cell differentiation in vitro by controlled modifications to the cell substrate. *Biomaterials* **27**, 4783–4793 (2006).
12. Trappmann, B. *et al.* Extracellular-matrix tethering regulates stem-cell fate. *Nat Mater* **11**, 642–649 (2012).
13. McMurray, R. J. *et al.* Nanoscale surfaces for the long-term maintenance of mesenchymal stem cell phenotype and multipotency. *Nat Mater* **10**, 637–644 (2011).
14. Reilly, G. C. & Engler, A. J. Intrinsic extracellular matrix properties regulate stem cell differentiation. *J. Biomech.* **43**, 55–62 (2010).
15. Mao, Y. & Schwarzbauer, J. E. Fibronectin fibrillogenesis, a cell-mediated matrix assembly process. *Matrix Biology* **24**, 389–399 (2005).
16. Viswanathan, P. Emulsion Templated Porous Scaffolds for Bone Tissue Engineering. *MPhil Thesis, The University of Sheffield* 1–46 (2010).
17. Lee, K.-Y. & Mooney, D. J. Hydrogels for Tissue Engineering. *Chem. Rev.* **101**, 1869–1880 (2001).
18. Liu, S. Q. *et al.* Synthetic hydrogels for controlled stem cell differentiation. *Soft Matter* **6**, 67 (2009).
19. Massignani, M. *et al.* Controlling Cellular Uptake by Surface Chemistry, Size, and Surface Topology at the Nanoscale. *Small* **5**, 2424–2432 (2009).
20. LoPresti, C. *et al.* Controlling Polymersome Surface Topology at the Nanoscale by Membrane Confined Polymer/Polymer Phase Separation. *ACS Nano* **5**, 1775–1784 (2011).
21. Chirasatitsin, S. & Engler, A. J. Detecting cell-adhesive sites in extracellular matrix using force spectroscopy mapping. *J. Phys.: Condens. Matter* **22**, 194102 (2010).

22. Fernyhough, C., Ryan, A. J. & Battaglia, G. pH controlled assembly of a polybutadiene–poly(methacrylic acid) copolymer in water: packing considerations and kinetic limitations. *Soft Matter* **5**, 1674 (2009).
23. Israels, R., Leermakers, F. & Fleer, G. J. On the Theory of Grafted Weak Polyacids. *Macromolecules* **27**, 3087–3093 (1994).
24. Ballauff, M. & Borisov, O. Polyelectrolyte brushes. *Curr. Opin. Colloid Interface Sci.* **11**, 316–323 (2006).
25. de Peppo, G. M. *et al.* Human Embryonic Stem Cell-Derived Mesodermal Progenitors Display Substantially Increased Tissue Formation Compared to Human Mesenchymal Stem Cells Under Dynamic Culture Conditions in a Packed Bed/Column Bioreactor. *Tissue Eng. Part A* **19**, 175–187 (2013).
26. de Peppo, G. M. *et al.* Osteogenic Potential of Human Mesenchymal Stem Cells and Human Embryonic Stem Cell-Derived Mesodermal Progenitors: A Tissue Engineering Perspective. *Tissue Eng. Part A* **16**, 3413–3426 (2010).
27. Maheshwari, G., Brown, G., Lauffenburger, D. A., Wells, A. & Griffith, L. G. Cell adhesion and motility depend on nanoscale RGD clustering. *J Cell Sci.* **113**, 1677–1686 (2000).
28. Gallant, N. D., Michael, K. E. & Garcia, A. J. Cell Adhesion Strengthening: Contributions of Adhesive Area, Integrin Binding, and Focal Adhesion Assembly. *Mol. Biol. Cell* **16**, 4329–4340 (2005).
29. McBeath, R., Pirone, D. M., Nelson, C. M., Bhadriraju, K. & Chen, C. S. Cell Shape, Cytoskeletal Tension, and RhoA Regulate Stem Cell Lineage Commitment. *Dev Cell* **6**, 483–495 (2012).
30. Hollister, S. J. Porous scaffold design for tissue engineering. *Nat Mater* **4**, 518–524 (2005).
31. Karageorgiuo, V. & Kaplan, D. Porosity of 3D biomaterial scaffolds and osteogenesis. *Biomaterials* **26**, 5474–5491 (2005).
32. Nehrer, S. *et al.* Matrix collagen type and pore size influence behaviour of seeded canine chondrocytes. *Biomaterials* **18**, 769–776 (1997).
33. George, P. A., Donose, B. C. & Cooper-White, J. J. Self-assembling polystyrene-block-poly(ethylene oxide) copolymer surface coatings: Resistance to protein and cell adhesion. *Biomaterials* **30**, 2449–2456 (2009).
34. Geblinger, D., Addadi, L. & Geiger, B. Nano-topography sensing by osteoclasts. *J. Cell Sci.* **123**, 1814–1814 (2010).
35. Oh, S. *et al.* Stem cell fate dictated solely by altered nanotube dimension. *PNAS* **106**, 2130–2135 (2007).
36. Kilian, K. A., Bugarija, B., Lahn, B. T. & Mrksich, M. Geometric cues for directing the differentiation of mesenchymal stem cells. *PNAS* **107**, 4872–4877 (2010).
37. Tan, J. L., Pirone, D. M., Gray, D. S., Bhadriraju, K. & Chen, C. S. Cells lying on a bed of microneedles: An approach to isolate mechanical force. *PNAS* **100**, 1484–1489 (2003).
38. Lee, J., Leonard, M., Oliver, T., Ishihara, A. & Jacobson, K. Traction Forces Generated by Locomoting Keratocytes. *J. Cell Biol.* **127**, 1957–1964 (1994).
39. Ayala, R. *et al.* Engineering the cell–material interface for controlling stem cell adhesion, migration, and differentiation. *Biomaterials* **32**, 3700–3711 (2011).
40. Keselowsky, B. G., Collard, D. M. & García, A. J. Surface chemistry modulates focal adhesion composition and signaling through changes in integrin binding. *Biomaterials* **25**, 5947–5954 (2004).
41. Vogler, E. A. Structure and reactivity of water at biomaterials surfaces. *Adv. Colloid. Interfac.* **74**, 69–117 (1998).
42. Keselowsky, B. G., Collard, D. M. & García, A. J. Integrin binding specificity regulates biomaterial surface chemistry effects on cell differentiation. *PNAS* **102**, 5953–5957 (2005).

43. Cameron, N. R. & Sherrington, D. C. Preparation and glass transition temperatures of elastomeric PolyHIPE materials. *J. Mater. Chem.* **7**, 2209–2212 (1997).
44. Discher, D. E., Mooney, D. J. & Zandstra, P. W. Growth Factors, Matrices, and Forces Combine and Control Stem Cells. *Science* **324**, 1673–1677 (2009).
45. Huebsch, N. *et al.* Harnessing traction-mediated manipulation of the cell/matrix interface to control stem-cell fate. *Nat Mater* **9**, 518–526 (2010).
46. Rowlands, A. S., George, P. A. & Cooper-White, J. J. Directing osteogenic and myogenic differentiation of MSCs: interplay of stiffness and adhesive ligand presentation. *Am. J. Physiol. Cell Physiol.* **295**, 1037–1044 (2008).
47. Salasnyk, R. M., Klees, R. F., Boskey, A. & Plopper, G. E. Activation of FAK is necessary for the osteogenic differentiation of human mesenchymal stem cells on laminin-5. *J. Cell. Biochem.* **100**, 499–514 (2007).
48. Kundu, A. K. & Putnam, A. J. Vitronectin and collagen I differentially regulate osteogenesis in mesenchymal stem cells. *Biochem. Biophys. Res. Commun.* **347**, 347–357 (2006).
49. Salasnyk, R. M., Klees, R. F., Williams, W. A., Boskey, A. & Plopper, G. E. Focal adhesion kinase signaling pathways regulate the osteogenic differentiation of human mesenchymal stem cells. *Exp. Cell Res.* **313**, 22–37 (2007).
50. Fong, E. L. S., Watson, B. M., Kasper, F. K. & Mikos, A. G. Building Bridges: Leveraging Interdisciplinary Collaborations in the Development of Biomaterials to Meet Clinical Needs. *Adv. Mater.* **24**, 4995–5013 (2012).
51. Shin, H., Quinten Ruhé, P., Mikos, A. G. & Jansen, J. A. In vivo bone and soft tissue response to injectable, biodegradable oligo(poly(ethylene glycol) fumarate) hydrogels. *Biomaterials* **24**, 3201–3211 (2003).
52. Wennerberg, A. & Albrektsson, T. Effects of titanium surface topography on bone integration: a systematic review. *Clin. Oral Implan. Res.* **20**, 172–184 (2009).
53. Klymov, A., Prodanov, L., Lamers, E., Jansen, J. A. & Walboomers, X. F. Understanding the role of nano-topography on the surface of a bone-implant. *Biomater. Sci.* (2013).doi:10.1039/c2bm00032f
54. Mendonça, G. *et al.* The effects of implant surface nanoscale features on osteoblast-specific gene expression. *Biomaterials* **30**, 4053–4062 (2009).
55. Lumelsky, Y., Zoldan, J., Levenberg, S. & Silverstein, M. S. Porous Polycaprolactone–Polystyrene Semi-interpenetrating Polymer Networks Synthesized within High Internal Phase Emulsions. *Macromolecules* **41**, 1469–1474 (2008).
56. Busby, W., Cameron, N. R. & Jahoda, C. A. B. Tissue engineering matrixes by emulsion templating. *Polym. Int.* **51**, 871–881 (2002).

Chapter 7: Functionalisation of electrospun fibres using PLA- amphiphilic block copolymers

This chapter is in preparation for publication as:

Directing surface topology and functionality in biodegradable electrospun fibres

7.1 Introduction

Electrospinning is a versatile and facile method technique for generating fibrous mats from a variety of synthetic and natural polymers. The structure and morphology of such fibrous matrices can be controlled from the nano- to the micro- scale and be fabricated as randomly oriented or highly aligned. Much of the literature on electrospinning deals with determining various electrospinning parameters for a specific polymer or gaining control over fibre structure and morphology^{1,2}. Yet surface wettability of substrates is of great importance in many applications in biomedical materials including the creation of protein adhesive or repellent surfaces for applications such as tissue engineering and regenerative medicine. To this end, strategies in surface functionalisation include, but are not limited to plasma treatment³, polymer grafting⁴, physisorption⁵ and chemisorption⁶. Despite these efforts, one of the main challenges with multistep processes is the efficiency of surface functionalisation.

To this effect, recent research has shown that amphiphilic block copolymers may be a candidate for inducing surface segregation. One of the first examples of controlling surface chemistry of electrospun fibres was demonstrated by Deitzel *et al.*, who reported fibre surface modification using fluorinated homopolymers blended with random copolymers of poly(methyl methacrylate) (PMMA)⁷. Similarly, Spontak and coworkers^{8,9} investigated the effects of electric field driven surface segregation by showing that a polarisable peptide segment consisting of serine-glutamic acid-glutamic acid (Ser-Glu-Glu)₃ allowed for the functionalisation of poly(ethylene oxide) (PEO) fibres associated with an increase in solution conductivity⁷. More recently Grafahrend *et al.*¹⁰ utilised a six arm- star PEG polymer blended with poly(lactic-co-glycolic acid) (PLGA) presenting fibre surface hydrophilicity. These

functionalised fibres were shown not only to be protein repellent, but were also found to be biocompatible *in vivo*. *In vitro* studies showed that upon conjugation of bioactive ligands such as RGD in various concentrations, fibres, supported human dermal fibroblast growth and proliferation over 17 days. Many other studies have also demonstrated the use of biodegradable electrospun fibres for hMSC differentiation by controlling matrix physical and chemical properties^{11,12}. As discussed in Chapter 6, the native ECM presents discrete cell binding sites in a 3D fibrillar matrix. However, multi-step surface functionalisation of electrospun fibrous mats often yield in homogeneous surface chemistries.

The aim of this chapter is to demonstrate 3D surface functionalisation of electrospun fibres (figure 3.9, See Chapter 3 Aims and Objectives) of PDLLA (which is inherently hydrophobic) using the amphiphilic block copolymers PMPC-PLA, POEGMA-PLA, PEG-PLA and PDMA-PLA and thus rendering the electrospun fibres hydrophilic in 3D. This approach differs to the ones previously discussed in Chapters 5 and 6 in that electrospinning provides a ‘top-down’ approach to fabricating hierarchically structured materials.

To introduce surface topology as with the foams described in Chapters 6, mixtures of PMPC-PLA and POEGMA-PLA in various molar ratios were electrospun as blends with PDLLA homopolymer to drive phase separation of the POEGMA and PMPC blocks on the surface of the fibres. Since the surface segregation in this case does not rely on interface confinement (like the oil-water interface in HIPEs), parameters controlling surface segregation were explored. Given that both hydrophilic blocks (PMPC and POEGMA) have non-fouling properties, the POEGMA was subsequently functionalised with a linear RGD peptide, thus providing chemistries of adhesive and inert domains to control protein and cell adhesion.

7.2 Methods

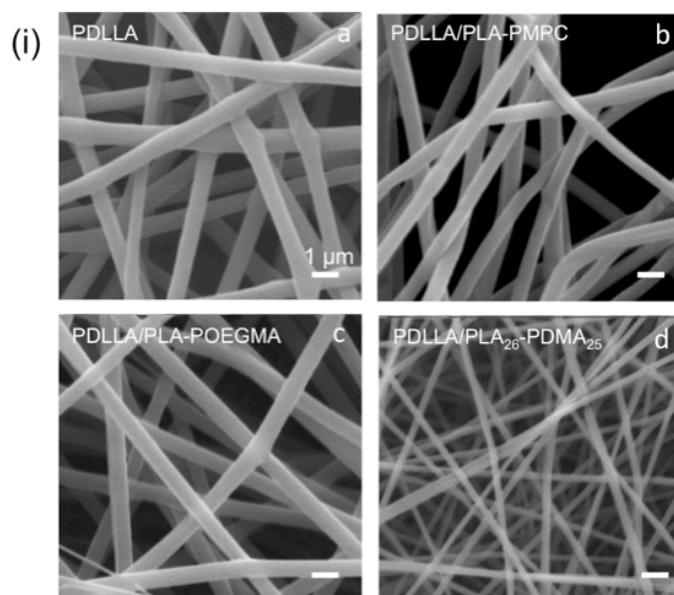
Electrospun fibres of PDLLA mixed with block copolymers of POEGMA-PLA, PEG-PLA, PDMA-PLA and PMPC-PLA were fabricated. Surface functionality and morphology was assessed using scanning electron microscopy, image analysis, and degradation profiles under physiological conditions. Protein (BSA) adsorption after 30 minutes and hES-MP adhesion at 48 hours were qualitatively assessed. hES-MPs cultured on fibres of copolymer mixtures, using RGDC and scrambled DRGC conjugation were assessed for morphologies and cell number after 72 hours. All methods are further detailed in Chapter 4.

7.3 Results and Discussion

7.3.1 Electrospinning and fibre morphologies

Electrospun fibre diameters ranged from $312 \text{ nm} \pm 52 \text{ nm}$ – $931 \text{ nm} \pm 127 \text{ nm}$ for all compositions as shown in Figure 7.1. Consistent bead free fibres were prepared for PDLLA homopolymer and its mixtures with PMPC-PLA and POEGMA-PLA using a solvent mixture of 2:1 by volume of CHCl_3 :MeOH. PDLLA mixtures with PDMA-PLA on the other hand required 3:1 by volume CHCl_3 : DMF. Electrospun fibres of PDLLA are well known to be hydrophobic and is supported here by a static water contact angle of $120^\circ \pm 4^\circ$. All electrospun fibres that incorporated block copolymers on the other hand resulted in hydrophilic fibres (Figure 7.1) indicating surface segregation of the copolymer.

Hydrophilic electrospun fibrous mats using amphiphilic block copolymers demonstrated by Grafahrend *et al.* using PEG-PCL block copolymers of various molecular weights¹³. However, high copolymer solution concentrations ($\sim 30 \text{ wt}\%$) were required to produce bead-free fibres. More recently however, the use of a six-arm star PEG macromer incorporated in the spinning of PLGA fibres resulted in surface functionalisation of the fibres¹⁰.



(ii)

	Fibre diameter / nm	Contact angle/ °
PDLLA	893 ± 143	120 ± 4
PDLLA/ PLA-PMPC	872 ± 210	1 ± 1
PDLLA/PLA-PDMA	312 ± 52	2 ± 1
PDLLA/PLA-POEGMA	931 ± 127	2 ± 1
PDLLA/PLA-PEG	969 ± 146	72 ± 6

Figure 7.1 Representative scanning electron micrographs i) of electrospun fibre morphologies of PDLLA and block copolymer functionalised PDLLA fibres. Average fibre diameters are shown in ii) with PDMA-PLA modified surfaces exhibiting the lowest fibre diameters. Contact angle measurements indicate surface functionalisation. Data is mean ± SD.

Here we demonstrate the universality of this latter approach using PDMA, POEGMA and PMPC chemistries in addition to a commercially available PEG-PLA block copolymer. Electrospinning of block copolymers at molecular weights in the order of 10 kDa is exceedingly difficult at low solution concentrations as sufficient chain entanglement is required for the formation of fibres, yet addition of only a small amount in the electrospinning process (~2-6 wt% in solution, depending on the molecular weight of the copolymer) is exclusively segregated on the surface of the fibre mesh. It has been hypothesised^{8,10} that the charges in the polymer solution may favour the more polar component of the solution, which results in electrostatically driven surface segregation. For example, Spontak *et al.* reported the field driven surface functionalisation of peptide (Ser-Glu-Glu)₃ conjugated PEO⁸. This effect is

further enhanced by charged polymers¹⁰, associated with the PDMA and PMPC blocks in the present studies. Although the PEG-PLA functionalised fibres are more hydrophilic than PDLLA fibres, surface modification using this copolymer was found to be less efficient than all other block copolymer used. This may be a result of the specific block length required and was therefore investigated next.

7.3.2 Block length dependency on surface segregation

The successful surface functionalisation of electrospun fibres using block copolymer additives may depend on the hydrophilic component of the copolymer as well as its molecular weight. To begin with, the effect of the hydrophobic block length was investigated. In these studies, the PDMA block length was maintained between 24-30 while the PLA block length was varied from 26-195 (Table 7.1). Electrospinning conditions (20 kV at a flow rate of 1 ml/hour and tip to needle distance of 15 cm) were kept constant for morphological comparisons. PDLLA fibres formed using the same solvent and spinning conditions had an average fibre diameter of 912 nm \pm 152 nm.

Table 7.1 : PDMA-PLA block copolymers used to study the effect of block lengths. Average fibre diameters (of 100 random fibres) and matrix wettability measured at pH7. n=3

Block Copolymer	M_w / g mol⁻¹	Average Fibre diameter / μm	Contact angle/^o (pH 7)
PDMA ₂₅ -PLA ₂₆	8,060	312 \pm 52	2 \pm 1
PDMA ₃₀ -PLA ₄₁	11,000	523 \pm 92	12 \pm 2
PDMA ₂₈ -PLA ₄₈	11,700	512 \pm 91	17 \pm 2
PDMA ₂₇ -PLA ₅₈	12,980	587 \pm 96	122 \pm 5
PDMA ₂₅ -PLA ₁₁₅	21,200	562 \pm 82	120 \pm 3
PDMA ₂₄ -PLA ₁₉₅	32,260	667 \pm 103	125 \pm 1

Several morphological differences were observed when PDMA-PLA of varying blocks lengths was used. Firstly, for all copolymer block lengths, average fibre diameters were consistently lower than that of PDLLA alone (Figure 7.2a,b). Secondly, as the PLA block length increased from 26 to 195, average fibre diameters increased from 312 nm \pm 52nm to 667 nm \pm 103 nm. Most importantly however, static contact angle measurements indicated complete wettability for fibre meshes

containing PDMA₂₅-PLA₂₆. Fibres with PDMA₃₀-PLA₄₁ and PDMA₂₈-PLA₄₈ exhibited hydrophilicity with contact angles at pH 7 of $12^\circ \pm 3^\circ$ and $17^\circ \pm 4^\circ$ respectively.

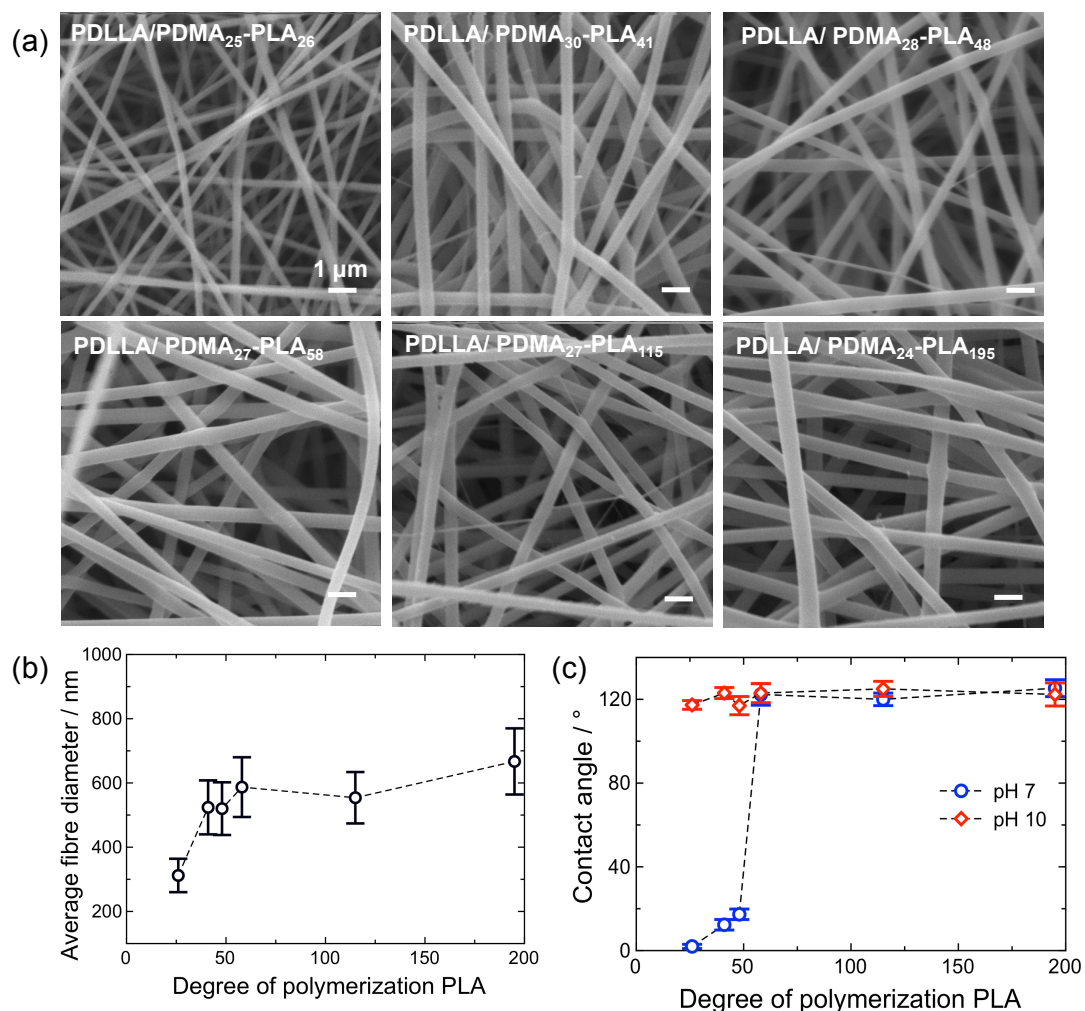


Figure 7.2 a) Representative scanning electron micrographs of PDLLA fibre morphologies using PDMA-PLA copolymers. b) Average fibre diameters of the fibres as a function of PLA block length and c) pH dependent static water contact angle measurements.

All other PDMA-PLA formulations however displayed hydrophobic behaviour. Surface functionalisation with PDMA ($pK_a \sim 7$) was further demonstrated by their wettability at pH 10, where all contact angles were in the hydrophobic range (Figure 7.2c). Interestingly, a gradual decrease in the hydrophilic behaviour of the electrospun fibres was not observed but rather a sudden increase in contact angle from PLA₄₈ to PLA₅₈ demonstrating the region of ideal hydrophobic : hydrophilic block length ratio for fibre surface segregation. Surface segregation is further enhanced by the copolymer with the lowest molecular weight, which in theory exhibits the greatest motility in the polymer solution. Thus during electrospinning,

the process of fibre formation which occurs in the milli- second time scale^{2,7}, PDMA₂₅-PLA₂₆ and to a certain extent PDMA₃₀-PLA₄₁ and PDMA₂₈-PLA₄₈ are sufficiently small enough for segregation at the fibre-air interface to occur.

7.3.3 Degradation profile of functionalised PDLA fibres

The degradation properties of aliphatic polyesters such as PLLA and PDLA have been extensively studied as they are common biodegradable polymers used in a variety of biomedical applications^{12,14}. Polylactides undergo a bulk degradation mechanism by random scissions of the ester backbone with the by-product, lactic acid, broken down in the Krebs cycle¹⁵. However, when implanted, localised increase in the concentration of acidic by products occurs with bulk eroding polymers such as polylactides, and this has shown to produce cytotoxicity^{15,10}. Due to its amorphous nature, PDLA has a lower tensile strength (1.9 GPa)¹⁶ than that of PLLA (4.8 GPa)¹⁷, and consequently loses its tensile strength within the first 1-2 months of hydrolysis¹⁶. Complete mass loss due to hydrolysis has been reported to be within 12-16 months¹⁶. Yet, there are very few reports investigating the effects of hydrophilic additives to the degradation of hydrophobic polymers. The degradation profile of block copolymer functionalised fibres was therefore studied during the first month under physiological conditions. SE micrographs (Figure 7.3) show swollen fibre morphologies in the first 24 hours of degradation at physiological conditions. Fibres continued to swell after 4 weeks, in particular PDLA fibres displayed fused morphologies compared to those with block copolymer formulations. Fibre meshes containing PEG-PLA, resembled PDLA fibre morphologies more closely than the other copolymer ones.

To assess more accurately the degradation of PDMA-PLA functionalised fibres for PLA blocks of 26, 41, 48 which exhibit average fibre diameters from 300 nm-500 nm, electrospun fibres of PDLA homopolymer with fibre diameters in the range of 380 nm ±120 nm were utilised. These fibrous mats were prepared by adjusting the flow rate during the electrospinning process in order to achieve comparable diameters (effects of flow rates discussed in detail, Materials and Methods Chapter 4).

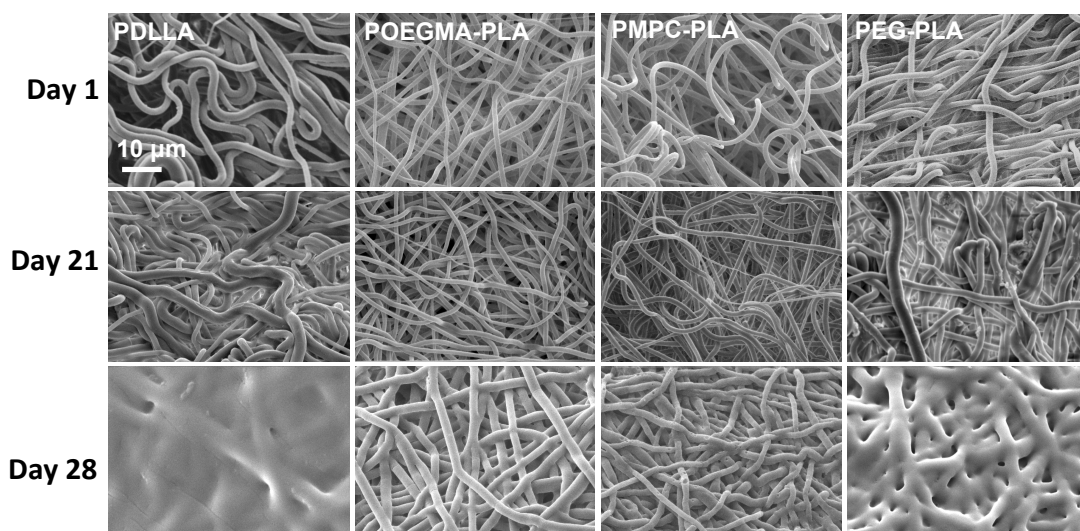


Figure 7.3 Scanning electron micrographs of degradation morphologies of PDLLA electrospun fibres after day 1, day 21 and day 28. Block copolymers POEGMA-PLA, PMPC-PLA and commercially available PEG-PLA were used to functionalise the PDLLA fibres.

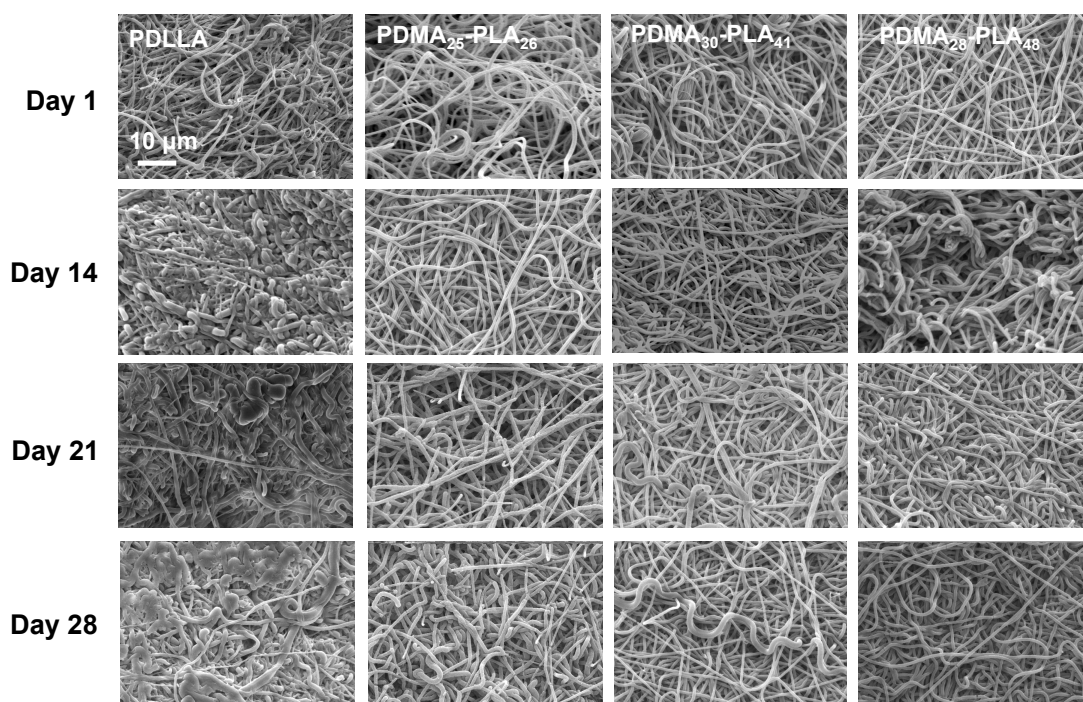


Figure 7.4 Scanning electron micrographs of electrospun fibre morphologies up to 28 days. PDLLA with an average fibre diameter of $310 \text{ nm} \pm 180 \text{ nm}$ was compared with hydrophilic PDMA-PLA functionalised fibres with varying PLA blocks.

PDLLA fibres with lower average diameters showed swelling at day 14 (earlier than those with an average diameter of $893 \text{ nm} \pm 143 \text{ nm}$ electrospun with 2:1 $\text{CHCl}_3:\text{MeOH}$). Interestingly, hydrophilic fibres of PDMA-PLA did not exhibit the same level of fibre swelling or fusing up to 28 days compared to all other copolymer functionalised fibres.

Determination of mass loss during the degradation process indicated a 9% loss for POEGMA-PLA and 7% for PMPC-PLA and 2% for PEG-PLA over 7 days with a continued increase in mass loss over 28 days (Figure 7.5). However, minimal mass loss was exhibited for PDLLA during this period. Similarly, PDLLA fibres of lower average fibre diameters also exhibited no significant mass loss over the 28 days period, despite displaying the most extreme changes in morphology (Figure 7.3, 7.4). In comparison, PDMA-PLA fibres all experienced mass loss after day 1 and this trend continued over 4 weeks. Despite PDMA₃₀-PLA₄₁ and PDMA₂₈-PLA₄₈ having higher contact angles than PDMA₂₅-PLA₂₆, no significant differences was observed in their % mass loss at any measured time point.

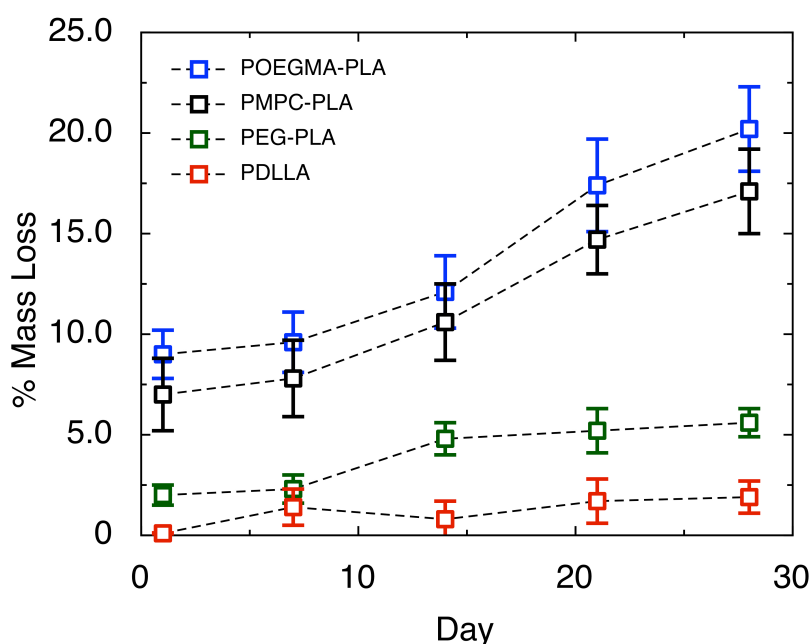


Figure 7.5. Degradation mass loss over a 4 week period of fibres functionalised with PMPC-PLA, POEGMA-PLA, PEG-PLA and PDLLA homopolymer.

The apparent lack of PDLLA degradation may be explained as follows. Due to their hydrophobic nature, PDLLA fibres swell in the initial stages of the degradation process. After a long period of time (months), it is predicted that the swollen state (of PDLLA) leads to rapid disintegration of the material (i.e. hydrolysis of the ester bonds) as polymer chains have sufficiently decreased in length to diffuse out into the aqueous media by this time¹⁶. However, later time points of degradation were not evaluated in this study and therefore, disintegration of the material was not observed.

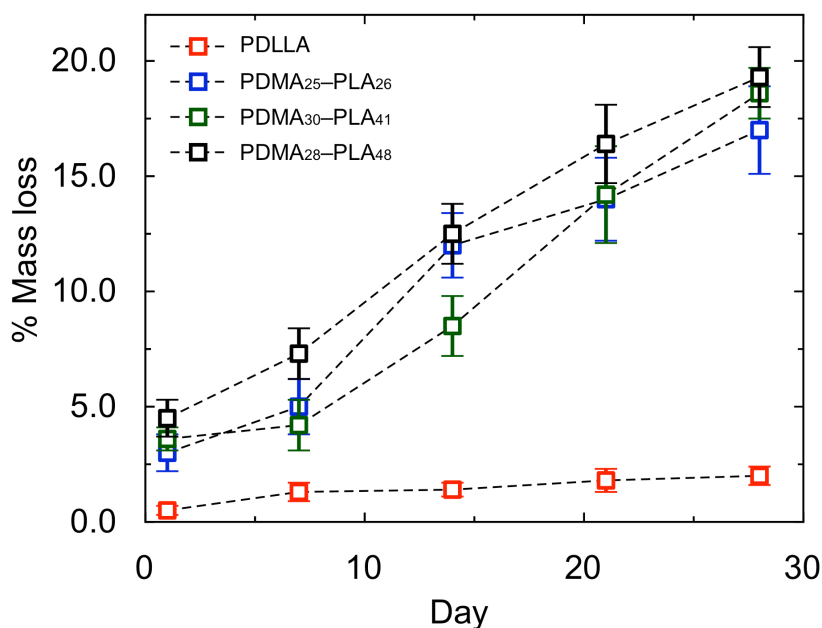


Figure 7.6 Degradation mass loss over a 4 week period of fibres functionalised with PDMA-PLA with varying PLA block lengths and PDLLA homopolymer.

On the other hand, it is expected that hydrophilic materials such as the copolymer functionalised fibres studied here, would undergo surface degradation¹⁸. This would result in loss of mass from the surface of the fibre and a gradual decrease in fibre diameter. Calculated mass loss data (Figures 7.5 and 7.6) clearly showed a greater mass loss profile for POEGMA-PLA and PMPC-PLA functionalised fibres, particularly after the first 24 hours. The apparent exponential increase in mass loss for all copolymer functionalised fibres stems from the loss of the hydrophilic block of the copolymer. For the example shown in Figure 7.7, for PLA-POEGMA versus PLA homopolymer, cleavage by hydrolysis of even one unit of PLA results in the loss of the entire hydrophilic block (for PLA-POEGMA) compared to only one unit of PLA in the case of the homopolymer.

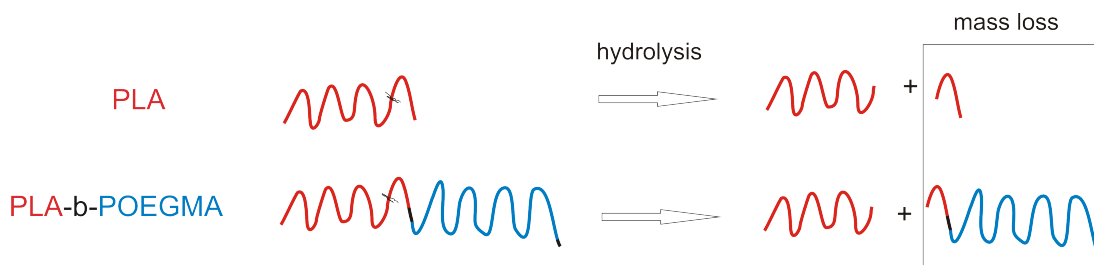


Figure 7.7 Schematic of the degradation mechanism of PLA homopolymer versus PLA-POEGMA functionalised fibres.

However, SE micrographs exhibited morphologies with swollen fibres over 28 days rather than a decrease in fibre diameters, which is not indicative of a surface degradation mechanism. The wettability of the copolymer functionalised fibres results in rapid mass loss of the fibrous mats and also increases accessibility of the aqueous media to the PDLLA core compared to electrospun fibres of PDLLA homopolymer which causes the fibres to swell. I hypothesise that the combination of bulk degradation of the PDLLA matrix and surface degradation of the fibre mesh due to the hydrophilic block of the copolymer results in no visual differences in fibre morphologies.

Understanding degradation rates of the functionalised fibres is of importance in tissue engineering applications. For example, Mooney *et al.* showed that the tailored degradation rates of alginate gels controlled mouse calvarial osteoblast maturation. The authors noted that gels that degraded the fastest, allowed for improved bone formation *in vivo*, and demonstrated greater levels of mineralised and vascularised tissue compared to gels that degraded slower. Degradation at physiological temperatures over 28 days also altered the porosity of these fibres. PDLLA fibres showed the greatest decrease in porosity during this time period (for both fibre diameter ranges) compared to functionalised fibres. Loss of porosity could ultimately hinder cell proliferation, nutrient exchange and removal of metabolic wastes for long term cultures *in vitro* and vascularisation *in vivo*. Whether cultured cells could prevent or delay such morphological changes remains to be investigated. Furthermore, the modification of hydrophobic fibres enables the modification of degradation rates having important consequences for TE implants. Increased hydrophilicity of the PDLLA fibres may result in a more controlled release of acidic by-products and thus reduce cytotoxic effects. To demonstrate this however, longer term degradation studies will need to be conducted.

7.3.4 Adsorption of BSA and adhesion hES-MP

To evaluate the non-fouling (or fouling) properties of the functionalised fibres, the fibres were treated with bovine serum albumin (BSA) conjugated Alexa Fluor 594 for 30 minutes. Qualitative assessment showed protein inhibition on the PEOGMA-PLA and PMPC-PLA functionalised fibres. On the other hand, PDLLA and PDMA-

PLA functionalised fibres indicated BSA adsorption (Figure 7.8). However, BSA was also found to adsorb on PEG-PLA fibres demonstrating insufficient surface functionalisation of PDLLA fibres. To further establish fibre surface functionalisation, the adhesion of human mesenchymal progenitors (hES-MP) was assessed by their ability to spread on the fibrous mats after 48 hours (Figure 7.9).

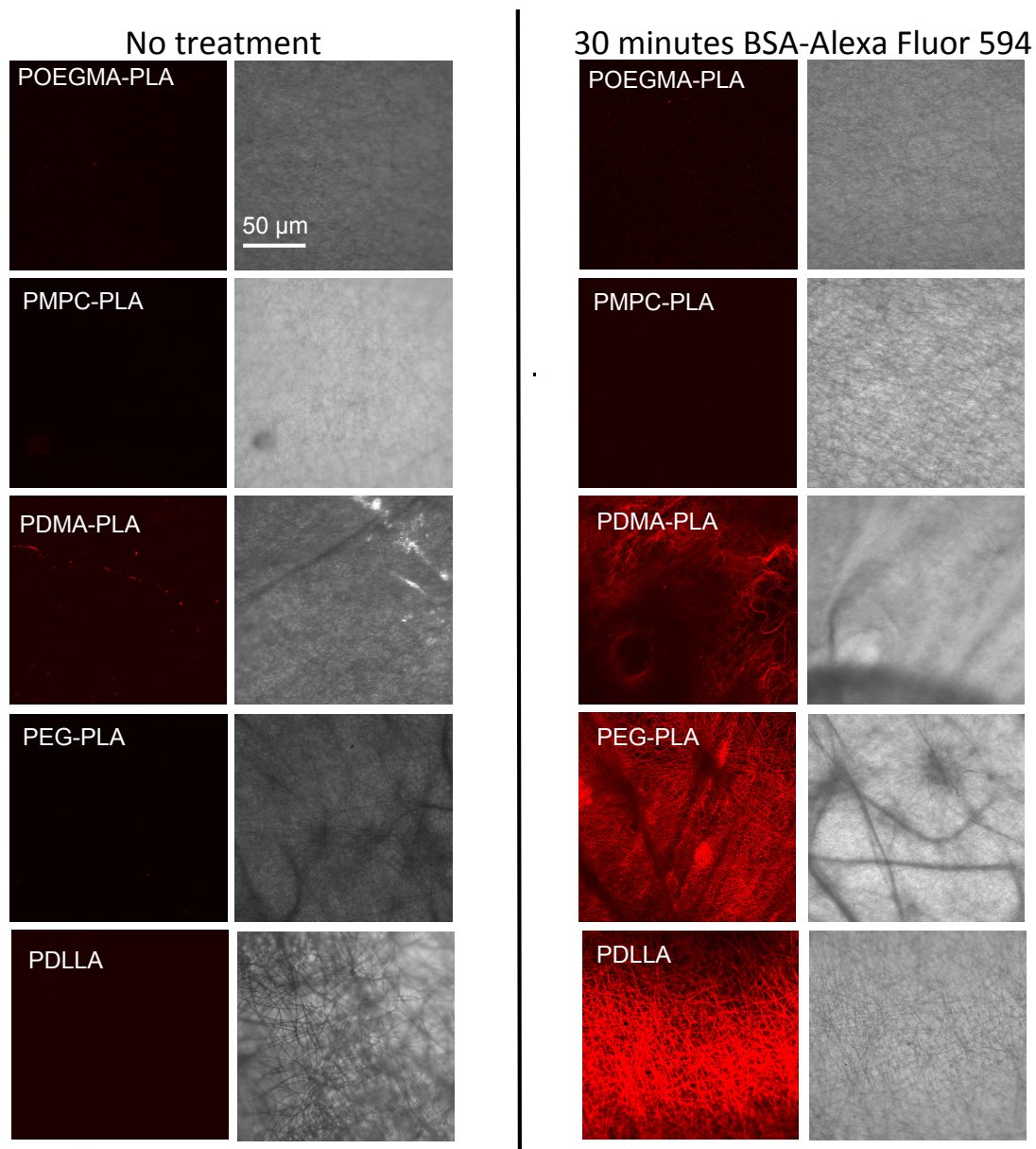


Figure 7.8 Qualitative assessment of protein adsorption on electrospun fibres. (Left) Fluorescence background and optical image of fibres prior to BSA treatment and (Right) Fluorescence of BSA-Alexa Fluor 594 (red) and optical images of electrospun fibres after 30 minutes of protein adsorption compared to untreated samples.

Poor or no cell spreading was noted on PMPC-PLA and POEGMA-PLA functionalised surfaces. On the other hand, hES-MPs were well spread on both PEG-PLA functionalised fibres and PDLLA homopolymer fibres. A large number of cells were observed on PEG-PLA surfaces and this is supported by previous observations with BSA fouling and lower rates of degradation (compared with functionalised

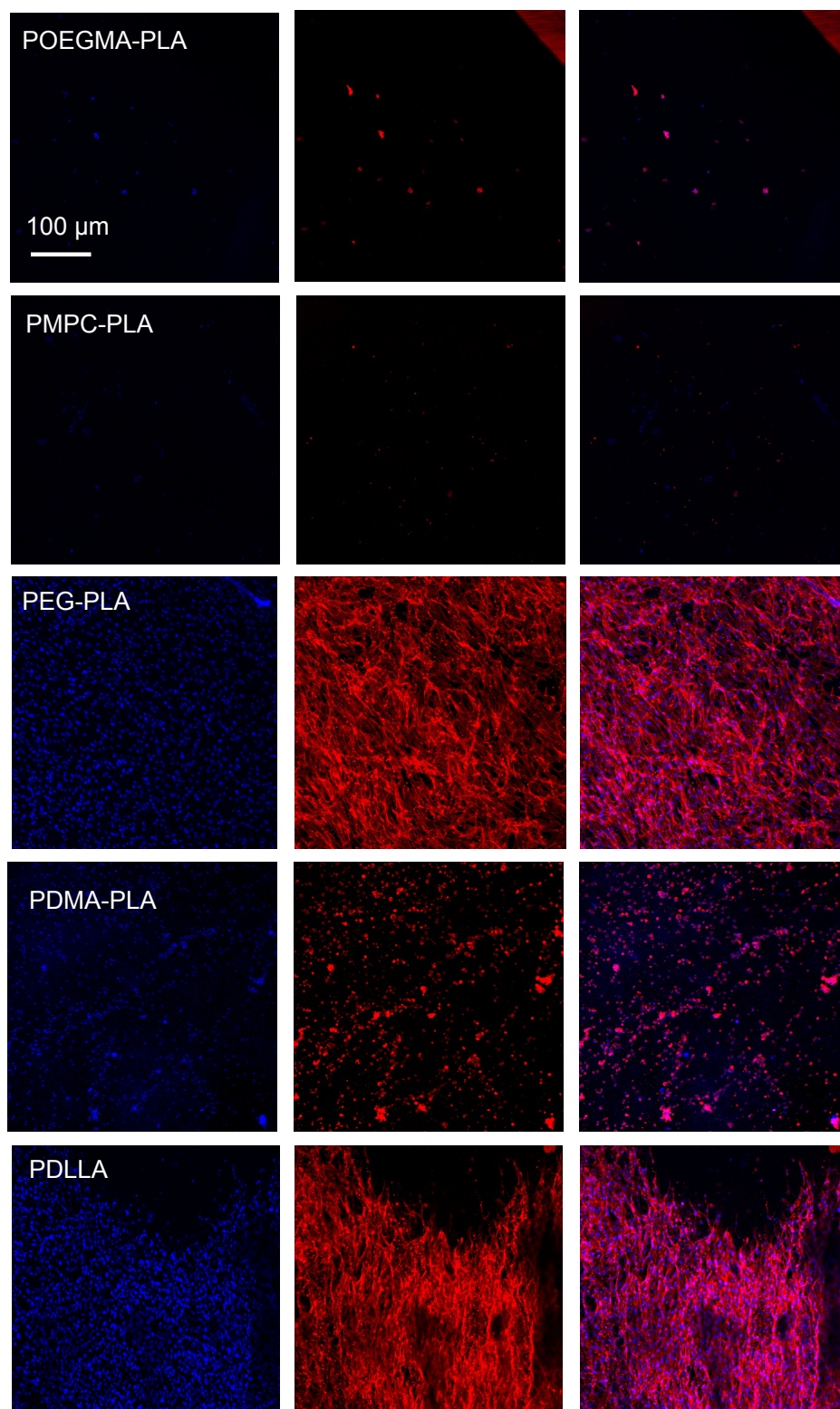


Figure 7.9 hES-MP adhesion after 48 hours of seeding showing well spread morphologies on PDLLA fibres and no cell attachment on both PMPC-PLA and POEGMA-PLA based fibres. Nucleus was stained with DAPI (blue) and the cytoskeleton with Phalloidin Texas Red (red). Images are representative of n=9

fibres of POEGMA-PLA, PMPC-PLA and PDMA-PLA. The apparent inefficiency of surface functionalisation using the PEG-PLA copolymer is probably due to its hydrophobic-hydrophilic ratio. Cells cultured on PDMA-PLA modified fibres

exhibited rounded cell morphologies after 48 hours. Previous studies have demonstrated that cationic polymers in solutions often produce cytotoxicity and cellular stress¹⁹ and this may explain hES-MP morphology on PDMA-PLA modified fibres.

7.3.5 Surface topological effects on hES-MP adhesion and spreading

Fibres functionalised with copolymer mixtures are labelled using the same nomenclature as the foams as indicated in Table 7.2.

Table 7.2 Block copolymer compositions by molar ratio

Name	POEGMA-PLA molar fraction	PMPC-PLA molar fraction
POEGMA100	100	0
POEGMA75	75	25
POEGMA50	50	50
POEGMA25	25	75
PMPC100	0	100

Linear RGDC and scrambled DRGC adhesive peptides were conjugated to the POEGMA block as described in Materials and Methods (Chapter 4). To assess the *in vitro* biocompatibility of the copolymer functionalised electrospun fibres, a non-contact toxicity test was performed as described in Chapter 4 and Chapter 6. hES-MPs cultured for 24 hours were treated with scaffold conditioned media for a period of 48 hours. Figure 7.10 shows cell viability was maintained compared to untreated cells cultured in tissue culture plastic .

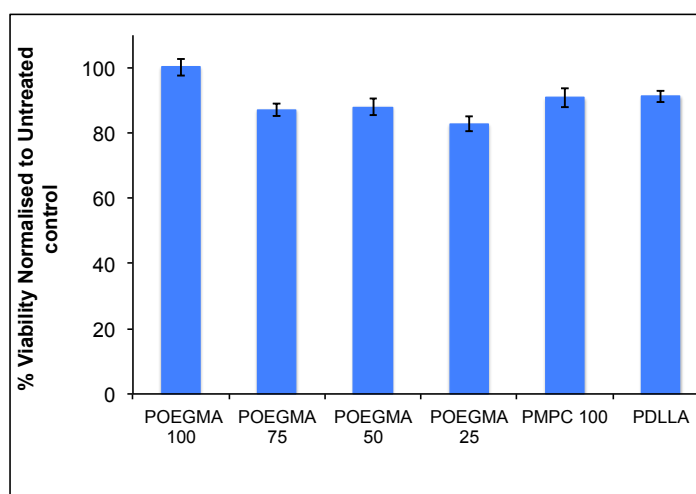


Figure 7.10 Cell viability of hES-MPs cultured on surface functionalised fibres normalised to untreated tissue culture plastic controls. Scaffolds show no toxicity. Data are mean \pm SD, n=3.

The effect of fibre surface copolymer mixtures on hES-MP adhesion and spreading was assessed next. Here, cells were cultured on RGDC and DRGC functionalised fibres through the terminal cysteine of the peptide to the -SH functionalised POEGMA block rendering the POEGMA block as adhesive and the PMPC block as inert. After 72 hours, few cells were found on the scrambled RGD functionalised fibres (Figure 7.11a). The greatest number of cells/mm² were found to be on the PDLLA fibres consistent with images shown in Figure 7.7. PDLLA is a hydrophobic polymer that enhances adsorption of serum proteins (Figure 7.8) and thus allows for a large number of cells to adhere. On the other hand, hES-MPs cultured on RGD functionalised fibres, exhibited a low number of cells adhering to the surfaces with the POEGMA50 surfaces exhibiting not only the largest number of cells compared to other copolymer compositions (Figure 7.11a) but also showed highly spread cells (Figure 7.11b). These preliminary results indicate that the POEGMA50 functionalised fibres support cell adhesion and spreading after the 72 hour time point. However, longer term cell cultures will need to be performed in order to determine if morphological changes occur within the first week (day 7).

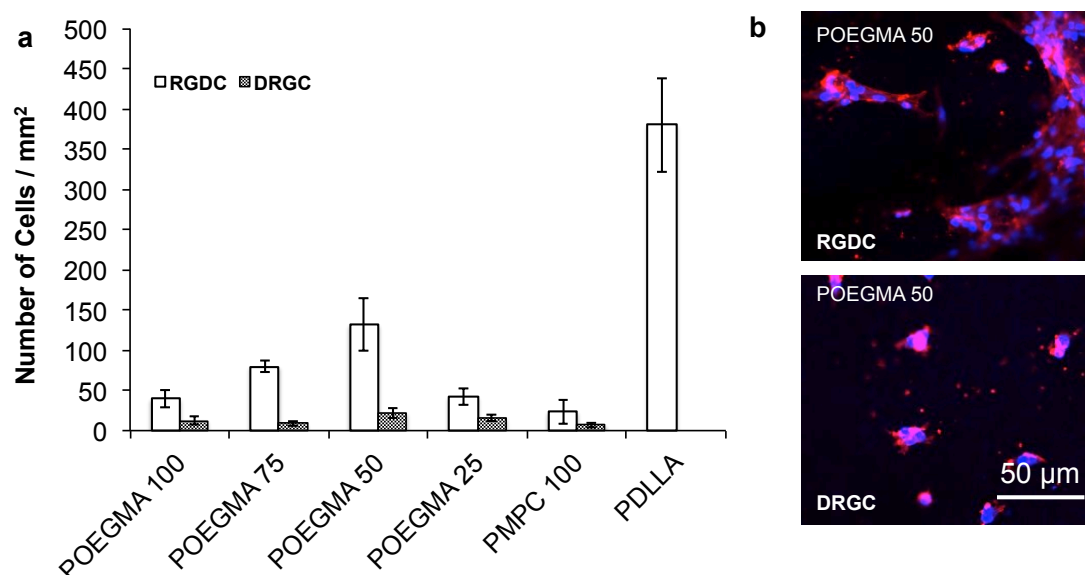


Figure 7.11 Total number of hES-MPs cultured on copolymer functionalised fibres conjugated with both RGDC and DRGC peptide were counted for each composition represented in a). Cell morphology of hES-MPs cultured on POEGMA 50 fibres in b). Data are mean \pm SD, n=3.

It has been shown that fibre diameter and pore size of electrospun fibrous mats are two parameters that are important in influencing cell function. Pore sizes of

electrospun fibres are mainly controlled by the fibre diameter, which in turn can be controlled by processing parameters. Typical cell sizes range from 10 μm - 100 μm ²⁰ and native ECM fibres range from 10nm - 500nm depending on tissue type²¹. Thus scaffold fibre diameters and pore size must be sufficient to support cell attachment, proliferation and the infiltration of cells within the scaffold. For example, on nanometer sized fibres ranging from 100 nm-600 nm, cell migration was found to be greater on the larger fibres (50 μm versus 18 μm) owing to matrix porosity²². Cell attachment and morphology has also shown to be influenced by fibre diameter. Micron sized ($\sim 3 \mu\text{m}$) PLGA fibres have shown to regulate NIH3T3 fibroblast cell morphology by forming larger focal adhesions compared to cells cultured on nanometre sized fibres ($\sim 140 \text{ nm}$)²³. Regulation of cell morphologies can also influence hMSC differentiation mediated by integrin clustering, due to cell-biomaterial interactions²⁴.

In the current studies, POEGMA-PLA and PMPC-PLA functionalised fibres consisted of fibre diameters in the the range of 0.8 μm -1.2 μm . Though this is roughly two-fold larger than native ECM fibres, pore sizes were sufficient to support cell adhesion. However, the effects of the physical architecture of the fibres (e.g. fibre dimensions, alignment) in combination with block copolymer domains and how these parameters affect hES-MP adhesion in long-term cultures and differentiation remain to be investigated further.

7.4 Summary and further work

This chapter describes the functionalisation of PDLLA electrospun fibres using PLA-based amphiphilic block copolymers, in a one step process, which can be controlled by the block copolymer architecture of the copolymer additive. Solvent or temperature annealing protocols could be employed which may affect the kinetics of block copolymer surface segregation and will need to be further investigated.

Functionalised electrospun fibres using amphiphilic block copolymers provides a facile method of fabricating 3D matrices with desired wettability, degradation and protein repellent properties. Conjugation of biologically active motifs such as RGDC to the POEGMA block allows for the regulation of cell-matrix interactions.

Furthermore, the adhesive heterogeneity introduced on the surface of the fibres allows us to control cell shape and morphology as the combination of cell inert and adhesive domains mimics the heterogeneity of the extracellular matrix, though surface mapping remains to be investigated. How these copolymer domains influence hES-MP differentiation based on regulation of cell shape will need to be further investigated. Additionally, how scaffold physical architectures such as fibre alignment, fibre diameter, and pore sizes which have been shown to alter cell responses based on materials properties²² will need to be studied. Regardless of potential scaffold modifications possible with the electrospinning process, the work here suggests that careful choice of block copolymer chemistries using biodegradable polymers could potentially control cell adhesion and stem cell differentiation suitable for *in vivo* applications.

7.5 References

1. Li, D. & Xia, Y. Electrospinning of Nanofibers: Reinventing the Wheel? *Adv. Mater.* **16**, 1151–1170 (2004).
2. Greiner, A. & Wendorff, J. H. Electrospinning: A Fascinating Method for the Preparation of Ultrathin Fibers. *Angew. Chem. Int. Ed.* **46**, 5670–5703 (2007).
3. Yao, C., Li, X., Neoh, K. G., Shi, Z. & Kang, E. T. Surface modification and antibacterial activity of electrospun polyurethane fibrous membranes with quaternary ammonium moieties. *J. Membrane Sci.* **320**, 259–267 (2008).
4. Källrot, M., Edlund, U. & Albertsson, A.-C. Covalent Grafting of Poly(l-lactide) to Tune the In Vitro Degradation Rate. *Biomacromolecules* **8**, 2492–2496 (2007).
5. Casper, C. L., Yamaguchi, N., Kiick, K. L. & Rabolt, J. F. Functionalizing Electrospun Fibers with Biologically Relevant Macromolecules. *Biomacromolecules* **6**, 1998–2007 (2005).
6. Park, K., Ju, Y. M., Son, J. S., K, A. & Han, D. K. Surface modification of biodegradable electrospun nanofiber scaffolds and their interaction with fibroblasts. *J. Biomater. Sci. Polym. Ed.* **18**, 369–382 (2007).
7. Deitzel, J. M. *et al.* Electrospinning of polymer nanofibers with specific surface chemistry. *Polymer* **43**, 1025–1029 (2002).
8. Sun, X. Y., Shankar, R., Börner, H. G., Ghosh, T. K. & Spontak, R. J. Field-Driven Biofunctionalization of Polymer Fiber Surfaces during Electrospinning. *Adv. Mater.* **19**, 87–91 (2007).
9. Sun, X.-Y., Nobles, L. R., Börner, H. G. & Spontak, R. J. Field-Driven Surface Segregation of Biofunctional Species on Electrospun PMMA/PEO Microfibers. *Macromol. Rapid Commun.* **29**, 1455–1460 (2008).
10. Grafahrend, D. *et al.* Degradable polyester scaffolds with controlled surface chemistry combining minimal protein adsorption with specific bioactivation. *Nat Mater* **10**, 67–73 (2010).
11. Yoo, H. S., Kim, T. G. & Park, T. G. Advanced Drug Delivery Reviews. *Adv. Drug Deliver. Rev.* **61**, 1033–1042 (2009).
12. Liang, D., Hsiao, B. S. & Chu, B. Functional electrospun nanofibrous scaffolds for biomedical applications. *Adv. Drug Deliver. Rev.* **59**, 1392–1412 (2007).
13. Grafahrend, D. *et al.* Control of protein adsorption on functionalized electrospun fibers. *Biotechnol. Bioeng.* **101**, 609–621 (2008).
14. Pham, Q. P., Sharma, U. & Mikos, A. Electrospinning of Polymeric Nanofibers for Tissue Engineering Applications: A Review. *Tissue Eng.* **12**, 1197–1211 (2006).
15. Nair, L. S. & Laurencin, C. T. Biodegradable polymers as biomaterials. *Prog. Polym. Sci.* **32**, 762–798 (2007).
16. Tsuji, H. In vitro hydrolysis of blends from enantiomeric poly(lactide)s Part 1. Well-stereo-complexed blend and non-blended films. *Polymer* **41**, 3621–3630 (2000).
17. Tsuji, H. In vitro hydrolysis of blends from enantiomeric poly(lactide)s. Part 4: well-homocrystallized blend and nonblended films. *Biomaterials* **24**, 537–547 (2003).
18. Burkersroda, von, F., Schedl, L. & Gopferich, A. Why degradable polymers undergo surface erosion or bulk erosion. *Biomaterials* **23**, 4221–4231 (2002).
19. Fischer, D., Li, Y., Ahlemeyer, B., Kriegelstein, J. & Kissel, T. In vitro cytotoxicity testing of polycations: influence of polymer structure on cell viability and hemolysis. *Biomaterials* **24**, 1121–1131 (2003).

20. Stevens, M. M. Exploring and Engineering the Cell Surface Interface. *Science* **310**, 1135–1138 (2005).
21. Stevens, M. M. Biomaterials for bone tissue engineering. *Materials Today* **11**, 18-25 (2008).
22. Bashur, C. A., Dahlgren, L. A. & Goldstein, A. S. Effect of fiber diameter and orientation on fibroblast morphology and proliferation on electrospun poly(d,l-lactic-co-glycolic acid) meshes. *Biomaterials* **27**, 5681–5688 (2006).
23. Sisson, K., Zhang, C., Farach-Carson, M. C., Chase, D. B. & Rabolt, J. F. Fiber diameters control osteoblastic cell migration and differentiation in electrospun gelatin. *J. Biomed. Mater. Res.* **94a**, 1312-1320 (2009).
24. Xie, J. *et al.* The differentiation of embryonic stem cells seeded on electrospun nanofibers into neural lineages. *Biomaterials* **30**, 354–362 (2009).

Chapter 8: Conclusions and Future Directions

8.1 Development of 3D matrices- What's been achieved

The three-dimensional functionalisation of porous polystyrene foams was achieved by employing amphiphilic block copolymer surfactants in the HIPE process with molecular weights two orders of magnitude higher than that of traditional low molecular weight surfactants such as Span 80. Functionalisation was hypothesised to occur either through chemical or physical entanglement. Controlling the architecture of the polyHIPE foams is important for tissue engineering applications. The open porosity and interconnectivity of the foams was found to be dependent on the locus of the radical initiator used. Oil phase initiation led to open porous foams while aqueous phase initiation led to closed porous foams. It was proposed that the location of the initiator determined the rate of droplet coalescence and this alone was sufficient to determine the final porosity of the foams. The physical architecture of the foams could be further fine-tuned by optimising emulsion processing conditions.

For the specific application of TE construct design requires complexity in the scaffold's physical and chemical properties mimicking the native extracellular matrix. Therefore, the ability of two dissimilar block copolymers to phase separate at the oil-water interface of the emulsion was exploited by mixing two different block copolymers with cell specific chemistries i.e. PEO (cell inert) and PAA (cell adhesive). This generated 3D functionalised foams with heterogenous adhesive sites, mimicking this property of native extracellular matrix. To date, such well defined surfaces have been produced widely in 2D substrates but not in 3D.

Electrospinning, which is used extensively to fabricate porous fibrous matrices as TE constructs was used as a top down approach for surface functionalisation. Furthermore, the use of a biodegradable and FDA approved polymer such as PDLA, which allows translation into *in vivo* applications. The work done here, using amphiphilic PLA block copolymers as additives is in agreement with recently published work by Grafarhend *et al.* who demonstrate similar findings using a 6-arm

star PEG polymer¹. Here, the authors electrospun a blend of the amphiphilic polymer (5 wt%) with PLGA which resulted in a surface functionalised fibrous matrix. The fibres also exhibited faster degradation rates compared to hydrophobic electrospun PLGA fibres. Here however, the universality of this approach was demonstrated using a variety of block copolymer chemistries, opening the possibility of using a wide range of amphiphilic block copolymers to functionalise electrospun fibres. Protein adsorption and degradation profiles of functionalised fibres were in good agreement with the study published by Grafarhend *et al.* As with the foams, the mixing of two dissimilar copolymers PLA-POEGMA and PLA-PMPC was attempted, though the phase separation between POEGMA and PMPC resulting in 'patchy' fibres will need to be fully characterised. The conjugation of a cell recognizable peptide on the POEGMA block enabled direct analysis of cell-matrix responses to surface domains.

8.1.1 Future directions

There are still many physical and chemical aspects yet to be developed with the polyHIPE foams.

- 1) Physical architecture of the foams will still need to be optimised to understand the origin of surface roughness and topographical features. Though experiments in this thesis found this effect to be dependent on the polymerisation radical initiators chosen, further experiments open up the possibility to further control foam surface topographies and study its effects on hMSC differentiation *in vitro*.
- 2) Further chemical modifications could be introduced by either altering the choice of block copolymer surfactants or through conjugation of functional groups, peptides or enzymes that are potentially useful for many applications including solid phase supports for heterogeneous catalysis, bio catalysis, water purification or separation processes.
- 3) To make polyHIPE foams translatable into *in vivo* applications, the underlying matrix, i.e. the oil phase monomers could be replaced with biodegradable monomers such as poly(lactic acid), poly(caprolactone) or in particular poly(propylene fumarate) which has been shown to be osteoinductive and have the ideal mechanical properties for bone implants^{2,3}. The combination of

osteoinductive materials and block copolymer adhesive domains, polyHIPE foams may potentially provide the ideal scaffold properties for bone tissue engineering.

Electrospun fibres are currently being used for many applications besides three-dimensional matrices for regenerative medicine applications. The development of functionalised fibres from super hydrophobic materials to hydrophilic materials are in demand for applications such as supports for enzymes and catalysis, membrane filters, and as 'smart' textiles. Development of current electrospun functionalised fibres include:

- 1) Exploring annealing protocols to determine efficiency of surface functionalisation for those fibres that exhibited inefficient surface functionalisation
- 2) Investigating block copolymer architecture required for surface modification. As we investigated the dependence of hydrophobic:hydrophilic block length ratio of PDMA-PLA block copolymers and their efficiency in surface functionalisation, the effect of the chemical nature itself may play an important role in functionalisation, for example, differences in the polymer brush configuration at the air-solid interface. Extreme examples of this would be PMPC-PLA (or POEGMA-PLA) and PEO-PLA, all having biologically inert properties but have very different brush conformations.
- 3) Although the primary aim of block copolymer additives to functionalise the surface of PDLLA fibres, the presence of the hydrophobic core introduces the possibility of copolymer self-assembly (e.g. micellisation) within the fibre to form a composite. As the block length ratio determines surface functionality, the question remains as to whether block length ratio could also determine block copolymer self assembly within the fibre; micelles, vesicles, or cylinders. Furthermore, the degradability of these fibres means that such composites could be used to encapsulate cargo that would be released over time in addition to controlling cell-matrix interactions.

8.2 Stem cell response- What's been achieved

Human embryonic stem cell derived mesenchymal progenitors (hES-MPsTM) were used as the cell source in all experiments for their ease of availability and their potential to differentiate towards the mesoderm lineage (bone, fat, cartilage, muscle).

When grown on polystyrene foams functionalised with mixtures of PBD-PEO and PS-PAA, hES-MPs were found to adhere in a block copolymer domain dependent manner, with maximal adhesion found to be on PEO75 and PEO50 foams. Stem cell adhesion in this case was found to be directly related to adsorption of serum proteins, also domain dependent, possibly by altering integrin binding and clustering. These compositions furthermore were shown to mimic the adhesive heterogeneity found in native matrix by labeling adhesive sites in fibronectin. As adhesion and morphology has been widely implicated in hMSC fate, the ability of hES-MP differentiation into various lineages was determined by a qPCR microarray with osteogenesis being favoured on PEO75 and PEO50 based foams. Analysis of mineral deposition indicated that specific copolymer foam compositions could potentially direct adhesion and differentiation in the absence of soluble growth factors. Chapter 7 demonstrated that the hES-MPs cultured on 'patchy' fibres of POEGMA-PLA and PMPC-PLA mixtures where RGDC was conjugated to the POEGMA block, enabled cell adhesion to its matrix to be controlled directly through biologically active motifs. Preliminary studies identified that a surface consisting of 50% adhesive binding sites (RGD-POEGMA 50) allowed hES-MPs to spread the greatest.

8.2.1 Future directions

Further work in understanding cell-matrix interactions in stem cell differentiation would require work on identifying specific mechanotransduction pathways involved.

- 1) The MAPK and ERK1/2 pathways have been widely implicated in osteogenesis⁴ in studies that use mesenchymal stem cells and other progenitor cells. Together with the observations of block copolymer domain dependent osteogenesis, investigations of specific pathways involved and osteogenic gene regulation will need to be studied further.
- 2) Cell adhesion to a substrate is mediated by integrins and are possibly one of the earliest cues in mediating cell responses. For block copolymer dependent cell adhesion and spreading, it will be interesting to determine specific integrins involved in hES-MP (or hMSC) adhesion and the eventual lineage fate decisions.
- 3) Mechanical stimulus of hMSCs such as tensile loading or fluid flow induced shear stress has shown to be important has shown to influence osteo- and chondrogenesis^{5,6}. This is not surprising as bone and cartilage are load bearing

tissue. Thus, a bioreactor for 3D cell culture could be used to subject cells seeded onto the scaffold with fluid induced shear forces. Subsequent analysis on gene regulation and matrix production will need to be investigated. This will not only test the effects of mechanical stimulus but also test the robustness of the scaffolds patterned with adhesive sites.

Stem cell responses to electrospun fibres was limited to adhesion and thus many aspects of this project still require further work:

- 1) As with the polyHIPE foams, the hMSC differentiation inducing capabilities of functionalised fibres need to be investigated.
- 2) Aligned electrospun fibres have been primarily used for neuronal cell alignment and outgrowth. They have also shown to enhance osteogenesis and mineral production of hES-MPs and control collagen alignment⁵. It would be interesting to explore the effects of fibre alignment and adhesive heterogeneity on a) osteogenic differential capability of hMSCs and b) compare the outcomes with randomly oriented fibres.
- 3) Degradation of fibres could ultimately affect cell-matrix interactions and hESMP differentiation. In the work presented in Chapter 7, the PLA copolymers are not covalently linked to the matrix and thus surface functionality is temporary. The effect of changing the matrix core to PCL (slower degradation rate than PDLLA) or PLGA 50/50 (which degrades in approximately 1 week) and subsequent hMSC adhesion and differentiation will need to be investigated.

8.3 The life and times of tissue engineering and regenerative medicine: where are we headed next?

Though the field of tissue engineering and regenerative medicine enjoyed much success in the 1990's; for example, TE skin equivalents were entering clinical trials in 1997 as well as a myriad of replacement devices were already approved by the FDA or in clinical trials for a variety of organ replacement therapies. Much of this success was attributed to financing from the private sector, which accounted for roughly 90% of the funding. By the early part of 2000, this resulted in 70 start-up companies yielding a combined annual expenditure of \$600 million growing at rate of 16% each year. By 2001 however, the tissue engineering industry suffered through

a period of colossal failures coinciding with the world wide dot-com crash. Exponential decrease in private investment lead to the failure and decline of many of these start-up companies that relied heavily on investment capital for daily operations of their business. To worsen the situation, initial private investment in regenerative medicine increased the emphasis on applied research and product development rather than research in basic science which lead to problems in product shelf-life, product scale-up, quality control and other product related issues. This meant that many of the existing products failed to get FDA approval and many of the clinical trials abandoned either due to problems with the product or for financial reasons⁸.

Despite this collapse, the regenerative medicine industry bounced back in 2003 hoping to keep its promise to provide a routine, cost-effective and functional replacement of failed or deteriorated organs or tissues. Firstly, interest from the public sector provided much needed help; by 2008 U.S government spending on organ replacement had reached \$2.4 billion, accounting for two-thirds of total funding for tissue engineering⁹. Most importantly however, the focus on research has shifted towards understanding the basic sciences and principles underlying product development- particularly in the design and synthesis of new biomaterials. This has emerged from understanding the effects of physical and chemical properties of materials in controlling cellular behaviour and functions at the molecular level in order to effectively restore normal tissue function. The clinical drive for regenerative medicine will remain particularly in musculoskeletal disorders as the costs related to their treatments continue to rise in the developed world, particularly with the aging population. Thus, the need for tissue engineering and regenerative medicine alongside continued fundamental research in biological, materials and physical sciences will produce fruitful results for this field in the hope of improving patient healthcare in the future.

8.4 References

1. Grafahrend, D. *et al.* Degradable polyester scaffolds with controlled surface chemistry combining minimal protein adsorption with specific bioactivation. *Nat Mater* **10**, 67–73 (2010).
2. Fong, E. L. S., Watson, B. M., Kasper, F. K. & Mikos, A. G. Building Bridges: Leveraging Interdisciplinary Collaborations in the Development of Biomaterials to Meet Clinical Needs. *Adv Mater*. **24**, 4995–5013 (2012).
3. Christenson, E. M., Soofi, W., Holm, J. L., Cameron, N. R. & Mikos, A. G. Biodegradable Fumarate-Based PolyHIPEs as Tissue Engineering Scaffolds. *Biomacromolecules* **8**, 3806–3814 (2007).
4. Yee, K. L., Weaver, V. M. & Hammer, D. A. Integrin-mediated signalling through the MAP-kinase pathway. *IET Syst. Biol.* **2**, 8 (2008).
5. Delaine-Smith, R. M. Mechanical and physical guidance of osteogenic differentiation and matrix production. *PhD Thesis, The University of Sheffield* 1–238 (2013).
6. Delaine-Smith, R. M. & Reilly, G. C. *Vitamins & Hormones*. **87**, 417–480 (2011).
7. Xiao, Z. S. & Quarles, L. D. Role of the polycytin-primary cilia complex in bone development and mechanosensing. *Annals of the New York Academy of Sciences* **1192**, 410–421 (2010).
8. Mason, C. The Industry Comes of Age. *Medical Device TEchnology* 25–28 (2007).
9. Place, E. S., Evans, N. D. & Stevens, M. M. Complexity in biomaterials for tissue engineering. *Nat Mater* **8**, 457–470 (2009).

Appendix

Table 1. Data of heat map of hES-MP gene expression after 7 days in culture on the indicated foams. All data is displayed as a fold change from undifferentiated cells.

Symbol-GID	Description	PAA100	PEO25	PEO50	PEO75	PEO100	Note
CD4- Hs00181217_m1	CD4 antigen (p55)	1.370116	3.207447	1.288065	0.871861	0.833891	MSC-like
CD44- Hs01075861_m1	CD44 antigen	1.176511	2.001224	1.483954	1.134273	1.43661	MSC-like
CD9- Hs00233521_m1	CD9 antigen (p24)	1.229727	1.684523	1.662585	0.516272	0.686614	MSC-like
ITGA1- Hs00235030_m1	Integrin, alpha 1	-0.34598	0.84502	-0.15684	0.689366	-0.18697	MSC-like
ITGA2- Hs00158127_m1	Integrin, alpha 2 (CD49B, alpha 2 subunit of VLA-2 receptor)	1.748009	2.602612	2.182825	1.009742	1.94884	MSC-like
ITGA3- Hs01076873_m1	Integrin, alpha 3 (antigen CD49C)	0.998752	0.900416	1.244429	1.114809	1.265821	MSC-like
ITGA4- Hs00168433_m1	Integrin, alpha 4 (antigen CD49D)	-1.33921	-0.37502	-0.60694	-0.35844	-0.74294	MSC-like
IL2RA- Hs00907778_m1	Interleukin 2 receptor, alpha (IL2RA)	1.210702	2.089822	0.02299	-0.84001	11.65834	MSC-like
CD34- Hs02576480_m1	CD34 antigen	-1.28782	1.352201	0.323038	0.898934	0.952242	MSC-like
PTPRC- Hs00236304_m1	Protein tyrosine phosphatase, receptor type, C	-0.53591	1.689225	-1.72363	-2.58662	-0.09922	MSC-like
ENG- Hs00923986_m1	Endoglin; CD105	1.074315	1.405897	1.005838	0.625478	1.149467	MSC-like
THY1- Hs00174816_m1	Thy-1 cell surface antigen	1.342088	0.568154	1.085017	0.423678	0.635098	MSC-like
PAX3- Hs00992437_m1	Paired box gene 3	6.127621	4.307693	5.631713	0.983098	2.78054	Myo-like
PAX7- Hs00242962_m1	Paired box gene 7	-1.07343	1.687007	2.817901	3.669572	1.654872	Myo-like
MYOD1- Hs00159528_m1	Myogenic Factor 3 (MYOD1)	4.07241	2.089822	0.02299	-0.84001	0.298948	Myo-like
MYOG- Hs01072232_m1	Myogenic Factor 4 (Myogenin)	0.802932	4.779949	-3.69376	2.824708	3.91242	Myo-like
MYF5- Hs00271574_m1	Myogenic Factor 5	3.806667	-3.00146	7.241888	13.18011	1.483662	Myo-like
MYF6- Hs00231165_m1	Myogenic Factor 6 (herculin)/Mrf4	5.932363	2.089822	8.570708	-0.84001	5.620987	Myo-like
MEOX2- Hs00232248_m1	Mesenchyme homeo box 2 (growth arrest-specific homeo box)	3.978212	2.089822	0.02299	-0.84001	10.9817	Myo-like
FOXC1- Hs01595620_m1	Forkhead box K1 (KIAA0415)/MNF	0.429692	0.142743	0.743707	0.533281	1.036883	Myo-like
MSTN- Hs00976237_m1	Growth differentiation factor 8 (GDF8)/myostatin	6.655553	5.731352	6.52493	6.472233	3.562145	Myo-like
MEF2A- Hs00271535_m1	MADS box transcription enhancer factor 2, polypeptide A	-0.45182	1.829737	0.954687	1.25474	1.1662	Myo-like
LOC729991- MEF2B;MEF2B- Hs01021286_m1	MADS box transcription enhancer factor 2, polypeptide B	0.352557	0.144381	0.684146	0.829969	1.224284	Myo-like

Symbol-GID	Description	PAA100	PEO25	PEO50	PEO75	PEO100	Note
MEF2C- Hs00231149_m1	MADS box transcription enhancer factor 2, polypeptide C	1.435345	1.414376	1.624878	0.842315	1.328415	Myo-like
MEF2D- Hs00232237_m1	MADS box transcription enhancer factor 2, polypeptide D	0.744234	2.122654	1.382121	0.937969	1.0437	Myo-like
GRB2- Hs00157817_m1	Growth factor receptor- bound protein 2	1.517617	2.076399	1.458747	1.00447	1.284202	Myo-like
DES- Hs00157258_m1	Desmin	-0.07962	-0.62614	-1.26241	-0.42643	-1.62812	Myo-like
MSX1- Hs00427183_m1	Msh homeo box homolog 1	0.806522	0.952505	1.657293	0.941516	1.899899	Myo-like
MSX2- Hs00741177_m1	Msh homeo box homolog 2	0.238	1.107536	0.786418	-0.1385	0.93713	Myo-like
LBX1- Hs00198080_m1	Ladybird homeobox homolog 1	0.522552	0.709087	0.072645	0.291362	-2.31762	Myo-like
NRAP- Hs00328987_m1	Nebulin-related anchoring protein	1.210702	2.089822	0.02299	-0.84001	0.298948	Myo-like
MYOT- Hs00199016_m1	Titin immunoglobulin domain protein (myotilin)	-8.27747	-4.494	-8.09781	-6.86087	-8.43879	Myo-like
TTN- Hs00399225_m1	Titin	1.210702	2.089822	2.386893	-0.84001	1.402737	Myo-like
CDH15- Hs00170504_m1	Cadherin 15, M-cadherin (myotubule)	1.210702	6.980902	0.02299	9.540572	0.298948	Myo-like
ITGB1- Hs01127543_m1	Integrin, Beta 1D	0.088255	0.847759	0.314917	0.222432	0.069572	Myo-like
ITGA7- Hs01056475_m1	Integrin, Alpha 7 (Muscle)	1.144128	0.232152	0.45989	-0.12575	-1.65607	Myo-like
RUNX2- Hs01047976_m1	Core Binding Factor Alpha 1	-0.04613	1.116269	0.29063	0.457558	0.965867	Osteo-like
CDH11- Hs00901475_m1	Cadherin 11, type 2, OB- cadherin (osteoblast)	-0.19213	0.391462	-0.10014	0.248083	-0.24644	Osteo-like
SPP1- Hs00959009_m1	Secreted phosphoprotein 1 (osteopontin)	2.486393	3.239134	3.664667	2.603084	2.966988	Osteo-like
TFIP11- Hs00201749_m1	Tuftelin interacting protein 11	0.771565	2.062508	1.155049	0.443461	0.751975	Osteo-like
TWIST1- Hs00361186_m1	Twist homolog 1 (acrocephalosyndactyly 3)	0.510055	0.994984	0.979656	0.740772	0.234266	Osteo-like
TWIST2- Hs00382379_m1	Twist homolog 2	4.580946	6.480531	2.331914	0.824672	0.721357	Osteo-like
SOX9- Hs00165814_m1	SRY (sex determining region Y)-box 9	1.044182	0.796241	1.926098	1.555717	1.698624	Osteo-like
SMAD1- Hs00195432_m1	SMAD, mothers against DPP homolog 1	0.144588	0.631538	-0.1777	0.085283	0.155667	Osteo-like
SMAD2- Hs00183425_m1	SMAD, mothers against DPP homolog 2	0.351553	1.364225	0.513051	0.270203	0.445436	Osteo-like
SMAD3- Hs00232222_m1	SMAD, mothers against DPP homolog 3	-0.03329	0.989969	0.694163	0.744128	0.764377	Osteo-like
SMAD4- Hs00929647_m1	SMAD, mothers against DPP homolog 4	-0.00774	0.701569	-0.00271	0.116345	-0.0424	Osteo-like
SMAD5- Hs00195437_m1	SMAD, mothers against DPP homolog 5	0.204285	1.051782	0.627987	0.227967	0.683526	Osteo-like
SMAD6- Hs00178579_m1	SMAD, mothers against DPP homolog 6	1.523452	0.319158	1.659174	0.949842	1.287539	Osteo-like
SMAD7- Hs00998193_m1	SMAD, mothers against DPP homolog 7	0.411051	-0.781	0.337799	-0.12491	0.078205	Osteo-like
SMAD9- Hs00195441_m1	SMAD, mothers against DPP homolog 9	-0.41438	-0.29953	0.121894	0.072878	0.300673	Osteo-like

Symbol-GID	Description	PAA100	PEO25	PEO50	PEO75	PEO100	Note
VDR- Hs00172113_m1	Vitamin D receptor (1,25-dihydroxyvitamin D3)	-0.18337	-0.245	-0.04795	0.292137	0.574133	Osteo-like
BGLAP;PMF1- BGLAP- Hs00609452_g1	Bone gamma-carboxyglutamate (gla) protein (osteocalcin)	1.291338	1.123254	1.126962	0.393117	1.12273	Osteo-like
BMP1- Hs00241807_m1	Bone morphogenetic protein 1	0.194126	-0.2465	-0.05183	0.339318	0.138458	Osteo-like
BMP2- Hs01055564_m1	Bone morphogenetic protein 2	-0.19121	1.838459	2.071197	1.080267	1.610882	Osteo-like
BMP3- Hs00609638_m1	Bone morphogenetic protein 3	-2.03472	-5.01265	-6.31602	-6.16644	3.178457	Osteo-like
BMP4- Hs00370078_m1	Bone morphogenetic protein 4	-1.16564	1.209286	-1.12888	-2.5328	-0.48264	Osteo-like
BMP5- Hs00234930_m1	Bone morphogenetic protein 5	7.703177	4.572305	2.185741	6.525733	-2.62943	Osteo-like
BMP6- Hs01099594_m1	Bone morphogenetic protein 6	7.738475	7.984426	7.112194	5.675396	5.317488	Osteo-like
BMP7- Hs00233476_m1	Bone morphogenetic protein 7 (osteogenic protein 1)	3.043535	0.802279	3.64567	-0.7133	-6.46586	Osteo-like
BMP8B;BMP8A- Hs00236942_m1	Bone morphogenetic protein 8b (osteogenic protein 2)	-6.16931	-8.43494	-6.62353	-10.8985	-9.8516	Osteo-like
BMPR1A- Hs01034909_g1	Bone morphogenetic protein receptor, type IA	0.597017	1.840109	0.642963	0.430449	0.656216	Osteo-like
MGP- Hs00179899_m1	Matrix Gla protein	4.095873	1.221681	4.963249	1.142971	0.843895	Osteo-like
COL1A1- Hs00164004_m1	Collagen, type I, alpha 1	-0.45081	-0.26598	-0.64372	0.046753	-0.4184	Osteo-like
COL1A2- Hs01028970_m1	Collagen, type I, alpha 2	-0.16931	0.05346	-0.45877	0.393743	0.222525	Osteo-like
COL3A1- Hs00164103_m1	Collagen, type 3, alpha 1	-0.95812	-0.58057	-1.4792	-0.50082	-0.85869	Osteo-like
DLK1- Hs00171584_m1	transmembrane protein containing six epidermal growth factor repeats	-1.51341	-0.63429	0.305733	-0.76796	-2.42517	Preadipocyte
PPARG- Hs01115510_m1	peroxisome proliferator-activated receptor (PPAR)	2.884077	1.902169	-5.13058	-1.32321	0.181024	Early Adipose
CEBPA- Hs00269972_s1	modulates the expression of the gene encoding leptin	1.109925	3.260406	1.697435	1.183068	2.677248	Early Adipose
CEBPB- Hs00270923_s1	modulates the expression of the gene encoding leptin	0.20261	0.930149	0.697707	0.206839	0.421634	Early Adipose
KLF15- Hs00362736_m1	Regulation of gluconeogenesis	-0.18834	5.92683	2.97898	2.368645	0.10195	Early Adipose
FABP4- Hs01086177_m1	fatty acid binding protein found in adipocytes; aP2	0.572557	0.424745	0.732056	1.023433	1.456367	Early Adipose
SREBF1- Hs00231674_m1	sterol regulatory element binding transcription factor 1	1.750349	2.166658	1.48862	1.014325	1.389521	General Adipose
GPD1L- Hs00380515_m1	metabolism gene	0.315069	1.07094	0.324758	-0.1343	0.227317	Mid Adipose
LPL- Hs01012569_m1	lipoprotein lipase, which is expressed in adipose tissue	-4.2548	-3.37568	2.977596	6.277777	0.493999	Mid Adipose
NR1H3- Hs00172885_m1	The liver X receptors, LXRA	0.126815	1.287173	0.285751	-0.19987	0.073988	Late Adipose

Symbol-GID	Description	PAA100	PEO25	PEO50	PEO75	PEO100	Note
LEP- Hs00174877_m1	a protein that is secreted by white adipocytes	2.016579	3.978195	6.897295	7.205626	5.162063	Late Adipose
ADIPOQ- Hs00605917_m1	C1Q and collagen domain containing, transcript variant 1	3.49098	6.730573	-1.24541	3.660935	-0.2521	Late Adipose
LIPE- Hs00193510_m1	hydrolyzes stored triglycerides to fatty acids	-1.77349	-0.89437	-2.96121	-3.8242	-2.68525	Late Adipose
GATA2- Hs00231119_m1	Development and proliferation of hematopoietic cell lineage	2.087541	1.62549	2.431866	0.590451	0.605632	Adipose inhibition

Table 2. Significant gene expression of hES-MP after 7 days on each foam grouped by material composition and listed by increasing PEO percentage. Fold change was calculated as a change from undifferentiated cells. P-values were computed for each gene between undifferentiated cells and those cultured on each specific foam composition from triplicate cultures.

Sample	Detector	log ₂ (Fold Change)	-log ₁₀ (P-value)
PAA100	CD44	1.4366095	1.307543438
PAA100	ITGA2	1.948839833	1.008702687
PAA100	ITGA3	1.265820833	1.215043462
PAA100	MEF2A	1.166200167	1.290926129
PAA100	MEF2B	1.2242835	3.721489701
PAA100	MEF2C	1.3284145	1.209596635
PAA100	MEF2D	1.043700167	1.026369774
PAA100	MSX1	1.899899167	1.117417621
PAA100	SPP1	2.9669875	1.804377441
PAA100	SOX9	1.698624167	1.182337561
PAA100	SMAD6	1.2875385	1.134273711
PAA100	BGLAP	1.122729833	1.288320838
PAA100	BMP2	1.610882167	1.621803068
PAA100	BMP3	3.178457167	1.409106909
PAA100	BMP6	5.3174875	1.416550525
PAA100	BMP8B	-9.8516035	1.035096739
PAA100	FABP4	1.4563665	1.839356588
PEO25	CD44	1.134272667	1.569715275
PEO25	ITGA3	1.114809	1.613121156
PEO25	PTPRC	-2.586621667	1.028808262
PEO25	MYF5	13.18011267	1.226736176
PEO25	MSTN	6.472233	1.125586802
PEO25	MEF2A	1.254740333	1.154167363
PEO25	SPP1	2.603084333	1.57664235
PEO25	SOX9	1.555717333	2.045561063
PEO25	BMP2	1.080267	1.54148329
PEO25	BMP6	5.675395667	1.007705118
PEO25	PPARG	-1.323205333	1.080011901
PEO25	KLF15	2.368644667	1.064725403

Sample	Detector	log ₂ (Fold Change)	-log ₁₀ (P-value)
PEO25	SREBF1	1.014325333	1.884200214
PEO25	LEP	7.205625667	1.315838073
PEO25	ADIPOQ	3.660934667	1.534615411
PEO50	CD44	1.4839535	2.529265442
PEO50	CD9	1.662585167	1.645607639
PEO50	ITGA2	2.182825167	1.288776806
PEO50	ITGA3	1.244429167	1.728283709
PEO50	ENG	1.0058375	1.856256035
PEO50	THY1	1.085017167	1.851071757
PEO50	MYF6	8.570707833	1.012208215
PEO50	MEF2C	1.6248775	1.437276164
PEO50	MEF2D	1.382121167	2.37014295
PEO50	GRB2	1.458747167	1.049378102
PEO50	DES	-1.2624065	1.068247905
PEO50	MSX1	1.657293167	1.377289433
PEO50	TTN	2.386892833	1.311853587
PEO50	SPP1	3.664666833	2.383501272
PEO50	TFIP11	1.155049167	2.354892867
PEO50	TWIST2	2.331913833	1.526118402
PEO50	SOX9	1.926097833	2.107487381
PEO50	SMAD6	1.6591735	1.479702586
PEO50	BGLAP	1.126962167	1.002812984
PEO50	BMP2	2.0711965	1.178982348
PEO50	BMP6	7.112193833	1.72532184
PEO50	BMP8B	-6.623532833	1.100109809
PEO50	COL3A1	-1.479204167	1.742023257
PEO50	CEBPA	1.697434833	1.03504124
PEO50	SREBF1	1.488619833	1.404231995
PEO50	LEP	6.897294833	1.270421415
PEO50	GATA2	2.4318655	1.578645186
PEO75	CD4	3.207447167	1.214351228
PEO75	PAX3	4.307693167	1.098657343
PEO75	GRB2	2.0763985	1.09129317
PEO75	TWIST2	6.4805305	1.129542469
PEO75	BMP6	7.9844255	1.086522966
PEO75	BMP8B	-8.434944167	1.754147148
PEO75	KLF15	5.9268295	1.713031612
PEO75	GATA2	1.6254895	1.173399208
PEO100	CD44	1.176510667	1.66269296
PEO100	CD9	1.229727333	1.266974467
PEO100	ITGA2	1.748009333	1.052503485
PEO100	ITGA4	-1.339206333	1.423176711
PEO100	CD34	-1.287815667	1.177140828
PEO100	ENG	1.074314667	1.418569402
PEO100	THY1	1.342087667	1.251046141
PEO100	MSTN	6.655553	1.304053967
PEO100	MEF2C	1.435344667	1.448546672

Sample	Detector	log ₂ (Fold Change)	-log ₁₀ (P-value)
PEO100	GRB2	1.517617333	1.519616411
PEO100	ITGA7	1.144128	1.276446775
PEO100	SPP1	2.486393	1.585573713
PEO100	TWIST2	4.580946333	1.056819717
PEO100	SOX9	1.044181667	1.244705266
PEO100	SMAD6	1.523452	1.52062264
PEO100	BMP4	-1.165639667	2.112114297
PEO100	BMP6	7.738475333	1.12833142
PEO100	BMP8B	-6.169314	1.04879365
PEO100	DLK1	-1.513414	1.046645458
PEO100	SREBF1	1.750348667	1.158045395
PEO100	GATA2	2.087541333	1.353223268

Table 3. Non-significant gene expression of hES-MP after 7 days on each foam grouped by material composition and listed by increasing PEO percentage. Fold change was calculated as a change from undifferentiated cells. P-values were computed for each gene between undifferentiated cells and those cultured on each specific foam composition from triplicate cultures.

Sample	Gene	log ₂ (Fold Change)	-log(P-value)
PAA100	CD4	0.833891	0.56019
PAA100	ITGA1	-0.18697	0.596999
PAA100	CD9	0.686614	0.977806
PAA100	ITGA4	-0.74294	1.501993
PAA100	IL2R	11.65834	0.72076
PAA100	CD34	0.952242	0.54375
PAA100	PTPRC	-0.09922	0.324934
PAA100	ENG	1.149467	0.99152
PAA100	THY1	0.635098	1.092978
PAA100	PAX3	2.78054	0.702173
PAA100	PAX7	1.654872	0.359519
PAA100	MYOD1	0.298948	0.384326
PAA100	MYOG	3.91242	0.600968
PAA100	MYF5	1.483662	0.347402
PAA100	MYF6	5.620987	0.699576
PAA100	MEOX2	10.9817	0.689841
PAA100	FOXK1	1.036883	0.854469
PAA100	MSTN	3.562145	0.822947
PAA100	GRB2	1.284202	0.794028
PAA100	DES	-1.62812	0.765722
PAA100	MSX2	0.93713	0.848409
PAA100	LBX1	-2.31762	0.715958
PAA100	NRAP	0.298948	0.384326
PAA100	MYOT	-8.43879	0.588055
PAA100	TTN	1.402737	0.646946
PAA100	CDH15	0.298948	0.384326

PAA100	ITGB1	0.069572	0.511293
PAA100	ITGA7	-1.65607	0.98175
PAA100	CBFA1	0.965867	0.780886
PAA100	CDH11	-0.24644	1.297909
PAA100	TFIP11	0.751975	0.834324
PAA100	TWIST1	0.234266	0.724392
PAA100	TWIST2	0.721357	0.650768
PAA100	SMAD1	0.155667	0.442296
PAA100	SMAD2	0.445436	1.595488
PAA100	SMAD3	0.764377	1.069225
PAA100	SMAD4	-0.0424	0.385304
PAA100	SMAD5	0.683526	0.973287
PAA100	SMAD7	0.078205	0.428199
PAA100	SMAD9	0.300673	0.415934
PAA100	VDR	0.574133	0.597551
PAA100	BMP1	0.138458	0.498476
PAA100	BMP4	-0.48264	0.377449
PAA100	BMP5	-2.62943	0.542815
PAA100	BMP7	-6.46586	0.84251
PAA100	BMPR1A	0.656216	0.837909
PAA100	MGP	0.843895	0.474238
PAA100	COL1A1	-0.4184	0.832867
PAA100	COL1A2	0.222525	0.576828
PAA100	COL3A1	-0.85869	1.202895
PAA100	DLK1	-2.42517	0.660644
PAA100	PPARG	0.181024	0.307808
PAA100	CEBPA	2.677248	0.862746
PAA100	CEBPB	0.421634	0.817176
PAA100	KLF15	0.10195	0.333013
PAA100	SREBF1	1.389521	0.945024
PAA100	GPD1	0.227317	0.642828
PAA100	LPL	0.493999	0.327143
PAA100	NR1H3	0.073988	0.363055
PAA100	LEP	5.162063	0.68351
PAA100	ADIPOQ	-0.2521	0.348218
PAA100	LIPE	-2.68525	0.54472
PAA100	GATA2	0.605632	0.494272
PEO25	CD4	0.871861	1.043839
PEO25	ITGA1	0.689366	1.338536
PEO25	CD9	0.516272	1.311751
PEO25	ITGA2	1.009742	0.832361
PEO25	ITGA4	-0.35844	1.127891
PEO25	IL2R	-0.84001	0.731369
PEO25	CD34	0.898934	0.579892
PEO25	ENG	0.625478	1.328467
PEO25	THY1	0.423678	1.561236
PEO25	PAX3	0.983098	0.378375
PEO25	PAX7	3.669572	0.458926
PEO25	MYOD1	-0.84001	0.731369
PEO25	MYOG	2.824708	0.679217

PEO25	MYF6	-0.84001	0.731369
PEO25	MEOX2	-0.84001	0.731369
PEO25	FOXK1	0.533281	1.085383
PEO25	MEF2B	0.829969	1.824522
PEO25	MEF2C	0.842315	1.850764
PEO25	MEF2D	0.937969	1.09062
PEO25	GRB2	1.00447	0.85786
PEO25	DES	-0.42643	0.553649
PEO25	MSX1	0.941516	1.23078
PEO25	MSX2	-0.1385	0.467251
PEO25	LBX1	0.291362	0.595063
PEO25	NRAP	-0.84001	0.731369
PEO25	MYOT	-6.86087	0.507383
PEO25	TTN	-0.84001	0.731369
PEO25	CDH15	9.540572	0.740189
PEO25	ITGB1	0.222432	0.756293
PEO25	ITGA7	-0.12575	0.372448
PEO25	CBFA1	0.457558	2.985653
PEO25	CDH11	0.248083	1.815997
PEO25	TFIP11	0.443461	0.996556
PEO25	TWIST1	0.740772	1.19407
PEO25	TWIST2	0.824672	0.83698
PEO25	SMAD1	0.085283	0.981506
PEO25	SMAD2	0.270203	1.59053
PEO25	SMAD3	0.744128	1.286194
PEO25	SMAD4	0.116345	0.679931
PEO25	SMAD5	0.227967	0.884665
PEO25	SMAD6	0.949842	1.91889
PEO25	SMAD7	-0.12491	0.689743
PEO25	SMAD9	0.072878	0.833049
PEO25	VDR	0.292137	0.577797
PEO25	BGLAP	0.393117	0.771672
PEO25	BMP1	0.339318	1.795353
PEO25	BMP3	-6.16644	0.53803
PEO25	BMP4	-2.5328	0.860695
PEO25	BMP5	6.525733	0.613505
PEO25	BMP7	-0.7133	0.343275
PEO25	BMP8B	-10.8985	0.889646
PEO25	BMPR1A	0.430449	1.767304
PEO25	MGP	1.142971	0.468695
PEO25	COL1A1	0.046753	0.467261
PEO25	COL1A2	0.393743	1.037264
PEO25	COL3A1	-0.50082	0.919565
PEO25	DLK1	-0.76796	0.576987
PEO25	CEBPA	1.183068	0.855128
PEO25	CEBPB	0.206839	1.140496
PEO25	FABP4	1.023433	0.783693
PEO25	GPD1	-0.1343	0.520459
PEO25	LPL	6.277777	0.805977
PEO25	NR1H3	-0.19987	0.748088

PEO25	LIPE	-3.8242	0.689036
PEO25	GATA2	0.590451	0.805216
PEO50	CD4	1.288065	0.789179
PEO50	ITGA1	-0.15684	0.389531
PEO50	ITGA4	-0.60694	1.949835
PEO50	IL2R	0.02299	0.315465
PEO50	CD34	0.323038	0.383781
PEO50	PTPRC	-1.72363	0.814043
PEO50	PAX3	5.631713	0.95397
PEO50	PAX7	2.817901	0.396401
PEO50	MYOD1	0.02299	0.315465
PEO50	MYOG	-3.69376	0.655011
PEO50	MYF5	7.241888	0.786365
PEO50	MEOX2	0.02299	0.315465
PEO50	FOKK1	0.743707	0.955182
PEO50	MSTN	6.52493	0.69753
PEO50	MEF2A	0.954687	1.010857
PEO50	MEF2B	0.684146	1.105588
PEO50	MSX2	0.786418	0.957328
PEO50	LBX1	0.072645	0.36207
PEO50	NRAP	0.02299	0.315465
PEO50	MYOT	-8.09781	0.591494
PEO50	CDH15	0.02299	0.315465
PEO50	ITGB1	0.314917	0.93693
PEO50	ITGA7	0.45989	0.610072
PEO50	CBFA1	0.29063	0.579836
PEO50	CDH11	-0.10014	1.3717
PEO50	TWIST1	0.979656	2.348017
PEO50	SMAD1	-0.1777	1.841045
PEO50	SMAD2	0.513051	1.223528
PEO50	SMAD3	0.694163	1.455309
PEO50	SMAD4	-0.00271	0.307004
PEO50	SMAD5	0.627987	1.081983
PEO50	SMAD7	0.337799	0.661724
PEO50	SMAD9	0.121894	0.367507
PEO50	VDR	-0.04795	0.328327
PEO50	BMP1	-0.05183	0.342686
PEO50	BMP3	-6.31602	0.558212
PEO50	BMP4	-1.12888	0.50489
PEO50	BMP5	2.185741	0.353361
PEO50	BMP7	3.64567	0.685545
PEO50	BMPR1A	0.642963	1.226201
PEO50	MGP	4.963249	0.953509
PEO50	COL1A1	-0.64372	1.254904
PEO50	COL1A2	-0.45877	0.903999
PEO50	DLK1	0.305733	0.470358
PEO50	PPARG	-5.13058	0.887252
PEO50	CEBPB	0.697707	0.802679
PEO50	KLF15	2.97898	0.976182
PEO50	FABP4	0.732056	0.571476

PEO50	GPD1	0.324758	0.717779
PEO50	LPL	2.977596	0.702883
PEO50	NR1H3	0.285751	0.625068
PEO50	ADIPOQ	-1.24541	0.427525
PEO50	LIPE	-2.96121	0.649556
PEO75	CD44	2.001224	0.957376
PEO75	ITGA1	0.84502	0.764125
PEO75	CD9	1.684523	0.867042
PEO75	ITGA2	2.602612	0.73057
PEO75	ITGA3	0.900416	1.259719
PEO75	ITGA4	-0.37502	1.317978
PEO75	IL2R	2.089822	0.679279
PEO75	CD34	1.352201	0.73083
PEO75	PTPRC	1.689225	0.46231
PEO75	ENG	1.405897	0.922458
PEO75	THY1	0.568154	1.701189
PEO75	PAX7	1.687007	0.353166
PEO75	MYOD1	2.089822	0.679279
PEO75	MYOG	4.779949	0.665716
PEO75	MYF5	-3.00146	0.669988
PEO75	MYF6	2.089822	0.679279
PEO75	MEOX2	2.089822	0.679279
PEO75	FOXK1	0.142743	0.365708
PEO75	MSTN	5.731352	0.93811
PEO75	MEF2A	1.829737	0.64341
PEO75	MEF2B	0.144381	0.445515
PEO75	MEF2C	1.414376	0.695133
PEO75	MEF2D	2.122654	0.710029
PEO75	DES	-0.62614	1.251718
PEO75	MSX1	0.952505	0.759535
PEO75	MSX2	1.107536	0.525976
PEO75	LBX1	0.709087	1.429359
PEO75	NRAP	2.089822	0.679279
PEO75	MYOT	-4.494	0.478461
PEO75	TTN	2.089822	0.679279
PEO75	CDH15	6.980902	0.676707
PEO75	ITGB1	0.847759	0.961006
PEO75	ITGA7	0.232152	0.439416
PEO75	CBFA1	1.116269	0.702249
PEO75	CDH11	0.391462	0.808456
PEO75	SPP1	3.239134	0.816574
PEO75	TFIP11	2.062508	0.781522
PEO75	TWIST1	0.994984	1.148876
PEO75	SOX9	0.796241	1.633957
PEO75	SMAD1	0.631538	0.959076
PEO75	SMAD2	1.364225	0.75577
PEO75	SMAD3	0.989969	0.747221
PEO75	SMAD4	0.701569	0.824521
PEO75	SMAD5	1.051782	0.838272
PEO75	SMAD6	0.319158	0.471825

PEO75	SMAD7	-0.781	0.554698
PEO75	SMAD9	-0.29953	0.456347
PEO75	VDR	-0.245	0.410207
PEO75	BGLAP	1.123254	0.660117
PEO75	BMP1	-0.2465	0.417375
PEO75	BMP2	1.838459	0.817535
PEO75	BMP3	-5.01265	0.495574
PEO75	BMP4	1.209286	0.469539
PEO75	BMP5	4.572305	0.438353
PEO75	BMP7	0.802279	0.383863
PEO75	BMPR1A	1.840109	0.744446
PEO75	MGP	1.221681	0.390048
PEO75	COL1A1	-0.26598	0.459374
PEO75	COL1A2	0.05346	0.32583
PEO75	COL3A1	-0.58057	0.588652
PEO75	DLK1	-0.63429	0.414138
PEO75	PPARG	1.902169	0.431454
PEO75	CEBPA	3.260406	0.827986
PEO75	CEBPB	0.930149	0.673349
PEO75	FABP4	0.424745	0.453197
PEO75	SREBF1	2.166658	0.87794
PEO75	GPD1	1.07094	0.833764
PEO75	LPL	-3.37568	0.979455
PEO75	NR1H3	1.287173	0.640781
PEO75	LEP	3.978195	0.983742
PEO75	ADIPOQ	6.730573	0.732371
PEO75	LIPE	-0.89437	0.652451
PEO100	CD4	1.370116	0.756285
PEO100	ITGA1	-0.34598	0.55906
PEO100	ITGA3	0.998752	2.394753
PEO100	IL2R	1.210702	0.981945
PEO100	PTPRC	-0.53591	0.405808
PEO100	PAX3	6.127621	0.962124
PEO100	PAX7	-1.07343	0.345964
PEO100	MYOD1	4.07241	0.977558
PEO100	MYOG	0.802932	0.344737
PEO100	MYF5	3.806667	0.441186
PEO100	MYF6	5.932363	0.756505
PEO100	MEOX2	3.978212	0.757598
PEO100	FO XK1	0.429692	1.680422
PEO100	MEF2A	-0.45182	0.485854
PEO100	MEF2B	0.352557	0.525981
PEO100	MEF2D	0.744234	0.740492
PEO100	DES	-0.07962	0.342829
PEO100	MSX1	0.806522	1.114461
PEO100	MSX2	0.238	0.43344
PEO100	LBX1	0.522552	1.622484
PEO100	NRAP	1.210702	0.981945
PEO100	MYOT	-8.27747	0.732846
PEO100	TTN	1.210702	0.981945

PEO100	CDH15	1.210702	0.981945
PEO100	ITGB1	0.088255	0.49215
PEO100	CBFA1	-0.04613	0.462086
PEO100	CDH11	-0.19213	1.655917
PEO100	TFIP11	0.771565	1.790276
PEO100	TWIST1	0.510055	1.511759
PEO100	SMAD1	0.144588	0.44844
PEO100	SMAD2	0.351553	1.008139
PEO100	SMAD3	-0.03329	0.480252
PEO100	SMAD4	-0.00774	0.325843
PEO100	SMAD5	0.204285	0.734232
PEO100	SMAD7	0.411051	1.909378
PEO100	SMAD9	-0.41438	0.797263
PEO100	VDR	-0.18337	0.380349
PEO100	BGLAP	1.291338	0.881465
PEO100	BMP1	0.194126	1.116722
PEO100	BMP2	-0.19121	0.325783
PEO100	BMP3	-2.03472	0.375724
PEO100	BMP5	7.703177	0.701647
PEO100	BMP7	3.043535	0.799823
PEO100	BMPR1A	0.597017	0.985523
PEO100	MGP	4.095873	0.786124
PEO100	COL1A1	-0.45081	0.979023
PEO100	COL1A2	-0.16931	0.553459
PEO100	COL3A1	-0.95812	1.04123
PEO100	PPARG	2.884077	0.536932
PEO100	CEBPA	1.109925	0.910057
PEO100	CEBPB	0.20261	0.503924
PEO100	KLF15	-0.18834	0.315086
PEO100	FABP4	0.572557	0.593758
PEO100	GPD1	0.315069	0.602728
PEO100	LPL	-4.2548	0.858015
PEO100	NR1H3	0.126815	0.411545
PEO100	LEP	2.016579	0.428001
PEO100	ADIPOQ	3.49098	0.486457
PEO100	LIPE	-1.77349	0.555169